Memo 20-01

SKA1 Beyond 15GHz: The Science case for Band 6

J. Conway, R.Beswick, T.Bourke, M.Coriat, C.Ferrari, I.Jimenez-Serra, S.Muller, M.Sargent

February 2020

Contents

1 Introduction

John Conway (Onsala Space Observatory, Chalmers University of Technology, Sweden),
Mark Sargent (University of Sussex, Brighton, UK)

1.1 Background

The Square Kilometre Array telescope is the next huge step for global radio astronomy; enabling new categories of transformational science. The SKA is designed for at least a 50-year lifetime, i.e. stretching into the 2070s and beyond; during this time SKA's performance is expected to expand well beyond its initial capabilities. This growth is expected to include enormous advances in data processing and computing capabilities together with a target of substantially increased collecting area. An expanded SKA is also anticipated to incorporate new receivers/technologies to increase its field of view, bandwidth and frequency coverage.

At present the SKA community is fully concentrated on the task of building the initial stage of the SKA project, SKA Phase 1 (SKA1), including a baseline design for SKA1-Mid that stretches to a maximum frequency of 15.4 GHz. A possible expansion of SKA1-Mid to higher frequencies is however already included as an option in this initial design, with spaces provided to allow the installation of new receivers on SKA1-Mid dishes. Initial predictions of high frequency performance of the SKA1-Mid dish and site indicate that SKA1 could operate with a sensitivity many times better than current instruments at least up to 25 GHz and perhaps as high as 50 GHz (see Figure 1). SKA1's wide range of baselines, and its southern hemisphere location, supporting galactic science and providing synergies with ALMA and large optical/IR telescopes, are additional important advantages of a high frequency SKA1 compared to other instruments.

As the initial SKA1 baseline design begins construction, it is not too early to consider science beyond its initial deployment. In particular, it is anticipated that during the SKA construction phase there will be an ongoing SKA Observatory Development Programme (ODP) engaging worldwide partners to develop new technology for the SKA. Which future enhancement paths are eventually taken for SKA will depend on a combination of science impact, technical feasibility and cost. This memo presents the science case for including higher frequencies on SKA1. Based on the high impact science cases described in this memo, and given the low technical risk of adding such a capability, it seems likely that capabilities at frequencies higher than 15 GHz will eventually be added. This will allow SKA1-Mid's collecting area to be exploited over the full frequency range accessible to the SKA1-Mid dish and site.

1.2 Origin of this memo and relationship to engineering studies

This memo has been created by a process of soliciting science cases for frequencies higher than 15 GHz from the SKA science community via the SKA Science Working Groups. Within these contributions this high frequency SKA capability is referred to as 'Band 6' or 'Band 5+'. The technical aspects of whether the full range of frequency 15 - 50 GHz would be covered and whether this would be achieved by one or two receiver bands is not considered in this memo. A separate engineering Advanced Instrumentation Programme/Observatory Development Programme group for 'Advanced Single Pixel Feeds and Receivers' (ASPFR) is considering high frequency SKA receceivers as one possible future upgrade to the SKA receiver suite (other goals include the final design of Bands 3 and 4, future ultra wide-band receivers covering multiple existing SKA bands, and advanced enabling technologies such as cryogenic and ambient temperature LNAs, cooling systems, digitisers etc).

1.3 Sensitivity Assumptions

Until designs of high frequency receivers are finalised and the high frequency dish performance is fully characterised exact sensitivity numbers for SKA1-Mid at high frequency will remain uncertain. In guiding the science cases in this memo performance estimates were given to contributors based on the document 'Anticipated SKA1 Science Performance' (SKA-TEL-SKO-0000818, 2017-10-17, see also *arXiv:1912.12699*). These high frequency performance estimates, especially around the 22 GHz water line, are also affected by the amount of atmospheric water vapour at the site. While there are as of yet no in-situ measurements of water vapour statistics at the SKA1-Mid site, global weather forecasting models can be used to predict the statistical distribution of the precipitable water vapour (pwv) column. These models, as summarised in the above SKA1 performance document, predict that during winter pwv < 5 mm conditions should be relatively common, therefore in this memo a pwv $=$ 5 mm has been used in calculating the array sensitivity versus frequency (see Figure 1). The same assumption is used for calculating the expected image noise per one hour integration (see Figure 2) for spectral line and continuum observations. These image noise levels are estimated at 2/2.5 times (for respectively continuum and lines) the natural weighting noise to take into account typical losses in sensitivity due to uv weighting to achieve different spatial resolutions (see Section 10 of Science Performance document for details). Because many of the > 15 GHz science cases are extensions of cases for Bands 5a,b and/or require complementary observations in these bands sensitivity estimates are shown in Fig 2 and in the Appendix over the full Band 5/6 range of 4.6 - 50 GHz.

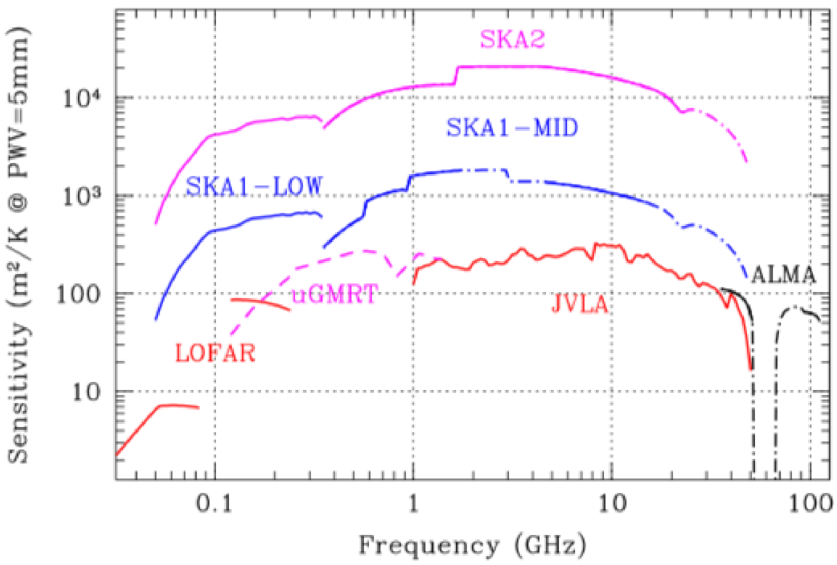

[h!]

Figure 1: Expected array sensitivity of SKA1 compared to existing and planned facilities, taken from 'Anticipated SKA1 Science Performance' (SKA-TEL-SKO-0000818, 2017-10-17) Braun et al. 2017 (SKA-TEL-SKO-0000818, see also *arXiv:1912.12699*). The estimated performance at frequencies not covered by the initial SKA1 receiver deployment are shown by dot-dashed lines. Dry conditions (PWV = 5mm) are assumed for the SKA and VLA sites while the same PWV = 5mm corresponds to poor conditions for the ALMA site.

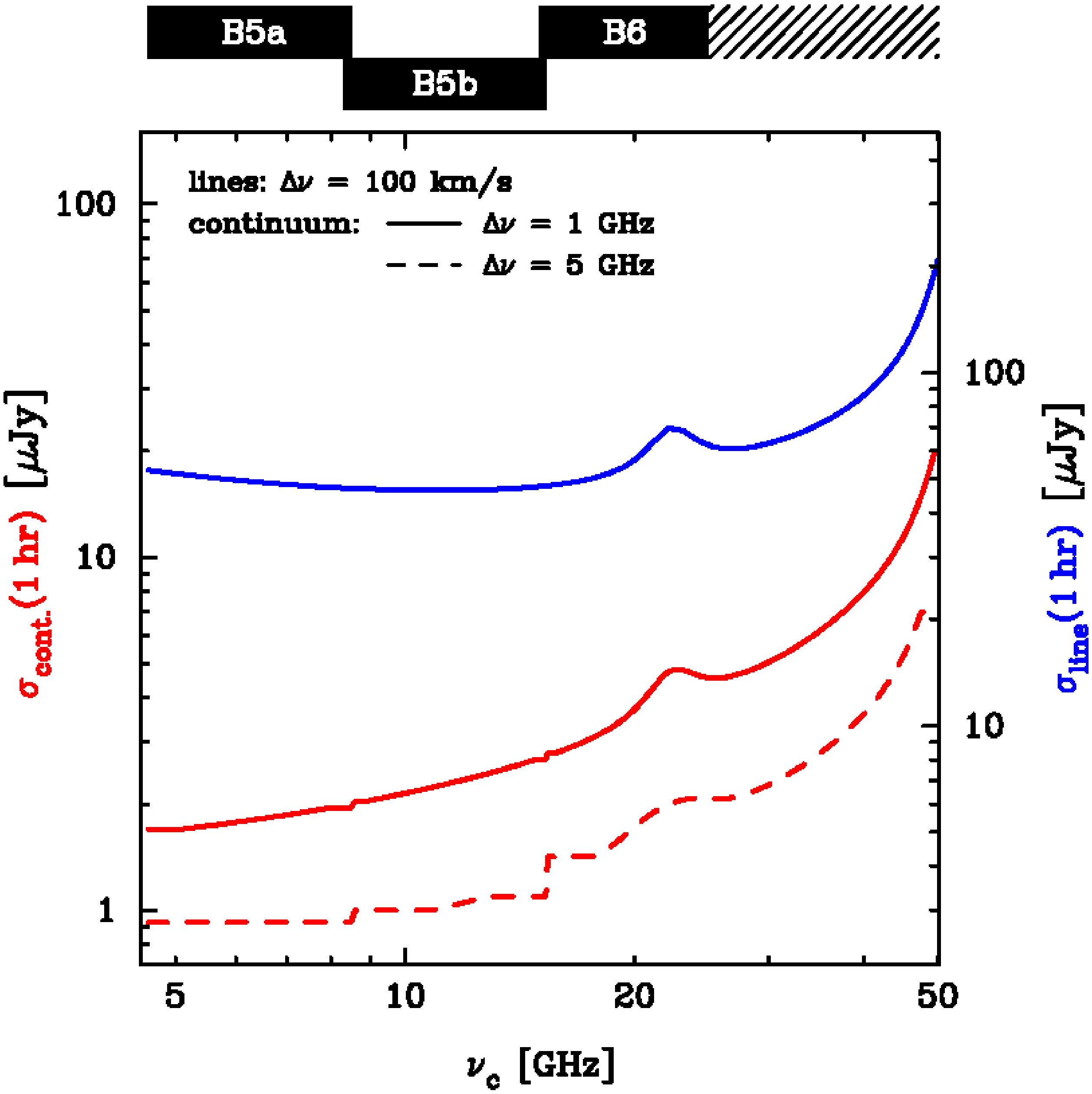

[h!]

Figure 2: Anticipated imaging sensitivity performance of SKA1-MID in the 4.6–50 GHz frequency range, assuming receiver deployment on 133 MID dishes and 1 hr on-source integration (see text for further details). Sensitivity estimates for continuum observations (red lines) are shown assuming continuum bandwidths of 1 GHz (full line) and for the maximal available instantaneous bandwidth of 5 GHz (dashed line). The line sensitivity (blue line) is shown for a 100 km/s frequency. The scales for the continuum and line sensitivity are shown on the left and right, respectively. The tuning ranges of SKA1-MID band 5a, 5b and 6 are shown along the upper edge of the figure

In Figure 2 image sensitivity estimates are given for instantaneous continuum bandwidths of 1 and 5 GHz (red lines), as well as for a 100 km/s window for spectroscopic applications (blue line). The latter corresponds to a frequency-dependent instantaneous bandwidth $\Delta\nu$ in frequency space, leading to different slopes for the red and blue lines in Figure 2. For continuum observations the current maximum available instantaneous bandwidth in the SKA1 design is two tuneable 2.5 GHz wide bands per polarisation i.e. a 5 GHz spanned bandwidth in each polarisation. This maximum limit is set by the designs for SKA1-Mid data transport, correlator and science data processor. In calculating sensitivity versus frequency, ν_c, the instantaneous continuum bandwidth $\Delta\nu$ is assumed centred on ν_c, unless this causes the spanned band to extend beyond the edge of a given receiver band. In such cases, the continuum bandpass is instead centred at the closest permissible frequency, i.e. offset by an amount $\Delta\nu/2$ from the band edge. Since the full Band 5a (4.6–8.5 GHz) is narrower than the available instantaneous bandwidth of 5 GHz (giving an effective maximum Band 5a bandwidth 3.9 GHz) a single continuum sensitivity is plotted for Band 5a continuum observations made at full bandwidth. Similarly, for Band 5b the wide-band sensitivity can effectively be approximated by just two values, representing the performance in the lower and upper half of the band respectively.

2 Solar System

2.1 Trans-Neptunian Objects and Centaurs with the SKA

Pablo Santos-Sanz (Instituto de Astrofísica de Andalucía-CSIC, Granada, Spain), Thomas G. Müller (Max-Planck-Institut für extraterrestrische Physik (MPE), Garching, Germany), Jorma Harju (Department of Physics, University of Helsinki, Finland / MPE, Garching, Germany), Emmanuel Lellouch (LESIA-Observatoire de Paris, CNRS, France), Iván Agudo (Instituto de Astrofísica de Andalucía-CSIC, Granada, Spain)

SKA will be particularly important to characterize distant Solar System objects, like Trans-Neptunian Objects (TNOs) and Centaurs. It is believed that these objects, together with Comets, are the most pristine leftovers of the Solar System formation and in that sense they provide a link to protoplanetary disks observed around other stars. SKA observations will be pivotal for the physical, thermal and compositional characterization of individual TNOs/Centaurs and to understand alteration processes that take place on the (sub-)surface of these bodies. SKA will contribute to a better understanding of the thermal, dynamical and collisional history of the primitive Solar System (e.g. DeMeo & Carry, 2014). The SKA results on outer Solar System bodies will provide hints about formation locations of different dynamical families, like the various TNO populations (including Centaurs), Jupiter-family comets, Trojans and some of the satellites of the giant planets. Planetary migration theories can also be constrained using SKA results for these bodies.

2.1.1 Science Justification

Previous studies of the thermal emission of TNOs and Centaurs were based on Spitzer Space Telescope (Stansberry et al., 2008), Herschel (Müller et al., 2009), WISE (Bauer et al., 2013), and very recently also on ALMA (Moullet et al., 2011; Gerdes et al., 2017; Brown & Butler, 2017, 2018; Lellouch et al., 2017). A summary of the results of these thermal studies was presented by Müller et al. (2019). In the near-to-mid-term future, there will be no airborne- or space-based option to directly measure these remote and cold objects at their thermal emission peak (around 50-100 micron): SOFIA or potential balloon-borne observatories do not reach the required sensitivity, except maybe for the very largest TNOs or closeby Centaurs. JWST's wavelength coverage will end at 28 micron (MIRI: Rieke et al., 2015) and it will not be efficient to measure radiometric diameters, albedos or surface emission properties. From the ground, the thermal emission of TNOs can only be reached at the mm/cm wavelength range. Recent ALMA measurements of 10 objects (Brown & Butler, 2017; Lellouch et al., 2017) show long-wavelength emissivity effects and spectral emissivity variations. Grain sizes certainly play a key role to explain part of the findings, but no clear correlations with physical or compositional properties were found. ngVLA (de Pater et al., 2018) will provide a small improvement (in terms of SNR and spatial resolution) over VLA or ALMA, but the TNO studies will still be limited to a very small number of the largest objects only.

-Thermal emission of TNOs and Centaurs with the SKA The measure of the thermal emission of TNOs and Centaurs provides a unique way to obtain sizes, albedos and information on the thermal regime (e.g. thermal inertia –Γ–, surface roughness, etc) of the (sub-)surfaces of these objects via thermal and thermo-physical models, as has been extensively demonstrated by the 'TNOs are Cool' Herschel Space Observatory key project (Müller et al., 2009; Lellouch et al., 2013; Santos-Sanz et al., 2017, and references therein). We explore here if it would be possible to detect the thermal emission of TNOs/Centaurs with the SKA in order to derive their sizes, albedos and Γ's. To reply to this question we used the current expected sensitivity of the SKA (based on the report *SKA-TEL-SKO-0000818-01, 2017*) to estimate the minimum observable flux at 5σ on broad band continuum observations for the SKA1 at different wavelengths of Band 5 (6.5 cm, 3.5 cm, 2 cm) and Band 6 (1.2 cm, 0.7 cm) -see Table 1.

We can estimate the expected thermal fluxes for the largest TNOs and Centaurs at the Band 5 and Band 6 wavelengths of Table 1, assuming a relative spectral emissivity (i.e. $\epsilon_\lambda/\epsilon_b$, where ϵ_λ is the emissivity at the observing wavelength and ϵ_b is the bolometric emissivity) of 0.7 as obtained from

Table 1: Minimum observable flux on broad band continuum observations for the SKA1 and VLA (5σ) at different Band 5 and Band 6 wavelengths for 60 minutes observations. VLA fluxes are obtained from the VLA simulator (https://obs.vla.nrao.edu/ect/). The SKA1 sensitivity is about a factor of 3 better than VLA.

Band [cm]	**Flux(SKA1)** [μ**Jy**]	**Flux(VLA)** [μ**Jy**]
0.7	16.00	45
1.2	8.50	25
2.0	6.25	24
3.5	6.00	14
6.5	7.50	25

Herschel and Spitzer measurements combined with new ALMA observations at millimeter wavelengths (Lellouch et al., 2017; Brown & Butler, 2017). We extrapolate the thermophysical models used to fit the Herschel/Spitzer/ALMA thermal data in order to obtain the expected thermal fluxes at the SKA Band 5 and Band 6 wavelengths. The estimated thermal fluxes for 10 of the largest TNOs and Centaurs obtained in this way are shown in Table 2. From Table 1 and Table 2 it is clear that all the objects will be detectable (in 1 hour at 5σ) at 0.7 cm and half of them at 1.2 cm. We have extended the flux estimations of Table 2 to the 30 largest TNOs and Centaurs and our general conclusion is that it will be possible to detect the thermal emission with the SKA1 for most of the TNOs larger than 300 km and for the largest Centaurs. With the SKA2 (around 10 times more sensitive than the SKA1) it will be possible to detect the thermal emission for all the (currently) known TNOs and Centaurs. These measurements will be mostly feasible at the shortest SKA wavelengths (1.2 cm and 0.7 cm) so, to detect the thermal emission of TNOs and Centaurs with the SKA, Band 5 and Band 6 will be required.

Thermal emission measurements of TNOs/Centaurs with the SKA will allow to study what happens with the relative spectral emissivity at long (centimeter) wavelengths, and what it tells us about the subsurface of these bodies. In general, the spectral emissivity of TNOs decreases longwards of ~ 200 micron and up to at least the mm range (Fornasier et al., 2013; Lellouch et al., 2017), sometimes in a strongly chromatic manner (Brown & Butler, 2017). Causes for this decrease include (i) subsurface sounding of a colder (on the dayside) sub-surface, up to meter- or more depths, possibly probing the seasonal wave, (ii) dielectric reflection at the surface of the upward thermal radiation, (iii) volume scattering of voids or impurities, that produces emissivity minima for typical particle size of $\lambda/4\pi$. Obtaining multi-wavelength continuum fluxes with SKA, and combining results with other facilites such as ALMA would be a great asset to disentangle these various effects and constrain the thermal / physical properties of the sub-surfaces. These emissivity studies can be done for TNOs/Centaurs for which we have already size and thermal inertia estimates (mostly from Spitzer/Herschel data), this would provide a benchmark study on the emissivity behaviour. These results on the emissivity can be used to obtain sizes and thermal properties for many more TNOs/Centaurs for which we haven't thermal data. Last but not least, these SKA results will enable us (i) to improve the number of objects with determined size, albedo and thermal properties, (ii) to obtain mass densities for multiple/binary systems for which the masses are known (e.g. Mommert et al., 2012; Santos-Sanz et al., 2012; Vilenius et al., 2012, 2014; Fornasier et al., 2013), (iii) to refine the knowledge of the size distribution of these bodies that is related with the collisional history of the outer Solar System.

Other possible science cases with the SKA at Band 5 and Band 6 that we are exploring and that deserve a more exhaustive analysis include (a) the separate detection of the thermal emission from binary/multiple systems –all large TNOs have satellites–, (b) the detection of thermal spatial features of large to intermediate-size objects, (c) the detection and characterization of rings around these objects, as those discovered around the TNO and dwarf planet Haumea (Ortiz et al., 2017) and the Centaurs Chariklo (Braga-Ribas et al., 2014) and Chiron (Ortiz et al., 2015), (d) the possibility to use VLBI + SKA1-Mid South Africa to directly measure sizes and shapes of these bodies, etc. Finally, at lower SKA frequencies (e.g. the OH lines at ~ 1.7 GHz of Band 2) we could open up a field to study these water-ice objects and if they develop local/global atmospheres, if there is outgassing, cryovolcanism, which would be of great relevance to understand their formation, surface processes and composition.

Table 2: Expected thermal fluxes for 10 of the largest TNOs and Centaurs at a few selected wavelengths of Band 5 and Band 6. **Object** is the name of the TNO/Centaur; **Type** is the dynamical classification of the object; **D** is the area-equivalent diameter in kilometers and milliarcseconds (mas); $\mathbf{F}_{0.7cm}$-$\mathbf{F}_{6.5cm}$ are the estimated thermal fluxes in micro-Jansky (μJy) at these wavelengths; $\mathbf{T}_b$ is the brightness temperature in Kelvin.

Object	**Type**	**D** [km/mas]	$F_{0.7cm}$ [μJy]	$F_{1.2cm}$ [μJy]	F_{2cm} [μJy]	$F_{3.5cm}$ [μJy]	$F_{6.5cm}$ [μJy]	T_b [K]
Pluto	TNO Plutino	2380/100	477.8	120.9	48.4	15.8	4.60	36.5
Eris	TNO Detached	2326/33	28.77	7.35	3.05	1.00	0.29	22.1
Haumea	TNO Classical	1595/43	63.63	16.19	6.70	2.20	0.64	28.3
2007 OR_{10}	TNO SDO	1535/24	18.53	4.72	1.96	0.64	0.19	26.2
Makemake	TNO Classical	1430/38	44.97	11.45	4.75	1.56	0.45	26.6
Quaoar	TNO Classical	1071/34	51.80	13.12	5.26	1.72	0.50	36.4
Chariklo	Centaur	241/21	38.02	9.57	3.95	1.29	0.37	68.4
2002 GZ_{32}	Centaur	237/17	24.78	6.24	2.58	0.84	0.25	66.4
Chiron	Centaur	210/15	18.43	4.64	1.91	0.62	0.18	66.3
Bienor	Centaur	199/16	21.46	5.40	2.23	0.73	0.21	63.5

- Radio occultations by TNOs and Centaurs with the SKA

Radio occultation observations provide an efficient way to determine sizes and shapes of minor bodies, as well as their positions during occultation events (Lehtinen et al., 2016; Harju et al., 2018). SKA will observe the radio "shadows" of most of the known TNOs in the Fraunhofer diffraction regime, where the extent of the dark and bright fringes exceeds greatly the geometrical silhouette of the object (Trahan & Hyland , 2014). This spreading out (in space and time) makes occultations more frequent in a particular spot, but it also weakens the signal, that is, the amplitude and phase changes caused by the diffraction of background radiation from the edges of the occulter.

An extension of the SKA1-MID frequency range above 15 GHz will be beneficial for occultation observations. The diffraction patterns become sharper at higher frequencies, and the starker contrasts between minima and maxima more than compensate the decrease of the SKA sensitivity at least up to 30 GHz. Also, the shorter duration of the occultation event at higher frequencies put less stringent demands on the phase stability. These improvements facilitate the determination of the exact time and distance of closest approach to the background source, and the detection of asymmetries that can be used to infer the TNO shape and the existence of possible binary companions or moons.

The contrasts between the maxima and minima in the observable amplitude and phase time series during an occultation depend on the Fresnel number, F, defined by $F = a^2/z\lambda$, where a is the TNO radius, z is the distance to the observer, and λ is the wavelength. Using the anticipated Band 6 ($\lambda \sim 1\,\mathrm{cm}$) sensitivity of SKA1-MID ($A_\mathrm{e}/T_\mathrm{sys} \sim 450\,\mathrm{m}^2\,\mathrm{K}^{-1}$ for the full array), and a time resolution (correlator integration time) of 0.1 s, one can estimate that the minimum size of a TNO detectable by an occultation measurement at $\lambda = 1\,\mathrm{cm}$ with a S/N ratio of 50 is $a_\mathrm{min}[\mathrm{km}] \sim 10\sqrt{z[\mathrm{au}]}$. Here we have used the minimum Fresnel number criterium $F \geq 0.1$, and the assumption that only half of the baselines are useful because of the finite size of the diffraction pattern. For the background source flux density we have used the median of Radio Fundamental Catalog[1] sources detected in the K-band (270 mJy).

The diffraction patterns of detectable TNOs are typically larger than the full extent of the SKA-MID array ($\sim$ 150 km). Measuring both the amplitude and phase changes (see Figure 2.1.1) would ideally require that a phase reference is observed also during the occultation. This can be accomplished using VLBI, where part of the antennas staring at the background source remain outside the shadow.

[1]http://astrogeo.org/rfc

In case VLBI cannot be used, phase calibration relies on the measurements before and after the occultation. The time-scales of the phase drifts caused by instrumental effects and the atmosphere are sufficiently long for this. The possibility of employing multiple beams within the FOV of the SKA-MID antenna is probably not helpful here because of the scarcity of suitable K-band calibrators.

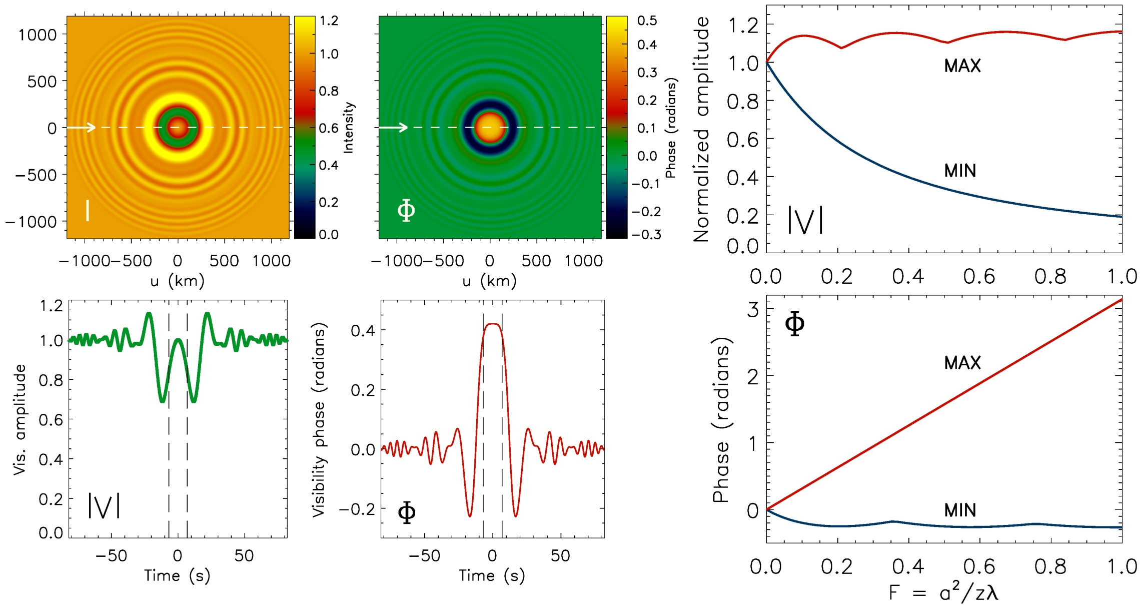

Figure 3: **Left:** Diffraction patterns observed on Earth during a radio occultation by a TNO with a circular shape. The diameter and the distance of the TNO are assumed to be 200 km and 50 au, respectively. The frequency is 30 GHz ($\lambda = 1$ cm). The Fresnel number is $F = 0.13$. The top panels show the intensity and phase patterns projected on a plane perpendicular to the direction of the source. The bottom panels show the time-series of the visibility amplitude and phase observed with a radio interferometer as the "shadow" sweeps across the instrument. Here the occultation is central as indicated by the dashed lines in the top panels. The vertical lines in the bottom panels correspond to the immersion and emergence times at visual wavelengths. Note the Arago spot indicating the moment of the closest approach. **Right:** Maximum and minimum visibility amplitudes and phases as functions of the Fresnel number.

2.1.2 Technical Justification

In previous sections we show that the thermal emission from both TNOs and Centaurs typically peaks in the far-IR, more concretely in the $\sim$ 50-100 micron wavelength range. The emission then fades rapidly towards the radio spectral domain. So much that current radio instrumentation makes high SNR observations in the centimeter wavelength range of these objects feasible only for Pluto. In the long millimeter range ($\sim$ 7 mm), three additional TNOs may just exceed the detection levels of the JVLA. This is simply not enough for developing the two science cases described in the sections above, i.e. both measurements of the thermal emission of TNOs and Centaurs, and measurements of their sizes and shapes by occultations of background radio sources.

Our estimates shown in Tables 1 and 2 clearly point out that, thanks to the superior sensitivity of SKA1-MID, the two bigger and closer objects (Pluto and Haumea) will already be detected at 15 GHz ($\sim$ 2 cm) within Band 5. This is an improvement of only one single additional object in reach with SKA1-MID with regard to JVLA. Therefore, Band 5 alone will not help to allow for a major breakthrough in the field. This situation is reverted with the addition of Band 5+, which will allow SKA1-MID observations up to at least 25 GHz ($\sim$ 1 cm) of four additional objects not currently in reach. But perhaps, an actual breakthrough will come with Band 6, where observations at the high end of the band ($\sim$ 43 GHz, 0.7cm) will allow all the largest currently known TNOs and Centaurus to be observed –at high SNR in most of the cases. Clearly, this will allow for statistical characterization of the thermal emission of these objects. Even small number statistics will be extremely informative. Therefore, science with radio observations of TNOs and Centaurs will experience a dramatic boost thanks to the development of Band 6, but also of Band 5+.

References

Bauer, J. M., Grav, T., Blauvelt, E., et al. 2013, ApJ, 773, 22
Braga-Ribas, F., Sicardy, B., Ortiz, J. L., et al. 2014, Nature, 508, 72
Brown, M. E., & Butler, B. J. 2017, AJ, 154, 19
Brown, M. E., & Butler, B. J. 2018, AJ, 156, 164
DeMeo, F. E., & Carry, B. 2014, Nature, 505, 629
de Pater, I., Butler, B., Sault, R. J., et al. 2018, Science with a Next Generation Very Large Array, 49
Fornasier, S., Lellouch, E., Müller, T., et al. 2013, A&A, 555, A15
Gerdes, D. W., Sako, M., Hamilton, S., et al. 2017, ApJL, 839, L15
Harju, J., Lehtinen, K., Romney, J., et al. 2018, AJ, 156, 155
Lehtinen, K., Bach, U., Muinonen, K., et al. 2016, ApJ, 822, L21
Lellouch, E., Santos-Sanz, P., Lacerda, P., et al. 2013, A&A, 557, A60
Lellouch, E., Moreno, R., Müller, T., et al. 2017, A&A, 608, A45
Mommert, M., Harris, A. W., Kiss, C., et al. 2012, A&A, 541, A93
Moullet, A., Lellouch, E., Moreno, R., et al. 2011, Icarus, 213, 382
Müller, T. G., Lellouch, E., Böhnhardt, H., et al. 2009, Earth Moon and Planets, 105, 209
Müller, T., Lellouch, E., & Fornasier, S. 2019, arXiv e-prints, arXiv:1905.07158
Ortiz, J. L., Duffard, R., Pinilla-Alonso, N., et al. 2015, A&A, 576, A18
Ortiz, J. L., Santos-Sanz, P., Sicardy, B., et al. 2017, Nature, 550, 219
Rieke, G. H., Wright, G. S., Böker, T., et al. 2015, PASP, 127, 584
Santos-Sanz, P., Lellouch, E., Fornasier, S., et al. 2012, A&A, 541, A92
Santos-Sanz, P., Lellouch, E., Groussin, O., et al. 2017, A&A, 604, A95
Stansberry, J., Grundy, W., Brown, M., et al. 2008, The Solar System Beyond Neptune, 161
Trahan R. & Hyland, D. 2014, ApOpt, 53, 3540
Vilenius, E., Kiss, C., Mommert, M., et al. 2012, A&A, 541, A94
Vilenius, E., Kiss, C., Müller, T., et al. 2014, A&A, 564, A35

2.2 Microwave Emission of Solar Flares

Siming Liu (Purple Mountain Observatory), Ping Zhang (Purple Mountain Observatory), Lu Wang (Purple Mountain Observatory)

As the brightest source in the Sky, the Sun is one of the primary targets of many radio telescopes. In the micro-wave range, besides quiescent emission from the solar disk, solar flares can produce prominent emission via the synchrotron and bremsstrahlung processes (Dulk 1985). The former reveals physics of high-energy electron acceleration. The latter is associated with the coronal response to the flare energy input (Zhang et al. 2018).

Figure 4 shows microwave observations of a solar flare occurred on Aug 27 2015 by the Nobeyama radio polarimeter and Heliograph (17 and 34 GHz). The impulsive emission mostly comes from a compact emission region as shown in the insert image. This emission is produced by energetic electrons via the gyrosynchrotron process. The gradually evolving emission component has contributions from both the gyrosynchrotron and bremsstrahlung processes.

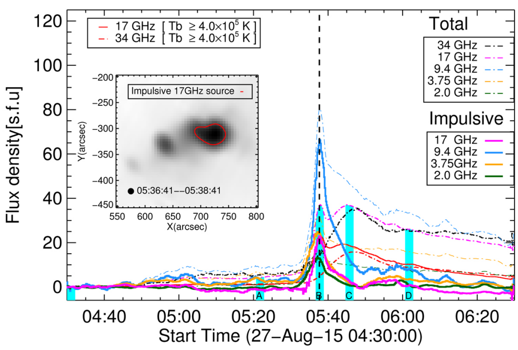

Figure 4: Microwave flux variation from different emission regions of a solar flare obtained with Nobeyama Radio Polarimeter and Heliograph.

2.2.1 Spectrum

Figure 23 shows the spectrum of the impulsive emission at the flux peak. It can be seen that the spectrum peaks in the microwave range. The location of this peak can be used to constrain the magnetic field of the emission region. The overall spectral shape can be used to constrain the energy distribution of the accelerated electrons.

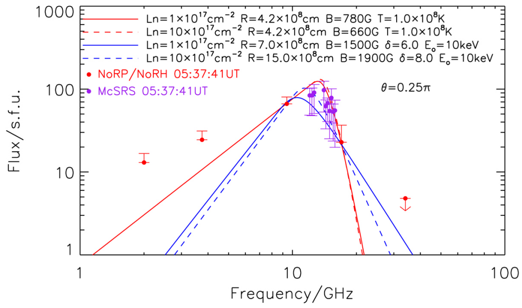

Figure 5: Microwave spectrum of the impulsive emission component of the flare in Figure 48 at the emission peak.

2.2.2 Imaging

Figure 6 shows the structure of hot plasmas revealed with EUV images of the Solar Dynamics Observatory. These hot plasmas can produce microwave emission via the bremsstrahlung process.

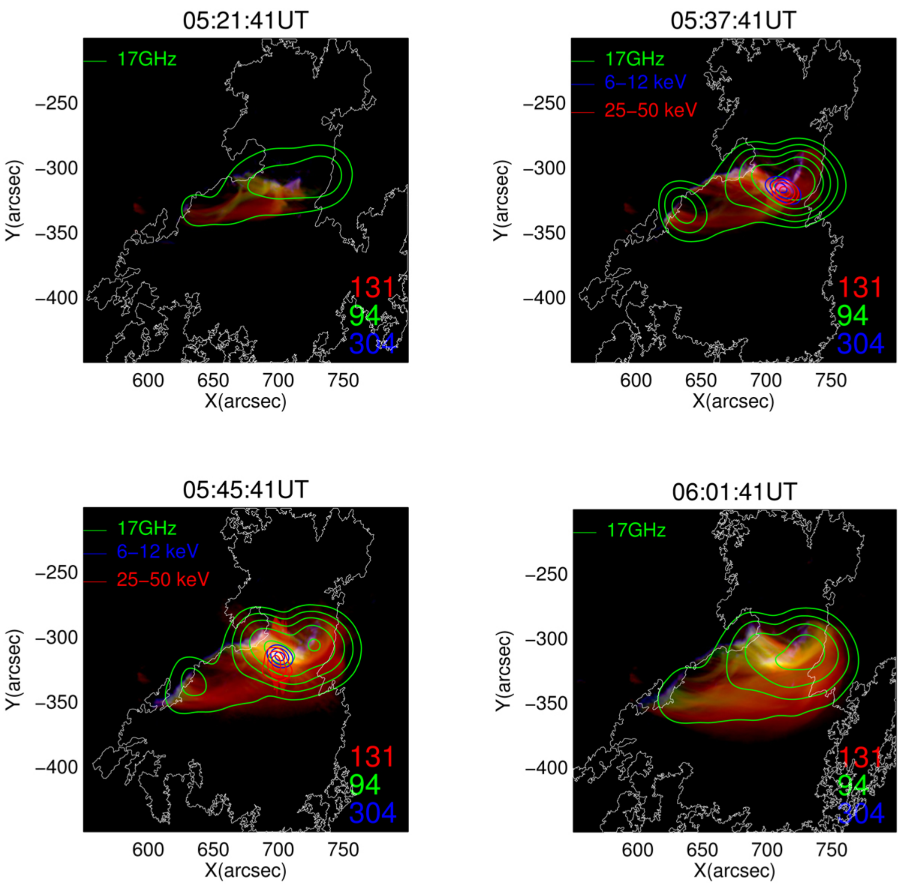

Figure 6: Contours of radio image at 17 GHz overplotted on EUV images obtained with the Solar Dynamics Observatory. X-ray contours in the impulsive are also indicated.

2.2.3 Technical Justification

Solar flares are driven by complex magnetic energy release processes. Their energy release can spread over many orders of magnitude. Prominent microwave emission are usually produced by large flares. The emission usually peaks in the frequency range of 1 to 100GHz. It is evident that the electron acceleration process can be better studied with high resolution polarimetric imaging spectroscopy. To optimize the study of electron acceleration in large solar flares, the angular resolution needs to be better than 1 arcsec, the time resolution should be better than 1 second, while a spectral resolution of hundreds of MHz is sufficient. Given the high microwave flux from solar flares (usually much more than 10 kJy), the signal can be easily detected. However, one does need to consider the relatively high level of steady background emission from the solar disk. In most cases, microwave emission from solar flares is also strongly polarized. Polarization measurement is desirable.

References

Dulk, G. A., 1985, ARAA, 23, 169
Zhang, P., Guo, Y., Wang, L., & Liu,S.M., 2018, A&A, 615,48

3 Star formation, astrochemistry and life

3.1 Grain growth and planet formation with the SKA

Josep Miquel Girart (Institut de Ciències de l'Espai - CSIC / IEEC, Catalonia), John Ilee (University of Leeds, UK), Cassandra Hall (University of Leicester, UK), Izaskun Jiménez-Serra (Centro de Astrobiología, INTA-CSIC, Spain), Melvin Hoare (University of Leeds, UK), Gemma Busquet (Institut de Ciències de l'Espai - CSIC / IEEC, Catalonia), Kazy L. J. Rygl (INAF Istituto di Radioastronomia & Italian ALMA Regional Centre, Italy), Wouter H. T. Vlemmings (Chalmers University of Technology, Onsala Space Observatory, Sweden), and Leonardo Testi (European Southern Observatory, Germany)

3.1.1 The ALMA View

It is currently accepted that protoplanetary disks are the birth-place of planets. The physical processes that lead to the formation of planets, however, remain vastly uncertain. The growth of small (μm–mm size) dust grains to larger (km size) planetesimals is an essential step in this process, and therefore, most of the efforts of the star formation community in the past years have focused on understanding how dust grains grow and evolve in protoplanetary disks.

Thanks to ALMA, it has become clear that most protoplanetary disks present a common physical structure with concentric rings and gaps (e.g. Huang, et al., 2018). Although still controversial[2], there is increasing evidence that gaps in protoplanetary disks are produced by the presence of young protoplanets or planetary embryos (Isella et al., 2019; Tsukagoshi et al., 2019). As shown in Figure 1 of Hoare et al. (2015), at centimeter wavelengths dust opacity is dominated by centimeter-sized particles, while at millimeter wavelengths the brightest dust emission arises from millimeter-sized dust grains. As a result, ALMA, which covers the wavelength range between 3 mm up to 0.3 mm, can observe millimeter-sized dust grain particles in disks, but is *blind* to dust grains of centimeter-sizes and larger. The best way to probe grain growth is thus to carry out observations of the dust thermal emission at long wavelengths, not only to measure whether protoplanetary disks host large dust grains (>1 cm), but also to establish whether the dust grain sizes evolve with time within protoplanetary disks.

3.1.2 Dust grain properties from the spectral index

The optical properties of dust grains change with their size. One can therefore use the slope (or spectral index, α) of the mm–cm spectral energy distribution ($F_\nu \propto \nu^\alpha$) to derive a dust opacity law

[2] Note that the formation of gaps in disks can also be explained by a change in dust opacity due to a change in material grain composition (see e.g. Carrasco-González et al. 2016).

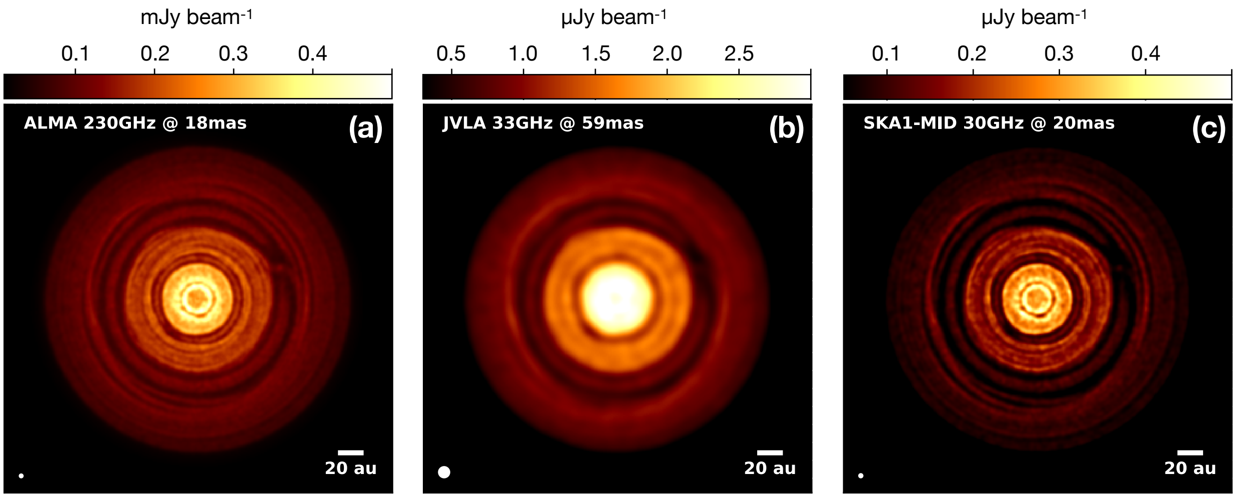

Figure 7: Radiative transfer modelling of a planet forming within a protoplanetary disk, simulated using hydrodynamics with a decoupled dust component. Panels show frequencies and angular resolutions appropriate for *(a)* ALMA, *(b)* JVLA and *(c)* SKA1-MID. In order to achieve comparable angular resolution between the mm and cm regimes, SKA1-MID is required at frequencies $\gtrsim$25GHz (Hall & Ilee, in prep.)

($\kappa_\nu \propto \nu^\beta$) in order to measure changes in dust properties, particularly their maximum size (Testi, et al., 2014, and references therein). In the optically thin case, the relationship between the spectral index α and opacity index β is such that $\alpha = \beta + 2$. In the interstellar medium, measured values of α are approximately 3.5, indicating dust grains of sizes no larger than a few microns. In protoplanetary disks measured spectral indices are much lower, with $\alpha \sim 2$, indicating grains have grown to at least millimetre sizes (see, e.g., Wilner, et al., 2000).

Measurement of the spectral index α in protoplanetary disks requires high precision photometry that, crucially, covers a large enough 'lever-arm' in frequency to allow an accurate slope to be determined. Spatially-resolved observations are also essential to measure localised variations across disks. First attempts at this hinted at (azimuthally-averaged) radial variations in dust properties in disks (e.g. Isella, et al., 2010), but the limited frequency spacing between 100–230 GHz (3–1.3 mm) resulted in significant uncertainties. However, utilisation of the Karl G. Jansky Very Large Array (JVLA) with frequencies down to ~30 GHz (1cm) confirmed this radial variation (see Pérez, et al., 2015). It is therefore clear that observations at these frequencies are essential in measuring spectral indices in protoplanetary disks.

The recent discovery of small-scale (a few au) substructure in sub-mm observations of protoplanetary disks has resulted in numerous theories about their origin (e.g. vortices, instabilities, dust traps, or young planets). Measuring the spectral index, and therefore the properties of the dust grains within these features is an essential requirement in determining their nature. However, it is currently not possible to produce maps of azimuthal variations in spectral index across disks at these scales. This is due to the limited spatial resolution of currently available instruments operating at 10's of GHz. Figures 7a & 7b show a comparison of the best available spatial resolution for ALMA operating at 230 GHz (1.3mm) and the JVLA at 33 GHz (1cm). The JVLA observations are almost a factor of 3 worse in terms of spatial resolution, resulting in a significant loss of information on the scales of these features (e.g. a few au for disks in nearby star forming regions). Comparably high resolution observations at lower frequencies are therefore essential if we are to determine the local properties of dust in disks.

3.1.3 Polarization as a tool to study grain growth and evolution

In addition to the small-scale structure revealed by ALMA in protoplanetary disks, the polarization capabilities of this interferometer have also triggered a boost of new results regarding the dust linear polarization from core (few thousands of au) to disk (few tens of au) scales. On one hand, at cores scales, dust polarization appears to be produced by fast-rotating aspherical grains aligned with the magnetic field (Lazarian, & Hoang, 2007; Hoang, & Lazarian, 2008). Thus, dust polarization observations are key to better understand the role of the magnetic field in this phase. ALMA has revealed polarization features in the outflow cavities and in filament-like dust structures that cannot be easily explained by current alignment theories (Maury et al., 2018; Le Gouellec et al., 2019; Hull et al., 2019). On the other hand, the dust polarization measured at disk scales has shown that the main mechanism appears to be produced by self-scattering of large dust grains, $\sim$50–500 μm (Kataoka et al., 2015, 2016; Fernández-López et al., 2016; Girart et al., 2018; Hull et al., 2018; Bacciotti et al., 2018; Dent et al., 2019; Sadavoy et al., 2019). Self-scattering is a powerful tool to study dust grain growth and dust settling/drifting process in disks (Kataoka et al., 2016; Yang et al., 2016, 2017). However, there are a number of sources where self-scattering can not explain partially or totally the observed polarization properties (Stephens et al., 2017; Alves et al., 2018; Ohashi et al., 2018; Sadavoy et al., 2019). Different physical mechanisms have been invoked to generate the dust polarized emission, which in most cases requires non-spherical grains: the classical alignment with magnetic fields, mechanical alignment due to gas to dust drift, or anisotropic radiation alignment grains (Tazaki et al., 2017; Kataoka et al., 2019; Yang et al., 2019). Despite of all these different mechanisms, these works show that polarization is a powerful tool to study the physical properties of the disks and the evolution of dust particles, which may be related to planet formation. Deep multi-frequency and high angular resolution observations are necessary to fully characterize the polarization properties and differentiate between the various polarization machenisms. In particular, as described in Section 3.1.2, the frequencies covered by Band 5 and 6 are important to trace large, pebble-like, dust grains.

3.1.4 Band 5 versus Band 6 receivers

Given the above requirements for a sufficiently large frequency coverage, the SKA Band 5 (4.6–15.3 GHz) receivers may initially seem optimal for measurements of spectral index between the mm and cm regimes. However, at frequencies $\lesssim$15 GHz, significant contamination from free-free and synchrotron emission is expected in young stellar objects (see AMI Consortium: Ainsworth et al., 2012; Coutens, et al., 2019), making measurements of changes in spectral index due to dust in the disk non-trivial. Higher frequencies in Band 6 (between 15–50 GHz) would reduce any contamination from these two components (free-free and synchrotron) with the added benefit of significantly improved spatial resolution. Figure 7 compares the best available resolution of ALMA at 230 GHz (18mas), the JVLA at 33 GHz (59mas), and SKA1-MID at 30 GHz (20mas). Only by moving to these Band 6 frequencies will SKA1-MID be able to observe dust emission in protoplanetary disks at comparable spatial resolution to ALMA. Such high spatial resolution is key if we are to determine the properties of dust in small scale features, and also toward the inner disk (<10 au) where terrestrial planets are thought to form. Using the results in Figure 7c as a guide, a typical surface brightness within a radius of $\sim$20 au at 30 GHz is $0.4\,\mu\mathrm{Jy\,beam}^{-1}$. Based on the predicted sensitivity of SKA at this frequency, using a bandwidth of 5 GHz, this region could be imaged with a signal-to-noise ratio of 3 in approximately 300 hours of integration time. While not possible with a single observation, this would be easily achievable by combining observations across multiple epochs, as proposed by the 'Young Cluster Deep Field' key science project (see Hoare et al., 2015; Coutens, et al., 2019).

Regarding polarization studies, the level of dust polarization in disks is generally quite low ($\leq$3% for self-scattering, $\simeq$5% for aligned grains). Therefore, studying the polarization properties in the SKA frequency domain is challenging but not impossible. We use frequencies at 13 GHz (Band 5b), 25 and 35 GHz (Band 6) to evaluate the feasibility of detecting the dust polarization from self-scattering. The maximum degree is $\simeq$1–3% at a wavelength of $\simeq a/2\pi$ (a is the grain size), where the polarization is maximum (Kataoka et al., 2016). This means that the frequencies of 13, 25 and 35 GHz are most sensitive to grain sizes between 4 and 1 mm. In order to check the feasibility of detecting the dust polarization in disks with SKA1-MID in Band 5b and Band 6 we have selected the prototypical and very well studied HL Tau and IM Lup disks. There are at least half a dozen disks reported in the literature that are expected to have similar polarized emission at centimeter wavelengths (e.g., Girart et al., 2018; Dent et al., 2019; Sadavoy et al., 2019; Alves et al., 2019). For HL Tau, we selected two different regions in the disk: the polarized ring detected at 3 mm and an inner ring that is well detected at centimeter wavelengths, which suggests the presence of large grains in this inner ring. Table 3 shows the on-source integration times required to detect the linear dust polarization from large grains with SKA1-MID. It is clear that with the present Band 5b, only observations with extremely long integration times (> 100 hours) would allow to detect this type of emission. In contrast, deep (but not prohibitively long) observations, especially at 35 GHz, will allow us to pinpoint the presence of large grains. Therefore, advances in this scientific field will be possible only if Band 5a and Band 6 receivers are installed on SKA1-MID.

Table 3: Disk polarization with SKA1-MID

	HL Tau				IM Lup[3]	
	3mm pol ring[1]		Inner ring[2]			
ν (GHz)	Flux (μJy)	Time (hrs)	Flux (μJy)	Time (hrs)	Flux (μJy)	Time (hrs)
13	0.2	500	0.2	500	0.3	330
25	1.7	40	1.1	80	1.4	55
35	4.6	9	2.6	28	2.9	23

[1] ALMA 3mm polarization ring Kataoka et al. (2017) at a radius of $\sim$60 au. The values derived are obtained extrapolating the 3 mm polarization using $\alpha = 3.0$ (Carrasco-González et al., 2019).
[2] Inner ring at a radius of $\sim$20 au (Carrasco-González et al., 2019). The values derived are obtained extrapolating the 8 mm polarization using $\alpha = 2.5$ (Carrasco-González et al., 2019).
[3] Polarization extrapolated from the ALMA 0.87 mm image by Hull et al. (2018) assuming $\alpha = 2.5$

References

Altwegg, K., Balsiger, H., Bar-Nun, A. et al. 2016, Science Advances, 2, no 5
Alves, F. O., Girart, J. M., Padovani, M., et al. 2018, A&A, 616, A56
Alves, F. O., Caselli, P., Girart, J. M., et al. 2019, Science, 366, 90
AMI Consortium, et al., 2012, MNRAS, 423, 1089
Bacciotti, F., Girart, J. M., Padovani, M., et al. 2018, ApJ, 865, L12
Carrasco-González, C., Henning, T., Chandler, C. J., Linz, H., Pérez, L. et al. 2016, ApJ, 821, L16
Carrasco-González, C., Sierra, A., Flock, M., et al. 2019, ApJ, 883, 71
Coutens A., Liu, H. B., Jimnez-Serra, I., Bourke, T. L., Hoare, M. et al., 2019, A&A, 631, A58
Dent, W. R. F., Pinte, C., Cortes, P. C., et al. 2019, MNRAS, 482, L29
Fernández-López, M., Stephens, I. W., Girart, J. M., et al. 2016, ApJ, 832, 200
Girart, J. M., Fernández-López, M., Li, Z.-Y., et al. 2018, ApJ, 856, L27
Hoare, M., Perez, L., Bourke, T. L., Testi, L., Jimenez-Serra, I., et al. 2015, Proceedings of Advancing Astrophysics with the Square Kilometre Array, 115
Hoang, T., & Lazarian, A. 2008, MNRAS, 388, 117
Huang J., et al., 2018, ApJL, 869, L42
Hull, C. L. H., Yang, H., Li, Z.-Y., et al. 2018, ApJ, 860, 82
Hull, C. L. H., Le Gouellec, V. J. M., Girart, J. M., et al. 2019, arXiv e-prints, arXiv:1910.07290
Isella A., Carpenter J. M., Sargent A. I., 2010, ApJ, 714, 1746
Isella, A., Benisty, M., Teague, R., Bae, J., Keppler, M., Facchini, S., Pérez, L. 2019, ApJ, 879, L25
Kataoka, A., Muto, T., Momose, M., et al. 2015, ApJ, 809, 78
Kataoka, A., Muto, T., Momose, M., et al. 2016, ApJ, 820, 54
Kataoka, A., Tsukagoshi, T., Pohl, A., et al. 2017, ApJ, 844, L5
Kataoka, A., Okuzumi, S., & Tazaki, R. 2019, ApJ, 874, L6
Lazarian, A., & Hoang, T. 2007, MNRAS, 378, 910
Le Gouellec, V. J. M., Hull, C. L. H., Maury, A. J., et al. 2019, ApJ, 885, 106
Maury, A. J., Girart, J. M., Zhang, Q., et al. 2018, MNRAS, 477, 2760
Ohashi, S., Kataoka, A., Nagai, H., et al. 2018, ApJ, 864, 81
Pérez L. M., et al., 2015, ApJ, 813, 41
Sadavoy, S. I., Stephens, I. W., Myers, P. C., et al. 2019, ApJS, 245, 2
Stephens, I. W., Yang, H., Li, Z.-Y., et al. 2017, ApJ, 851, 55
Tazaki, R., Lazarian, A., & Nomura, H. 2017, ApJ, 839, 56
Testi L., et al., 2014, prpl.conf, 339, prpl.conf
Tsukagoshi, T., Muto, T., Nomura, H., Kawabe, R., Kanagawa, K. D. et al. 2019, ApJ, 878, L8
Wilner D. J., Ho P. T. P., Kastner J. H., Rodríguez L. F., 2000, ApJL, 534, L101
Yang, H., Li, Z.-Y., Looney, L., et al. 2016, MNRAS, 456, 2794
Yang, H., Li, Z.-Y., Looney, L. W., et al. 2017, MNRAS, 472, 373
Yang, H., Li, Z.-Y., Stephens, I. W., et al. 2019, MNRAS, 483, 2371

3.2 Detection of Exoplanets

J.C. Guirado (Univ. Valencia, Spain), I. Jiménez-Serra (Centro de Astrobiologa, CSIC-INTA), R. Dodson (ICRAR, Australia), C. García-Miró (SKAO, UK), M. Rioja (ICRAR, Australia / OAN, Spain)

3.2.1 Science Justification

New exoplanets are discovered every day, showing the ubiquitous character of the planetary objects. The discovery of new worlds will continue in the next years, even more efficiently counting with new and more sophisticated instruments, which will help to provide a complete knowledge of the formation and evolution processes of these new objects. Observations are being carried out covering the complete electromagnetic spectrum. However, and despite the extraordinary capabilities of present interferometric arrays, the contribution of radio wavelengths to the science of exoplanets is yet to be developed. The SKA, in any of its realizations, will represent a fundamental breakthrough in this field.

Direct Detection

Direct detection of exoplanets at GHz frequencies would require extraordinary sensitivities. Most of the continuum exoplanet emission would correspond to thermal black body emission ($\propto \nu^2$), which, following the Rayleigh-Jeans approximation, at a frequency of 30 GHz, would be well below the μJy level for a Jupiter-like planet, even if located as close as 1 pc. This is in principle inaccessible to SKA-MID in its present configuration. However, other, more promising, radiation mechanisms may be present in exoplanets: the increasing number of radio detections in ultracool stellar and substellar objects (late M, L, and T objects) show substantial evidence for radio emission from cm- (Hallinan et al. 2008; Pineda et al. 2017; Guirado et al. 2018) to mm-wavelengths (Williams et al. 2015; Climent et al. 2019) at levels of tens of μJy in objects with spectral types as cool as T6.5 (Kao et al. 2016; 2018). This radio emission is consistent with incoherent gyrosynchrotron with at least another pulsed, auroral emission. The persistence of magnetic activity ($\sim$kG) in these very low mass objects suggests that there is probably a continuum of physical conditions from low-mass star to brown dwarfs and exoplanets (Zarka et al 2015), which may open an alternative, suitable route to the detection of radio emission of exoplanets.

On the other hand, perspectives for the detection of exoplanets during their early stages of formation are favoured at frequencies $\geq$15 GHz. Hotter and bigger than evolved planets, protoplanets still embedded in the circumstellar disks will radiate substantial thermal emission: assuming a 1 Myr old, Jovian mass protoplanet, Papaloizou et al.(2005) predict a radius of $30\,R_J$ and a temperature of $\sim$2000 K; with the values above, the Rayleigh-Jeans approximation yields flux densities of $\sim 6\,\mu$Jy for (proto)planetary sytems as far as 10 pc at 30 GHz, well within the capabilities of the Band 6 of SKA-MID. Additionally, measurements of non-Keplerian motions of the protoplanet would provide direct information of the density and viscosity of the disk (Pinte et al. 2018).

Indirect Detection

Both transit and spectroscopic methods have shown to be extraordinarily effective in detecting exoplanets around nearby stars. However, astrometry, i.e. measurement of the wobble of the host star around the star-planet barycenter, is still the only technique able to determine the mass of the planet without coupling with the orbit inclination; likewise, astrometry favors the detection of companions with longer periods and larger distances from the host star, which will allow the characterization of the planet population on the outer side of the planetary systems, a region relatively unexplored in present optical/infrared exoplanet searches, biased towards inner planets near the host star.

Ground-based astrometry at radio wavelengths routinely provides the position of celestial bodies with μas precision, and a number of astronomical events have been discovered with this technique (see Reid & Honma 2014). However, there are some caveats that prevent achieving such a high precision or planetary searches: first, the poor radio emission of the (solar type) stars, in general below the sensitivity limit of most of the present interferometers; and, second, the stochastic nature, both in time and location, of the stellar flares, typically associated to the continuum stellar radio emission at centimeter radio wavelengths. Accordingly, the efficiency of the monitoring campaigns at cm-wavelengths is penalized by frequent non-detections associated to periods of low stellar activity; even worse, the radio emission could potentially originate anywhere within the stellar corona, extending several stellar radii, therefore imposing a limit to the astrometric precision.

The extension of the SKA to 50 GHz would allow a successful application of astrometric techniques for detection of exoplanets, solving the above limitations. First, the μJy sensitivity of the Band 6 at frequencies $\geq$15 GHz would suffice to detect the thermal, black body emission of nearby solar-like stars (tens of μJy at 30 GHz; Villadsen et al 2018); and second, at $>$30 GHz, the stellar radio emission is dominated by the permanent and more stable thermal emission (not excluding a non-thermal component) associated to the stellar photosphere. Regarding the astrometric precision, and considering a resolution of 10 mas at 30 GHz and a SNR$\sim$10 detection on a solar-type star, SKA-MID Band 6 will provide just the precision (0.5 mas) to detect Jupiter-like planets at 10 pc.

References

Climent, J. B., Berger, J. P., Guirado, J. C., et al. 2019, ApJ, 886, L9
Guirado, J. C., Azulay, R., Gauza, B., et al. 2018, A&A, 610, A23
Hallinan, G., Antonova, A., Doyle, J. G., et al. 2008, ApJ, 684, 644
Kao, M. M., Hallinan, G., Pineda, J. S., et al. 2016, ApJ, 818, 24
Kao, M. M., Hallinan, G., Pineda, J. S., et al. 2018, ApJS, 237, 25
Papaloizou, J. C. B., & Nelson, R. P. 2005, A&A, 433, 247
Pineda, J. S., Hallinan, G., & Kao, M. M. 2017, ApJ, 846, 75
Pinte, C., Price, D. J., Ménard, F., et al. 2018, ApJ, 860, L13
Reid, M. J., & Honma, M. 2014, ARA&A, 52, 339
Villadsen, J., Hallinan, G., Bourke, S., et al. 2014, ApJ, 788, 112
Williams, P. K. G., Casewell, S. L., Stark, C. R., et al. 2015, ApJ, 815, 64
Zarka, P., Lazio, J., & Hallinan, G. 2015, Advancing Astrophysics with the Square Kilometre Array (AASKA14), 120

3.3 From Astrochemistry to the Origin of Life

Jiménez-Serra, I. (Centro de Astrobiología, INTA-CSIC, Spain), Serena Viti (University College London, UK), Rivilla, V. M. (INAF-Osservatorio Astrofisico di Arcetri, Italy), Liton Majumdar (National Institute of Science Education and Research, India), Doug Johnstone (NRC-CNRC), and Pamela Klaassen (STFC, UK)

3.3.1 Prebiotic Molecules in space

The question of the origin of life has intrigued human beings for centuries. Life appeared on Earth about 4 billion years ago, but we ignore the processes that made it possible. The two most popular hypotheses are the primordial soup scenario in sub-oceanic thermal vents, and panspermia where the building blocks of life may have come from outer space via the impact of meteorites and comets on a young Earth's surface.

Since the detection of the first molecules in space in the late 30's (CN, CH and CH^+; Swings & Rosenfeld, 1937), Astrochemistry has revealed that the medium in between stars and around stars (the interstellar and circumstellar medium, the ISM and CSM, respectively) is full of molecules. Over 200 molecular species have been detected in space to date, some of them of prebiotic interest. Indeed, molecules such as cyanamide (NH_2CN), cyanoacetylene (HC_3N), glycolaldehyde ($HOCH_2CHO$), amino acetonitrile (NH_2CH_2CN), or urea (NH_2CONH_2), which are precursors of amino acids, sugars and ribonucleotides (Powner et al., 2009; Patel et al., 2015), have been detected in regions forming massive stars and in the natal environs of Solar-type systems (Belloche et al., 2008, 2013, 2019; Jorgensen et al., 2012; Coutens et al., 2018).

Despite this huge progress, the actual building blocks of life such as amino acids (as e.g. glycine) have not been reported in the ISM yet (Kuan et al., 2003; Snyder et al., 2005; Jones et al., 2007). We know, however, that they must form in space because they have been found in meteorites (Pizzarello et al., 2006) and comets (see the recent detection of glycine in comet 67P/Churyumov-Gerasimenko; Altwegg et al., 2016). One possibility is that they appear at some point in the ISM during the star formation process, being subsequently transferred first to the disks around young stars, and finally to small Solar-system bodies. Branched and chiral molecules such as iso-propyl cyanide (i-C_3H_7CN) and propylene oxyde (c-C_3H_6O)[3], have indeed been detected in the ISM toward a high-mass star-forming region (i.e. toward the SgrB2 N massive hot core Belloche et al., 2014; McGuire et al., 2016), which supports the idea that amino acids (which are branched and chiral molecules themselves) could also form in the ISM.

3.3.2 The SKA as a prebiotic molecule detector

The search for amino acids in the ISM has been attempted to date only in the millimeter and submillimeter wavelength regimes (Kuan et al., 2003; Snyder et al., 2005; Jones et al., 2007; Ceccarelli et al.,

[3] A branched molecule is a carbon-bearing molecular species with a side-chain structure, while a chiral molecule has a non-superposable structure on its mirror image.

2000; Jiménez-Serra et al., 2016). However, the identification of such a large molecule at these wavelength ranges is non-trivial as one faces several limitations. The regions in the ISM that present the highest level of chemical complexity are low-mass hot corinos and high-mass hot cores. These sources are hot (T$\geq$100 K). At such high temperatures, interstellar ices are sublimated releasing all organic material into the gas phase. As a result, the sub-/millimetre spectra of hot corinos and hot cores are populated by a myriad of molecular lines, which yields very high levels of line confusion. In addition, the line profiles in hot corinos and hot cores, when observed with single-dish telescopes, show broad linewidths ($\sim$5-10 km s^{-1}), which leads to high levels of line blending making line identification difficult. Hot corinos and hot cores are very compact (size $\leq$0.1 pc) and, therefore, if observed with single-dish telescopes, their emission gets largely diluted into the large single-dish beam, making the observed lines even weaker than what they actually are. On top of this, amino acids are macro-molecules and, thus, their partition function is large; this spreads their emission over many energy levels, making their transitions very weak. And finally, at high temperatures, the sub-/millimeter spectra of these macro-molecules shift toward frequencies >80 GHz where most lighter molecules emit, yielding higher levels of line confusion.

Being an interferometer, and operating at frequencies lower than those from other instruments such as the Atacama Large Millimeter Array, the SKA has the potential to become a prebiotic molecule detector because:

- a) centimeter wavelengths are cleaner from the rotational transitions of lighter and smaller molecules such as CH_3OH or CH_3CN, reducing the level of confusion;
- b) the velocity separation between different molecular rotational transitions becomes larger at centimeter wavelengths, which minimises line bending;
- c) interferometers filter out any extended emission in the line of sight, significantly decreasing the observed linewidths of the molecular line emission; this reduces the level of line blending;
- d) interferometers can resolve the spatial scales of hot corinos and hot cores, avoiding beam dilution of the molecular line flux in a large beam.

From all this, the SKA would fulfill all the theoretical capabilities needed to perform deep searches of prebiotic molecules such as amino acids in the ISM. However, as shown in the next section, the current frequency coverage of SKA1-Mid (from 4.6 to 15.3 GHz) does not allow the search of even the simplest amino acid in space: glycine.

3.3.3 Band 5 (4.6-15.3 GHz) versus Band 6 (15.3-50 GHz) receivers

The current deployment plan for SKA1 only considers frequencies from 4.6 GHz up to 15.3 GHz. In Figure 8, we present simulations of the spectrum of glycine obtained for the physical properties of the hot corino IRAS16293-2422 B. This hot corino not only is a proto-Sun (i.e. a precursor of a Solar-type system), but it shows an extremely high level of chemical complexity that has allowed the detection of prebiotic complex organic molecules such as glycolaldehyde (the simplest sugar; Jorgensen et al., 2012) or cyanamide (NH_2CN; Coutens et al., 2018), a precursor of ribonucleotides (Patel et al., 2015).

To generate the spectrum of glycine shown in Figure 8 we have used MADCUBA, a spectral line identification and modelling software[4]. MADCUBA can simulate the spectra of any molecular species using the information contained in the JPL and CDMS molecular line catalogues (Pickett et al., 1998; Müller et al., 2005), given the physical conditions of the source (e.g. molecular column density, excitation temperature, linewidth, central radial velocity and source size). For IRAS16293-2422 B, we have assumed an excitation temperature T_{ex}=100 K, linewidth Δv=1 km s^{-1}, central radial velocity $v_{\rm LSR}$=2.6 km s^{-1}, and source size θ_s = 0.5”. As glycine column density, we have considered the most stringent upper limit obtained toward this source of $\leq 5.8\times10^{15}$ cm^{-2} (Jiménez-Serra et al., 2019). For an H_2 column density of 2.8×10^{25} cm^{-2} measured toward IRAS16293-2422 B (Martín-Doménech et al.,

[4]MADCUBA or Madrid Data Cube Analysis on ImageJ is a software developed at the Astrobiology Center (CAB) in Madrid (Martín et al., 2019).

2017), this corresponds to a glycine abundance of $\leq 2\times10^{-10}$. This is consistent with the abundances predicted by (Garrod, 2013) for hot sources, and it is a conservative value for the most recent models of Suzuki et al. (2018).

As reported in Figure 8, the brightest transitions of glycine appear at frequencies $\geq$40 GHz. If we compare the transitions covered by the Band 5 and the Band 6 receivers, the glycine lines at 49 GHz are factors $\sim$25-30 brighter that those found at 15 GHz within Band 5, which suggests that Band 6 should be favoured for SKA molecular line experiments. Although the expected rms for Band 6 molecular line observations is a factor of $\leq$4 higher than that for Band 5 (48 μJy for Band 5 versus 180 μJy for Band 6, for 1 hour integration time and a velocity resolution of 100 km s^{-1}), the much brighter lines of glycine in Band 6 would enable detection experiments of this amino acid. Indeed, while the glycine lines at 49 GHz could be detected with a signal-to-noise ratio $\sim$5 in 1000 hours of total observing time, this experiment would be unfeasible with the Band 5 receivers. Such large integration time fits nicely in the context of the SKA Key Science Projects, where the glycine lines can be observed simultaneously with the continuum emission in proto-planetary disks to study grain growth and planet formation. Thanks to the large field-of-view of the SKA (about 1.5 arcmin at the upper end of the Band 6 receivers), the glycine lines could be imaged simultaneously toward multiple sources located within the same low-mass star-forming proto-cluster (as e.g. the Ophiucus A cluster; see the pilot study recently carried out by Coutens et al., 2019, with the JVLA). Therefore, while the search of amino acids is unreachable with the current deployment plan of the SKA, these searches could be attempted with the SKA if the high-frequency Band 6 receivers were deployed.

We note that the behaviour of the spectrum of glycine to peak and present its brightest transitions at high frequencies in hot sources, can be extrapolated to any other prebiotic complex organic molecule since this is the expected behaviour for any large molecular species. In fact, even in the case of cold sources (or sources with low excitation temperature of the gas such as pre-stellar cores or the quiescent giant molecular clouds in the Galactic center; see e.g. Jiménez-Serra et al., 2014; Zeng et al., 2018), the peak of the spectrum shifts toward lower frequencies but still presents its brightest lines in the frequency range between 40 and 50 GHz. Since this range is still free from many of the rotational transitions from lighter molecules, all this makes the frequencies between 40 and 50 GHz the best frequency range for the detection and discovery of new prebiotic species in the ISM.

In summary, if supplied with the Band 6 high-frequency receivers, the SKA could become a pioneer instrument in the detection of large prebiotic molecules in space. An extension of the frequency coverage of the SKA to frequencies >15 GHz, would allow searches of large prebiotic molecules such as the amino acid glycine, opening a new era of discovery. The discovery of amino acids in the ISM would settle the question of whether these macro-molecules could form in space, providing key information about the origin of life on Earth and having important implications for the origin of life in other planetary systems.

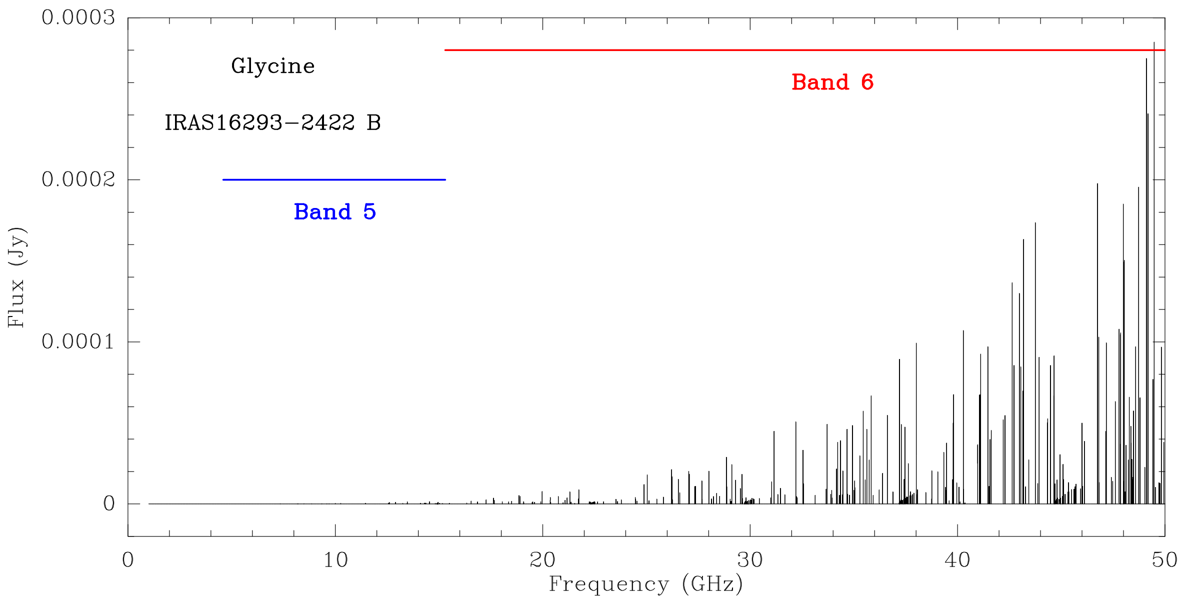

Figure 8: Spectrum of glycine simulated for the physical conditions and glycine abundance predicted for the hot corino IRAS16293-2422 B (see text for details). The glycine transitions covered by the high-frequency receivers of Band 6 are factors ∼25-30 brighter than those covered within Band 5.

References

Altwegg, K., Balsiger, H., Bar-Nun, A. et al. 2016, Science Advances, 2, no 5
Belloche, A., Garrod, R. T., Müller, H. S. P. et al. 2019, A&A, 628A, 10B
Belloche, Arnaud; Garrod, Robin T.; Mller, Holger S. P. et al. 2014, Science, 345, 1584B
Belloche, A., Müller, H. S. P., Menten, K. M. et al. 2013, A&A, 559A, 47B
Belloche, A., Menten, K. M., Comito, C. et al. 2008, A&A, 482, 179B
Ceccarelli, C., Loinard, L., Castets, A. et al. 2000, A&A, 362, 1122C
Coutens, A., Liu, H. B., Jiménez-Serra, I. et al. 2019, A&A, accepted (arXiv:190903515C)
Coutens, A., Willis, E. R., Garrod, R. T. et al. 2018, A&A, 612A, 107C
Garrod, R. T. 2013, ApJ, 765, 60
Jiménez-Serra, I., Martín-Pintado, J., Rivilla, V. et al. 2019, Astrobiology, submitted
Jiménez-Serra, I., Vasyunin, A. I., Caselli, P. et al. 2016, ApJ, 830, L6J
Jiménez-Serra, I., Testi, L., Caselli, P. et al. 2014, ApJ, 787, L33J
Jones, P. A., Cunningham, M. R., Godfrey, P. D. et al. 2007, MNRAS, 374, 579
Jorgensen, J., van der Wiel, M., Coutens, A. et al. 2012, A&A, 595, A117
Kuan, Y., Yan, C., Charnley, S. et al. 2003, MNRAS, 345, 650
Martín, S., Martín-Pintado, J., Blanco-Sánchez, C. et al. 2019, accepted in A&A, arXiv:1909.02147
Martín-Doménech R., Rivilla V. M., Jiménez-Serra I., Quénard D., Testi L., Martín-Pintado J., 2017, MNRAS, 469, 2230
McGuire, B. A., Carroll, P. B., Loomis, R. A. et al. 2016, Science, 352, 1449M
Müller, H. S. P., Schlder, F., Stutzki, J., & Winnewisser, G. 2005, JMoSt, 742, 215
Patel, B. H., Percivalle, C., Ritson, D. J. et al. 2015, Nature Chemistry, 7, 301
Pickett, H. M., Poynter, R. L., Cohen, E. A., et al. 1998, JQSRT, 60, 883
Pizzarello, S., Cooper, G. W., & Flynn, G. J. 2006, Meteorites and the Early Solar System II, D. S. Lauretta and H. Y. McSween Jr. (eds.), University of Arizona Press, Tucson, 943 pp., p.625-651
Powner, M. W., Gerland, B., & Sutherland, J. D. 2009, Nature, 459, 239
Snyder, L. E., Lovas, F. J., Hollis, J. M. et al. 2005, ApJ, 619, 914
Suzuki, T., Majumdar, L., Ohishi, M. et al. 2018, ApJ, 863, 51S
Swings, P., & Rosenfeld, L. 1937, Molecules. Astrophys. J., 86, 483
Zeng, S., Jiménez-Serra, I., Rivilla, V. et al. 2018, MNRAS, 478, 2962

3.4 Complex organic molecules in planet-forming discs

John D. Ilee (University of Leeds, UK), Claudio Codella (INAF-Osservatorio Astrofisico di Arcetri, Italy), Catherine Walsh (University of Leeds, UK), Linda Podio (INAF-Osservatorio Astrofisico di Arcetri, Italy), Izaskun Jimenez-Serra (Centro de Astrobiología, INTA-CSIS, Spain), Pamela Klaassen (UK ATC, STFC, UK)

3.4.1 Molecular complexity across star and planet formation

The origin of the building blocks of life is unknown. Simple versions of prebiotic molecules, so-called complex organic molecules (COMs; those containing carbon and with $\gtrsim$6 atoms) have been observed across many stages of the star and planet formation process. These include interstellar dark clouds (Vasyunina et al., 2011), dense pre-stellar cores (Vastel et al., 2014; Jiménez-Serra, et al., 2016), protostars (Jörgensen et al., 2016), protoplanetary discs (Öberg, et al., 2015; Walsh et al., 2016), and comets (Altwegg et al., 2016). It has been demonstrated that COMs are important precursors to the formation of biologically-relevant molecules, such as amino acids (Saladino et al., 2012) and nucleobases (Oba et al., 2019). Therefore, if we are to determine the propensity for the seeds of life to be found in extra-solar planetary systems, it is vital that we understand how COMs form and evolve during the entirety of the planet formation process.

3.4.2 Current observations of COMs

The Atacama Large Millimetre/submillimetre Array (ALMA) has been instrumental in the detection of COMs. The unmatched sensitivity of ALMA across ~100 – 900 GHz (~3 – 0.3 mm) has enabled the detection and characterisation of increasingly more complex molecules (see McGuire 2018 for an overview). However, in terms of the detection of COMs within protoplanetary discs, it is becoming clear that ALMA is reaching the limits of its operating frequencies.

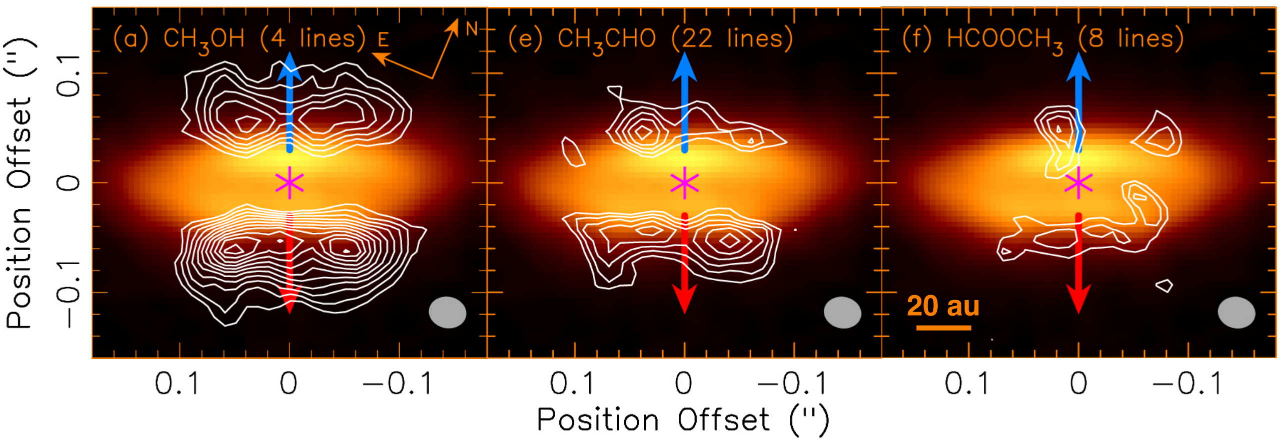

Figure 9: ALMA observations of emission from complex organic molecules (contours) overlaid on the 340 GHz continuum emission (colourscale) toward HH 212, a young low-mass protostar hosting a bipolar outflow and edge-on protoplanetary disk (Lee et al., 2019).

The innermost regions of protoplanetary discs ($r < 10$ au, $0\farcs1$ at 100 pc) are the most important when considering the formation of terrestrial planets like Earth. However, these regions are difficult to study due to their high continuum optical depths at millimetre wavelengths. This prevents direct measurements of the dust mass within these regions (and thus the determination of the raw material available for planet formation), and can also act to obscure line emission. Figure 9 shows observations of methanol (CH_3OH), acetaldehyde (CH_3CHO) and methyl formate ($HCOOCH_3$) toward HH 212, a young protostar with an edge on protoplanetary disc (Lee et al., 2019). The lack of emission toward the disk midplane is clear to see, but what is not clear is the origin of such a morphology. Possibilities include the aforementioned effects of dust continuum opacity (Codella, et al., 2019), but also a reduced abundance of these molecules in these regions. Therefore, if we are to characterise the complex molecular content of the midplanes of protoplanetary discs (e.g. the location in which planets form), observations at lower frequencies (10's of GHz, cm-wavelengths) are essential.

3.4.3 Simulating SKA observations of COMs toward TW Hya

TW Hya is the closest T Tauri star to Earth, located at a distance of 60 pc (Bailer-Jones, et al., 2018). With a stellar mass of 0.8 $M_\odot$ and an age of 10 Myr (Andrews, et al., 2016), it is one of the best studied analogues to the young Solar System. It is also surrounded by one of the few protoplanetary discs around a low-mass star in which complex molecules have been found, with emission from methanol (CH_3OH) being detected by ALMA (Walsh et al., 2016). TW Hya therefore serves as an important benchmark to determine the observability of COMs across lower frequencies.

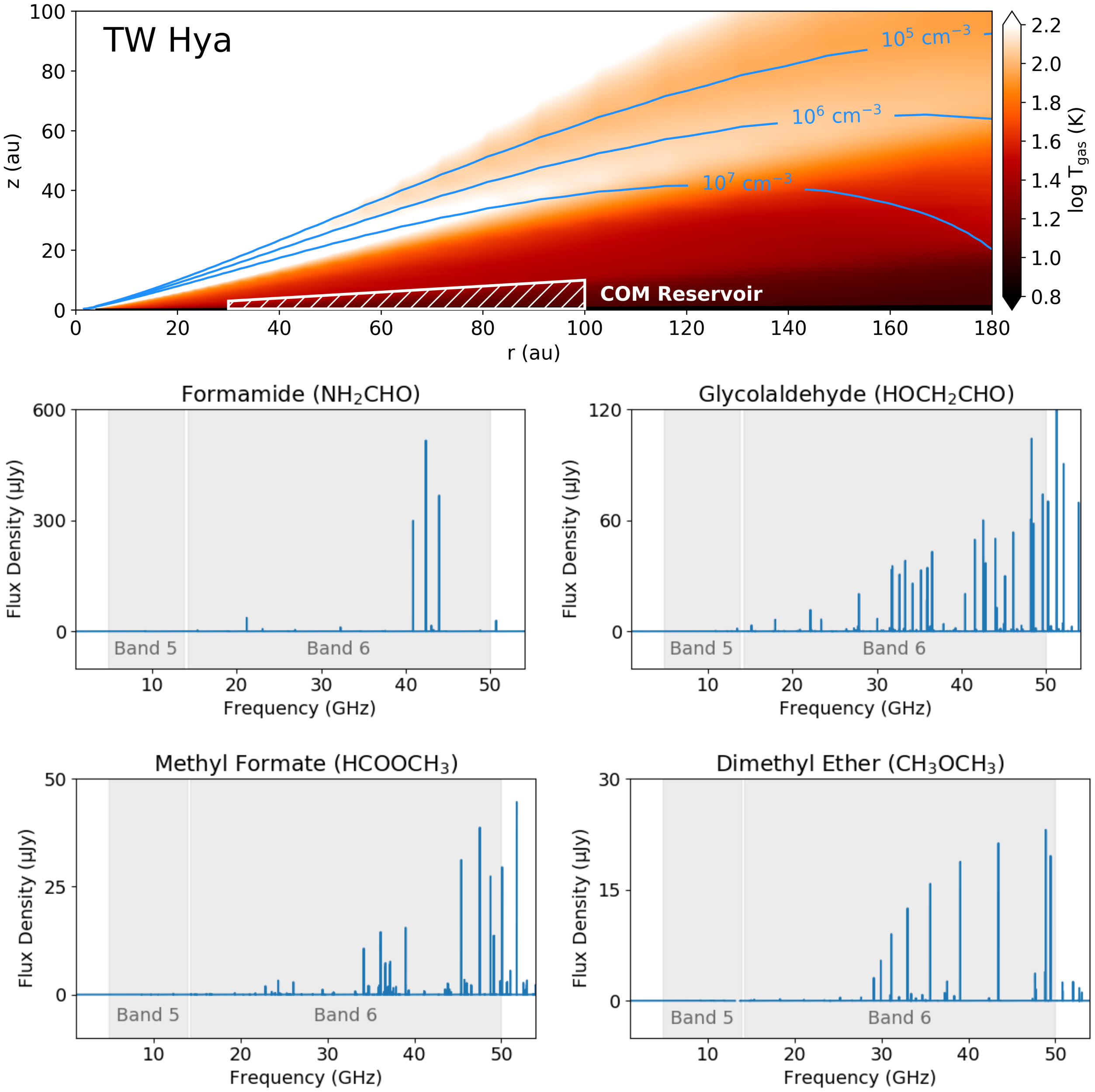

Figure 10: The physical structure of the TW Hya model (top), along with the resulting simulated spectra (bottom) of COMs of interest across SKA Band 5 (4.8–13.8 GHz) and the proposed Band 6 (15–50 GHz). Frequencies greater than ∼30 GHz cover transitions up to 500 times stronger than those within Band 5, offering the best chance to detect and characterise these molecules in protoplanetary discs with the SKA.

Following the approach of Walsh et al. (2014), we have calculated the disk-integrated line flux density under local thermodynamic equilibrium for several COMs of interest: formamide (NH_2CHO), glycoaldehyde ($HOCH_2CHO$), methyl formate ($HCOOCH_3$) and dimethyl ether (CH_3OCH_3) for TW Hya. For the calculations, we utilise the disc physical structure determined by Kama et al. (2016), which is assumed to sit in a face-on orientation ($i = 0°$). We assume the reservoir of each COMs is located in the midplane ($z/r = 0 - 0.1$) between radial distances of 30–100 au from the central star. This well fits the methanol emission in TW Hya detected by ALMA. Such regions are characterised by gas temperatures of between 15–30 K. We take the fractional abundance of each molecule to be 1×10^{-10} within the reservoir, and 1×10^{-16} elsewhere, in order to approximate results from dedicated COM modelling (Walsh et al., 2014). Figure 10 shows the physical structure of the disk, along with the resulting line emission for each species. A clear result emerges from these simulated observations – ***the strongest transitions of these molecules are located between ~30–50 GHz.***

3.4.4 The need for SKA Band 6 (beyond 25 GHz)

Observations of transitions of complex molecules at lower (10–50 GHz) frequencies offer significant advantages over observations in the millimetre (100–900 GHz) regime. In the first instance, larger molecules preferentially emit at lower frequencies, increasing the chance of any given spectral window covering their transitions over more simple molecules. Secondly, the spacing between rotational transitions increases as frequency decreases, reducing the effects of line blending or confusion. Finally, continuum opacities at 10's of GHz (cm-wavelengths) are expected to be up to an order of magnitude lower than those in the millimetre regime (see, e.g. Woitke, et al., 2016). However, the receivers currently planned for the SKA are not optimised to observe transitions of complex molecules. Figure 10 shows that no detectable transitions lie within the Band 5 frequency window (4.6–15.3 GHz). However, the proposed Band 6 receivers have the potential to cover many tens of transitions from these molecules, with strengths up to 500 times those across Band 5. ***This is possible only if their frequency coverage is extended beyond 25 GHz.***

A proposed Key Science Project (KSP) for the SKA involves a 1000 hr deep field integration of a young stellar cluster such as Oph A (see Coutens et al., 2019, for a full description). Under such a KSP, the expected 3σ sensitivity of SKA1-MID across Band 6 (15–50 GHz) would be 60–200 μJy across a 1 km/s channel. Therefore, based on our simulations above, we could expect to detect emission from strongly emitting COMs (e.g. formamide) in Class II protoplanetary discs with peak signal-to-noise ratios of up to 9. While emission from COMs with weaker transitions (e.g. glycoaldehyde, methyl formate and dimethyl ether) initially appears difficult to detect, the large number of transitions across this frequency range would enable the use of a variety of techniques to significantly enhance signal-to-noise ratio. These include line stacking and matched filtering (Loomis, et al., 2018), which have been demonstrated to improve signal-to-noise ratios in ALMA data by up to 500 per cent (see Carney, et al., 2017).

In addition, there is increasing evidence that planet formation happens quickly (e.g. Clarke, et al., 2018), and may occur during the younger Class I phase of evolution (Harsono, et al., 2018). Determining the chemical composition of these discs around Class I objects (e.g. Podio et al., 2019) is therefore essential if we are to understand the degree of (complex) chemical inheritance during the planet formation process. Such discs are warmer than their Class II counterparts (van 't Hoff, et al., 2018), and can undergo instabilities that can increase the abundance of COMs in the gas-phase (Quénard, et al., 2018). Hence, Class I disks offer a compelling target in which to characterise the abundance and distribution of COMs in early planet-forming environments, where the line strength is expected to be significantly stronger than that predicted for Class II disks such as TW Hya.

In summary, the combination of unprecedented spatial resolution and high sensitivity means that the SKA has the potential to provide breakthrough results in terms of detecting biologically-relevant molecules across the star and planet formation process. However, the current Band 5 receivers are not optimised to observe the strongest transitions of these molecules. The addition of Band 6 receivers, stretching to frequencies between 25–50 GHz, will unlock the potential of the SKA to observe and characterise these important prebiotic species across the evolutionary stages of planet-forming disks.

References

Altwegg, K., et al., 2016, Sci. Adv., 2, 5
Andrews S. M., et al., 2016, ApJL, 820, L40
Bailer-Jones C. A. L., et al., 2018, AJ, 156, 58
Carney M. T., et al., 2017, A&A, 605, A21
Clarke C. J., et al., 2018, ApJL, 866, L6
Codella C., et al., 2019, arXiv, arXiv:1910.04442
Coutens A., et al., 2019, arXiv, arXiv:1909.03515
Harsono D., et al., 2018, NatAs, 2, 646
Jiménez-Serra I., et al., 2016, ApJL, 830, L6
Jörgensen J., et al., 2016, A&A, 595, 117
Kama M., et al., 2016, A&A, 592, A83
Lee C.-F., et al., 2019, ApJ, 876, L63
Loomis R. A., et al., 2018, AJ, 155, 182
McGuire, B. A., 2018, ApJS, 239, 17
Oba Y., et al. 2019, Nat. Commun., 10, 4413
Öberg K. I., et al., 2015, Nature, 520, 198
Podio L., et al., 2019, A&A, 563, A33
Quénard D., et al., 2018, ApJ, 868, 9
Saladino R., et al., 2012, PhLRv, 9, 84
van 't Hoff M. L. R., et al., 2018, A&A, 615, A83
Vastel C., et al., 2014, ApJ, 795, 2
Vasyunina T., et al., 2011, A&A 527, 88
Walsh C., et al., 2014, A&A, 623, L6
Walsh C., et al., 2016, ApJ, 823, 10
Woitke P., et al., 2016, A&A, 586, A103

3.5 The search for molecules with heavy elements in star-forming regions

Francesco Fontani (INAF-Osservatorio Astrofisico di Arcetri, L.go E. Fermi 5, 50125, Florence, Italy)

Star forming regions are the cradle where future stars of all masses are born. Many of these regions are believed to be precursors of stellar systems like our own, hence the chemical content of the matter associated with these regions can be considered as the rough material out of which the Sun (and all the other bodies formed with it, i.e. planets, comets and asteroids), have been formed. In recent years, a big effort has been devoted to identify and study molecules containing the most abundant, and important, elements, namely H, C, O, N, and, to some extent, S, Si, and P. However, almost nothing is known about molecules with heavier elements, some of which can potentially influence the emergence of life as we know it, such as Ca, Mg, Na, K, Fe, and others. The combined use of SKA Band-5 and -6 is perfectly suited to open and expand this new research window.

3.5.1 Molecules with heavy elements in the interstellar medium

About 200 molecules made of 16 different elements have been detected in the interstellar and circumstellar medium so far (see McGuire 2018 for a review), most of which are made of only four elements: H, O, C, and N. Along with these, several simple molecules containing Sulphur and Silicon have been detected (e.g. Edwards & Ziurys 2014, Podio et al. 2017), due to their relatively high abundance with respect to other elements with similar atomic mass (Asplund et al. 2009). Recently, the identification and study of Phosphorus-bearing molecules has also gained attention due to the possible implications of phosphates in pre-biotic chemistry (e.g. Agúndez et al. 2015, Rivilla et al. 2016, Fontani et al. 2019). However, molecules with elements such as alkali and alkaline-earth metals (e.g. Na, K, Mg, Ca), halogens (e.g. Cl), or other metals (e.g. Al, Fe, Ti) belonging to the 3rd group or higher, have only rarely been detected in space (McGuire 2018). Moreover, most of these molecules have been found in the envelope of evolved stars rather than in star-forming regions. For this reason, **so far abundance and metallicity estimates based on these rare elements in the molecular gas in which new stars and planets are formed, as well as their use as probe of local physical conditions, has remained very limited**. The detection and identification of these species is also important to solve the problem of the (still too) high number of spectral features unidentified in the radio- and (sub-)mm spectral surveys, part of which could be due to such heavy molecules.

3.5.2 The state of the art in star-forming regions

In large majority, the first detection of several molecules belonging to the 3rd group or heavier (KCl, NaCl, AlCl, MgNC, NaCN, KCN, FeCN, AlNC, TiO_2, CCP, HCP) have been reported in the extremely chemically rich circumstellar envelope of evolved stars, such as IRC+10216 (e.g. Guélin et al. 1986, Cernicharo & Guélin 1987, Turner et al. 1994, Ziurys et al. 2002, Pulliam et al. 2010, Zack et al. 2011, Agúndez et al. 2007, Halfen et al. 2008) or VY Canis Majoris (Kaminski et al. 2013), with single-dish radio-telescopes (IRAM-30m telescope, NRAO-12m telescope, etc.). The fact that these rare species were almost exclusively detected in circumstellar envelopes indicated that they survive in the gas phase for a short time before being depleted onto dust grains, and be locked in the solid phase. Thanks to the increased sensitivity and spectral bandwidth of the new generation radio- and mm-telescopes, like the Atacama Large Millimeter Array (ALMA), some of these rare molecules have been identified also in star-forming regions. For example, emission lines of KCl and NaCl were recently found towards Orion SrcI (Ginsburg et al. 2019), bringing to the first detection of a "salty" disk around a high-mass forming (proto-)star. Ginsburg et al. (2019) detected ~ 60 roto-vibrational lines of KCl and NaCl, and of their isotopologues, in a limited observing band, which show the great diagnostic potential of these molecules to derive physical parameters. However, most of these lines are faint and in excited vibrational states, with energies of the upper level ≥ 500 K, and hence they can be detected only in very nearby objects like Orion SrcI, for sensitivity reasons, and in very hot gas. In fact, *the gas in which stars form is generally colder than ~ 100 K*, which makes it very unlikely the excitation and the detection of the high energy transitions like those observed towards Orion SrcI, as well as those of similar heavy molecules, in other star-forming regions.

Usually, **the primary molecular emission in regions with intermediate density ($n(H_2) \sim 10^4 - 10^6$ cm^{-3}) and temperature ($T \sim 10 - 100$ K), like those in which stars form, is from low-J rotational transitions in the ground vibrational state.** For a linear molecule, such as the simple species discussed above, the energy level of the J rotational state is given, to first order, by the simple equation $E_J = hBJ(J+1)$, where B is the rotational constant of the molecule (in s^{-1} units), and the frequency ν of a transition $J \rightarrow J-1$ is $\nu = \hbar J/2\pi I$, with I the momentum of inertia of the molecule. Because B, like ν, is inversely proportional to I, which is larger for heavier and/or longer molecules, **heavier molecules will have smaller B and lower ν (for the same J) with respect to lighter molecules.**

3.5.3 Technical justification: the need for SKA Band 5 and 6

For the reasons discussed above, **the SKA Bands 5 and 6 are appropriate to detect the lowest J transitions of simple molecules with heavy elements.** In fact, most of them have frequencies in between ~ 1 and ~ 50 GHz. For example, the first three J rotational transitions of salt, NaCl, fall at ~ 13, ~ 26, and ~ 39 GHz, respectively. Similarly, for KCl one can detect up to the $J = 6 \rightarrow 5$ transition (at ~ 46 GHz) in the SKA Band-5 and -6. Magnesium, in the form of MgCN or MgNC, as detected in the envelope of evolved stars (McGuire 2018 and references therein) can be detected in between ~ 10 to ~ 48 GHz (rotational transitions up to $N = 4-3$).

Band-5 contains one or two transitions of these species at most, but having multiple lines is crucial to: (1) properly identify the molecule through multi-line detection, and (2) derive an accurate estimate of the excitation temperature from the multi-line analysis and, from this, of the column density and abundance w.r.t. H_2. Moreover, the lowest-J rotational lines detectable at the lowest frequencies (Band-5) are intrinsically fainter than the transitions with higher J, so that **Band-6 maximises the chance of detecting these species**. As an example, let us estimate the intensities of KCl rotational lines for Ori SrcI that can be observed in these two bands: assuming a conservative total column density of $\sim 10^{13}$ cm^{-2} and an excitation temperature of ~ 100 K in an angular emitting region of $\sim 0.1''$, as estimated from rotational diagrams by Ginsburg et al. (2019), a simple LTE calculation of the intensity of the lowest-J transitions provides peak intensities of ~ 1, ~ 4, ~ 8, ~ 14, ~ 20 and ~ 27 K, from the $J = 1 \rightarrow 0$ to the $J = 6 \rightarrow 5$ line.

Among these transitions, only the ground state one falls in Band-5, while those from $J = 2 \rightarrow 1$ to $J = 6 \rightarrow 5$ are in Band-6. Therefore, the (faintest) transition that can be observed in Band-

5 cannot assure a firm identification of the species, and derive accurate estimates of its physical parameters. **The transitions that can be observed in Band-6 will allow us to detect more lines, and with better S/N ratios.** For example: the peak intensity of the $J = 2 \rightarrow 1$ line of KCl at 15.378 GHz, converted in flux density units, is $\sim 40\ \mu$Jy. Assuming an array consisting of 133 MID dishes, an integration time of 10 hr, source elevation near zenith, the line sensitivity is $\sim 14\ \mu$Jy/beam, providing a S/N$\sim$ 3; the peak intensity of the $J = 6 \rightarrow 5$ at $\sim$ 46.132 GHz, converted in flux density units, is $\sim 480\ \mu$Jy. Because the line sensitivity at this frequency in the same integration time is $\sim 45\ \mu$Jy, the line will be detected with S/N$\sim$ 10. This shows clearly how the highest frequency window of Band-6 is most appropriate to detect the rotational transitions of these species in a reasonable amount of time.

Overall, the spectral window covered by Band-5 and -6 is ideal because it is less "polluted" by the strongest transitions of the lighter, more abundant species, for which the transitions with the same quantum numbers fall at higher frequencies. Finally, because the emission is expected to arise from very compact angular scales ($\sim 0.1''$, see Fig. 1 taken from Ginsburg et al. 2019 for KCl and NaCl), interferometric images are absolutely required to resolve the emission and avoid beam dilution problems that likely affect single-dish observations.

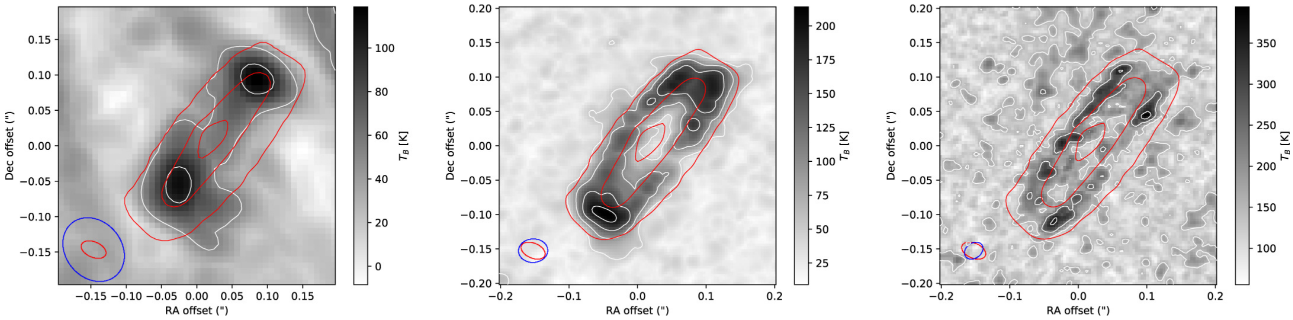

Figure 11: ALMA peak intensity images of NaCl lines in Orion SrcI. From left to right, the lines are: 87.26 GHz NaCl v = 3 J = 7–6, 232.51 GHz NaCl v = 1 J = 18–17, and 333.01 GHz NaCl v = 2 J = 26–25. The red contours show the ALMA Band 6 226 GHz continuum at levels of 50, 300, and 500 K. White contours are shown at 50 and 100 K (left), 50, 100, 150, and 200 K (center), and 150, 250, and 350 K (right). The red and blue ellipses show the beams for the continuum and the line emission, respectively.
From Ginsburg et al. (2019).

References

Agúndez, M., Cernicharo, J., Decin, L., Encrenaz, P., Teyssier, D. 2014, ApJ, 2014, 790, L27
Agúndez, M., Cernicharo, J., & Guélin, M. 2007, ApJL, 662, L91
Asplund, M., Grevesse, N., Jacques Sauval, A., Scott, P. 2009, ARA&A, 47, 481
Cernicharo, J., & Guélin, M. 1987, A&A, 183, L10
Edwards, J.L. & Ziurys, L.M. 2014, ApJ, 794, L27
Fontani, F., Rivilla, V.M., van der Tak, F.F.S., Mininni, C., Beltrán, M.T., Caselli, P. 2019, in press
Ginsburg, A., McGuire, B.A., Plambeck, R., Bally, J., Goddi, C., Wright, M. 2019, ApJ, 872, 54
Guélin, M., Cernicharo, J., Kahane, C., & Gomez-Gonzales, J. 1986, A&A,157, L17
Halfen, D.T., Clouthier, D.J., & Ziurys, L.M. 2008, ApJL, 677, L101
Kaminski, T., Gottlieb, C.A., Menten, K.M., et al. 2013, A&A, 551, 113
McGuire, B.A. 2018, ApJS, 239, 17
Podio, L., Codella, C., Lefloch, B., Balucani, N., Ceccarelli, C., et al. 2017, MNRAS, 470, L16
Rivilla, V.M., Fontani, F., Beltrán, M.T., Vasyunin, A., Caselli, P., Martín-Pintado, J., Cesaroni, R. 2016, ApJ, 826, 161
Pulliam, R.L., Savage, C., Agúndez, M., et al. 2010, ApJL, 725, L181
Turner, B.E., Steimle, T.C., & Meerts, L. 1994,ApJL, 426, L97
Zack, L.N., Halfen, D.T., & Ziurys, L.M. 2011,ApJL,733, L36
Ziurys, L.M., Savage, C., Highberger, J.L., et al. 2002, ApJL, 564, L45

3.6 Searching for Interstellar Beacons Above 15 GHz

Ian Morrison (Curtin Institute of Radio Astronomy, Curtin University, Australia)

Summary: Increased emphasis should be placed on conducting the Search for Extraterrestrial Intelligence (SETI) at higher frequencies, above the traditional microwave window. Intentional beacons are an important sub-class of SETI targets, and consideration of system efficiency/cost suggests beacons are more likely to operate above 15 GHz, a region largely unexplored by SETI to date. Such beacons are also likely to employ wideband signaling, and may not be discoverable via conventional narrowband SETI detection methods.

3.6.1 Science Justification

SETI has traditionally focused on the "microwave window" between about 1 and 10 GHz, pictured in Figure 1. In this region the natural sources of noise are at a minimum, creating a "well" between galactic noise and atmospheric noise (and the quantum limit due to shot noise).

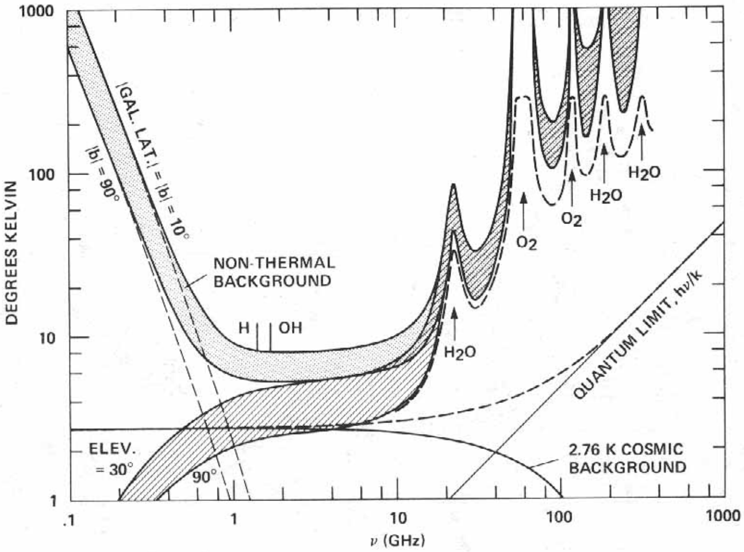

Figure 12: The terrestrial microwave window: sources of radio noise and atmospheric attenuation [credit: Oliver et al. (1971)].

When considering the optimum frequency band for intentionally transmitted interstellar beacon signals, other factors come into play. Assuming there are other civilizations that, like us, do not have access to unlimited resources, we may expect beacon builders in those civilizations to be concerned with efficient use of resources. Specifically, we should expect them to prefer an operating frequency that maximizes the efficiency of the system. For the same resources, this will allow signaling to a greater number of targets, or more distant targets, or transmission of longer messages, or transmissions that are more persistent in time (or any combination of the above). That is, an efficient beacon design will be better able to achieve its design objectives than an inefficient one. Even if resources were inexpensive to the civilization, there would appear to be no benefit to using these resources inefficiently. Efficiency can broadly be equated with minimizing the costs associated with building and operating the beacon transmitter. Cost is impacted by various factors; some technological and some due to fundamental physics.

Cost considerations led Benford et al. to note that the higher end of the microwave window should be favored for beacons, due to the increased directivity of a given antenna area with increasing frequency [Benford (2010)]. A more detailed costing exercise has been conducted by the author to better constrain the optimum frequency band for interstellar beacons [Morrison (2017)]. That model takes account of the fundamental physics of antenna systems, the required signal strength needed in different regions of the spectrum where different noise mechanisms dominate, a broad range of costing relationships for antennas and RF power sources, and various cost balance assumptions. It is argued that beacon builders should not assume target receivers are constrained to be located below an atmosphere, meaning that atmospheric attenuation should not factor into the choice of beacon operating frequency. That being the case, the modeling results, summarized in Figure 2, strongly suggest beacons are better operated above 15 GHz. Over a wide range of starting assumptions, the frequency found to give the lowest total system cost was always found to fall within the range 20 to 100 GHz - the lower end of the EHF band.

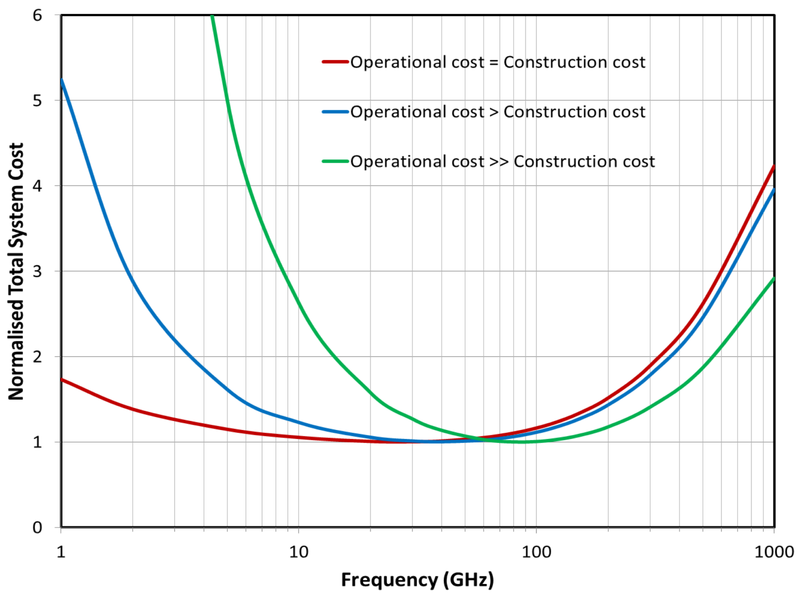

Figure 13: Modelled end-to-end beacon transmitter-receiver system cost as a function of beacon operating frequency, for three alternative cost balance assumptions [Morrison (2017)].

The factor found to have the highest influence on the choice of operating frequency was the relative emphasis on operational versus construction cost. The red curve in Figure 2 corresponds to the scenario where both operational and construction costs are of equal concern to the beacon builder. If we expect a beacon to transmit over a long time duration (centuries, millennia or longer), then operational cost may be expected to dominate the beacon builder's concerns. The scenario where operational cost is significantly more of a concern than construction cost is represented by the blue curve, and where operational cost totally dominates over construction cost is shown in green. In all cases, there is a convex cost relationship as a function of frequency, with a minimum total cost at a frequency falling in the range 20 to 100 GHz. Crucially, there were no modeling assumptions that supported the selection of a frequency below 15 GHz. This suggests that beacons may be rare below 15 GHz.

3.6.2 Technical Justification

The discussion above suggests that searches for intentionally transmitted beacon signals may be ineffective with SKA1-Mid unless and until Band 6 becomes available. The range of 15 to 25 GHz goes some way to opening up the parameter space of interest. However, coverage from 15 to 50 GHz would be preferred given that the mean optimum frequency of the various scenarios considered in [Morrison (2017)] is $\approx$ 50 GHz.

Traditionally SETI has made the strong assumption that intentional beacons are likely to employ narrowband signaling, to help distinguish the signal from natural radio sources. However, it seems likely that a beacon builder would wish to embed a message within their signal, and if this is the case, information theory tells us that wideband signal types are necessary for energy-efficient communication [Messerschmitt (2015), Morrison (2017)], which will be particularly important over interstellar distances. Therefore, it would seem appropriate for high-frequency searches to focus on wideband signal detection.

While narrowband searches have dominated SETI over the past 50 years, the field of wideband SETI is now rapidly emerging. An overview of techniques suitable for detecting wideband SETI signals is provided in [Morrison (2017)]. Many of these techniques offer good potential to discover the classes of signals we anticipate may be applicable to interstellar beacons. Already some of the simpler algorithms (such as energy detection or autocorrelation) could easily be integrated into back-end processing systems for the SKA and pre-cursor telescopes for execution in real-time. Over time, more advanced algorithms with higher sensitivity could be brought into service as implementations become more optimized and back-end processing capabilities improve.

Maximum sensitivity for both narrowband and wideband SETI detection will require access to tied-array beam complex voltage streams. The larger the available bandwidth the better in terms of parameter space coverage and maximization of sensitivity. Beams may be coarsely channelized, e.g. to widths of order a MHz. It is not expected that any individual beacon signal would span more than 1 MHz, and for narrowband SETI each coarse channel can be further channelized to provide finer resolution, e.g. down to 1 Hz.

The tied-array beamformer currently planned for deployment on SKA-Mid for pulsar timing purposes will be perfectly suited to supporting Band 6 SETI.

References

Benford, J., Benford, G. and Benford, D., 2010, Astrobiology vol. 10, 475, 490

Messerschmitt, D.G., 2015, Acta Astronautica, vol. 107, 20, 39

Morrison, I., 2017,"Constraining the discovery space for artificial interstellar signals, PhD dissertation, University of New South Wales

Oliver, B. M., et al., 1971, "Project Cyclops: A Design Study of a System for Detecting Extraterrestrial Intelligent Life", Stanford/NASA/Ames Research Center Summer Faculty Program in Engineering Systems Design, Technical Report

3.7 Radio Jets from Young Stellar Objects

Guillem Anglada (IAA-CSIC, Granada, Spain)

3.7.1 Introduction

Accretion disks and collimated outflows (jets) are intrinsically associated with the star-formation process. In particular, the youngest, deeply embedded protostars are usually radio sources of free-free emission that trace the (partially) ionized region, very close to the exciting star (∼10-100 au), where the outflow phenomenon originates, and are referred to as "thermal radio jets" (see Anglada et al., 2015, 2018 for recent reviews; see also Hoare, 2004).

Thermal radio jets have been found during all the stages of the star-formation process, from Class 0 protostars to stars associated with transitional disks. Also, these radio jets are present in young stars across the whole stellar spectrum (Fig. 14), from O-type protostars and possibly to proto-brown dwarfs. This radio emission is relatively weak, and correlated with the bolometric luminosity. The observed 3.6 cm radio luminosities (taken to be $S_\nu d^2$, with d being the distance) go from ∼100 mJy kpc^2 for massive young stars to $\sim 3 \times 10^{-3}$ mJy kpc^2 for young brown dwarfs (Anglada et al., 2018). Dynamical timescales of these radio jets are short, and these observations provide information on the physical properties, direction and collimation of the gas ejected by the young system in the last few months/years.

Despite in a number of young stellar objects (YSOs) non-thermal synchrotron emission has been found in the jet lobes (Carrasco-González et al., 2010), at relatively large distances from the origin, the jet core is always characterized by thermal emission with a positive spectral index. Thus, this emission is stronger at higher frequencies, improving its detectability and making it possible to reach a higher angular resolution. Implementing in SKA the Band 6 frequencies, would benefit the study of

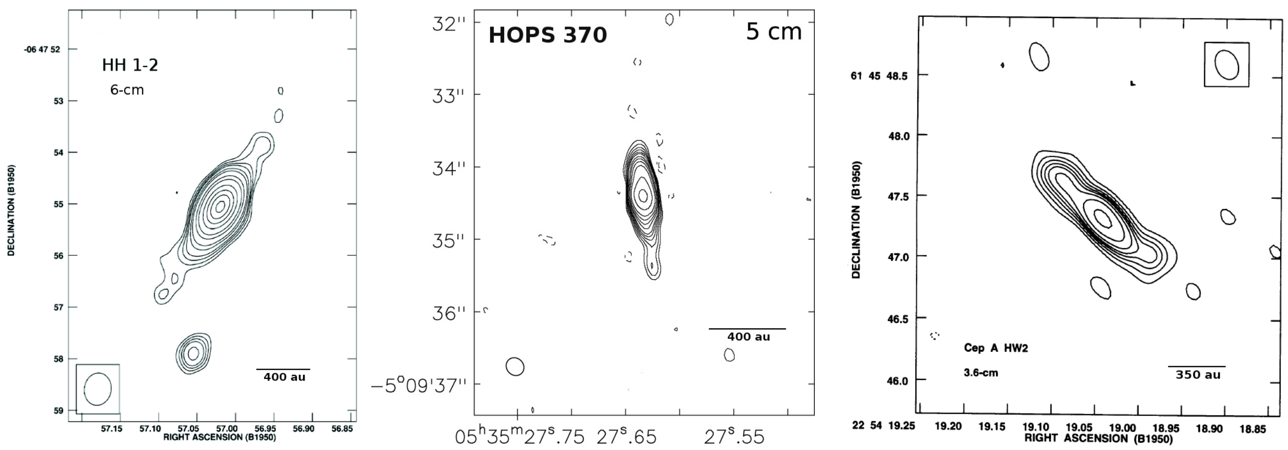

Figure 14: Radio jets from low-, intermediate-, and high-mass protostars, observed at cm wavelengths with the VLA (from Rodríguez et al., 2000, Osorio et al., 2017, and Rodríguez et al., 1994).

YSO radio jets in several aspects, particularly in the study of the launching and collimation processes, and the jet kinematics.

3.7.2 Observation of the launching region

One of the key problems in the study of jets is to determine how they are accelerated and collimated. In this respect, observations in the cm range are most useful to trace the base of the ionized jets, close to the young central object and its accretion disk, where optical or near-IR images are obscured by the high extinction present.

There is a general consensus in that jets in young stars are produced by a magnetocentrifugal mechanism, similar to the one proposed by Blandford & Payne (1982) to explain extragalactic jets. In this mechanism, material from the accretion disk is accelerated and ejected in the presence of a magnetic field anchored to the star-disk system (e.g., Konigl, & Pudritz, 2000; Shu et al., 2000). In this way, energy and angular momentum are removed magnetically from accretion disks. However, direct observational evidence of this mechanism is poor and there is still controversy over where these magnetic fields are anchored to the disk. In the X-wind model (e.g., Shu et al., 1994) the jet is ejected from a narrow region at the truncation radius R_X of the disk by the stellar magnetosphere, while in the extended disk wind model (e.g., Pudritz, & Norman, 1983) jet material is ejected from a wider range of radii.

Indirect estimates from optical and near-IR observations suggest launching radii from $\sim$0.07 au (the typical disk corotation radius) to $\sim$3 au (e.g., Anderson et al., 2003; Estalella et al., 2012; Belloche, 2013 and references therein). On the other hand, ALMA observations of the molecular outflow TMC1A (Bjerkeli et al., 2016) suggest that in this source the gas is ejected from a region extending a radial distance from $\sim$2 au to 20 au, but this molecular gas is more difficult to distinguish from the entrained ambient gas than the ionized material. SKA Band 6 observations can reach angular resolutions of $\sim$0.02-0.01 arcsec in the 25-40 GHz frequency range. Therefore, in nearby radio jets ($d \simeq 150$ pc), sensitive SKA Band 6 free-free continuum observations have the capability of directly resolving details of the ionized jet structure at physical scales of 1.5-3 au, close to the launching radius.

It is worth noting that, given that the typical velocities of the jets are a few hundred km s^{-1}, the dynamical time scale of the observed material in this very small region is of the order of only one week. Therefore, SKA Band 6 observations of YSO jets have the potential to explore "in real time" the process of knot generation and launching, as well as their proper motions. Also, as part of the emission processes of the plasma, radio jets are believed to show RRLs whose detection is expected to be feasible with SKA (Anglada et al., 2015, 2018), providing (in combination with proper motions) the complete 3D kinematics of the region where jets originate. However, we note that, given the thermal nature of the emission, high sensitivities (rms of the order of $\sim$0.1-1 μJy beam^{-1}) will be necessary for these very high angular resolution studies (0.01-0.02 arcsec). Thus, deep integrations (likely several tens of hours) will be required, even for the strongest YSO radio jets (flux densities of a few mJy).

Jets are common in many kinds of astrophysical scenarios. Consequently, characterizing radio jets in YSOs, where thermal emission allows us to determine their physical conditions in a reliable way, would be also useful in understanding acceleration and collimation mechanisms in all kinds of astrophysical jets.

Additionally, we note that a good knowledge of the jet properties is indispensable for grain growth studies in protoplanetary disks. Jets persist along most of the star-formation process, with free-free emission being present even in transitional disks (Rodríguez et al., 2014), where dust grains have grown to mm sizes and planet formation has already started. Typically, at decimeter wavelengths the free-free emission of the jet dominates over the dust emission of the associated disk while at millimeter wavelengths the dust emission is the dominant. However, at wavelengths around 1 cm, which are well-suited to study the dust grains that have grown to cm-sized pebbles, the free-free and dust emissions become comparable, making it necessary to properly separate these two contributions. Moving in frequency across Band 6 will allow us to progressively image the ionized jet and disk contributions with an angular resolution high enough to identify and separate well these two emissions, and to be able to follow both the processes of ejection of the jet and grain growth in the disk. SKA observations at lower frequencies (Band 5) would lack the necessary angular resolution to reach this goal.

3.7.3 Outflow rotation

At the scale of the molecular outflows, several cases have been found that show a suggestion of rotation, with a small velocity gradient perpendicular to the major axis of the outflow (e.g., Launhardt et al., 2009; Lee et al., 2009; Bjerkeli et al., 2016; Hirota et al., 2017; see also Belloche, 2013). Evidence of outflow rotation has also been found in optical/IR microjets from T Tauri stars (e.g., Bacciotti et al., 2002; Anderson et al., 2003; Coffey et al., 2007). The observed velocity difference across the minor axis of the molecular outflow is typically a few km s^{-1}, while in the case of optical/IR microjets (that trace the inner, more collimated component) it can reach a few tens of km s^{-1}. These signatures of jet rotation about its symmetry axis represent the best way to test the hypothesis that jets extract angular momentum from the star-disk systems. However, there is considerable debate on the actual nature and origin of these gradients (Frank et al., 2014; De Colle et al., 2016). The presence of precession, asymmetric shocks or multiple sources could also produce apparent jet rotation. Also, it is possible that most of the angular momentum could be stored in magnetic form, rather than in rotation of matter (Coffey et al., 2015). To ensure that the true jet rotation is being probed it should be checked that rotation signatures are consistent at different positions along the jet, and that the jet gradient goes in the same direction as that of the disk. These kind of tests have been carried out only in very few objects (see Coffey et al., 2015) with disparate results.

It is imperative that the jet is observed as close as possible to the star, where any evidence of angular momentum transfer is still preserved, since far from the star the interaction with the environment can hide and confuse rotation signatures. Therefore, high angular resolution SKA Band 6 observations of radio recombination lines from radio jets, reaching the region close to the star, are best suited to solve these problems. With these kind of observations, it could be possible to observe the jet near its launching region and compare the velocity gradients with those observed at larger scales.

3.7.4 Jets and ionized disks

Photoionization is considered the main mechanism for gas dispersal in disks. In a few massive objects there is evidence of elongated centimeter sources that trace photoionized disks (S106IR: Hoare et al., 1994; S140-IRS: Hoare, 2006; Orion Source I: Reid et al., 2007). These sources show a similar centimeter spectral index to that of jets and one cannot discriminate using this criterion. The high sensitivity and angular resolution of SKA will enable continuum imaging and RRL dynamical studies of the equatorial winds, probably driven by radiation pressure acting on the gas on the surface layers of the disk, that have been observed in a number of massive young stars (Hoare, 2004).

Ionized disks are also possibly present in the case of low-mass YSOs, where it is believed that extreme-UV (EUV) radiation from the star is the main ionizing mechanism of the disk surface. The high resolution images of GM Aur presented by Macías et al. (2016) show that, after subtracting the expected dust emission from the disk (which is well traced by the 7 mm emission), the 3 cm emission from this source is composed of an ionized radio jet and a photoevaporative wind arising from the disk perpendicular to the jet (see Fig. 15). Thus, the Band 6 of the SKA will cover the full frequency range needed to trace both the neutral and ionized components of the disk, as well as the ionized jet, allowing us to image in great detail the onset of the photoevaporative disk winds.

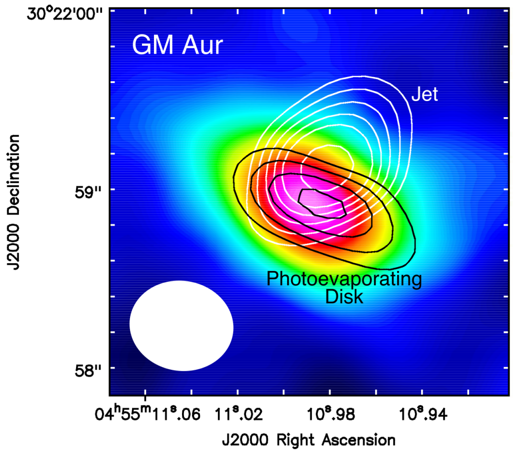

Figure 15: Decomposition of the emission of GM Aur at cm wavelengths. The free-free emission at 3 cm of the radio jet is shown in white contours and that of the photoevaporative wind from the disk is shown in black contours. The dust emission from the disk at 7 mm is shown in color scale. (From Macías et al., 2016).

References

Anderson, J. M., Li, Z.-Y., Krasnopolsky, R., et al. 2003, ApJ, 590, L107
Anglada, G., Rodríguez, L. F., & Carrasco-Gonzalez, C. 2015, Advancing Astrophysics with the Square Kilometre Array (AASKA14), 121
Anglada, G., Rodríguez, L. F., & Carrasco-González, C. 2018, A&A Rev., 26, 3
Bacciotti, F., Ray, T. P., Mundt, R., et al. 2002, ApJ, 576, 222
Bjerkeli, P., van der Wiel, M. H. D., Harsono, D., et al. 2016, Nature, 540, 406
Belloche, A. 2013, EAS Publications Series, 25
Blandford, R. D., & Payne, D. G. 1982, MNRAS, 199, 883
Carrasco-González, C., Rodríguez, L. F., Anglada, G., et al. 2010, Science, 330, 1209
Coffey, D., Bacciotti, F., Ray, T. P., et al. 2007, ApJ, 663, 350
Coffey, D., Dougados, C., Cabrit, S., et al. 2015, ApJ, 804, 2
De Colle, F., Cerqueira, A. H., & Riera, A. 2016, ApJ, 832, 152
Estalella, R., López, R., Anglada, G., et al. 2012, AJ, 144, 61
Frank, A., Ray, T. P., Cabrit, S., et al. 2014, Protostars and Planets VI, 451
Hirota, T., Machida, M. N., Matsushita, Y., et al. 2017, Nature Astronomy, 1, 0146
Hoare, M. G., Drew, J. E., Muxlow, T. B., et al. 1994, ApJ, 421, L51
Hoare, M. G. 2004, New A Rev., 48, 1327
Hoare, M. G. 2006, ApJ, 649, 856
Konigl, A., & Pudritz, R. E. 2000, Protostars and Planets IV, 759
Launhardt, R., Pavlyuchenkov, Y., Gueth, F., et al. 2009, A&A, 494, 147
Lee, C.-F., Hirano, N., Palau, A., et al. 2009, ApJ, 699, 1584
Macías, E., Anglada, G., Osorio, M., et al. 2016, ApJ, 829, 1
Osorio, M., Díaz-Rodríguez, A. K., Anglada, G., et al. 2017, ApJ, 840, 36
Pudritz, R. E., & Norman, C. A. 1983, ApJ, 274, 677
Reid, M. J., Menten, K. M., Greenhill, L. J., et al. 2007, ApJ, 664, 950
Rodríguez, L. F., Garay, G., Curiel, S., et al. 1994, ApJ, 430, L65
Rodríguez, L. F., Delgado-Arellano, V. G., Gómez, Y., et al. 2000, AJ, 119, 882
Rodríguez, L. F., Zapata, L. A., Dzib, S. A., et al. 2014, ApJ, 793, L21
Shu, F., Najita, J., Ostriker, E., et al. 1994, ApJ, 429, 781
Shu, F. H., Najita, J. R., Shang, H., et al. 2000, Protostars and Planets IV, 789

3.8 Astronomical Masers Associated with Young Stellar Objects (YSOs)

Tomoya Hirota (NAOJ, Tokyo, Japan), Huib Jan van Langevelde (JIVE/Leiden University, The Netherlands), Wouter Vlemmings (Chalmers University of Technology, Sweden), Busaba Kramer (MPIfR, Bonn, Germany/NARIT, Thailand), James Green (CSIRO Astronomy and Space Science, Australia), Gabriele Surcis (INAF-Cagliari, Italy), Kazi Rygl (INAF-Institute for Radioastronomy and Italian ALMA Regional Centre, Italy), Hiroshi Imai (University of Kagoshima, Japan), Koichiro Sugiyama (NAOJ, Tokyo, Japan/NARIT, Thailand)

3.8.1 Introduction

From the very early phase of radio molecular spectroscopy starting in late 1960's, strong astronomical masers have been recognized as a powerful tool for understanding stellar evolution, in particular for the very early phase of star formation and late stages after the main-sequence. Due to the specific physical conditions required for the pumping and amplification, maser emission is always associated with the regions with high temperature, high density, and/or a strong radiation field. Thus, they are used to pinpoint the positions of young stellar objects (YSOs) and late-type stars sometimes hidden in the optical/infrared dark clouds and dust envelopes. Thanks to their spatially compact structures and extremely high brightness, they are detectable with high resolution interferometers and very long baseline interferometer (VLBI) networks. The sharp spectral profiles, which are sometimes narrower than the thermal line widths, enables one to investigate accurate radial velocities of the target maser sources. Through high resolution proper motion measurements using the VLBI technique, masers have played a unique role in providing three dimensional velocity fields of astronomical objects. Accurate VLBI astrometry allows one to determine the distances toward maser sources through trigonometric parallax measurements. Masers are also employed to study the dynamical structure of galaxies including the Milky Way Galaxy through VLBI astrometry, and the central parts of the active galactic nuclei (AGNs). Observations of the Zeeman effect in masers provide not only in-situ magnetic field directions, but also the field strengths. These observational studies will be advanced by utilizing the SKA's capabilities to explore star-formation studies. In this chapter, we will discuss potential science cases for star-formation studies through maser observations in the high frequency regime.

3.8.2 Masers transitions above 15 GHz

In star-forming regions, several molecular lines show maser emission. At frequencies higher than 15 GHz, SKA will be able to cover a number of representative maser transitions such as water (H_2O), methanol (CH_3OH), ammonia (NH_3), and silicon oxide (SiO) as summarized in Table 6. Notably, the H_2O maser at 22 GHz is the strongest among known astronomical maser lines. For CH_3OH masers, a classification has been made that identifies interstellar masers as either class I or class II (Menten, 1991). The class I CH_3OH masers are thought to be pumped by molecular collisions in shocked regions and hence, they are sometimes located far away from the central YSOs. In contrast, the class II CH_3OH masers are detected only in close vicinity to the central YSOs, presumably because a strong infrared radiation field is required to excite the masers, which is provided by warm dust emission, heated by the forming star. The H_2O masers and class I CH_3OH masers are detected in low- to high-mass star-forming regions while the class II CH_3OH masers are identified only in high- and intermediate-mass ($>10\,M_\odot$) star-forming regions (Minier et al., 2003). The NH_3 and SiO masers at $\sim$23 GHz and $\sim$43 GHz, respectively, are much rarer compared with those of H_2O and CH_3OH. In the subsequent sections we discuss the scientific uses of these maser transitions.

3.8.3 Three-dimensional dynamical structures of YSOs

The 22 GHz H_2O masers have been recognized as the brightest radio emission line and hence have long been observed with VLBI. Most of the target Galactic sources in star-forming regions are high-mass YSOs and a number of survey observations have been carried out. These demonstrated the 3-dimensional velocity field of the mass ejection via high-velocity jets and outflows driven by central

Table 4: Target maser lines in the 15-50 GHz band

Molecule	Transition	Frequency (GHz)	Note
H_2O	$6_{1,6}$-$5_{2,3}$	22	
SiO	J=1-0 v=0, 1, 2	42-43	Including ^{29}SiO and ^{30}SiO.
NH_3	(J, K)	20-40?	∼10 inversion transitions.
CH_3OH	2_1-3_0E	19	Class II
CH_3OH	9_2-10_1A$^+$	23	Class II
CH_3OH	J_2-J_1E	24-28	Class I, J range from 2 to 17.
CH_3OH	8_2-9_1A$^-$	28	Class II
CH_3OH	4_{-1}-3_0E	36	Class I
CH_3OH	7_{-2}-8_{-1}E	37	Class II
CH_3OH	6_2-5_3A$^+$/A$^-$	38	Class II
CH_3OH	7_0-6_1A$^+$	44	Class I

YSOs (e.g. Torrelles et al., 2003). It is natural that SKA will enhance a number of the H_2O maser samples with higher sensitivity and wider field of view, providing a census of high-mass YSOs in various mass ranges and evolutionary phases. Furthermore, the H_2O masers are also associated with low-mass Solar-type YSOs (Furuya et al., 2003). Class I CH_3OH masers are also associated with low-mass YSOs as well (Kalenskii et al., 2010) unlike the 6.7 GHz class II CH_3OH masers. However, they are in general weaker and have fewer numbers of maser features compared with high-mass YSOs. When using VLBI, maser features in nearby H_2O maser and class I CH_3OH maser sources are easily resolved out (Imai, 2007; Matsumoto et al., 2014). Higher sensitivity will recover maser features in low-mass YSOs to prove the 3D velocity field more accurately. These studies will solve the ambiguity in the inclination angles employed to estimate velocity fields of disk and outflows associated with low-mass YSOs.

Class I CH_3OH masers are excited in the shocked molecular gas associated with outflows from YSOs. The representative lines are the 36 GHz (4_{-1}-3_0E) and 44 GHz (7_0-6_1A$^+$) transitions (Voronkov et al., 2012), and several large-scale surveys have been carried out. Although these class I CH_3OH masers show strong emission in single-dish and interferometer observations, VLBI observations have failed, because the spatially extended structures are easily resolved out with 1000 km VLBI baselines. A recent detection with KaVA (the combination of the Korean VLBI Network and the Japanese VERA Array) of the 44 GHz maser towards a high-mass star-forming region IRAS18151-1208 (Matsumoto et al., 2014) demonstrates that baselines of a few 100 km can recover compact components in Class I CH_3OH masers, showing features with a size scale of ∼10 au or a few milli-arcseconds (mas) at 3 kpc. The extremely dense uv coverage, together with the long baselines of SKA will achieve sufficiently high sensitivity to recover both the extended and compact emission of the class I CH_3OH maser features. Compact structures can then be used to measure the proper motions of the low-velocity outflows traced by the class I CH_3OH masers. The low-velocity outflows could have a typical velocity of 10 km s^{-1} or the corresponding proper motion of $2/D$ mas yr^{-1} where D is the distance from us in kpc. Thus, high resolution (∼10–20 mas) and long-term monitoring (∼a few years) with SKA will provide dynamical properties of the outflows such as mass loss rate, momentum rate, mechanical luminosity, and dynamical timescale, after correcting for the inclination angles.

SiO masers are widely observed in late-type stars while they are detected only toward a handful of high-mass star-forming regions (Zapata et al., 2009), such as Orion Source I, W51N, and Sgr B2(M). Very recently, high sensitivity observations with ALMA identified new star-forming regions associated with the J=2-1 SiO masers at 86 GHz (Higuchi et al., 2015; Cho et al., 2016). These results demonstrate that higher sensitivity observations have a potential to detect new weaker SiO maser sources in star-forming regions. Thus, if the observing band covers 43 GHz, it is expected that SKA will be able to find new SiO J=1-0 masers associated with YSOs. The only extensively observed YSO with the SiO masers is Orion Source I (Menten, & Reid, 1995), showing various SiO masers including vibrationally ground and excited maser transitions along with ^{29}Si and ^{30}Si isotopologues

(Goddi et al., 2009). These different masers trace different scales of the dynamical structure of disk-outflow around Source I with $\sim$100 au scale and hence, are good diagnostics to estimate their physical properties. Furthermore, higher resolution VLBI observations reveal the rotating-expanding motion of the outflows possibly driven by the magneto-centrifugal disk wind as shown in Figure 16 (Kim et al., 2008; Matthews et al., 2010; Vaidya, & Goddi, 2013). These SiO maser observations, along with the thermal line observations with ALMA (e.g. Hirota et al., 2017; Ginsburg et al., 2018), shed light on the outflow launching mechanism in high-mass star-formation processes. SKA will be able to extend similar studies for other possible new target sources associated with the SiO masers. Given that the flux densities of the SiO v=1 J=1-0 maser in Orion Source I, which is located at 420 pc from the Sun (Kim et al., 2008), are of the order 10^3 Jy, the other distant sources are expected to have the SiO maser flux densities at an order of $\sim$1 Jy at 5-10 kpc. Such sensitivity can already be achieved with the currently available telescopes, but the wider field-of-view with SKA will make it easier to carry out extensive survey observations of rarer SiO masers. In addition, the higher sensitivity of the SKA will be able to achieve detection of less abundant isotopologues which have three orders of magnitude weaker than the strongest ^{28}SiO v=1 masers. The 10 mas beamsize achievable with SKA will resolve the spatial structure of 10D au at D kpc. If new SiO maser sources are identified in the Galactic plane with SKA, most of their spatial structures will be resolved.

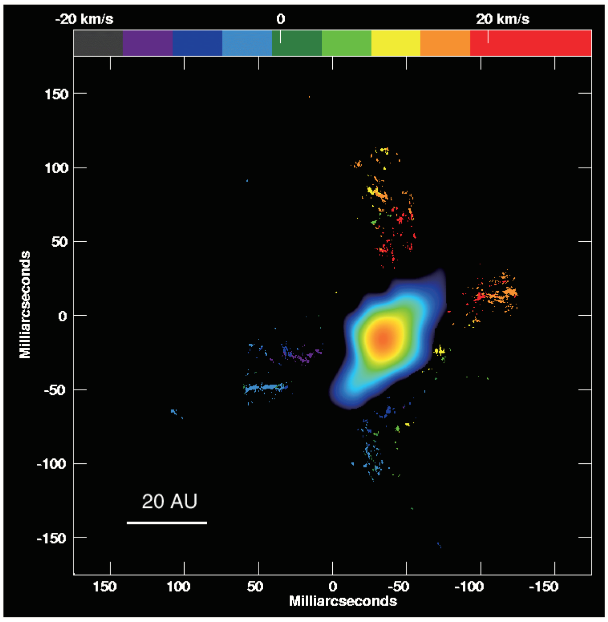

Figure 16: An example of the SiO maser source associated with high-mass YSO, Orion Source I, taken from Vaidya, & Goddi (2013). Colored symbols represent the positions of the SiO v=1, 2 J=1-0 maser emission observed with VLBA with their LSR velocities. The color-scale image shows the 43 GHz continuum emission mapped with the VLA. The SiO maser emission trace the disk-driven rotating outflow ejected from the edge-on disk as seen in the continuum emission.

Ammonia (NH_3), has a number of inversion transitions at the rotational energy levels of (J, K). For the metastable state, J=K, high excitation transitions such as (3, 3), (6, 6), (9, 9), ... and up to (13, 13) are detected with the VLA as compact maser emission sources (Goddi et al., 2015). In addition, some of non-metastable transitions ($J > K$), also show masers in various energy levels (Henkel et al., 2013). The upper-state energy level of the highest one (13, 13) lies at 1691 K. Thus, NH_3 masers could be new unique probes for high-temperature gas close to the high-mass YSOs. Except for a few strong transitions (e.g. (3, 3), (6, 6)), most of the NH_3 masers are much weaker than 1 Jy in the case of W51-North at the distance of 5 kpc (Goddi et al., 2015). Higher-sensitivity observations are crucial to search for other NH_3 maser sources.

3.8.4 Variability of masers as tools for accretion events

Recent discoveries of the sudden flux increase of the 6.7 GHz class II CH_3OH maser lines (called maser flares) suggest possible evidence of mass accretion burst events in high-mass YSOs, such as S255IR-NIR3 (Caratti o Garatti et al., 2017; Moscadelli et al., 2017) and NGC6334I-MM1 (Hunter et al., 2017; Brogan et al., 2018; MacLeod et al., 2018). The maser flare is caused by an increase in temperature in the maser emitting region due to the enhancement of accretion luminosity of the central YSO via the fragmentation of its circumstellar disk. One of the long-standing issues in high-mass star-formation studies is to understand mass accretion processes. To form high-mass YSOs, non-spherical (i.e. through the disk) mass accretion at high accretion rates of $\sim 10^{-3}$ $M_\odot$ yr^{-1} are required to overcome the strong feedback from high-mass YSOs. Hence, episodic mass accretion burst events in high-mass YSOs are essential for understanding of high-mass star-formation processes observationally.

The 6.7 GHz class II CH_3OH masers are used for intensive monitoring of variability. In addition, the H_2O maser flare is also reported during the mass accretion event in NGC 6334I-MM1 (Hunter et al., 2017; Brogan et al., 2018; MacLeod et al., 2018). Since the H_2O masers are excited in the shocked molecular gas between the outflows/jets and ambient gas, the H_2O maser flare will also be used as a probe of accretion burst events. Indeed, it is likely that the mass accretion trigger the ejection events of the outflow/jet (Cesaroni et al., 2018) which could also affect the masing gas clumps.

The maser flare provides the opportunity to initiate monitoring observations of continuum emission from radio to infrared to investigate changes in the accretion luminosity of the high-mass YSOs, along with their physical properties in the disk/outflow/envelopes. As discussed above, these masers will be used for revealing the 3D velocity structures of the circumstellar structures through VLBI proper motions.

Interestingly, new CH_3OH maser lines appear during the active phase in another YSO, G358.93-0.03 (Breen et al., 2019; Brogan et al., 2019), including transitions within the SKA band. These new/rare masers may be weak and possibly not excited in the quiescent phase. High sensitivity SKA will be able to constrain their flux density, which provides physical constraints on their pumping condition.

Furthermore, the 22 GHz H_2O maser is known to show extremely strong emissions sometimes recognized as the maser bursts or supermasers. Well known examples are Orion KL (Hirota et al., 2014, and references therein), W49N (Honma et al., 2003), and the recent detection in G25.65+1.05 (Burns et al., 2019). Although the origin of the H_2O maser burst is still unclear, they are thought to reflect changes in physical condition and/or are just caused by the change in geometrical configuration to enhance amplification. The H_2O maser burst is suggested to have periodicity of an order of years to 10 years (Honma et al., 2003; Hirota et al., 2014, and references therein). Thus, long-term monitoring with SKA will find more maser flares/bursts for statistical studies.

The maser flares/bursts are strong enough to be detected with small single-dish telescopes. To find maser flares/bursts efficiently and to share information rapidly, an international collaboration team "M2O" (Maser Monitoring Organization) was established in 2017, in which several maser lines are regularly observed with various radio telescopes (e.g. Brogan et al., 2018, 2019; MacLeod et al., 2018; Breen et al., 2019; Burns et al., 2019). However, these events are unpredictable and hence, monitoring observations for a number of maser sources which are candidates of maser flares are time consuming given the necessity of enough short interval of daily, weekly, or monthly depending on their timescale. Furthermore, it is ideal to conduct unbiased survey/monitoring of masers to search for unknown target sources. SKA can be utilized for such monitoring and survey with high sensitivity (i.e. short integration time) and large field-of-view as commensal observations of other Galactic plane spectral line survey projects.

3.8.5 Maser Polarization and magnetic fields

It is generally accepted that magnetic fields have an important role in star formation. However, it is not well quantified *how much* the magnetic fields contribute, with respect to turbulence or gravity for the various stages of star formation, mainly due to the difficulty and scarceness of observations.

The magnetic field orientation in the plane of the sky can be observed from dust polarisation,

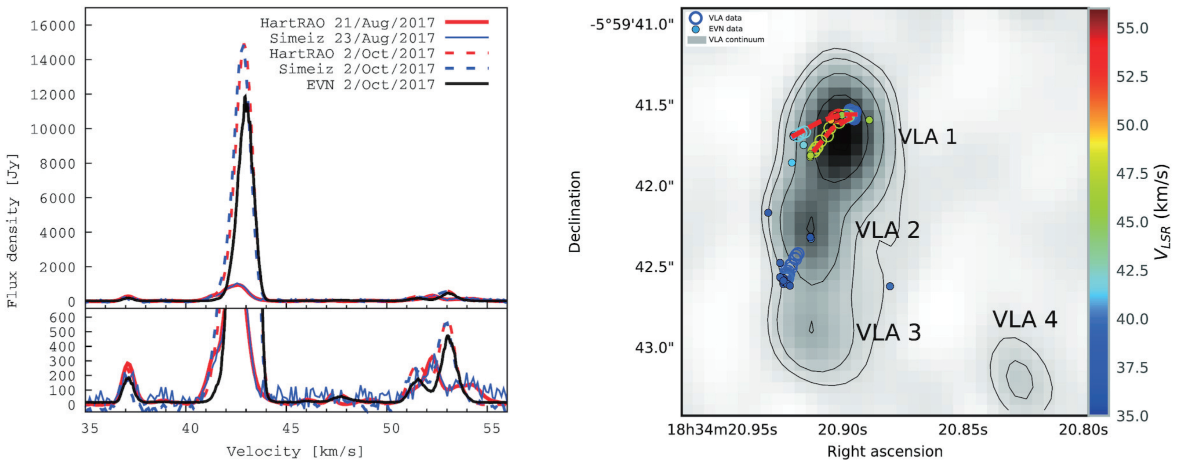

Figure 17: Spectra (left) and distribution (right) of the H_2O maser "superburst" in a high-mass YSO G25.65+1.05 discovered by the M2O collaboration (Burns et al., 2019).

which traces mostly the dense gas around the YSO or the disk (see also the contribution of Girart et al. in this white paper), but also from polarised maser emission. Polarised H_2O maser emission arises typically in outflows and complements the dust polarisation observations (Dall'Olio et al., 2017) through providing both an indication of the field in the plane of the sky and the orientation with respect to the line of sight, helping obtain a more complete picture of the magnetic fields.

CH_3OH masers can arise both in the disk, or the ambient medium between the disk and outflow, and with known Landé g-factors the magnetic field strength can be calculated for these masers (Lankhaar et al., 2018). With the European VLBI Network (EVN), Surcis et al. (2019) and references therein have detected polarised 6.7 GHz CH_3OH maser emission around numerous high-mass YSOs. Higher frequency CH_3OH masers, beyond 15 GHz, are weaker than the 6.7 GHz transition, but allow us to trace different temperature and density environments. During the last decade, an increasing number of polarimetric interferometric observations of the 36, 37, 38, and 44 GHz CH_3OH masers in YSOs were reported and in some cases with successful detection of Zeeman effect (see for example: Sarma & Momjian, 2009, 2011; Ellingsen et al., 2018; Momjian, & Sarma , 2019).

Finally, maser polarisation has the advantage of deriving gas dynamics *and* magnetic field orientations simultaneously (Sanna et al., 2015). While VLBI (and phased-SKA in an VLBI array!) can address the magnetic fields on scales down to 10 AU, sensitive SKA observations would investigate the more extended emission, which is missed by VLBI.

3.8.6 Masers as probes of the evolutionary phase of YSOs

Masers are also useful diagnostics of physical properties and their evolution in star-formation processes because the pumping conditions of maser emission are sensitive to the change in environments such as temperature, density, and the radiation field. For example, the well-known class II CH_3OH maser line at 6.7 GHz is observed to be associated exclusively in high- and intermediate-mass YSOs (Minier et al., 2003). Association of CH_3OH and H_2O masers with infrared, (sub)millimeter, and/or centimeter continuum sources in star-forming regions could provide a rough estimate of evolutionary phase (or age) of the central YSOs (Breen et al., 2010). Although such a maser chronology is still under debate due to insufficient number of high resolution observations that permit resolving individual YSOs in distant star-forming regions, future large-scale SKA surveys will contribute to establishing the scenario statistically by combining radio continuum data (see Anglada et al., in this memo).

3.8.7 VLBI applications

Maser sources in high-mass star-forming regions have been targeted by many VLBI arrays. Most of the VLBI maser astrometry of star-forming regions (and some evolved stars) is limited to the first, second and a part of the third Galactic quadrant (Reid et al., 2019). Access from the Southern sky will permit us to explore the fourth quadrant, that is very important as it would complete our picture of the spiral structure of the Milky Way and allow for a better modeling of Galactic parameters such as the rotation velocity at the Sun's position, Galactic rotation curve and distance to the Galactic Centre. Indeed, the astrometry of (Southern hemisphere) CH_3OH masers at 6.7 and 12 GHz is a recognised science case for VLBI with SKA (Green et al., 2015). Extending the band to higher frequencies will include other maser transitions that can be used for this, most notably the 22 GHz H_2O line, but possibly also the SiO at 43 GHz.

The 22 GHz H_2O line is an important tracer of the outflows in high mass star forming regions. VLBI observations of this transition have been used to study the dynamics of mass ejection, that is supposed to play an important role in both low- and high mass stars. Although these masers are already detectable in many sources, it is exciting to think how many more sources can be reached with the sensitivity of SKA-Mid in the array. For these studies it is particularly relevant that ALMA is in the same hemisphere and will have access to the same targets.

For astrometric studies, H_2O masers are not as widespread as CH_3OH masers, but they are usually at higher flux levels and offer higher resolution. When close calibrators are available, they can often have astrometric registration with higher accuracy: H_2O maser astrometry pinpointed a star-forming region on the Far side of the Milky Way at a distance of $20.4^{+2.8}_{-2.2}$ kpc (Sanna et al., 2017). Preliminary analysis shows that at 22 GHz, there are unlikely to be sufficient calibrators for high SNR in-beam calibration, however, even with switching astrometry it will be possible to reach higher accuracy (few μas) astrometry than is now possible.

SiO maser astrometry is not very common, as VLBI phase referencing at 7 millimeter is challenging. However, the distance to Orion KL has been determined also via SiO maser parallax (Kim et al., 2008). SiO masers are much more common in evolved stars and the possibility of observing their proper motions in the inner Galaxy is discussed in chapter (see Imai et al. in this memo).

We note that high frequency masers will be promising targets for joint observations with the ngVLA project, as discussed in Hunter et al. (2018), and for phased-SKA as part of VLBI Networks, such as the EVN. A direct collaboration will be possible with a VLBI network that includes both ngVLA and SKA in the future, providing intercontinental baselines with larger than 5000 km to achieve higher resolution of sub-mas at >15 GHz. If other higher sensitivity telescopes such as GBT, phased-ALMA at band 1, and/or some more new VLBI antennas (Q-band or SKA band 6) can join such an extremely high sensitivity global array, it will be able to map both masers and non-thermal continuum emission associated with radio jets (Anglada, in this white paper) at resolutions of an order of mas or better.

The inclusion of phased-SKA in the EVN, which are in overlapping time-zones, will be very important for high-resolution maser science in the Galactic centre region. With the future installation of K/Q/W receivers on several EVN antennas, the extension of the (phased-) SKA frequency range extremely valuable, as Q band observations are more challenging. The sensitivity of phased-SKA would permit detection of an order of magnitude weaker signals, much as the phased-ALMA array in the GMVA or EHT.

3.8.8 Summary

SKA will be utilized to extend current observational studies on star-formation through masers. In particular, masers will be unique probes to reveal the 3-dimensional velocity field, which is essential for understanding mass accretion processes in YSOs and their evolutionary sequence. Time-domain maser observations will uncover episodic mass accretion processes more efficiently with the SKA. The high sensitivity and wide field of view of SKA are powerful tools to census distant (high-mass) SFRs in various maser transitions including rarer and even newly discovered maser species. Finally, the combination of a phased-SKA with other radio telescopes, which could even include ALMA or the ngVLA, is expected to realize an unprecedented high-sensitivity global VLBI network for masers and radio continuum observations.

References

Breen, S. L., Ellingsen, S. P., Caswell, J. L., et al. 2010, MNRAS, 401, 2219
Breen, S. L., Sobolev, A. M., Kaczmarek, J. F., et al. 2019, ApJ, 876, L25
Brogan, C. L. , Hunter, T. R., Cyganowski, C. J., et al. 2018, ApJ, 866, 87
Brogan, C. L., Hunter, T. R., Towner, A. P. M., et al. 2019, ApJ, 881, L39
Burns, R. A., Orosz, G., Bayandina, O., et al. 2019, MNRAS, in press
Caratti o Garatti, A., et al. 2017, NatPh, 13, 276
Cesaroni, R., Moscadelli, L., Neri, R., et al. 2018, A&A, 612, A103
Cho, S.-H., Yun, Y., Kim, J., et al. 2016, ApJ, 826, 157
Dall'Olio, D., Vlemmings, W. H. T., Surcis, G., et al. 2017, A&A, 607, A111
Ellingsen S. P.,Voronkov, M. A., Breen, S. L. et al. 2018, MNRAS, 480, 4851
Furuya, R. S., Kitamura, Y., Wootten, A., et al. 2003, ApJS, 144, 71
Ginsburg, A., Bally, J., Goddi, C., et al. 2018, ApJ, 860, 119
Goddi, C., Greenhill, L. J., Chandler, C. J., et al. 2009, ApJ, 698, 1165
Goddi, C., Henkel, C., Zhang, Q., et al. 2015, A&A, 573, A109
Goddi, ., Surcis, G., Moscadelli, L., et al. 2017, A&A, 597, A43
Green, J., Van Langevelde, H. J., Brunthaler, A., et al. 2015, Advancing Astrophysics with the Square Kilometre Array (AASKA14), 119
Henkel, C., Wilson, T. L., Asiri, H., et al. 2013, A&A, 549, A90
Higuchi, A. E., Hasegawa, T., Saigo, K., et al. 2015, ApJ, 815, 106
Hirota, T., Machida, M. N., Matsushita, Y., et al. 2017, Nature Astronomy, 1, 0146
Hirota, T., Tsuboi, M., Kurono, Y., et al. 2014, PASJ, 66, 106
Honma, M., Fujii, T., Hirota, T., et al. 2003, PASJ, 55, L57
Hunter, T. R., Brogan, C. L., MacLeod, G. C., et al. 2017, ApJ, 837, L29
Hunter, T. R., Brogan, C. L., Bartkiewicz, A., et al. 2018, Science with a Next Generation Very Large Array, 321
Imai, H., Nakashima, K., Bushimata, T., et al. 2007, PASJ, 59, 1107
Kalenskii, S. V., Johansson, L. E. B., Bergman, P., et al. 2010, MNRAS, 405, 613
Kim, M. K., Hirota, T., Honma, M., et al. 2008, PASJ, 60, 991
Lankhaar, B., Vlemmings, W., Surcis, G., et al. 2018, Nature Astronomy, 2, 145
MacLeod, G. C., Smits, D. P., Goedhart, S., et al. 2018, MNRAS, 478, 1077
Matsumoto, N., Hirota, T., Sugiyama, K., et al. 2014, ApJ, 789, L1
Matthews, L. D., Greenhill, L. J., Goddi, C., et al. 2010, ApJ, 708, 80
Menten, K. M. 1991, Atoms, Ions and Molecules: New Results in Spectral Line Astrophysics, 119
Menten, K. M., & Reid, M. J. 1995, ApJ, 445, L157
Minier, V., Ellingsen, S. P., Norris, R. P., et al. 2003, A&A, 403, 1095
Momjian, E., & Sarma, A. P. 2019, ApJ, 872, 12
Moscadelli, L., Sanna, A., Goddi, C., et al. 2017, A&A, 600, L8
Reid, M. J., Menten, K. M., Brunthaler, A., et al. 2019, ApJ, 885, 131
Sanna, A., Reid, M. J., Dame, T. M., et al. 2017, Science, 358, 227
Sanna, A., Surcis, G., Moscadelli, L., et al. 2015, A&A, 583, L3
Sarma, A. P., & Momjian, E. 2009, ApJ, 705, L176
Sarma, A. P. & Momjian, E. 2011, ApJ, 730, L5
Surcis, G., Vlemmings, W. H. T., van Langevelde, H. J., et al. 2019, A&A, 623, A130
Torrelles, J. M., Patel, N. A., Anglada, G., et al. 2003, ApJ, 598, L115
Vaidya, B., & Goddi, C. 2013, MNRAS, 429, L50
Voronkov, M. A., Caswell, J. L., Ellingsen, S. P., et al. 2012, Cosmic Masers - from OH to H0, 433
Zapata, L. A., Menten, K., Reid, M., et al. 2009, ApJ, 691, 332

3.9 Ammonia in star-forming regions: from filaments to cores

Gemma Busquet (Institut de Ciències de l'Espai - CSIC /IEEC, Catalonia), Tyler Bourke (Square Kilometre Array Organization, Jodrell Bank, UK), Yushi Hirata, Takeru Murase, and Toshihiro Handa (Kagoshima University, Japan)

3.9.1 Science Justification

Star formation takes place in filamentary molecular clouds (e.g., André et al., 2014), which requires a high degree of cloud fragmentation to produce dense cores of molecular gas and dust with a typical size of 0.1 pc. Despite filaments having been recognized more than 30 years ago (Schneider & Elmegreen, 1979), the ubiquity of such structures in star-forming regions, which has been recently highlighted by *Herschel* programs, has brought special attention to their formation mechanism, their role in the star formation process, and the fragmentation process they undergo to produce dense cores that will ultimately form stars and star clusters.

Understanding how filaments gain their mass from the surrounding medium and their subsequent evolution are of paramount importance to establish the link between filaments and core formation. In this sense, observations of molecular line emission are crucial to determine the kinematical imprints of the gas and the dynamical state of the different structures involved in the star formation process, from the large-scale filaments down to the dense cores. Dense prestellar cores on the verge of gravitational collapse constitute the essential building blocks for star formation. They provide important insights of the initial stages of star formation that can be obtained by measuring the temperature and density structure, and the velocity field.

3.9.2 Ammonia: a key tracer of the star formation process with SKA

Since its first detection in the interstellar space in 1968 by Cheung et al. (1968), ammonia (NH_3) has been found to be omnipresent in the interstellar medium (ISM). Thanks to its distinct spectroscopic properties and the large number of transitions sensitive to a broad range of excitation conditions (see Table 5), observations of the inversion transitions of the ammonia molecule at ~ 24 GHz have been proven to be a precious tool for measuring the kinetic gas temperature (Ho & Townes, 1983; Maret et al., 2009) and the gas motions of the dense material in the ISM. The hyperfine structure of the NH_3 transitions further provides a direct measurement of the excitation temperature, optical depth, and the column density. NH_3 is an excellent tracer of the dense gas because it does not freeze out onto dust grains until densities of $\gtrsim 10^5$ cm^{-3}, where most carbon-bearing species have already been depleted from the gas phase (e.g., Tafalla et al., 2002). Furthermore, the high excitation transitions of the ammonia molecule, i.e, $(J, K) > (3, 3)$, are a valuable tool to obtain the physical conditions of the warm ($T_{\rm kin} > 100$ K) and dense molecular gas, typically associated with hot molecular cores. Such observations can provide important insights of the complex gas kinematics during the initial stages of massive star formation, where infall, outflow and rotation motions coexist.

Currently, there are several wide-field observational programs to map the NH_3 emission in star-forming regions (e.g., Friesen et al., 2017; Hogge et al., 2018; Keown et al., 2019). However, these surveys have been conducted using single-dish telescopes, hence only tracing core scales in the nearest ($d < 500$ pc) clouds. Despite the tremendous effort to characterize the dense gas material in star-forming regions, systematic surveys at high angular resolution, sensitive to different spatial scales (i.e., from the parsec-scale filaments within molecular clouds down to the fundamental prestellar cores of 0.1 pc in size), are lacking. Actually, the present facilities available to map the NH_3 emission at high angular resolution suffer from certain limitations: *i)* mapping large areas (of several parsecs) in the sky requires a huge amount of observing time; and *ii)* the emission from nearby prestellar cores can be filtered out[5].

There are only a few examples of wide-field ammonia mapping at high angular resolution (Wang et al., 2008; Devine et al., 2011; Busquet et al., 2013; Li et al., 2013; Williams et al., 2018; Dhabal et al., 2019; Sokolov et al., 2019). These works, conducted mainly toward Infrared Dark Clouds (IRDCs), reveal intriguing networks of filaments converging toward the so-called hubs (Myers, 2009) that display a complex kinematic pattern with signatures of inflowing material toward the hubs (see Figure 18).

Moving down to core scales, there are only very few examples where the density and temperature structures have been measured in dense prestellar cores using interferometric observations of the NH_3 molecule (Crapsi et al., 2007; Ruoskanen et al., 2011). For instance, in L1544 Crapsi et al. (2007) report a temperature drop toward the core center from 12 K down to 5.5 K. In addition, while the gas-phase chemistry of NH_3 is well established, the physical conditions and its evolution on dust grain surfaces remains uncertain. Several studies have attempted to elucidate the physical conditions for NH_3 to freeze out onto grain surfaces toward the core centers (e.g., Sipilä et al., 2019). However, observations of NH_3 depletion are scarce (e.g., Friesen et al., 2009; Ruoskanen et al., 2011), hence a fully understanding of NH_3 depletion, both observationally and theoretically, is still missing. Therefore, the decrease in temperature toward the core centers as well as the physical conditions of NH_3 depletion should be systematically investigated in a large sample of prestellar cores.

To summarize, high angular resolution observations of the NH_3 molecule are crucial to probe the kinematics, such as the inflowing material along filaments and the infalling gas at core scales, dynamical stability, and the physical conditions (temperature and density) of the different structures involved in the star formation process.

[5]At a distance of 140 pc, the largest angular scale that can recover the JVLA is ~ 0.05 pc, hence a large fraction of

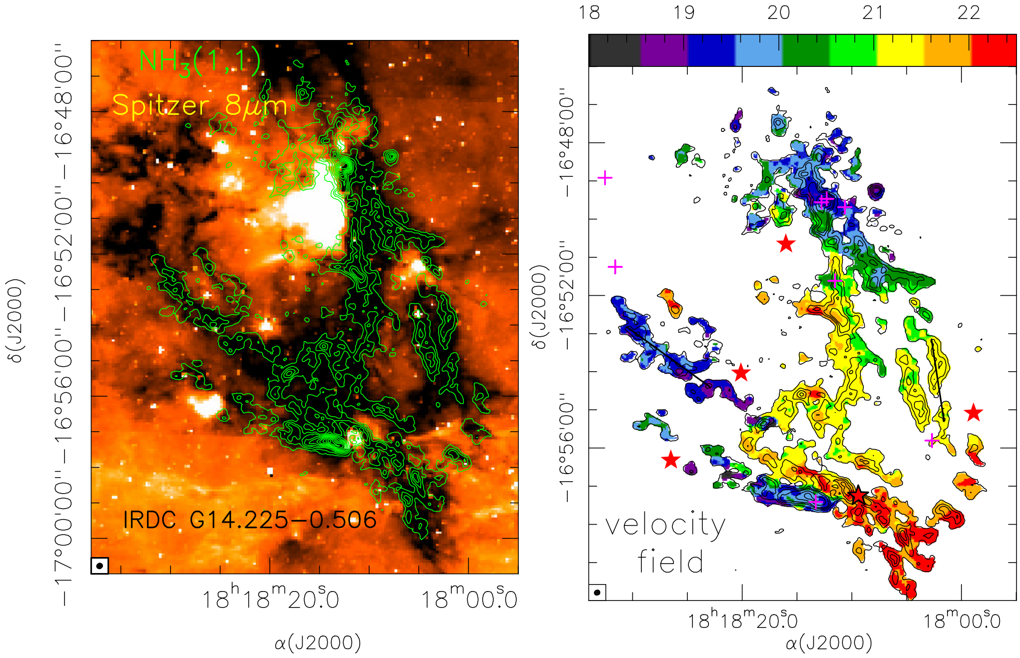

Figure 18: *Left:* combined (VLA + Effelsberg 100 m) integrated intensity map of the NH_3 (1,1) emission (contours) overlaid on the 8 μm *Spitzer* image (color scale) of the IRDC G14.225-0.506. The rms noise of the map is 9 mJy beam^{-1} km s^{-1}. *Right:* NH_3 (1,1) first-order moment map (units are km s^{-1}). Stars indicate IRAS sources in the field and crosses mark the position of H_2O masers. The synthesized beam, $8.2'' \times 7.0''$, is shown in the bottom left corner of each image. Figures from Busquet et al. (2013).

Thanks to the unique capabilities of the SKA (see the technical justification below), systematic unbiased surveys of all nearby star-forming regions (< 500 pc), such as the Pipe Nebula, Ophiuchus and Orion, to investigate the morphology, kinematics, and the physical conditions of filaments and its relation with dense cores, would be only possible with the SKA operating with the high-frequency Band 6 receivers. Such studies could then be extended to more distant regions, like IRDCs, providing a comprehensive picture of the star-formation process, from the progenitors of solar-type stars to massive star clusters. Ammonia is unique in its *i)* ease of observation, with multiple transitions around 24 GHz observable simultaneously with bright emission (see Table 5); *ii)* ubiquity in dense molecular clouds on many size scales, avoiding freeze out; *iii)* ability to determine both kinetic temperature and gas volume density; and *iv)* measurement of dense gas motions not available to the numerous thermal dust continuum surveys.

Table 5: Example of NH_3 transitions observable with SKA Band 6

Transition (J, K)	ν^a (MHz)	$E^a_{\rm up}$ (K)	$n^b_{\rm crit}$ ($\times 10^3$ cm^{-3})
(1,1)	23694.4955	23.26	1.9
(2,2)	23722.6330	64.45	2.1
(3,3)	23870.1292	123.64	2.2
(4,4)	24139.4163	200.52	2.2
(5,5)	24532.9887	295.38	2.3
(6,6)	25056.0250	408.07	2.5

[a] Frequencies and upper state energies taken from the JPL catalog.
[b] Critical density computed using the Einstein coefficient for spontaneous and collisional deexcitation at a temperature of 15 K obtained from the JPL catalog and Danby et al. (1988), respectively.

the emission from prestellar cores is filtered out by the interferometer.

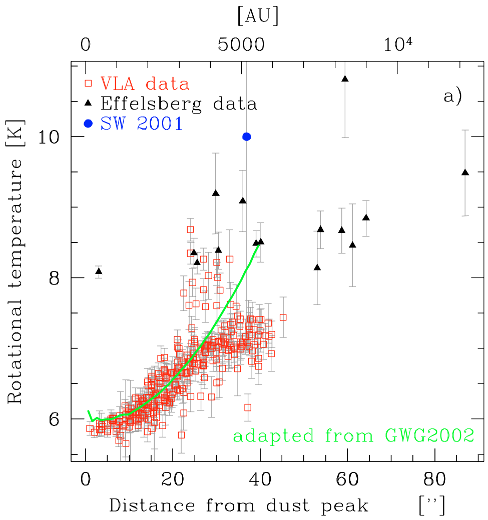

Figure 19: Gas temperature profile in L 1544 prestellar core derived from VLA NH_3 observations (empty red squares) and single-dish telescopes (triangles and circle). The solid line represents the model of Galli et al. (2002) using a central density of 2×10^6 cm^{-3}. Figure from Crapsi et al. (2007).

3.9.3 Technical Justification

As discussed above, the extension of the SKA frequency coverage to frequencies > 15 GHz will allow to perform systematic studies of the NH_3 emission in star-forming regions at high angular ($0.03'' - 5''$) and spectral ($\sim$0.1 km s^{-1}) resolution. The predicted extraordinary SKA1-MID survey speed (50 times larger than the JVLA) combined with the large field of view (twice the field of view of the JVLA) will allow for efficient mapping of all nearby star-forming complexes, and nearby IRDCs, with moderate amount a time. For instance, the NH_3 observations toward the IRDC G14.225-0.506 (hereafter G14, see Figure 18) were conducted using the JVLA with a 34 pointing mosaic covering an area of $7' \times 13'$, which corresponds to 4 pc$\times$7.5 pc at a distance of 1.98 kpc. With a relatively poor spectral resolution ($\sim$0.6 km s^{-1}) these observations required 3 hours of on-source integration time to obtain an rms of 8 mJy beam^{-1}. Now, with SKA, it will be possible to obtain a line sensitivity of 2 mJy beam^{-1} in 0.1 km s^{-1} resolution in only 1 hour of observing time (for a single SKA1 pointing with a FoV of $3.6'$). Furthermore, the excellent sampling of short baselines and the superb angular resolution provided by SKA will provide high fidelity images sensitive to different spatial scales. For example, in G14, scales from 50 to 10,000 au would be sampled with a sensitivity 4 times better than the data presented and with 6 times finer spectral resolution by performing a 17 mosaic pointings with SKA.

References

André, P., Di Francesco, J., Ward-Thompson, D., Inutsuka, S.-I., Pudritz, R. E., Pineda, J. E.2014, Protostars and Planets VI, 27
Busquet, G., Zhang, Q., Palau, Aina, Liu, H. B., Sánchez-Monge, A. et al. 2013, ApJ, 764, L26
Cheung, A. C., Rank, D. M., Townes, C. H., Thornton, D. D., Welch, W. J. 1968, PhRvL, 21, 1701
Crapsi, A., Caselli1, P., Walmsley, M. C., Tafalla, M. 2007, A&A, 470, 221
Danby, G., Flower, D. R., Valiron, P., Schilke, P., Walmsley, C. M. 1988, MNRAS, 235, 229
Devine, K. E., Chandler, C. J., Brogan, C., Churchwell, E., Indebetouw, R., Shirley, Y., Borg, K. J. 2011, ApJ, 733, 44
Dhabal, A., Mundy, L. G., Chen, C.-y., Teuben, P., Storm, S. 2019, ApJ, 876, 108
Friesen, R. K., Di Francesco, J., Shirley, Y. L., Myers, P. C. 2009, ApJ, 697, 1457
Friesen, R. K., Pineda, J. E., Rosolowsky, E., Alves, F., Chacón-Tanarro, A. et al. 2017, ApJ, 847, 63
Galli, D., Walmsley, M., Gonçalves, J. 2002, A&A, 394, 275
Ho, P. T. P., & Townes, C. H. 1983, ARA&A, 21 239
Hogge, T., Jackson, J., Stephens, I., Whitaker, S., Foster, J. et al. 2018, ApJS, 237, 27
Keown, J., Di Francesco, J., Rosolowsky, E., Singh, A., Figura, C. et al. 2019, ApJ, 884, 4
Li, D., Kauffmann, J., Zhang, Q., Chen, W. 2013, ApJ, 768, L5
Maret, S., Faure, A., Scifoni, E., Wiesenfeld, L. 2009, MNRAS, 399, 425
Myers, P. C. 2009, ApJ, 700, 1609
Ruoskanen, J., Harju, J., Juvela, M., Miettinen, O., Liljeström, A., M. V{äisäl, Lunttila, T., Kontinen, S. 2011, A&A, 534, A122
Schneider, S., Elmegreen, B. G. 1979, ApJS, 41, 87
Sipilä, O., Caselli, P., Redaelli, E., Juvela, M., Bizzocchi, L. 2019, MNRAS, 487, 1269
Sokolov, V., Wang, K., Pineda, J. E., Caselli, P., Henshaw, J. D., Barnes, A. T., Tan, J. C., Fontani, F., Jiménez-Serra, I. 2019, ApJ, 872, 30
Tafalla, M., Myers, P. C., Caselli, P., Walmsley, C. M., Comito, C. 2002, ApJ, 569, 815
Wang, Y., Zhang, Q., Pillai, T., Wyrowski, F., Wu, Y. 2008, ApJ, 672, L33
Williams, G. M., Peretto, N., Avison, A., Duarte-Cabral, A., Fuller, G. A. 2018, A&A, 613, A11

3.10 Magnetic Field Strengths via the Zeeman Effect

Tyler Bourke (SKAO), Tomoya Hirota (NAOJ), Wouter Vlemmings (Chalmers)

3.10.1 The role of magnetic fields in star formation

Magnetic fields are believed to be important in the process of star formation, perhaps regulating the efficiency at which stars form in molecular clouds and controlling the time-scales for star formation (Robishaw et al., 2015; Hennebelle & Inutsuka, 2019; Krumholz, & Federrath, 2019). However this view is supported by very little direct evidence, due to the difficulty in measuring field structure and strength on size scales and physical conditions relevant to the star formation process. Field structure is inferred from observations of linear polarisation of dust grains, either in emission in warm regions or in extinction against background stars in colder regions. In some instances the structure can be used to indirectly infer the field strength (Pattle & Fissel, 2019). However, the only direct measure of field strength in star-forming clouds is via the Zeeman effect in molecular and atomic spectral lines (see Crutcher & Kemball, 2019, for a review).

Measurements of the magnetic field strength in molecular clouds are rare due to the challenges in observing the Zeeman effect in radio spectral lines, for the field strengths believed to be typical in these regions. To date the Zeeman effect has only been observed in one atomic and four molecular lines in the interstellar medium, all at radio frequencies: HI, OH, CN, CH_3OH, and H_2O, with the latter two being maser transitions, for which the conditions being sampled and their relation to the star formation process are unclear. Of the thermal transitions (HI, OH, CN), CN is the only tracer of dense gas ($> 10^4$ cm^{-3}) where stars form, but detections to date have been extremely rare, and limited to high-mass star-forming regions.

In order to advance our understanding of the role of magnetic fields in star formation, a significant increase in the number of field strength measurements is needed. This is unlikely to happen without using Zeeman sensitive molecules (molecules with unpaired electrons in the electronic ground state) that are tracers of the conditions needed for star formation. Specific promising molecules and transitions are: CH @ 700 MHz; C_2H @ 87 GHz; SO @ 30 & 86 GHz; C_4H @ 9.5 GHz; and CCS @ 11, 22, 34, and 45 GHz. It may also be possible to use excited-state OH lines (Guesten et al., 1994) or radio recombination lines (see 3.10.3 below) to measure field strengths.

3.10.2 The promise of CCS for magnetic field strength measurements

The CCS molecule is a tracer of the early chemical and dynamical phases of low-mass star-formation, primarily before the formation of a protostar (Aikawa et al., 2001, 2005; Bergin & Tafalla, 2007). A number of observations have used CCS to investigate the early evolution of molecular cloud cores, i.e., prestellar cores and infrared dark cloud cores (Suzuki et al., 1992; Benson et al. , 1998; Lai & Crutcher, 2000; de Gregorio-Monsalvo et al., 2006; Sakai et al., 2008; Hirota et al., 2009; Tatematsu et al., 2010; Marka et al., 2012; Dirienzo et al., 2015). These observations have primarily used the transitions at 22 GHz and 45 GHz. We are unaware of any observations of the 11 GHz CCS transition. Attempts have been made to measure the Zeeman effect in CCS (e.g. Levin et al., 2001), with a recent marginal claim of success that needs to be verified (Nakamura et al., 2019). The greatly increased sensitivity and imaging fidelity of SKA over current facilites will increase the number of target sources for the Zeeman splitting measurements.

The primary target for SKA will be prestellar cores which show bright CCS emission (Hirota et al., 2011, and references therein). Some star-forming cores and infrared-dark clouds will also be potential targets showing relatively strong CCS emission (Hirota et al., 2010; Nakamura et al., 2014; Seo et al., 2019), while the possibility of detecting sufficiently bright CCS in disks remains to be tested observationally. The brightness temperatures in prestellar cores are typically 2 K toward the CCS peaks, and the typical line widths are 0.2-0.5 km s^{-1}. Assuming the LTE condition with the excitation temperature of 6.5 K in the cold prestellar cores and infrared dark clouds at the kinetic temperature of 10 K (Hirota et al., 2011), the brightness temperatures of the lower frequency transitions can be estimated as summarized in Table 6 and shown in Figure 20, although higher values are sometimes observed (Seo et al., 2019).

The width of the splittings do not depend on the transition or magnetic field strengths, as shown in Figure 20. This is because the profile of Stokes V is proportional to the derivative of Stokes I, which are common for all the transitions (i.e. the same velocity width with negligible contribution from the Zeeman shift between LCP and RCP). However, the brightness temperatures of the Stokes V strongly depend on the assumed line widths; the narrower Stokes I spectra tend to show brighter Stokes V. Thus, the target sources which have weaker intensity and/or broader line widths will be more difficult to detect their Zeeman splittings, such as chemically and dynamically evolved protostellar cores.

The Stokes V spectra show that the highest brightness temperatures are expected for the 22 GHz and 33 GHz lines (Figure 20). To detect Zeeman splittings for fields of $< 200\mu$G, the rms noise levels are required to be better than <1 mK at the frequency bands of 11 GHz, 22 GHz, 33 GHz and 45 GHz with the velocity resolution of 0.1 km s^{-1}. Assuming the observational parameters summarized in Table 6, on-source times of >100 h will be required to achieve a noise level of 1 mK for observations of the 33 GHz and 45 GHz lines, which remains challenging. The expected size of the Zeeman effect (Stokes V peak-to-peak intensity) is greatest for stronger fields and narrower lines. If the assumptions are relaxed, so that narrower line widths are observed and/or strong fields are present (which may be the case), then less stringent rms values are required (Figure 21). For example a 1 mG field instead of a 200μG field, with a line-width of 0.2 km/s (or even 0.5 km/s), would only require an rms of 2 mK, reducing the observing times listed in Table 6 by a factor of 4. CCS has the added advantage of multiple Zeeman sensitive transitions, so that confirmation of a Zeeman detection in any one CCS line can be confirmed through observations in one of the other CCS lines. In the case of a wide-band Band 6 for SKA1 (with a 3:1 ratio), covering $\sim$ 15-45 GHz, it may be possible to simultaneously observe three CCS lines and thus confirmed any Zeeman detection.

3.10.3 Other Zeeman lines

In addition to CCS there are a few other Zeeman sensitive molecular and atomic lines that will be accessible with high frequency capabilities (15-50 GHz) on the SKA1. Several more hydrogen recombination lines will be accessible. The first attempt to measure the Zeeman splitting of the H85α lines at 10 GHz was made in Troland, & Heiles (1977). The first successful, and so far only, measurement of the Zeeman splitting of the H30α line near 232 GHz was made around MWC 349 (Thum, & Morris, 1999). A high frequency extension to the SKA would encompass the H51α to H75α

Table 6: Time to reach 1 mK rms for candidate CCS lines for Zeeman splitting measurements

Transition (J_N)	Frequency^a (MHz)	$2\Delta\nu B^{-1\,a}$ (Hz μG^{-1})	T^b_B (K)	SEFD^c (Jy)	$\Delta\nu^d$ (kHz)	$t^e_{\rm integ}$ (hr)
1_0-0_1	11119.446	0.813	0.3	2.7	3.71	>5000
2_1-1_0	22344.033	0.767	1.0	5.8	7.45	605
3_2-2_1	33751.374	0.702	1.7	7	11.25	126
4_3-3_2	45379.033	0.629	2.0	14	15.14	115

a: Taken from Shinnaga, & Yamamoto (2000).

b: Assuming the LTE condition with T_B=2.0 K at 45 GHz and T_{ex}=6.5 K.

c: Using values from Braun et al. (2017).

d: Velocity resolution corresponding to 0.1 km s^{-1}.

e: Integration time to achieve rms of 1 mK/channel at 20" beam size.

lines. Additionally, several non-masing OH transitions will become available. The most useful one for Zeeman studies would likely be the 23.8 GHz line that was observed for example in absorption towards W3(OH) by Baudry & Menten (1995). This line can be a good probe of fairly hot gas around ultracompact HII regions. Using several different line tracers will allow the magnetic field to be measured across a wide range of physical conditions. There is also SO, which has transitions at ~30 GHz (SKA1) and ~86 GHz (ALMA), that are about twice as sensitive as CCS to the same field strength (Shinnaga, & Yamamoto, 2000). SO is generally observed in shocked regions so its usefulness as a tracer of the field in dense gas is not clear, but should be explored further.

3.10.4 Summary

In this paper we have argued that by using Zeeman observations of CCS, it should be possible to measure magnetic field strengths in regions of dense gas in nearby molecular clouds with SKA1, although the observations are challenging and may require significant investments of observing time. These observations require an extension of SKA1 to higher frequencies, with the primary lines being those at 22 GHz (Band 6 covering 15-25 GHz with a standard 1:1.8 ratio feed) and 33 GHz (Band 6 with a wide-band feed, or a Band 7 covering 25 GHz+). Simultaneous observations of as many of the CCS lines as possible are needed, to confirm Zeeman detections in the individual lines. An SKA1 band covering the 22, 33 and 45 GHz lines would be ideal, with a band covering the 11, 22 and 33 GHz lines the next best option. As a minimum any band should cover two of the CCS lines. For other Zeeman lines, a high-frequency extension could cover the excited-state OH line at 23.8 GHz, numerous recombination lines, and the SO line at 33 GHz, all of which are potentially important for magnetic field strength measurements using the Zeeman effect.

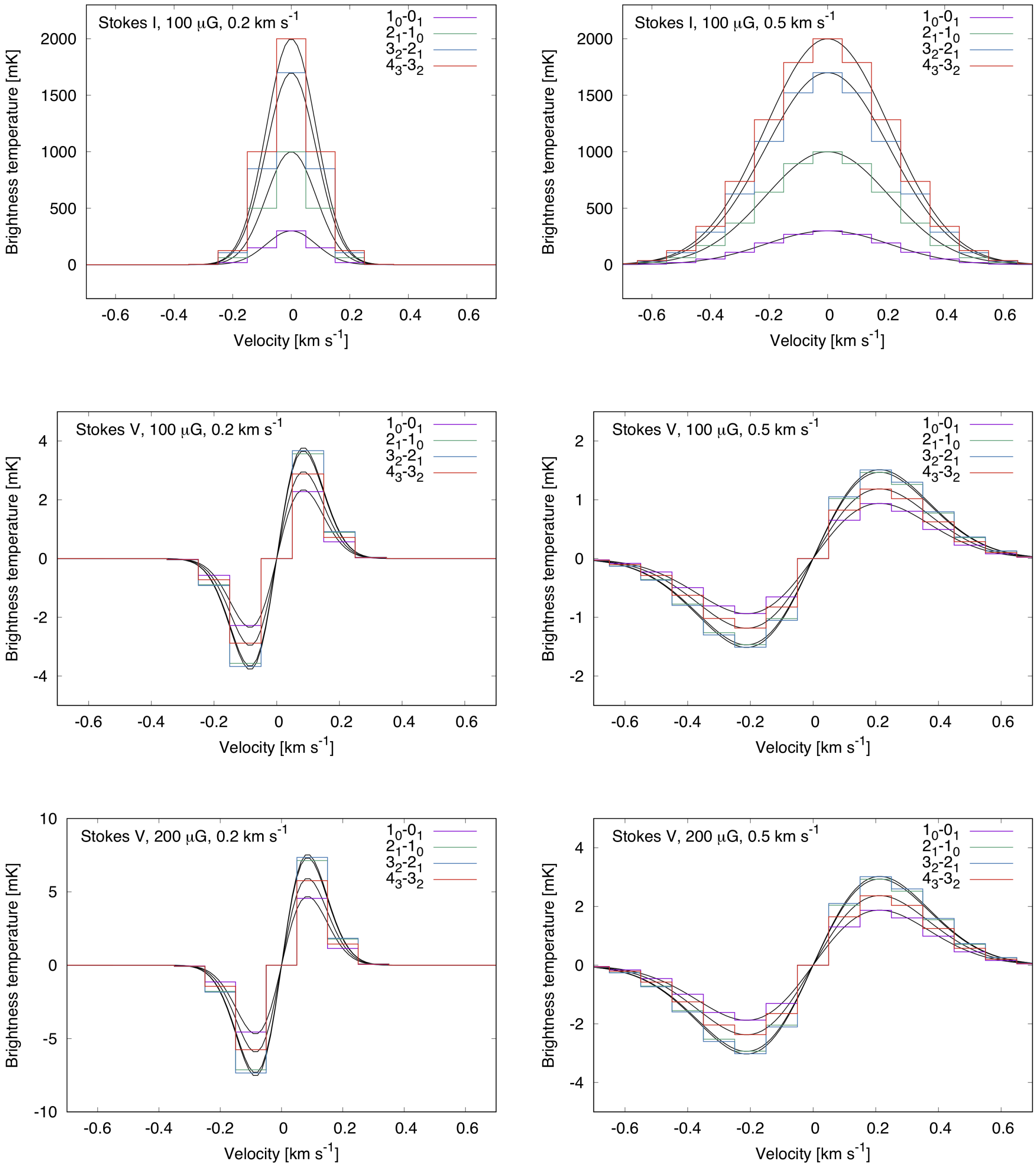

Figure 20: Expected Stokes I (top) and V (middle and bottom) spectra of the CCS lines. Left and right panels show the spectra with the line width of 0.2 km s^{-1} and 0.5 km s^{-1}, respectively. The line-of-sight magnetic field strengths are assumed to be 100 μG (middle) and 200 μG (bottom). The velocity resolution is fixed to be 0.1 km s^{-1} for all frequency bands.

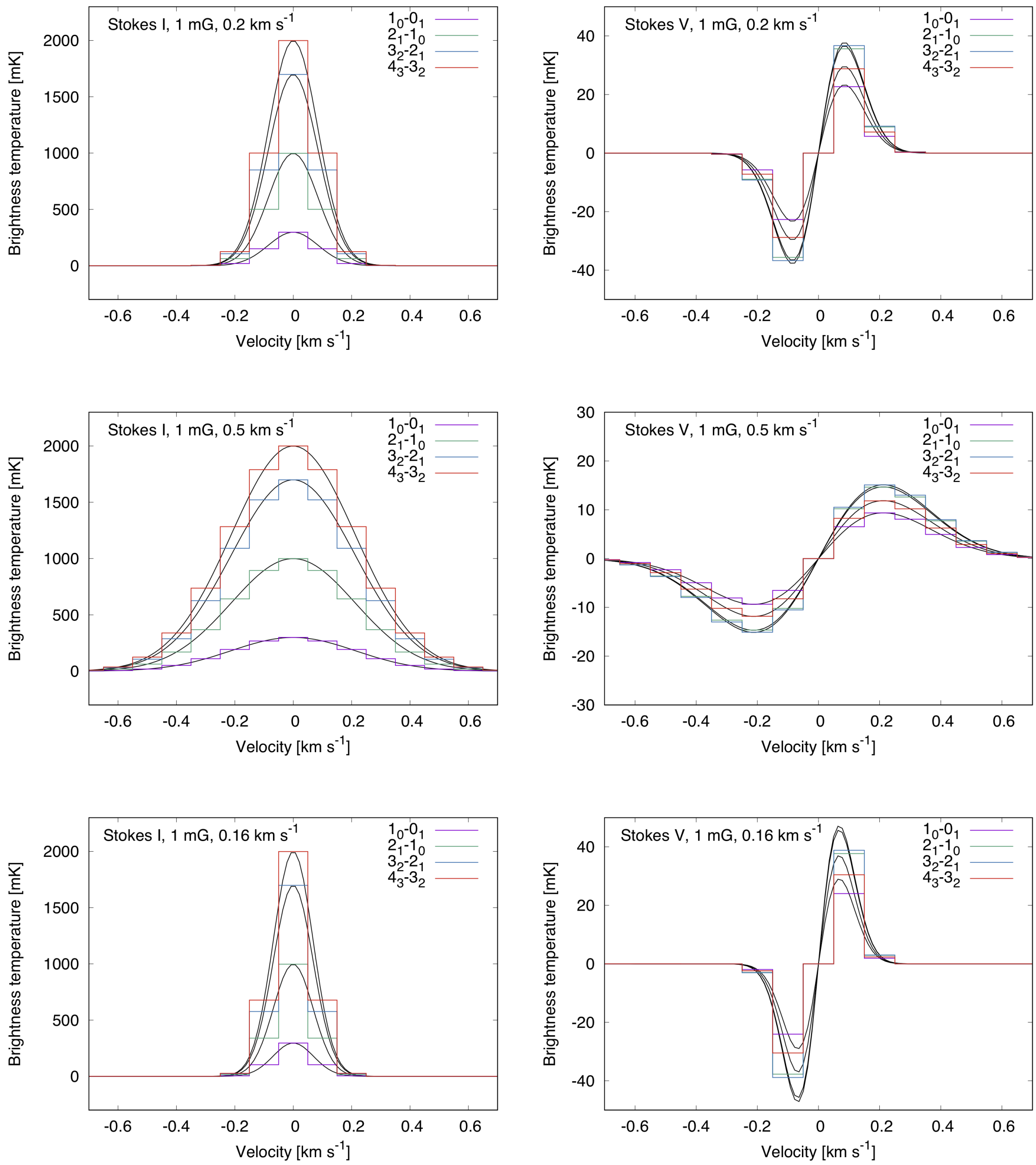

Figure 21: Expected Stokes I (left) and V (right) spectra of the CCS lines, for narrower lines and stronger fields, than shown in Figure 20. The field strength is 1 mG in all panels. The line-widths from top to bottom are 0.2 km s^{-1}, 0.5 km s^{-1}, and 0.16 km s^{-1}, respectively. The velocity resolution is fixed to be 0.1 km s^{-1} for all frequency bands.

References

Aikawa, Y., Ohashi, N., Inutsuka, S.-. ichiro ., et al. 2001, ApJ, 552, 639
Aikawa, Y., Herbst, E., Roberts, H., et al. 2005, ApJ, 620, 330
Baudry, A., & Menten, K. M. 1995, A&A, 298, 905
Bergin, E. A., & Tafalla, M. 2007, ARA&A, 45, 339
Benson, P. J., Caselli, P., & Myers, P. C. 1998, ApJ, 506, 743
Braun, R., Bonaldi, A., Bourke, T., Keane, E., & Wagg, J. 2017, "Anticipated SKA1 Science Performance", SKA document SKA-TEL-SKO-0000818, http://astronomers.skatelescope.org/wp-content/uploads/2017/10/SKA-TEL-SKO-0000818-01_SKA1_Science_Perform.pdf
Crutcher, R. M., & Kemball, A. J. 2019, Frontiers in Astronomy and Space Sciences, 6, 66
de Gregorio-Monsalvo, I., Gómez, J. F., Suárez, O., et al. 2006, ApJ, 642, 319
Dirienzo, W. J., Brogan, C., Indebetouw, R., et al. 2015, AJ, 150, 159
Guesten, R., Fiebig, D., & Uchida, K. I. 1994, A&A, 286, L51
Hennebelle, P., & Inutsuka, S.-. ichiro . 2019, Frontiers in Astronomy and Space Sciences, 6, 5
Hirota, T., Honma, M., Imai, H., et al. 2011, PASJ, 63, 1
Hirota, T., Ohishi, M., & Yamamoto, S. 2009, ApJ, 699, 585
Hirota, T., Sakai, N., & Yamamoto, S. 2010, ApJ, 720, 1370
Krumholz, M. R., & Federrath, C. 2019, Frontiers in Astronomy and Space Sciences, 6, 7
Lai, S.-P., & Crutcher, R. M. 2000, ApJS, 128, 271
Levin, S. M., Langer, W. D., Velusamy, T., et al. 2001, ApJ, 555, 850
Marka, C., Schreyer, K., Launhardt, R., et al. 2012, A&A, 537, A4
Nakamura, F., Kameno, S., Kusune, T., et al. 2019, PASJ, in press
Nakamura, F., Sugitani, K., Tanaka, T., et al. 2014, ApJ, 791, L23
Pattle, K., & Fissel, L. 2019, Frontiers in Astronomy and Space Sciences, 6, 15
Robishaw, T., Green, J., Surcis, G., et al. 2015, Advancing Astrophysics with the Square Kilometre Array (AASKA14), 110
Sakai, T., Sakai, N., Kamegai, K., et al. 2008, ApJ, 678, 1049
Seo, Y. M., Majumdar, L., Goldsmith, P. F., et al. 2019, ApJ, 871, 134
Shinnaga, H., & Yamamoto, S. 2000, ApJ, 544, 330
Suzuki, H., Yamamoto, S., Ohishi, M., et al. 1992, ApJ, 392, 551
Tatematsu, K., Hirota, T., Kandori, R., et al. 2010, PASJ, 62, 1473
Thum, C., & Morris, D. 1999, A&A, 344, 923
Troland, T. H., & Heiles, C. 1977, ApJ, 214, 703

4 Stellar Evolution and the Galactic Ecosystem

4.1 Anomalous Microwave Emission: an open question for modern astrophysics

Elia Stefano Battistelli (Sapienza University of Rome), Eric Murphy (National Radio Astronomy Observatory), Fatemeh Tabatabaei (Institute for Research in Fundamental Sciences-IPM), Ricardo Genova-Santos (Instituto de Astrofisica de Canarias), Matteo Murgia (Osservatorio Astronomico di Cagliari), Frederick Poidevin (Instituto de Astrofisica de Canarias), Rafael Rebolo-Lopez (Instituto de Astrofisica de Canarias)

This chapter focuses on the open question of Anomalous Microwave Emission. We describe its evidence both in the Galactic and extragalactic environment, open questions, and focus on the improvement that an experiment like SKA, with an extension in frequency to band 6, can achieve.

4.1.1 Introduction

The emission budget from astrophysical sources at microwave frequencies is mostly dominated by the well-studied and well-understood free-free, synchrotron, and thermal dust emission. Nevertheless, observations mainly carried out in our Galaxy have revealed an unexpected excess of emission in the microwave band from 10 to 70 GHz that cannot be explained by standard emission mechanisms or in terms of the cosmic microwave background (CMB). This excess emission (anomalous microwave emission, AME), first observed in the 1990s as dust-correlated emission in COBE maps (Kogut et al., 1996), is observable both as diffuse emission and in selected sky regions (see Dickinson et al., 2018 for a recent review). Its physical origin is not fully understood yet, but the most convincing models predict that AME is dominated by electric dipole emission from rapidly rotating small dust grains (spinning dust; Draine et al., 1998) although current observations remain inconclusive. Other physical emission mechanisms such as hot free-free, hard synchrotron, thermal fluctuations of magnetic dust grains (Dickinson et al., 2018), or thermal emission of amorphous dust (Nashimoto et al., 2019), should in fact play an important role in the AME budget and can be disentangled from spinning dust owing to their spectral behavior and polarization properties in the 10-70 GHz band.

Studies within the Galaxy have uncovered strong detections of AME in molecular clouds (see, e.g. Fig. 48) along with discrete locations adjacent to larger HII complexes (Dickinson et al., 2009; Tibbs et al., 2012; Battistelli et al., 2015) consistent with the theoretical expectation that it is a ubiquitous emission component in the interstellar medium (ISM). AME has also been detected in external galaxies (Murphy et al., 2010; Scaife, 2010), and most recently in proto-planetary disks (Greaves et al., 2018). AME is correlated with thermal dust emission and seems correlated with the strength of the radiation field rather than the column density of the dust grains (see e.g. Tibbs et al., 2012). However, similar regions such as compact HII regions do not result in the same AME abundance. Also, high angular resolution (i.e. ∼1') studies highlight the complexity of the emission of some Galactic regions with far from explained phenomenology (Battistelli et al., 2015; Hensley et al., 2017).

The importance of a full understanding of AME depends not only on our comprehension of the astrophysical mechanisms at its origin, but also on the need to study the star formation rate in galaxies for which a precise and accurate separation of thermal, non-thermal emissions is required. A careful thermal/nonthermal separation in NGC6946 shows for instance that the tangled magnetic field is strong where the AME is detected (Tabatabaei et al., 2013; Murphy et al., 2010), which can hint on the origin of this emission. Also, a full understanding of the AME mechanism is crucial for an accurate interpretation of data from CMB experiments in order to understand and remove foreground signals (e.g., BICEP2/Keck and Planck Collaborations, 2015). This is particularly important when considering polarized CMB foregrounds which present a particularly difficult challenge. Any significant (i.e. ∼1%) polarization from AME would significantly complicate analyses aiming to detect faint B-modes of the CMB polarization (Remazeilles et al., 2016).

4.1.2 Anomalous Microwave Emission models

The most accepted explanation for AME is rotational emission from ultra-small (radius $a \lesssim 1\,\mathrm{nm}$) dust grains: the spinning dust. Electric dipole emission from spinning dust grains was proposed long ago by Erickson et al. (1957) but only recently a detailed theory was formulated by Draine et al. (1998, 2012). Interstellar dust grains possessing permanent electric dipole, μ, can spin at high rates due to a number of excitation mechanisms. The power radiated by a dipole rotating at angular velocity ω, with electric dipole component μ_p perpendicular to ω is:

$$P = \frac{2}{3} \cdot \frac{\mu_p^2 \omega^4}{c^3} \tag{1}$$

emitted at frequency $\nu = \omega/\pi$. Integrating the emission over the distribution of grain sizes, dipole moments, and angular velocities (see e.g. Ali-Haimoud et al., 2009) one can obtain the emissivity per H atom. Larger grains, due to their larger momentum-of-inertia, emit at lower frequencies with fainter emission where synchrotron and free-free emission dominate. At high frequencies, the cut off is determined by the smallest grains such as the Very Small Grains (VSGs) and Polycyclic Aromatic Hydrocarbons (PAHs) resulting in a peaked spectrum with peak frequencies in the range 20-30GHz as indeed is observed. Spinning dust models require a large column of dust grains and a mechanism for rotationally exciting them (e.g. plasma drag, photons, collisions etc.). These conditions may for instance be found in HII regions, usually 'heated' by the UV radiation from O and B type stars, and are associated to a significant amount of dust grains. Magnetic dipole radiation from thermal fluctuations in the magnetization of interstellar dust grains (see e.g., Draine et al., 1999), may also be contributing to observed AME, particularly at higher frequencies ($\gtrsim$50 GHz).

Polarization of the AME is a key ingredient to distinguish between models. Electric dipole emission is largely unpolarized with expected polarization $\lesssim 1\%$ at $\sim$ 30GHz. At lower frequencies polarization is expected to give a larger contribution although possibly contaminated by synchrotron emission. Magnetic emission is predicted to emit highly polarized emission with strongly frequency dependent intensity and direction. Polarization of AME along the frequency would be a clear way to distinguish between models although it should be stressed that polarization only detects the coherent magnetic field with scales larger than the beam size. Hence, due to the beam-depolarization, no detection of polarization does not necessarily mean that the magnetic field is weak. This calls for spectro-polarimetric observations with improved angular resolution.

Among possible AME carriers, PAHs are considered as highly probable although this was recently questioned by Hensley et al. (2017). Ali-Haimoud et al. (2014) proposed that rotational spectroscopy at microwave frequencies could be used to uniquely determine asymmetric and quasi-symmetric PAHs having very regular and predictive spectra.

A number of unanswered questions and discrepancies arise. What is the carrier of AME? What's the role of PAHs and small silicate grains? Does magnetic emission play a role? AME appears to be correlated with the strength of the radiation field rather than the column density of small grains/PAHs (Tibbs et al., 2012). Also, in apparently similar regions (e.g. compact HII regions) data have failed to detect AME at all (Murphy et al., 2010). If spinning dust is the main mechanism, it can be used as a direct tracer of interstellar dust grains. In particular, it is highly sensitive to the grain size distribution and distribution of electric dipole moments. In combination with IR diagnostics, spinning dust studies can yield the abundance of nanoparticles in environments such as cold cores and protoplanetary disks. AME has the potential to constrain environmental properties of the ISM. Detailed spectral measurements can constrain parameters such as the density and interstellar radiation field strength. The degree of alignment of nanoparticles is sensitive to the magnetic field strength, although the alignment physics remains controversial.

4.1.3 AME observations

Some Galactic regions have been well studied and characterized (Watson et al., 2005; Battistelli et al., 2006; Genova-Santos et al., 2015). Typically, AME is found near HII regions and molecular clouds (e.g. Planck Collaboration, 2014b). However, in a recent study, AME was found in three protoplanetary disks, the only known systems hosting hydrogenated nano-diamonds (Greaves et al., 2018).

Perhaps the best example is that of the Perseus molecular cloud first detected as anomalous by Watson et al. (2005). *Planck* maps of the Perseus molecular cloud region, covering $30-857\,\mathrm{GHz}$, are shown in the left half of Fig. 48, along with the 1.4 GHz and Hα maps (taken from Planck Collaboration, 2011a). The strong dust-correlated AME at $10-70\,\mathrm{GHz}$ is evident; it has no obvious counterpart at 1.4 GHz but correlates well with the higher (>100 GHz) *Planck* frequencies, which are dominated by thermal dust. The majority of the AME comes from the northeast end of the molecular cloud, which harbors the dense IC 348 reflection nebula. In the right half of Fig. 48 the spectrum of AME-G160.26 − 18.62 in Perseus is shown, together with the best-fitting model, and is consistent with free-free emission at low frequencies ($< 4\,\mathrm{GHz}$), thermal dust emission at high frequencies ($>100\,\mathrm{GHz}$), and a strong excess at $\approx 10-70\,\mathrm{GHz}$ with a convex spectrum peaking at $\approx 25\,\mathrm{GHz}$.

Of great interest is clearly the possibility of detecting AME from extragalactic sources as this would represent a unique possibility to study astrophysical processes mainly studied only in our Galaxy. Extragalactic evidence of AME has been found in a limited number of cases. The first extragalactic detection of AME unexpectedly resulted from a multi-wavelength investigation of star formation activity towards HII region complexes in the nearby galaxy NGC 6946 (Murphy et al., 2010). Since this initial discovery, a number of searches for extragalactic AME have been undertaken with WMAP and *Planck* data (e.g., the Magellanic Clouds: Bot et al. , 2010; NGC 4945: Peel et al., 2011; NGC 6946: Scaife, 2010; Hensley et al., 2015), most of which have been largely inconclusive. Planck Collaboration (2011b) reported an emission from the Small Magellanic Cloud that was partly interpreted as spinning dust. The interpretation is however complicated by additional emission from thermal dust with possible contamination from magnetic dipole emission. One additional extragalactic detection is known in the star-forming disk of NGC 4725, which appears consistent with a highly-embedded ($A_V > 5\,\mathrm{mag}$) nascent star-forming region, in which young ($\lesssim 3\,\mathrm{Myr}$) massive stars are still enshrouded by their natal cocoons of gas and dust, lacking enough supernovae to produce measurable synchrotron emission (Murphy et al., 2018). A tentative 2.3 σ detection of AME in M31 has been reported by Planck Collaboration (2015), who integrated the emission over the whole galaxy. The latter, was confirmed and strengthened through observations of M31 with the Sardinia Radio Telescope, SRT (Battistelli et al., 2019) (see Fig. 23).

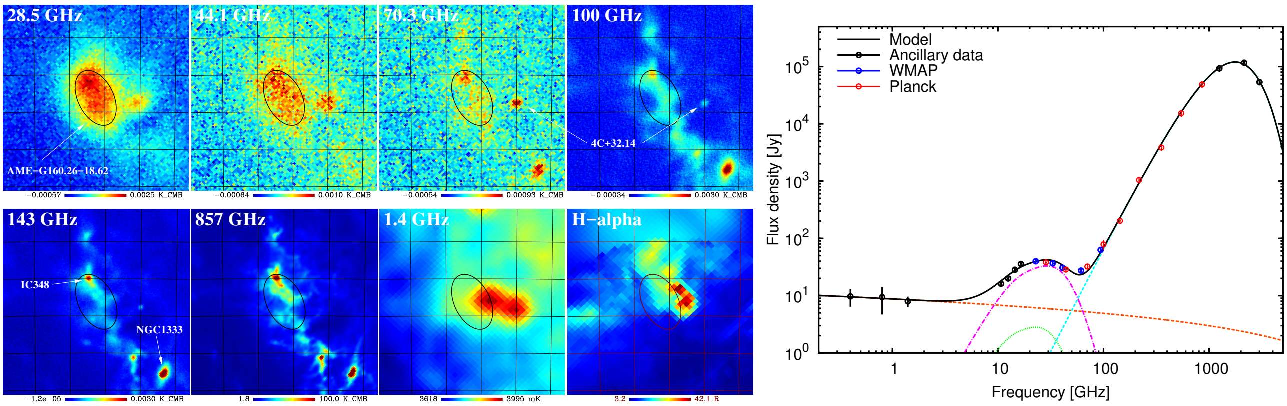

Figure 22: Adapted from Planck Collaboration (2011a). Left: maps of the Perseus molecular cloud region. From left to right – top row: *Planck* 28.5; 44.1; 70.3 and 100 GHz – bottom row: *Planck* 143 and 857 GHz; 1.4 GHz; and Hα. The maps cover $5^\circ \times 5^\circ$ and have linear colour scales. The FWHM of the elliptical Gaussian model used to fit the flux density for photometry is shown. Right: spectrum of AME-G160.26 – 8.62 in the Perseus molecular cloud. The best-fitting model consisting of free-free (orange dashed line), spinning dust, and thermal dust (light blue dashed line) is shown. The two-component spinning dust model consists of high density molecular gas (magenta dot-dashed line) and low density atomic gas (green dotted line).

AME has also been recently detected in three proto-planetary disks (Greaves et al., 2018). What is most striking about these findings is that AME was only detected in those disks around Herbig A-type emission-line objects hosting hydrogenated nano-diamands (Acke et al., 2006), where C-H bonds can provide suitable electric dipole moments. This is in contrast to the much more commonly detected PAHs, suggesting that nano-diamonds might indeed be the AME carrier. These are the only known systems that host hydrogenated nano-diamonds, in contrast to much more common detection of PAHs.

These seemingly uncorrelated instances of strong detections demonstrate that AME is indeed a major tracer of ISM conditions and that a complete model, which is still lacking, can lead to significant changes in our understanding of the astrophysics of the ISM and even stars and planets formation.

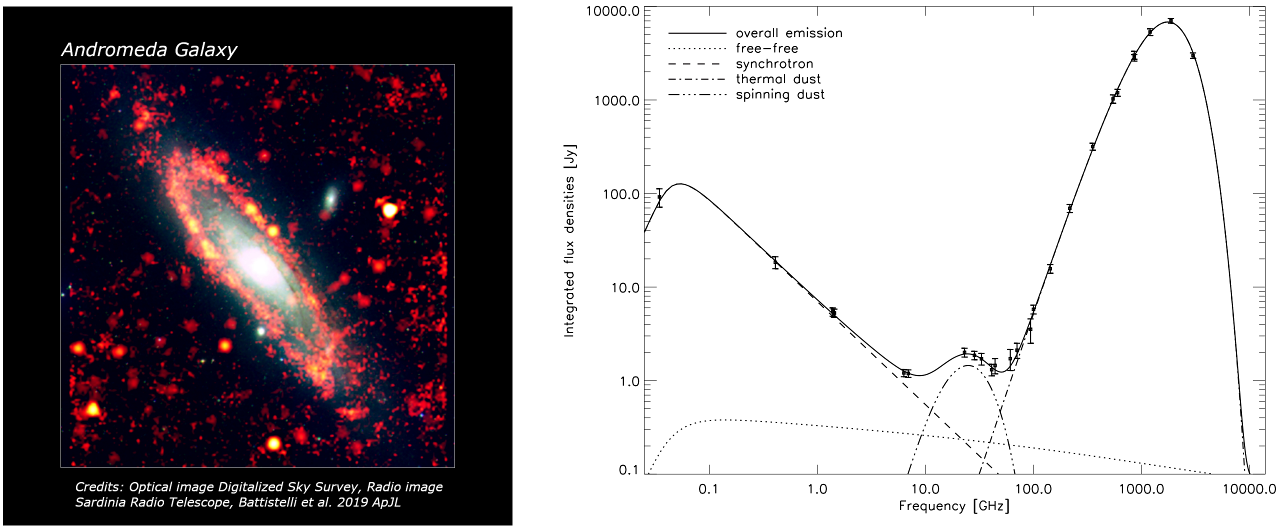

Figure 23: Adapted from Battistelli et al. (2019). Left: map of M31 at 6.7GHz obtained with the SRT superimposed to the optical image from the Digitized Sky Survey. Right: integrated flux density for M31. The best-fitting model consists of free-free (dotted line), synchrotron (dashed line), thermal dust (dot-dashed line), and spinning dust, (dot-dot-dashed line). The spectrum is the result of aperture photometry obtained with Planck plus ancillary data (Planck Collaboration, 2015) and the SRT at 6.7GHz resulting in an evidence of AME of $S=1.45^{+0.17}_{-0.19}$ Jy at the peaking frequency of $\simeq$25 GHz.

4.1.4 SKA contribution to AME science

With the extension of SKA1-MID beyond 15GHz, at frequencies where AME appears to increase with frequency and peak, we have a unique possibility to shed light on AME mechanisms using high angular resolution, polarization and spectroscopic informations which cannot be reached otherwise (see e.g. Dickinson et al., 2014). The occurrence of AME remains in fact highly unpredictable due to our lack of understanding of the carrier(s) and physical conditions favorable for triggering this emission mechanism. As is evident in Fig. 48, AME is not always coincident with structures seen in the higher frequency dust maps; this is most likely due to a combination of different environmental conditions and/or grain populations less favorable to powering strong AME. It should be stressed, in fact, that ISM structures emit over a wide range of scales allowing SKA1-MID observations to focus, with its high angular resolution, on regions with significant dust column densities. This will be possible taking advantage of the flexibility in terms of u-v coverage (including both short and long baselines) of SKA. In fact, the high angular-resolution provided by SKA1-MID could be fundamental to shed light into what are really the AME carriers. The lack of correlation between AME brightness and PAHs abundance found by Hensley et al. (2017) was totally unexpected because, as mentioned, for a long time PAHs have been considered the most promising AME carriers. However, this analysis was carried out at a degree scale angular resolution. Data with arcsecond angular resolution in the microwave range could be correlated with already existing data at similar resolution in the FIR tracing the PAHs abundances, therefore allowing to test the PAH hypothesis at smaller physical scales.

Among possible targets that would fit the extended band 6 SKA1-MID in terms of frequency and baseline coverage, we list: molecular clouds, photodissociation regions, dense pre-stellar cores, proto-planetary circumstellar disks, as well as external galaxies. In order to investigate these regions with the requisite sensitivity and frequency coverage at much higher ($\approx$10 pc) scale resolution, one would need accurate predictions of the conditions that power AME which however remain challenging and only high angular resolution follow-up observations can give important clues. Pre-stellar cores, with typical sizes of $\sim 1'$, are well matched with the SKA shorter baselines. Achieving an understanding of AME in proto-planetary disks on AU-scales may help constrain models of grain growth that feed into to estimating the timescales for the formation of the rocky cores of planets, which are completely at odds with current observations. Models have shown that electric dipole emission could contribute to the level of few mJy at 20GHz (Rafikov, 2006). SKA could provide the high angular resolution imaging for the separation of synchtrotron, free-free and AME, allowing to shed light and separate models. In order to monitor the possibility of AME being associated to PAH and its rotational emission lines, MHz resolution spectroscopic observations with $\simeq$ tens of μJy sensitivity, focusing on known PAH column densities (obtained from IR maps such as Spitzer 8μm) would be required.

Understanding the potential ubiquity of AME from extragalactic sources is of critical value (see e.g., Murphy et al., 2009). In nearby galaxies, it would be highly insightful to check for the AME correlation and magnetic field determined using radio-SED- independent tracers which further help constraining the SED itself. So far only a handle of extragalactic sources have been identified as AME sources (see e.g. Murphy et al., 2010; Battistelli et al., 2019). Investigation over other sources have failed questioning the effective ubiquity of AME in extragalactic sources. This might be particularly important for high-z (z>2) galaxies allowing to use the redshifted AME to monitor the SFR along redshift and to check weather grain properties are similar to that of Local Galaxies.

Progress in this field requires new observations of large heterogeneous samples of AME detections covering $\sim 1-30$ GHz, where AME spectrum rises, with a combination of sensitivity and high-angular resolution (from mas to arcsec level) that exceeds any extant facility. For extragalactic sources, high (i.e., 0".1) angular resolution is needed to map AME at $\sim$10's of pc in galaxies out to $d_L \approx 20$ Mpc. To this end, we foresee synergies with existing facilities monitoring different angular scales with different resolutions such as the Green Bank Telescope and the SRT already used for AME science and that could represent the pathfinder for possible extended SKA1-MID follow-up observations. As a working example, focusing on the evidence of AME arising from M31 (Battistelli et al., 2019), a K-band (22GHz) program is currently on-going for mapping the whole galaxy in order to search for AME with the SRT (SRT project 33-18). Even assuming (conservatively) a completely smooth (with no structures in it) anomalous emission from M31 consistent with the observed 1.45Jy overall emission at 25GHz, the signal would be expected of the order of 0.14mJy/arcmin^2. The aforementioned SRT project would allow to indicate regions of the galaxy, with $\simeq$0.9' resolution, where to focus, which would be observed with μJy sensitivity by the extended SKA1-MID at sub-arcsec resolution.

References

Acke, B. et al. 2006, A&A, 457, 171 (2006)
Ali-Haimoud Y. et al. 2009, MNRAS, 395, 1055 (2009)
Ali-Haimoud Y. et al. 2014, MNRAS, 437, 2728 (2014)
Battistelli E.S. et al. 2006, ApJL, 645, L141 (2006)
Battistelli E.S. et al. 2015, ApJ, 801, 111 (2015)
Battistelli E.S. et al. 2019, ApJL, 877, L31 (2019)
BICEP2/Keck and Planck Collaborations, 2015, PhRvL 114, 101301 (2015)
Bot C., et al. 2010, A&A, 523, 20 (2010)
Dickinson, C., et al., 2009, ApJ, 690, 1585 (2009)
Dickinson, C., et al., 2014, arXiv:1412.5054 (2014)
Dickinson, C., et al., 2018, NewAR, 80, 1-28 (2018)
Draine B.T. et al. 1998, ApJ, 494, L19 (1998)
Draine B.T. et al. 1999, ApJ, 512, 740 (1999)
Draine B.T. et al. 2012, ApJ, 757, 1 (2012)
Erickson, W.C. et al. 1957, ApJ, 126, 480 (1957)
Genova-Santos R. et al. 2015, MNRAS, 452, 4169 (2015)
Greaves J.S. et al., NatAs, 2, 662-667, (2018)
Hensley B.S. et al. 2015, MNRAS, 449, 809 (2015)
Hensley B.S. et al. 2017, ApJ, 836, 2, 179 (2017)
Kogut A. et al. 1996, ApJ, 460, 1 (1996)
Murphy E.J. et al. 2009, ApJL, 706, 482 (2009)
Murphy E.J. et al. 2010, ApJL, 709, L108 (2010)
Murphy E.J. et al. 2018, ApJ, 862, 1, 20, 7 (2018)
Nashimoto, M., et al., 2019, arXiv:1910.07270 (2019)
Peel et al. 2011, MNRAS, 416, L99 (2011)
Planck Collaboration 2011a, A&A 536, A20 (2011)
Planck Collaboration 2011b, A&A 536, A17 (2011)
Planck Collaboration 2014, A&A 565, A103 (2014)
Planck Collaboration 2015, A&A 582, A28 (2015)
Rafikov, R.R. 2006, ApJ, 646, 288 (2006)
Remazeilles, M. 2016, MNRAS, 458, 2032 (2016)
Scaife, A. 2010, MNRAS, 406, 1, L45-L49 (2010)
Tabatabaei F. et al. 2013, A&A 552, 19 (2013)
Tibbs, C. et al., 2012, ApJ, 754, 94 (2012)
Watson R.A., et al. 2005, ApJL, 624, L89 (2005)

4.2 The Galactic Centre

Rainer Schödel & Antxón Alberdi (IAA-CSIC, Granada, Spain)

At only 8 kpc from Earth, the Galactic Centre (GC) contains the nearest galactic nucleus. It is the only one in which we can examine the properties and dynamics of the interstellar medium (ISM), of stars, and of stellar remnants with a linear resolution on the order of milli-parsecs, as well as the detailed interactions of these entities with a four million solar mass black hole. The GC can be defined as the region outlined by the nuclear stellar disc (NSD), a flattened high-density, rotating stellar structure with a radius of 150-200 pc. The NSD overlaps with the central molecular zone, where $\sim$10% of the Galaxys molecular gas is concentrated in a ring with a radius of $\sim$200 pc (Launhardt et al., 2002). The NSD contains the nuclear star cluster (NSC), with a half-light radius of $\sim$5 pc and a mass of $\sim 2.5 \times 10^7\,M_\odot$ (Launhardt et al., 2002; Schödel et al., 2014). NSCs are very common in all types of galaxies, are characterised by a complex population, and frequently co-exist with MBHs (Neumayer, 2017). Together, the NSD and the NSC form the so-called Nuclear Bulge (NB).

The GC is the most extreme environment in the Milky Way. It is characterised by stellar densities of $10^{5-7}\,\mathrm{pc}^{-3}$, high turbulence and temperature of the ISM, a magnetic field 10-100 times stronger than in the Galactic Disk, intense UV radiation, and super solar metallicities. During periods of increased activity Sgr A* bathes the GC environment in X-rays. The GC is the Milky Ways most active massive star forming region and the closest proxy we have for the conditions in starburst galaxies.

Therefore, the GC is a unique template for galactic nuclei and extreme astrophysical environments. It is a prime target for the currently existing most advanced telescopes as well as for the upcoming generation of observatories, such as the SKA, the JWST, and the future Extremely Large Telescopes (ELTs).

4.2.1 GC science with the SKA

The SKA will be able to deliver key data to many science cases, as is summarised in the following long, but non-exhaustive list:

Star formation and ISM, e.g.:

1. Magnetic field strength and structure in the GC, e.g.: Extreme massive star formation environments: Sagittarius B2, Young stellar objects

2. Radio stars, e.g.: Post main-sequence evolution of massive stars; massive main sequence and post-main sequence stars; stellar remnants in the GC as probes of the dark cusp around Sagit-

tarius A*, as potential gravitational wave sources, and as tracers of the star formation history and initial mass function

3. Intermediate mass black holes

4. General relativity (GR): Tests of GR via pulsars in short-period orbits around Sgr A*; establishment of an ultra- precise absolute astrometric reference frame for GR studies in combination with infrared observations of stellar dynamics; observations of the dynamics of stars and stellar remnants near Sgr A* in the radio regime

Subsequently, we describe some of the science cases in more detail.

4.2.2 Star formation

The presence of massive stellar clusters and of classical Cepheids indicates that in the past ∼30 Myr star formation activity was very high in the GC (Matsunaga et al., 2011). In addition, several lines of observational evidence (infrared and radio) point toward the existence of numerous Young Stellar Objects (YSOs) and thus ongoing star formation at the GC (e.g. Yusef-Zadeh et al., 2009, 2016; Nandakumar et al., 2018). The stellar crowding at the GC along with the extreme and highly variable interstellar extinction make it extremely difficult to identify YSOs and massive main sequence and post-main sequence stars in infrared observations. The SKA will, however, be sufficiently sensitive to detect all massive MS and post MS stars at the GC. In addition, it will be able to trace YSOs via related shocks in the ISM (SiO maser emission) and via the detection of outflows. With SKA observations, complemented by near-infrared observations, it will thus be possible to obtain a complete census of recent star formation at the GC.

4.2.3 Stellar winds, massive stars

The GC contains the highest concentration of massive MS and post-MS stars, such as Wolf-Rayet stars, in the Galaxy. It is therefore an excellent location to study stellar winds with radio observations (free-free emission from ionised winds or synchrotron emission in wind shock regions in binaries, see Güdel, 2002; Umana et al., 2015). Just the Arches cluster, for example, is estimated to contain about 150 O-stars. The first discovery of massive post MS stars near Sgr A* was reported by Yusef-Zadeh et al. (2014), who used the JVLA observing at 42 GHz for their work (Fig. 25).

4.2.4 Stellar remnants, BHBs

Stellar remnants, in particular stellar mass black holes (SBHs) have probably accumulated at the GC over the lifetime of the Galaxy. Dynamical friction makes the heavy SBHs sink towards the centre and accumulate in the inner parsec around Sgr A* (Morris, 1993). In the environment of the nuclear star cluster (NSC), which surrounds Sgr A* and where stellar densities can exceed 10^6 stars per pc^3, SBHs can form black hole binaries via dynamical interaction (Antonini & Rasio, 2016), which can result in the formation low mass X-ray binaries (LMXBs), which suffer accretion-induced outbreaks on time scales of decades. Observations of X-ray transients have traced a potential excess of LMXBs/BHBs near Sgr A*, the predicted so-called dark cusp (Hailey et al., 2018). However, the numbers are very low and new transients get added only on time scales of years. In between outbreaks, LMXBs are in quiescent states, with very low emission. Here, the SKA can make a great impact.

The SKA will probably be able to detect all quiescent BHBs within 5 kpc of Earth in observations of a few tens of hours duration (Gallo et al., 2014; Fender et al., 2015). The GC is located at 8 kpc, so that with observations of ∼100h length all quiescent BHBs in the GC could be detected. This would provide a breakthrough and would allow us to directly confirm the existence of a cusp of black holes that increases steeply in density toward Sgr A*. The existence of such a dark cusp has direct consequences for gravitational wave astrophysics because so-called Extreme Mass Ratio Inspiral Events (EMRIs) are thought to occur in galactic nuclei when SBHs fall into supermassive BHs. Constraints from the GC would allow us to predict event rates and interpret the observations from future space-based GW observatories that may operate from the mid 2030s on (e.g. Amaro-Seoane et al., 2007). We may even be able to directly probe the dynamics of BHBs near Sgr A* in repeated deep observations.

Finally, pulsars and milli-second pulsars can be considered ultra-precise clocks in space. Finding them in orbit around a SBH or around Sgr A* will enable us to perform high precision tests of General Relativity (Eatough et al., 2015).

4.2.5 The case for band 6 receivers

Band 6 receivers would be of considerable importance for the GC science case: On the one hand, the emission from most stars becomes brighter toward higher frequencies, which is why recent radio observations of stars at the GC were performed with the JVLA at frequencies 34-44 GHz, achieving an angular resolution better than 0.1 and an rms noise of $\sim$60 μJy/beam (Yusef-Zadeh et al., 2014, 2015). On the other hand, the GC is an extremely complex and crowded target and only the highest angular resolution achievable will allow us to reliably separate sources and cross-identify them with other wavelengths (Figs. 25 and 24). The surface density of stars detectable with the current 8-10m telescopes ranges from $\sim$ 10 per square arcsecond at 1 pc from Sgr A* to several tens per square arcsecond at $\sim$2 from Sgr A*. With the ELT we expect to measure stellar surface densities that are $>$ 10 times higher. We must therefore be able to reach an angular resolution of $\lesssim$ 0.05 reliably. Although a comparable angular resolution can also be reached with band 5 receivers, a second band that allows high angular resolution observations, but at significantly different mean frequency, is necessary in order to measure the spectral index of the detected sources. In combination with multi-wavelength information, e.g. from high angular resolution near-infrared (NIR) observations, the nature of the sources can then be identified, for example.

4.2.6 Examples of GC Observations with the SKA

At 40 GHz the SKA1 could reach approximately 3.6 μJy/beam in 1h of integration time. A single 100h pointing toward Sgr A* could thus provide a sensitivity of 0.36 μJy/beam in a field of view of 30 armin^2. Such a field is sufficiently large to contain the entire nuclear star cluster around Sgr A*, which has a half-light radius on the order of 5 pc or 2 arcmin (Schödel et al., 2014). Gallo et al. (2014) detected the XRB XTE $J1118 + 480$ in quiescent state at a distance of 1.7 kpc at 5.4 GHz with 5 μJy flux density. Assuming a GC distance of 8 kpc and a flat radio spectrum of quiescent XRBs, we can thus expect to detect these objects with a flux density of $\sim$2 μJy, or more than 5 σ significance. At the same time we would pick up the radio emission of hundreds of stars.

A GC large field of 100 pc $\times$ 40 pc (0.2 deg^2), comprising most of the nuclear bulge, could be studied with the SKA1 in less than 1000 h at an rms level of 1.1 μJy/beam (assuming 10h of integration time per pointing). This would allow us to detect all WR-OB stars in the nuclear bulge (Umana et al., 2015) and even quiescent BH XRBs at $\sim$2 σ significance.

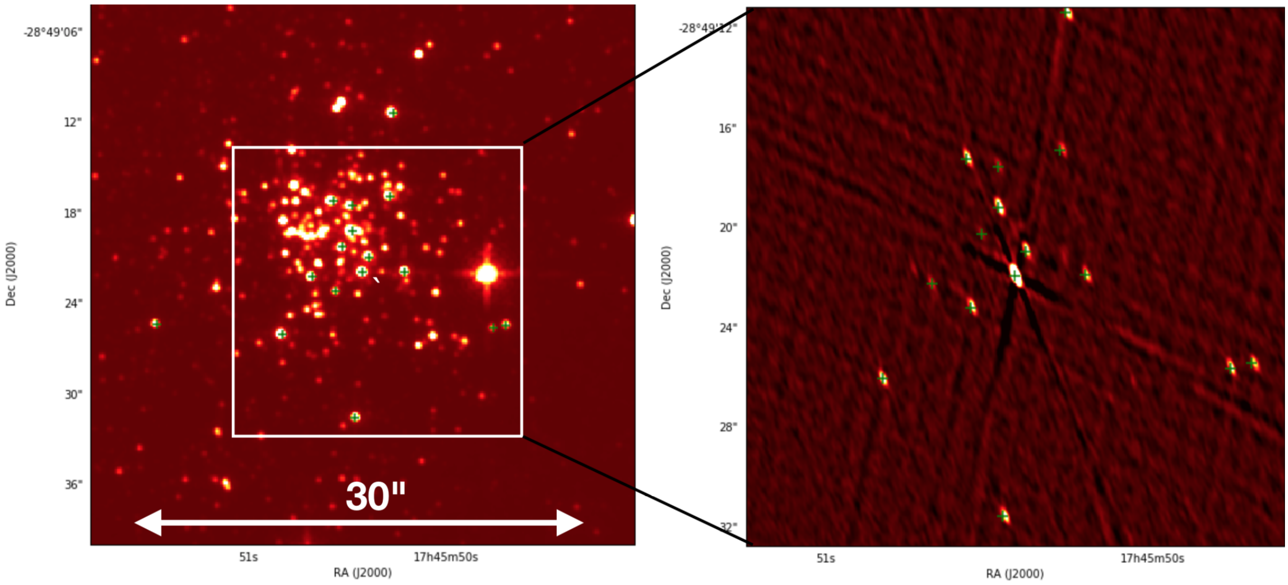

Figure 24: **The Arches cluster** is one of the most massive young clusters in the Milky Way and is located at about 30 pc in projection from Sgr A*. It contains > 150 O-stars, all of which will be detectable with SKA. The left image shows an HST near-infrared image of the Arches cluster. The right image shows a recent 10 GHz JVLA image (Gallego-Calvente et al., in prep.). All stars detected as compact radio sources are marked by green crosses in the left panel. SKA will practically detect all stars within the white square on the left. Avoiding source confusion requires an angular resolution of at least 0.05 and thus Band 5 and 6 receivers.

References

Launhardt, R. and Zylka, R. and Mezger, P. G., 2002, A&A, 384, 112

Schödel, R. and Feldmeier, A. and Kunneriath, D. and Stolovy, S. and Neumayer, N. and Amaro-Seoane, P. and Nishiyama, S., A&A, 566, A47

Neumayer, N., 2017, IAU Symposium, 316, 84-90

Matsunaga, N. and Kawadu, T. and Nishiyama, S. and Nagayama, T. and Kobayashi, N. and Tamura, M. and Bono, G. and Feast, M. W. and Nagata, T., Nature, 477, 188-190

Yusef-Zadeh, F. and Hewitt, J. W. and Arendt, R. G. and Whitney, B. and Rieke, G. and Wardle, M. and Hinz, J. L. and Stolovy, S. and Lang, C. C. and Burton, M. G. and Ramirez, S., ApJ, 702, 1778-225

Yusef-Zadeh, F. and Wardle, M. and Schdel, R. and Roberts, D. A. and Cotton, W. and Bushouse, H. and Arendt, R. and Royster, M., ApJ, 819, 60

Nandakumar, G. and Schultheis, M. and Feldmeier-Krause, A. and Schdel, R. and Neumayer, N. and Matteucci, F. and Ryde, N. and Rojas-Arriagada, A. and Tej, A., A&A, 609, A109

Güdel, M., 2002, ARA&A, 40, 217-261

Umana, G. and Trigilio, C. and Cerrigone, L. and Cesaroni, R. and Zijlstra, A. A. and Hoare, M. and Weis, K. and Beasley, A. and Bomans, D. and Hallinan, G., 2015, Advancing Astrophysics with the Square Kilometre Array (AASKA14), 118

Yusef-Zadeh, F. and Roberts, D. A. and Bushouse, H. and Wardle, M. and Cotton, W. and Royster, M. and van Moorsel, G., 2014, ApJL, 792, L1

Yusef-Zadeh, F. and Bushouse, H. and Schdel, R. and Wardle, M. and Cotton, W. and Roberts, D. A. and Nogueras-Lara, F. and Gallego-Cano, E., 2015, ApJ, 809, 10

Morris, M., 1993, ApJ, 408, 496-506

Antonini, F. and Rasio, F. A., 2016, ApJ, 831, 187

Hailey, C. J. and Mori, K. and Bauer, F. E. and Berkowitz, M. E. and Hong, J. and Hord, B. J., 2018, Nature, 556, 70-73

Gallo, E. and Miller-Jones, J. C. A. and Russell, D. M. and Jonker, P. G. and Homan, J. and Plotkin, R. M. and Markoff, S. and Miller, B. P. and Corbel, S. and Fender, R. P., 2014, MNRAS, 445, 290-300

Fender, R. and Stewart, A. and Macquart, J. P. and Donnarumma, I. and Murphy, T. and Deller, A. and Paragi, Z. and Chatterjee, S., 2015, Advancing Astrophysics with the Square Kilometre Array (AASKA14), 51

Amaro-Seoane, P. and Gair, J. R. and Freitag, M. and Miller, M. C. and Mandel, I. and Cutler, C. J. and Babak, S., Classical and Quantum Gravity, 24, 113

Eatough, R. and Lazio, T. J. W. and Casanellas, J. and Chatterjee, S. and Cordes, J. M. and Demorest, P. B. and Kramer, M. and Lee, K. J. and Liu, K. and Ransom, S. M. and Wex, N., 2015, Advancing Astrophysics with the Square Kilometre Array (AASKA14), 51

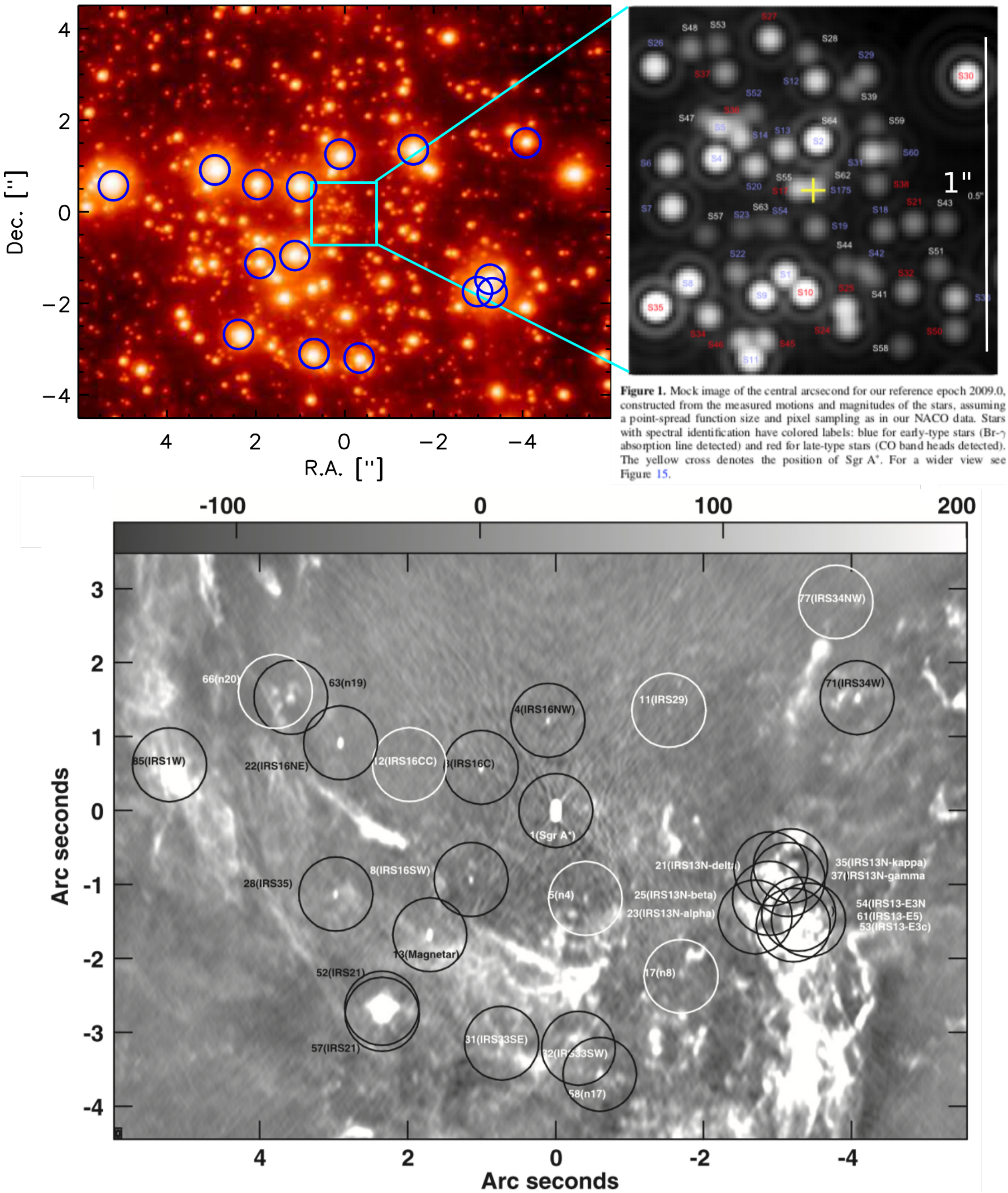

Figure 25: **Radio and near-infrared view of the Galactic Centre.** Top left: 2.2 μm image of the GC taken with NACO/VLT. North is up and east is to the left. Sgr A* is located at the origin. The blue circles mark some of the young, massive stars detected in radio observations (bottom). Top right: Zoom into the image on the left (Fig. 1 from Gillessen et al. 2017). The majority of stars near Sgr A* that can be classified with current instruments appear to be B-type main sequence stars (blue labels). The SKA may be able to detect some or all of them (Umana et al., 2015) and may also be able to pick up quiescent BHBs near Sgr A*. Bottom: 34.5 GHz image of the central 7×5 around Sgr A*, observed with the JVLA. The clean beam is 47×88 mas (Yusef-Zadeh et al., 2015). The circles mark point-sources, in particular radio stars near Sgr A*.

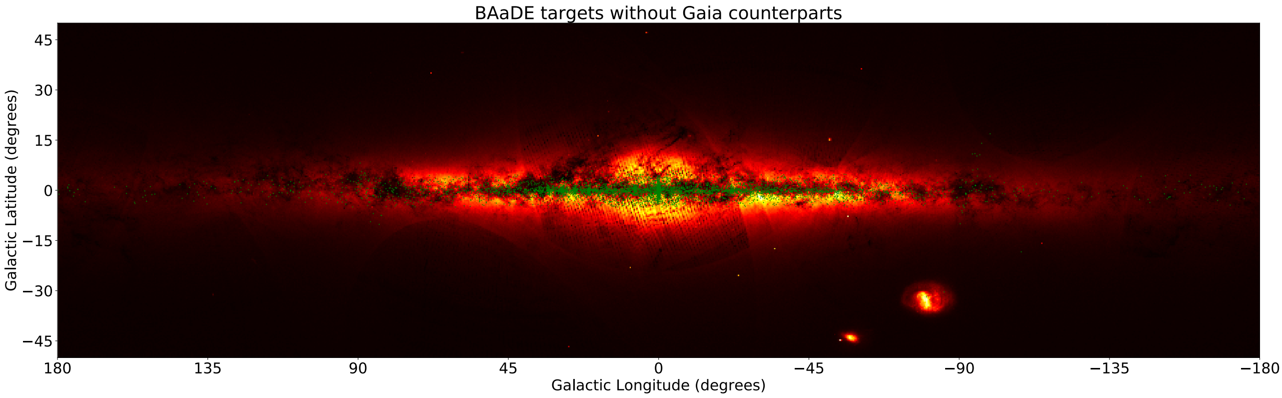

Figure 26: BAaDE targets without Gaia counterparts are AGB stars for which there is no optical identification. These stars are bright in the infrared and have an established high probability to have SiO masers (Quiroga et al., 2018)

4.3 Masers as tracers of evolved stars and the evolution of the Milky Way

Sandra Etoka (JBCA - Manchester University), Huib Jan van Langevelde (Jont Institute for VLBI ERIC (JIVE)/Sterrewacht Leiden, Leiden University), Hiroshi Imai (Kagoshima University), Wouter Vlemmings (Chalmers University of Technology)

4.3.1 Background

AGB (asymptotic giant branch) stars are low and intermediate mass stars going through their last phase of nuclear fusion before heading through the planetary nebulae (PNe) phase to die as white dwarfs. As stars of a large mass range are going through this phase, the ages of the objects can differ by orders of magnitude (Hofner & Olofsson, 2018). These stars are an important constituent of the Galaxy as they replenish the ISM with atomic species and dust particles. In the radio regime, some of the nearest and most luminous stars can be detected through their radio continuum (Reid & Menten, 2007), but they are also notable sources of circumstellar maser emission. OH, H_2O and SiO can be used as bright beacons to find these objects, study their kinetic processes and even their distances and motions in the Galaxy through VLBI (Reid & Honma, 2014).

Astrometric VLBI observations of evolved stars are of interest for a number of reasons. Firstly, it is a method to obtain unbiased distances to individual objects. This is fundamental to measure luminosity, mass-loss rates and other quantities. With accurate distances it is possible to quantitatively test the processes that govern variability and mass loss. If we want to understand the life cycle of baryons in the Galaxy, such measurements are key to calibrate the contribution of ordinary stars, depositing large amounts of matter back in the ISM towards the end of their lives. Note that the distances to individual AGB stars are typically not constrained well by Gaia as they are large and variable (also in colour, van Langevelde et al. (2019)).

Moreover, astrometric VLBI can be used to study the dynamics of the Galaxy and derive important information on the assembly history of the Galaxy, providing local constraints on the subject of cosmological structure formation. To contribute to this, one must be able to characterise a specific stellar population and determine how it occupies 6D phase space by determining, position, distance and motion in the line of sight and on the sky. The BeSSeL project does that for pre-main sequence, high-mass stars tied to the spiral arms in the Galactic plane (Reid et al., 2019). And of course the Gaia survey is making revolutionary contributions to this field (Antoja et al., 2018; Belokurov et al., 2019), but it cannot reach some regions of the Galaxy that are most interesting for this: the bulge and the bar. Future astrometric missions may probe further through the foreground dust by going to the near-infrared, but such projects will be limited in resolution for realistic mirror sizes that can be flown on spacecraft. VLBI astrometry can reach the inner Galaxy, especially when sensitive telescopes and innovative calibration techniques can be deployed (Fig. 26).

The total number of H_2O and SiO maser sources accessible for astrometry is expected to exceed

10,000 in the whole Galaxy, as demonstrated by large surveys towards targeted stars such as the BAaDE project (Bulge Asymmetries and Dynamic Evolution; Trapp et al. (2018); Stroh et al. (2019)) and unbiased Galactic plane surveys such as GASKAP and THOR in which some of the catalogued circumstellar OH masers will host H_2O and SiO masers. These 3 species, probing different radii (in particular pre- and post the dust formation region), provide us with valuable information of the overall dynamical and structural (including that of the magnetic field) properties of the circumstellar envelop (CSE).

Below we present first water maser applications, mostly focusing on projects that study the properties of stars going through the (post-)AGB phase. We then discuss large scale projects to do astrometric observations of a very large sample of SiO maser sources, aiming at revealing the structure and dynamics of the bar and bulge. We note that of course water masers can also be used to study galactic structure, and that SiO masers can be used to study mass loss in individual stars, but we have bundled these topics for convenience.

4.3.2 AGB physics/H_2O masers

Water masers at 22 GHz, typically probe the intermediate regions (5 to several 10s of stellar radius) of the CSE. They provide us with the means to probe the structure and kinematics in that part of the CSE where the wind is most strongly accelerated and passes through the escape velocity. In order to retrieve the most faithful shell structure, short baselines (a few tens of kms) and higher sensitivity are needed. On the other hand, mapping of the compact unresolved maser spots is required in order to investigate the origin of the rapid acceleration thought to be enhanced by the propagation of pulsation-driver waves as well as their significant location bias which is considered to be linked to asymmetric stellar mass loss.

How in the short transitional period in which spherical AGB stars turn into PNe, a substantial number of which display spectacular asymmetry with collimated-outflow signature, is a crucial point in stellar evolution still not well understood. Several scenarios as to how these asymmetries are triggered have been proposed. The recent advances in the topic favours binary action as the main agent in the development of asymmetries though the direct detection of a synchrotron jet from a post-AGB star (Perez-Sanchez et al., 2013) as well as maser observations (Vlemmings et al., 2006) strengthen the hypothesis that magnetic fields could be effectively contributing to the shaping process leading in particular to bipolar PNe. While traditional AGB stars have their H_2O maser emission dominated by spheroidal expansion (Richards et al., 2012), a sub-class of objects in the late-AGB/post-AGB stage, so-called "water fountains" (WFs), produce atypical water maser emission consisting of highly collimated outflows with velocity span much greater than that of the slowly expanding CSE. Internal proper motions of circumstellar H_2O maser spots can trace these stellar jets along with rotating gas tori around pre-planetary and planetary nebula. Because the duration of these stellar evolutionary phases is very short (<100 years; Imai (2007)), we can monitor their real-time spatio-morphological evolution. Recent multi-epoch interferometric observations of the structure and proper motion of the H_2O masers of a WF revealed episodic, jet-driven outflow ejections best explained by binarity (Orosz, 2019). Though only 15 WFs are confirmed so far, their {IR} properties do not differentiate them from other obscured post-AGBs (Gomez et al., 2017). This small number could then be due to variability and/or an orientation effect rather than age. Only observations at high sensitivity such that SKA1-MID would provide can address this question.

Maser polarization observations are the predominant source of information about the role of magnetic fields during the late stages of stellar evolution. Observations of OH, H_2O and SiO masers in the CSEs of AGB stars, have revealed strong magnetic fields throughout the entire CSE (Vlemmings et al., 2018). However, the interpretation of SiO maser polarization is uncertain (Lankhaar & Vlemmings, 2019). The circular polarization of H_2O masers has been shown to be due to the regular Zeeman effect, thus only H_2O maser polarization observations can accurately measure the magnetic field strength in the inner regions of the CSEs, at radii of a few tens of AU. Most of the H_2O maser polarization observations of evolved stars have thus far been done with the VLBA in order to fully resolve the various maser features (e.g. Vlemmings et al., 2005). The limited sensitivity and loss of maser flux in VLBI observations limit such studies to relatively few sources that are often selected based on particular properties. Observations with SKA1-MID at 22 GHz will overcome this limitation and will allow us to determine the magnetic field strength for all H_2O maser sources within ~ 1 kpc.

4.3.3 Galactic structure/SiO masers

SiO masers in the Galactic Disk and Bulge AGB stars bearing SiO (or H_2O) masers offer an exciting possibility to sample the inner Galaxy. AGB stars represent a stellar population with a large age range. The ages can be inferred from their variability periods and total luminosity. The oldest stars will be on dynamically relaxed orbits, while younger samples may carry the imprint of merger events or starburst episodes.

Observationally, they are bright in infrared continuum and the SiO masers provide distinctive, bright radio beacons (e.g. Messineo et al. (2018)). By making an infrared selection and following up in a survey mode with VLA and ALMA currently a sample of 40,000 stars with line-of-sight velocities is being constructed in the context of the BAaDE project (e.g. Stroh et al. (2019)). These very short 43 and 86 GHz observations provide direct velocities, but also characterise the stars by means of a few other molecular tracers. Having 43 GHz (or 22 GHz) options for SKA1-Mid will boost the survey capabilities for such projects, but more importantly it will enable VLBI astrometry for more and weaker SiO masers.

By doing VLBI astrometry of these targets we will sample the orbits of old stars in the bar. But VLBI astrometry for SiO masers is challenging even with SKA1-Mid. At 43 GHz, 7mm, the tropospheric conditions are tough and require antennas at dry sites. Atmospheric coherence times are as short as 1 minute, requiring fast switching of the telescopes between targets and calibrators. Moreover, at 7mm calibrators are few and we will be limited to reverse phase referencing, using the masers as calibrators for the weak quasars that are at fixed celestial positions. SiO masers are also variable in flux and structure, requiring us to do more frequent monitoring than was needed for the masers at other frequencies.

However, adding SKA1-Mid in a 7mm array would offer very important advantages. The impressive sensitivity allows fast detection — within the coherence time — of the masers, even at 100 mJy peak line flux density, as expected at the Galactic-centre distance. Additionally, weaker quasars become available for (reverse) phase referencing, although at such high frequency few suitable calibrators at ≈ 1 mJy will be available. Observing strategies will therefore most likely focus on masers with QSOs in beam. One particularly interesting field in this respect is the area centred on SgrA*. SiO masers (observed with the VLA/VLBA) are already being used to link the infrared and radio frames around our Galaxy's black hole and this connection can be made much tighter. Furthermore, it should be possible to link the motions of many SiO together by doing phase referencing between masers with close separation on the sky. Also note that high sensitivity mapping of SiO masers enables us to determine accurately the position of the star which should be located at the center of the maser ring. Finally, we mention that at some point there will be overlap with ALMA band 1, which should also cover SiO masers in the Southern hemisphere.

SiO masers in Galactic globular clusters SiO masers will provide an interesting opportunity to directly spatially resolve circumstellar envelopes around AGB stars in the unique atomic abundance environments of globular clusters. The size of an SiO maser ring (2–3 stellar diameter) around the AGB star is determined by the size of the radio photosphere and the diameter of dust condensation, which are well correlated with each other. Although the correlation of an SiO maser ring size and the stellar parameters should be further investigated, it is a good opportunity to test whether the spatio-kinematics of SiO masers will be a good probe of mass-loss properties of AGB stars in a variety of stellar population (but still in O-rich environment).

There are six SiO masers in globular clusters confirmed, all of which are weaker than 500 mJy (Matsunaga et al., 2005). In order to image an SiO maser ring, mJy-level sensitivity with the SKA1-MID is essential.

Forthcoming synergy with near-infrared space astrometry mission Radio astrometric projects have provided great synergy opportunities with Gaia regarding studies on population and evolution of radio emitting stars and the dynamics of the local universe. These projects led to accurate but independent astrometric measurements, enabling a 1%-level consistency check of trigonometric parallaxies. In the SKA-era, radio astrometry will enable a similar synergy with the Japan Astrometry Satellite Mission for INfrared Exploration (JASMINE). The aim of this mission is to measure 3D positions and 2D velocity vectors of 10^7 stars towards the Galactic Bulge ($-10^\circ \geq l \geq 10^\circ$, $-5^\circ \geq b \geq +5^\circ$) in order to explore the co-evolution of the Galactic Bulge and the central massive black hole, Sgr A*(Gouda, 2010). A small version of this enterprise (namely "small-JASMINE") has been recently approved by JAXA/ISAS (2019 May) and is due to be launched by mid-2020. It will explore $\sim 10^5$ stars in the inner bulge ($-1^\circ \geq l \geq 1.5^\circ$, $+0.2^\circ \geq b \geq +0.5^\circ$).

Within $30''$ of Sgr A*, corresponding to the 15-m antenna beam of the SKA1-MID, there exist many possible science cases in commensality with astrometry for the exploration of Sgr A* and its surrounding environment with deep exposure. In an 8 hour integration, SiO masers brighter than 2 mJy (7σ in velocity width of 0.4 km s^{-1}) will be detectable with the full SKA1-MID array, and those brighter than 50 mJy will certainly be good astrometric targets for SKA-VLBI. Note that there exist 15 SiO masers brighter than 50 mJy within $20''$ of Sgr A*(Reid et al., 2007) while proper motions of 6,000 stars have been measured in the same area (Schodel et al., 2009). Eventually, a wider area (within 0.5° of Sgr A*) will open up for radio astrometry, where stellar orbits associated with the Inner Lindblad Resonances or relics of super-massive black hole mergers will become visible.

References

Antoja, T., et al., 2018, Nature, 561 360
Belokurov, V., et al., 2019, arXiv:1909.04679
Höfner, S., & Olofsson, H., 2018, AAR 26 1
Imai, H., 2007, IAUS, 242, 279
Gómez, J. F., Suárez, O.; Rizzo, J. R., et al., 2017, MNRAS, 468, 2081
Gouda, N., 2010, Trans. JSASS, Aerospace Tech. Japan, 8, To_4_13
Lankhaar, B., & Vlemmings, W., 2019, A&A, 628, A14
Matusnaga, N., et al., 2005, PASJ, 57, L1
Messineo, M., et al., 2018, 619, A35
Orosz, G., 2019, MNRAS, 482, L40
Pérez-Sánchez, A.F., et al., 2013, MNRAS, 436L, 79
Quiroga-Nuñez, L. H., et al., 2018, IAU 336 184
Reid, M.J., et al., 2019, ApJ 885 131
Reid, M. J., Honma, M., 2014, ARAA, 52, 339
Reid, M.J., & Menten, K.M., 2007, ApJ 671 2078
Reid, M. J., et al., 2007, ApJ, 659, 378
Richards, A.M.S., Etoka, S., Gray, M.D., et al., 2012, A&A, 546A, 16
Schödel, R., Merritt, D., Eckart, A., 2009, AA, 502, 91
Stroh, M. C., et al., 2019, ApJ, 244, 25
Trapp, A. C., et al., 2018, ApJ, 861, 75
van Langevelde, H.J., et al., 2019, arXiv1901.07804
Vlemmings, W. H. T., van Langevelde, H. J., & Diamond, P. J., 2005, A&A, 434, 1029
Vlemmings, W. H. T., Diamond, P. J., & Imai, H., 2006, Nature, 440, 58
Vlemmings, W. H. T., 2018, Contributions of the Astronomical Observatory Skalnate Pleso, 48, 187

4.4 Stellar Continuum

Grazia Umana, Corrado Trigilio, Paolo Leto, Carla Buemi, Adriano Ingallinera, Francesco Cavallaro (INAF-Catania), Claudia Agliozzo (ESO), Wouter H. T. Vlemmings (Onsala/Chalmers), Ian Stevens (University of Birmingham)

4.4.1 The state-of-the-art

In the radio band, stars emit a negligible fraction of their total luminosity (the quiet Sun has a luminosity, integrated over the radio band, of 10^{21} erg s^{-1}, while its bolometric luminosity is 10^{33} erg s^{-1}). Nevertheless, in many cases, radio observations have revealed astrophysical phenomena, not detectable by other means, that play a fundamental role in our understanding of stellar evolution and of physical processes in a wider context.

Broadly speaking, the brightest stellar radio emission appears to be associated with active stellar phenomena (flares), related to the presence of a strong and/or variable magnetic field (**high brightness temperature**), or with mass-loss from massive stars (**large emitting surface**).

Much of our knowledge on microwave emission from radio stars comes from the study of active stars and binary systems since a large fraction of them have been found to be strong radio sources. Their radio flux density is highly variable and arises from the interaction between the stellar magnetic field and mildly relativistic particles, i.e. gyrosynchrotron emission. The same emission mechanism is at the origin of radio emission from pre-main-sequence (PMS) stars and X-ray binaries. Non-thermal radio emission also originates from shocks of colliding winds in massive binaries and from pulsars. There is a growing evidence that radio flares can occur also as narrow-band, rapid, intense and highly polarised (up to 100%) radio bursts, that are observed especially at low frequency (< 1.5 GHz). For their extreme characteristics, this kind of radio flare has generally been interpreted as a result of coherent emission mechanisms. Coherent bursts have been observed in different classes of stellar objects (RS CVns, flares stars, brown dwarfs, chemically peculiar stars), all characterised by a strong, and possibly variable, magnetic field and by a source of energetic particles. The number of stars where coherent emission has been detected is still limited to few tens, because of the sensitivity of the available instruments.

Thermal emission (bremsstrahlung emission) is expected from winds associated with Wolf–Rayet (WR) and OB stars, shells surrounding planetary nebulae (PNe) and novae and jets from symbiotic stars and class-0 PMS stars. In all these cases, the radio continuum emission usually constitutes the best diagnostics to derive important parameters for a comprehensive understanding of each particular class of objects. As an example, in the case of stellar winds, radio continuum observations are to most precise way to determine the mass-loss, and this is particularly important when other diagnostics can not be used, such as in the case of dust enshrouded objects.

Despite radio emission having been detected from all stages of stellar evolution across the HR diagram, our knowledge still relies on some hundreds targeted detections and strongly suffers from limited sensitivity (very few radio stars with radio luminosity of the quiescent Sun, $L_{\rm radio} \approx 10^{11}$ erg s^{-1}, have been detected so far) and from a selection bias (observations dedicated to addressing specific issues of some kinds of radio emission are typically focused only on peculiar sub-populations).

In Figure 27, adapted from Umana et al. (2015), the schematic continuum radio spectrum of several classes of radio-emitting stars is drawn. Flux densities were derived assuming a typical radio luminosity for each different type of radio stars. Distances are assumed as appropriate for individual types: 10 pc for flares stars, including late M-L, 100 pc for active binary systems, 1 kpc for supergiants, OB and WR, 500 pc for CP stars. The flux density of the quiet Sun was derived from the solar quiescent radio luminosity assuming a distance of 10 pc.

At a sensitivity of the order of microjansky level, as expected for SKA1, all kinds of radio stars considered, including also a flaring Sun twin at 10 pc, should be in principle easily detected in L-band. However, a quiescent Sun twin, even at 10 pc, can be detected only at higher frequencies. In fact, assuming that the photosphere emits as a black body, the spectrum increases as ν^2. The atmosphere is characterised by a non-linear behaviour and presents an inversion of temperature that increases going outwards and reaches millions of kelvin. This leads to an important deviation from the black-body curve in the centimetric. Since the radiation is generated at a depth where $\tau \approx 1$. Considering that for free-free emission the opacity goes approximately as $n^2 T^{-1.35} \nu^{-2.1}$, at centimetric wavelengths we probe the upper chromosphere and the lower corona. These regions are particularly affected by magnetic activity since both plasma density and temperature increase during active periods (Trigilio et al. 2018). In addition, the presence of thousand-gauss magnetic fields increases the opacity, making the corona optically thick, leading to a strong increase of the emission. At frequencies above 10 GHz, radio flux density measurements give us the opportunity to study the atmospheric structure, the magnetic activity and therefore the possible influence on planets through space weather.

An extension of the SKA to higher frequencies (higher than band 5) would make the SKA a unique instrument for Galactic Science, allowing us to detect many classes of stars over the entire Milky Way, producing a real revolution in stellar physics. As radio stars can be probed at many different frequencies in the radio, opening the frequency range will allow us to define the radio properties of

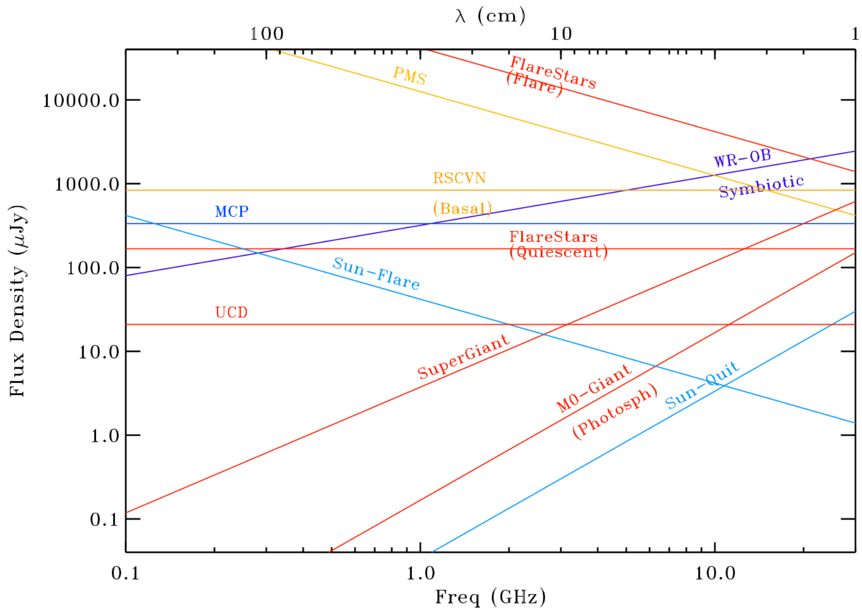

Figure 27: Adapted from Umana et al., 2015. Typical radio spectrum of several classes of radio emitting stars. Flux densities were derived from the radio luminosity, assuming a distance as appropriate for each type of radio stars

different stellar populations and to compare them with other stellar parameters, such as mass, magnetic fields, chemical composition, and evolutionary stages. Moreover, studies at higher frequencies will provide us with information on non-thermal processes (i.e. probing the optically thin part of the gyro synchrotron emission directly related to the stellar magnetic field and energy content of relativistic particles) and, in particular, with constraints on particle acceleration processes in different stellar environments.

There are some particular areas of stellar radio emission that will particularly benefit from SKA high-frequency observations, as indicated in the following sections.

4.4.2 Mass-loss from Massive stars (LBVs)

An O-type main-sequence (MS) star, whose mass may be as large as $150 M_{\odot}$, is predicted to evolve into a WR star, with a typical mass not in excess of $30 M_{\odot}$. However, MS mass-loss rates are insufficient to account for such a huge mass-loss. Severe mass-loss probably occurs through strong stellar winds and/or eruptions during the post-MS evolution. Many luminous classes of stars undergo this phase, hot supergiants (blue supergiants, B[e] stars and luminous blue variables), cool Yellow Hypergiants (YHGs) and Red Supergiant (RSGs) stars. The exact evolutionary path leading to a WR star, as a function of the mass and rotation, is however not well constrained. In fact a crucial piece of information, i.e. mass-loss rates and lifetime and thus the total amount of mass lost during the post-MS, is currently incomplete.

Luminous blue variables (LBVs) may play a key role in this scenario. Not only they are characterised by a strong mass-loss, but they can also show giant eruptions, in which larger amounts of mass are ejected.

Currently, the link between LBVs and other advanced evolutionary phases of massive stars, such as supernovae, is a hot topic of discussion. Recent observations suggest that LBVs may be (under certain conditions) direct progenitors of type IIn supernovae (Groh et al. 2013). Despite their rarity, LBVs play an important role in the chemical enrichment of the interstellar medium, due to the large amount of processed material ejected by means of continuous winds and intense eruptions. In addition, a growing interest in the study of LBV ejecta is coming from their possible role as primordial dust producers.

As a consequence of the strong stellar wind and/or the giant eruption, circumstellar nebulae around LBVs may form. Their mass ranges from few solar masses, in the wind scenario, to several solar masses during ejections. These nebulae are a few parsec in size and have expansion velocities between 10 – 200 km s^{-1}. In extreme cases, velocities of several 1000 km s^{-1} have been detected (Weis, 2011). The nebulae are seen in optical and IR emission lines, radio continuum emission and IR excess emission. The possibility that such spectacular mass-loss events may be metallicity-independent has greatly increased the interest in LBVs, as this can have important implications for the mass-loss and therefore the evolution of Population III stars.

Up to now, the Galactic population of LBV stars is extremely scarce, with less than twenty confirmed members and a few candidates which still require confirmation (Richardson & Mehner 2018). Increasing the number of studied LBVs and LBV candidates gives us an opportunity to confirm their classification and gain a better understanding of their evolutionary status. In particular, the comparison with the physical property of LBVs belonging to environments at lower metallicities will allow us to determine if the mass-loss phenomenon occurs independently of the metallicity.

Mass-loss rates from a number of LBVs and LBV candidates have been recently derived from radio observation in our Galaxy (Umana et al., 2005, 2010, 2012) and in the LMC (Agliozzo et al., 2012, 2017). Radio observations have also allowed us to determine the morphology of the ionized fraction of some LBV nebulae and to quantify the mass of ionised material (Buemi et al., 2010; Umana et al., 2011). When radio maps are combined with detailed mid-IR maps, tracing the dust component, the presence of multi-epoch mass-loss events become evident and estimates of the total mass content can be made (Umana et al., 2012; Agliozzo et al., 2014; Buemi, 2017).

As shown in Umana et al. (2015), using the SKA, at band 5, it will be possible to reach a detection limit of order of lower than $\sim 1\ \mu$Jy in an integration time of one hour. Such a detection limit is sufficient to measure very small mass-loss rates ($\sim 10^{-7} M_\odot$ yr^{-1}) at the distance of the Galactic Center. Moreover, since the dependence of the radio flux due to a stellar ionised wind on the frequency ($S_\nu \propto \nu^{0.1}$), radio observations, performed at higher frequencies will allow to measure mass-loss rates usually observed in LBVs (Smith N., 2017), at the distance of Magellanic Clouds (MCs) and Local Group Galaxies.

Considering a typical size of 1 pc for LBV nebulae, at such distances it will be also possible to resolve the wind associated to the central object from the free-free emission of the LBV nebula, allowing to explore a plethora of stellar winds and associated nebulae in different environment, such as the inside the three massive stellar clusters located near the Galactic Center (Arches, Quintuplet and the Central Cluster) or the the MCs or the Andromeda galaxy. The comparison among the derived physical parameters (mass lost during the LBV phase, kinematic age, morphology and density of the associated nebula) will allow to investigate the role of the environments in the LBV evolution.

4.4.3 Early-type magnetic stars, Chemically Peculiar stars

The magnetic fields of the main sequence B/A type stars have, on average, an intensity of a few kilogauss, their topology is mainly dipolar and stable. Strong magnetic fields induce surface chemical anisotropies, variable as a consequence of the stellar rotation. The currently accepted model is the Oblique Rotator Model, where the dipole field is tilted to the stellar rotation axis (Babcock 1949). In general, the early type magnetic stars are classified on the basis of their chemical peculiarity, they are then classified as Ap/Bp stars. About 7% of the stars across the upper main-sequence are magnetized (eg. Wade et al. 2016). These stars are sufficiently hot to drive radiatively stellar winds, which follow the magnetic field lines and co-rotates with the stars. The plasma accumulates near the equatorial plane, and can freely propagate along directions near the magnetic poles (Shore 1987; Shore & Brown 1990; Leone 1993).

Strong magnetic field and plasma wind are key ingredients for establishing a significant radio emission among early-type magnetic stars. In fact, about 25% of the magnetic Ap/Bp type stars are non-thermal radio sources (Drake et al. 1987; Linsky et al. 1992; Leone et al. 1994). The scenario explaining their radio emission is related to the interaction of the radiative driven ionised stellar wind and the ambient magnetic field. The ionised stellar wind opens the magnetic lines at the Alfvén point and a continuous acceleration occurs in the current sheets all around the star in the equatorial plane. Such non-thermal plasma, propagating within the stellar magnetosphere, radiates at the radio regime by the incoherent non-thermal gyro-synchrotron mechanism and produces a continuum radio emission partially circularly polarised (Trigilio et al. 2004; Leto et al. 2006).

The radio spectrum is flat within a broad radio frequency band (frequency range $1-100$ GHz) (Leto et al. 2018). The radio luminosities of the early-type magnetic stars are in the range $10^{17}-10^{18}$ ergs s^{-1} Hz^{-1}. Radio emission at different frequencies arises from different magnetospheric layers. In fact, the gyro-synchrotron emission mechanism is strongly sensitive to the magnetic field strength and topology and to the local density of the relativistic electrons, which vary with the radial distance from the stellar surface. Higher frequency radiation is generated close to the stellar surface, where the field strength is high, while lower frequencies probe regions farther out. The total intensity (Stokes I) is mainly sensitive to the magnetic field strength and to the density of the non-thermal electrons. The circularly polarised emission (Stokes V) probes also the local magnetic field topology. The fraction of the circularly polarised emission produced by the gyro-synchrotron mechanism increases with frequency. In particular, the circular polarisation fraction (Stokes-V / Stokes-I) can reach level as high as 10% in the range $15-25$ GHz (Leto et al. 2017; Leto et al. 2019).

The SKA band 6 is the optimal choice for studying the radio emission features of the early-type magnetic stars. In fact the higher observing frequencies are suitable to measure the circular polarization state of such kind of sources. The SKA measurements of the Stokes I and V in the band $15-25$ GHz has the capability to probe the density of the non-thermal electrons very close to the stellar surface and the true magnetic field topology just above the stellar surface.

The expected radio flux density of an early-type magnetic stars with radio luminosity 10^{18} ergs s^{-1} Hz^{-1} located close to the centre of the Galaxy (distance from Earth about 9 kpc) is about 10 μJy. At the observing frequency of about 20 GHz, the expected fraction of the circularly polarised emission is about 2 μJy. The SKA1 performance expected at band 6 ($15-25$ GHz), for observations 1-hour long the expected rms is lower than 1 μJy, ensures the robust detection of such a kind of hot magnetised star (total flux: Stokes I) and the possible tentative detection of the polarised flux (Stokes V).

The full operational state of the SKA will further lower the detection threshold, with an expected rms below 0.1 μJy. SKA will be then able to well characterise the radio emission features (total intensity and circular polarisation) of all the early type magnetic stars less distant than the Galactic centre.

4.4.4 AGB stars

Radio observations have provided important insights in the late stages of stellar evolution. Low- to intermediate mass stars up to $\sim 8M_{\odot}$ undergo extensive mass-loss while they evolve on the asymptotic giant branch (AGB). Through this mass-loss, they return processed material to the interstellar medium. It is thought that the AGB stars may be responsible for almost half of the chemical enrichment in our Galaxy. The mass-loss originates from the extended atmospheres of the stars, where material is transported outwards to cooler regions where dust can form and radiation pressure launches a wind. Sensitive high angular resolution continuum radio observations probe exactly this region, between one to two stellar (photospheric) radii. With the VLA and ALMA, observations have revealed the action of shocks, likely convection and pulsations (e.g. Matthews, Vlemmings). At wavelengths < 3 mm ALMA reaches an angular resolution < 30 mas, which has allowed us to resolve the extended atmospheres of AGB stars within 150 pc. Similarly, the VLA has marginally resolved these stars at longer wavelengths (~ 1 cm). Around 30 GHz, the SKA will provide a resolution of ~ 13 mas while still providing a continuum sensitivity of 3.6 μJy beam^{-1} in 1 hr of observations. This means we will be able to resolve all AGB stars within ~ 400 pc. At the same time, we will be able to detect the continuum emission from all AGB stars out to ~ 1.5 kpc. Together with observations at the ALMA bands, it will thus be possible to trace the activity in the stellar atmosphere from the photosphere out to the dust formation region and characterise temperature and density structures to directly constrain the 3D-hydrodynamical simulations of convective AGB stars.

References

Agliozzo, C., Umana, G., Trigilio, C., et al. 2012, MNRAS, 426, 181
Agliozzo, C., Noriega-Crespo, A., Umana, G., et al. 2014, MNRAS, 440, 1391
Agliozzo, C., Trigilio, C., Pignata, G., et al. 2017, ApJ, 841, 130
Babcock, H. W. 1949, The Observatory, 69, 191
Bomans, D. J., & Weis, K. 2011, Active OB Stars: Structure, Evolution, Mass Loss, and Critical Limits, 265
Buemi, C. S., Umana, G., Trigilio, C., et al. 2010, ApJ, 721, 1404
Buemi, C. S., Trigilio, C., Leto, P., et al. 2017, MNRAS, 465, 4147
Drake, S. A., Abbott, D. C., Bastian, T. S., et al. 1987, ApJ, 322, 902
Groh, J. H., Hillier, D. J., & Damineli, A. 2011, ApJ, 736, 46
Leto, P., Trigilio, C., Buemi, C. S., et al. 2006, A&A, 458, 831
Leto, P., Trigilio, C., Oskinova, L., et al. 2017, MNRAS, 467, 2820
Leto, P., Trigilio, C., Oskinova, L. M., et al. 2018, MNRAS, 476, 562
Leone, F. 1993, A&A, 273, 509
Leone, F., Trigilio, C., & Umana, G. 1994, A&A, 283, 908
Linsky, J. L., Drake, S. A., & Bastian, T. S. 1992, ApJ, 393, 341
Matthews, L. D., Reid, M. J., Menten, K. M., et al. 2018, AJ, 156, 15
Richardson, N. D., & Mehner, A. 2018, Research Notes of the American Astronomical Society, 2, 121
Shore, S. N. 1987, AJ, 94, 731
Shore, S. N., & Brown, D. N. 1990, ApJ, 365, 665
Smith, N. 2017, Philosophical Transactions of the Royal Society of London Series A, 375, 20160268
Trigilio, C., Leto, P., Umana, G., et al. 2004, A&A, 418, 593
Trigilio, C., Umana, G., Cavallaro, F., et al. 2018, MNRAS, 481, 217
Umana, G., Buemi, C. S., Trigilio, C., et al. 2005, A&A, 437, L1
Umana, G., Buemi, C. S., Trigilio, C., et al. 2010, ApJ, 718, 1036
Umana, G., Buemi, C. S., Trigilio, C., et al. 2011, ApJ, 739, L11
Umana, G., Ingallinera, A., Trigilio, C., et al. 2012, MNRAS, 427, 2975
Umana, G., Trigilio, C., Cerrigone, L., et al. 2015, Advancing Astrophysics with the Square Kilometre Array (AASKA14), 118
Vlemmings, W. H. T., Khouri, T., & Olofsson, H. 2019, A&A, 626, A81
Wade, G. A., Neiner, C., Alecian, E., et al. 2016, MNRAS, 456, 2
Weis, K. 2011, Active OB Stars: Structure, Evolution, Mass Loss, and Critical Limits, 372

4.5 Supernova Remnants

Filomena Bufano and Sara Loru (INAF-Osservatorio Astrofisico di Catania)

Supernova Remnants (SNRs) play an important role in the evolution of their own host galaxy. They are responsible for the chemical enrichment of the Interstellar Medium (ISM), providing it with new heavier elements produced during the explosion of the parent Supernova (SN). SNRs radiate energy over the entire electromagnetic spectrum, but the bulk of their emission lies in the radio band. For this reason, the radio band is probably the best to study and identify SNRs. In our Galaxy about 95% of the known Galactic SNRs are detected in radio (Dubner & Giacani 2015, A&AR, 23, 3) and many of them are detected only in this band. This is because the Galaxy is transparent at radio wavelengths and the SNR radio emission, due to synchrotron radiation of the accelerated electrons spiralling around the magnetic fields, is very intense. The interaction of the ionized material ejected by the SN and the surrounding medium, pervaded by magnetic fields, generates a strong shock that increases the temperature of the post-shock region (X-ray emission) and accelerates particles (1st order Fermi acceleration) up to relativistic energies ($N_{\rm REL} \propto E^{-\delta}$, with $\delta \approx 2-2.5$).
The huge amount of energy transferred to shocked gas provides populations of relativistic ions and electrons that produce the radio continuum radiation typically observed in these extended sources. The study of SNR radio emission may provide crucial information in order to understand the nature of the observed high-energy co-spatial emission: the two basic possible scenarios described by leptonic (Inverse Compton and Bremsstrahlung emission) and hadronic models (π^0 mesons decay emission) could be disentangled by the characterization of radio emission.
Finally, to date only about one fourth of theoretically expected galactic SNRs were observed and catalogued. This makes it hard to discriminate between the SNR characteristics associated with peculiar environmental conditions and those that can be considered a standard behaviour. For this reason, integrated and spatially resolved spectral studies covering a wide range of frequencies and extended to a statistically significant sample of these objects are crucial in order to better constrain the morphological and evolutionary classification of these complex objects.

Importance of SNR observations at high radio frequencies

The SNR shocks propagate in the ISM and the material accumulated forms a shell-like envelope. The presence of molecular clouds (MCs) can intensify the effects of the shocks and provides the synchrotron source with newly accelerated electrons, flatting the spectrum. This is the reason why the radio spectrum ($F_\nu \propto \nu^{-\alpha}$, with $\alpha = (\delta - 1)/2$) correlates with the energy spectrum of the radiating electrons and provides us a powerful insight for the understanding of such phenomena. Although the main characteristics of the radio continuum spectra of SNRs result from the synchrotron emission, other electron acceleration mechanisms can shape the spectra in specific ways. These features are connected to the age and the peculiar conditions of the local ISM interacting with the SNR and are detectable **especially at high radio frequencies**. For example, in the middle-aged IC443 SNR a spectral bump in the frequency range 20-70 GHz was observed and ascribed to a possible spinning dust component dominating over the synchontron emission (Fig.29).
On the other hand, also a spectral flattening at frequencies above ~10 GHz could be observed, resulting in a concave-up spectral feature. Some historical remnants (3C391 and 3C396, Oni et al. 2012) show radio spectra possibly indicating a concave-up curvature (Reynolds and Ellison 1992), which could be explained by efficient shock acceleration or by other concurring emission mechanisms like the thermal bremsstrahlung in case of expansion in high density environment (Oni, 2013). Thus it becomes crucial to observe the objects at frequencies >10 GHz to reveal these changes in the spectral slope.
It is worth noting that these features in the integrated spectrum could be related to the dominant contribution from electron populations located in peculiar SNR regions, and resulting from different shock conditions and magnetic field configuration. Spatially-resolved spectral index studies could be crucial to investigate in this regard. Indeed spectral index maps, like the one obtained with the Sardinia Radio Telescope in single-dish observing mode in the 1.5-7.0 GHz range, could provide indication on where the contribute of the different processes is dominant.

The different spectral shapes could be also related to a magnetic field amplification at SNR shocks, which results in an efficient CR acceleration. The co-spatial study of the magnetic field orientation, the continuum radio emission and related spectral proprieties could provide a crucial test for the processes of magnetic field amplification and their possible association with the interaction between the SNR and molecular clouds. In this framework, the production of sensitive spectral index maps are crucial to distinguish the features related to different electron populations and spectra, which result from peculiar shocks conditions and/or magnetic field amplification processes.

SNRs at SKA Band 6 frequency

To firmly establish a possible spectral break and features, and to identify regions or structures within the SNRs where they take place it is of high interest to obtain a well-sampled radio SED of the SNR. From the last census of Galactic SNRs (Green et al. 2019), we detected 294 SNRs. Taking into account the expected SKA Band 6 LAS (~3 arcmin), we would confidentially measure the radio emitted flux for only 8 of them. For the more extended ones, thanks to the high resolution we would be able anyway to define the morphology of the sub-structures and spot the shocked areas. In particular, it will be possible to conduct spectropolarimetric studies at unprecedented resolution on the filaments (observed in all known supernova remnants), searching for the MHD signature in the plasma interacting with the magnetic field. This could disclose plasma turbulence and instability and would be an ideal laboratory for MHD study at high particle energies. These studies will also provide a list of interesting targets to observe with single dish telescopes, complementing SKA data and giving us the most accurate and detailed view of Galactic SNRs obtained so far. At the same time, we will resolve all the known extragalactic SNRs: assuming an average linear dimension <D>~20 pc for a SNR and a projected angular dimension in the sky θ ~0.1 arcsec we will be able to resolve SNRs up to a distance of ~40 Mpc, or for a more conservative θ ~0.3 arcsec, up to ~13 Mpc. At these distances, all the known extragalactic SNRs (~1500 SNRs; see Tab.1 in Long, K.S., 2017) would be resolved making possible not only a precise measurements of the SED but also a detailed spectral index map.

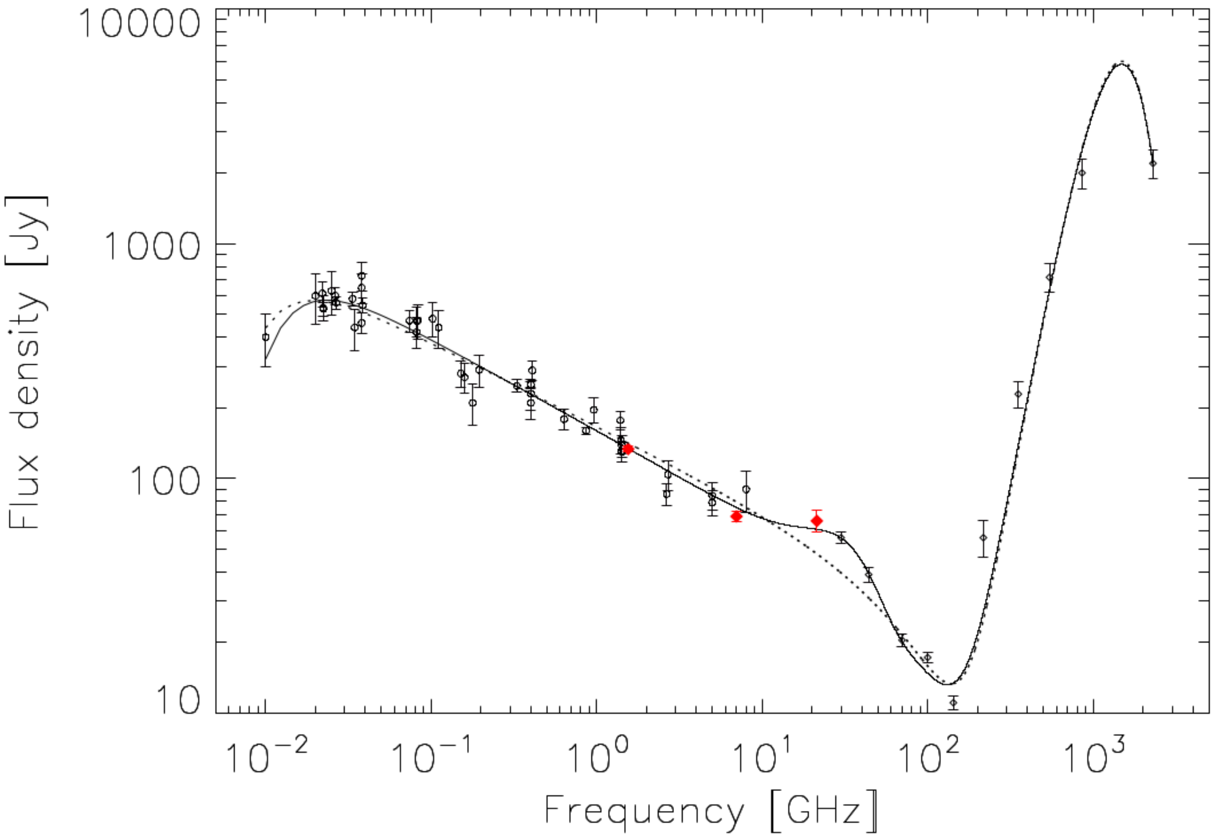

Figure 28: Spectral energy distribution of IC443 from 0.408 to 857 GHz. The solid and dashed lines represent the weighted least-square fit considering the spinning dust emission and without it, respectively (Loru et al. 2018).

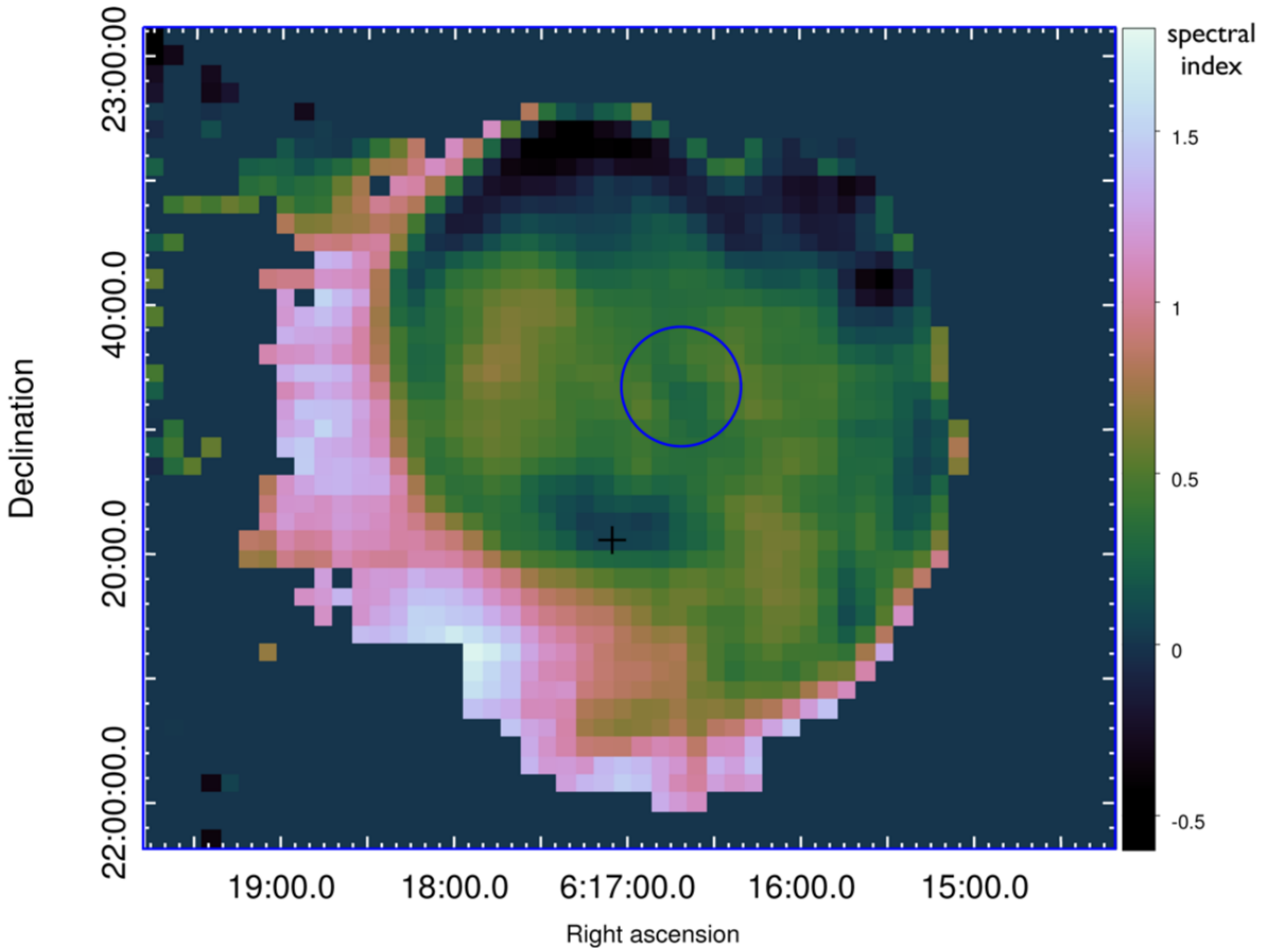

Figure 29: Spectral index map of IC443 obtained by using 1.55 and 7 GHz Sardinia Radio Telescope data. The black plus symbol indicates the position of the PWN, whereas the blue circle indicates the bulk of the gamma-ray emission seen with VERITAS and Fermi-LAT (Egron et al. 2017).

SKA will certainly represent a jump ahead in our understanding of SNRs, thanks to the great improvement in the quality of the data and possibly to a wider covered radio spectral range.

5 Nearby Galaxies

5.1 Dense gas in nearby galaxies

Viviana Casasola & Andrea Giannetti (INAF–Istituto di Radioastronomia Bologna, Italy)

Molecular lines play a crucial role in our understanding of star-formation activity and galaxy evolution. With molecular lines of different species and their different transitions, we can investigate the chemical composition of the interstellar medium (ISM) and derive its physical parameters, such as temperature, pressure, density, and non-collisional pumping. The creation and destruction of molecular species in the dense ($n_{\rm H_2} \gtrsim 10^5\,{\rm cm}^{-3}$) ISM, being strongly temperature- and density-dependent, can be used to investigate the physical processes taking place in molecular clouds such as large-scale shocks, and feedback from nascent stars, as well as the star formation process itself. Very detailed studies of the dense molecular gas are routinely carried out in the Milky Way (e.g., Kauffmann et al., 2017; Urquhart et al., 2018, 2019; Sabatini et al., 2019), but only in some nearby galaxies (e.g., Casasola et al., 2011; Combes et al., 2013; García-Burillo et al., 2014; Aladro et al., 2015; Costagliola et al., 2011, 2015; Meier et al., 2015; Jiang et al., 2017). The extragalactic studies on dense molecular gas are still mostly limited in terms of the size of their galaxy samples, always selected based on biased criteria such as Active Galactic Nucleus (AGN) and/or high IR luminosity (e.g., (Ultra-)Luminous IR Galaxies with $L_{\rm IR} > 10^{11-12}\ L_\odot$).

The frequency range and capabilities (e.g., sensitivity) of the SKA1 Band 6 receiver would offer the possibility to expand the extragalactic studies, both enlarging the samples and using molecular lines that are currently "forbidden" because of their weakness. This will permit to explore and characterize the dense gas in detail for different environments with respect to the Milky Way.

In particular, we propose to use the insight obtained in the field of star formation in the Milky Way to identify and put on a relative timeline star-forming regions in nearby galaxies similarly to what was done, for example, for ATLASGAL and HiGAL sources (e.g., Elia et al., 2017; Urquhart et al., 2018). Because it is not easy to understand the precise location of the spiral arms in our Galaxy, and, thus, if a star-forming source is associated with one of them or it is located between arms, repeating this kind of analysis in nearby galaxies would make it much easier to gauge the influence of spiral arms on the star formation activity, investigating if they trigger the collapse of the gas or only act as collectors of molecular material. In order to do this we need reliable tracers of physical conditions in the dense molecular clumps that constitute the progenitors of the next generation of clusters, that can be observed at a resolution similar to recent unbiased surveys of the Galactic disk, capable of identifying individual clumps. In the following, we present some examples of lines in the frequency ranges of 15–25 GHz and 25–50 GHz that can be used to trace the dense gas, and their scientific return in the context of nearby galaxies.

5.1.1 Formaldehyde - H_2CO

Formaldehyde (H_2CO) is an ubiquitous tracer of the moderately dense interstellar gas. The molecular structure of H_2CO makes it a good probe of both kinetic temperature ($T_{\rm kin}$) and density of the gas (e.g., Tang et al., 2018, and references therein). The observation of H_2CO lines provides, therefore, a powerful tool to understand the physical and chemical conditions of gas associated with starbursts. The 6-cm (4.8 GHz) $1_{11} - 1_{10}$ transition of H_2CO was one of the first molecular rotational transitions detected in the radio (Palmer et al., 1969). This line is always seen in absorption, even in dark clouds. This suggests that the molecule is absorbing the 2.7 K Cosmic Microwave Background radiation itself. Detections of the 6-cm absorption (and of that $2_{11} - 2_{12}$ at 2 cm) have also been made in external galaxies (e.g., NGC 253, Baan & Goss, 1992; Huettemeister et al., 1997). These observations provide evidence that H_2 is mostly in its para form, as expected from theoretical studies, and that these absorptions originate in regions of cores of moderate visual extinction ($A_{\rm V} \lesssim 0.5$ mag, Troscompt et al., 2009). These lines are interpreted as H_2CO megamasers. There are instead fewer observations of the rotational transitions of H_2CO at millimeter wavelengths.

Band 6 of SKA1 would offer the chance to observe two H_2CO transitions, the (3(1,2)–3(1,3)) and (4(1,3)–4(1,4)) at 29.0 and 48.3 GHz, respectively. This would allow us to determine the distribution and quantity of moderately dense gas, and to infer the ortho-to-para ratio of H_2, which gives an estimate of the cloud age (e.g., Brünken et al., 2014).

5.1.2 Ammonia - NH_3

Ammonia (NH_3) is the classical tracer of the kinetic temperature within the dense neutral ISM (e.g., Ho & Townes, 1983). It has numerous inversion transitions at centimeter wavelengths covering a large range of energies, meaning that NH_3 is able to probe a wide range of temperatures. While brightness temperatures of CO transitions are indicators of T_{kin} only for nearby dark clouds, where beam filling factors are close to unity, NH_3 multi-level studies can be used to determine T_{kin} even in cases where there is sub-structure smaller than the size of the beam. This is particularly useful for extragalactic studies. The most relevant NH_3 lines fall in the 1.2 cm band (~25 GHz). Relative calibration of these lines is typically good since they can be observed nearly simultaneously, under similar atmospheric conditions and with the same telescope in similar configuration. The first extragalactic detection of NH_3 was for IC 342 (Martin & Ho 1986), followed by those for other nearby galaxies (e.g., Henkel et al., 2000; Ott et al., 2005; Takano et al., 2005; Lebrón et al., 2011). Typical T_{kin} determined for the giant molecular clouds in the centers of observed nearby galaxies are 25 − 50 K. However, in some cases (e.g., IC 342) VLA NH_3 data have suggested a molecular component with T_{kin} as high as 700–900 K (Lebrón et al., 2011).

SKA1 Band 6 would allow us to observe many inversion transitions of NH_3 such as $(J, K) = (1, 1)$, (2, 2), (3, 3), (4, 4), (5, 5), (6, 6) at rest frequencies from 23.7 to 25.1 GHz. High-angular resolution maps of SKA1 would offer another way to characterize the small-scale spatial distribution of dense gas, and would allow us to use one of the most well-established ways to constrain T_{kin}, based on very extended Galactic studies, in different environments of nearby galaxies, thus investigating the feedback from forming stars on the parent cloud.

5.1.3 The cyanopolyynes - HC_3N and HC_5N

Bright emission of HC_3N is often observed in Galactic hot cores, i.e. warm and dense gas around massive young stars (e.g., de Vicente et al., 2000). Due to the small rotational constant (~1/13 of CO), there are many closely spaced rotational transitions of HC_3N (separated by 9.1 GHz), and its levels are very sensitive to changes in excitation (Meier & Turner, 2012). It's therefore easier to conduct multi-transition observations of HC_3N than of other dense molecular gas tracers, which can be used also to reliably determine the temperature of the emitting gas. In addition, HC_3N lines are very likely optically thin even in low-J transitions, due to the relatively low abundance (e.g., Lindberg et al., 2011). The condition of low opacity is fundamental to derive accurate estimates of dense molecular gas mass in studies on the relationship between dense molecular gas and star formation (e.g., Gao & Solomon, 2004; Wang et al., 2011; Zhang et al., 2014). High-frequency lines of HC_3N ((10–9) at 91.0 GHz and higher-J transitions) have been detected mainly in nearby AGN having faint HCO^+ emission (e.g., Costagliola et al., 2011). These conditions, consistent with models of hot cores (Bayet et al., 2008), could be signatures of embedded star formation, instead of AGN activity (Aalto et al., 2007). Vibrationally-excited lines from this molecule are also sensitive to the mid-IR radiation field and can be used to infer this quantity.

Similarly, HC_5N is a longer carbon chain molecule that can be used to trace the physical properties of the dense molecular gas. Observations and modeling show that also HC_5N can be formed in hot cores, and the relative abundance of the cyanopolyynes was proposed to be a chemical clock (Chapman et al., 2009). HC_5N has been observed towards Galactic cores of clouds (e.g., Rathborne et al., 2008) and tentatively (1–3σ level) detected for the first time outside the Milky Way, in NGC 253, for the transitions (33–31), (37–36), and (38–37) at 87.8, 98.5, and 101.2 GHz, respectively (Aladro et al., 2015).

SKA1 Band 6 would allow to observe multiple low-J emission lines of HC_3N ((2–1), (3–2), (4–3), and (5–4) at 18.2, 27.3, 36.4, and 45.5, respectively) and 13 emission lines of HC_5N (from the (6–5) at 16.0 GHz to the (18–17) at 47.9 GHz). The possibility to simultaneously observe several transitions of these two molecules and their sensitivity to excitation make them ideal thermometers for the dense, warm gas associated with star formation. In addition, being abundant in hot cores, they have the potential of tracing the embedded, current star formation activity in external galaxies.

5.1.4 The sulfur-bearing molecules SO and SO_2

Molecules with sulfur account for about 10% of the species identified in the interstellar gas and circumstellar envelopes. Sulfur-bearing molecules are considered to be an important tool for studying the presence of shocks within massive star-forming regions. Because of the relatively fast evolution of their chemistry, on time scale of tens of thousand years, S-bearing molecules are good candidates to be chemical clocks to study the evolution of outflows (e.g., Bachiller et al., 2001) and hot cores (e.g., Hatchell et al., 1998). The most prominent S-bearing molecule is sulfur dioxide (SO_2), which has been observed in many astronomical sources: hot cores in giant molecular clouds and low-mass young stellar objects (e.g., Schilke et al., 2001; Caux et al., 2011), circumstellar shells of late-type stars (e.g., Tenenbaum et al., 2010), cold dense molecular clouds (e.g., Turner, 1995), and external galaxies (e.g., NGC 253, Martín et al., 2003, 2005). Despite the high density of spectral lines and wide range of astronomical sources in which it is found, the formation of SO_2 in space and the chemistry of other prominent S-bearing molecules in the dense molecular gas such as the sulfur monoxide (SO) is not well understood (e.g., Wakelam et al., 2004).

SKA1 Band 6 would allow to search three SO_2 transitions (5(2,4)–6(1,5), 8(2,6)–9(1,9), and 4(0,4)–3(1,3) at 23.4, 24.1, and 29.3 GHz, respectively) and two SO lines (1_0–0_1 and 2_3–2_2 at 30.0 and 36.2 GHz, respectively). These observations could be used to define a relative timeline for extragalactic star-forming regions, especially in conjunction with the information coming from the previously-mentioned tracers that are able to probe the physical properties of the molecular gas. In fact, S-bearing molecules are effective tracers of active star formation activity, and the gas temperature is seen to increase with evolution in galactic regions. (e.g., König et al., 2017; Giannetti et al., 2017; Urquhart et al., 2018). One could therefore repeat this kind of approach for molecular fragments in external galaxies, exploiting the sensitivity and angular resolution of SKA.

References

Aalto, S., Monje, R., & Martín, S. 2007, A&A, 475, 479
Aladro, R., Martín, S., Riquelme, D., et al. 2015, A&A, 579, A101
Baan, W. A., & Goss, W. M. 1992, ApJ, 385, 188
Bachiller, R., Pérez Gutiérrez, M., Kumar, M. S. N., & Tafalla, M. 2001, A&A, 372, 899
Brünken, S., Sipilä, O., Chambers, E. T., et al. 2014, Nature, 516, 219
Bayet, E., Viti, S., Williams, D. A., & Rawlings, J. M. C. 2008, ApJ, 676, 978
Casasola, V., Hunt, L. K., Combes, F., García-Burillo, S., & Neri, R. 2011, A&A, 527, A92
Caux, E., Kahane, C., Castets, A., et al. 2011, A&A, 532, A23
Chapman, J. F., Millar, T. J., Wardle, M., Burton, M. G., & Walsh, A. J. 2009, MNRAS, 394, 221
Combes, F., García-Burillo, S., Casasola, V., et al. 2013, A&A, 558, A124
Costagliola, F., Aalto, S., Rodriguez, M. I., et al. 2011, A&A, 528, A30
Costagliola, F., Sakamoto, K., Muller, S., et al. 2015, A&A, 582, A91
de Vicente, P., Martín-Pintado, J., Neri, R., & Colom, P. 2000, A&A, 361, 1058
Elia, D., Molinari, S., Schisano, E., et al. 2017, MNRAS, 471, 100
Gao, Y., & Solomon, P. M. 2004, ApJ, 606, 271
García-Burillo, S., Combes, F., Usero, A., et al. 2014, A&A, 567, A125
Giannetti, A., Leurini, S., Wyrowski, F., et al. 2017, A&A, 603, A33
Hatchell, J., Thompson, M. A., Millar, T. J., & MacDonald, G. H. 1998, A&A, 338, 713
Henkel, C., Mauersberger, R., Peck, A. B., Falcke, H., & Hagiwara, Y. 2000, A&A, 361, L45
Ho, P. T. P., & Townes, C. H. 1983, ARA&A, 21, 239
Huettemeister, S., Mauersberger, R., & Henkel, C. 1997, A&A, 326, 59
Jiang, X.-J., Wang, J.-Z., Gao, Y., & Gu, Q.-S. 2017, A&A, 600, A15
Kauffmann, J., Goldsmith, P. F., Melnick, G., et al. 2017, A&A, 605, L5
König, C., Urquhart, J. S., Csengeri, T., et al. 2017, A&A, 599, A139
Lebrón, M., Mangum, J. G., Mauersberger, R., et al. 2011, A&A, 534, A56
Lindberg, J. E., Aalto, S., Costagliola, F., et al. 2011, A&A, 527, A150
Martín, S., Mauersberger, R., Martín-Pintado, J., García-Burillo, S., & Henkel, C. 2003, A&A, 411, L465
Martín, S., Martín-Pintado, J., Mauersberger, R., Henkel, C., & García-Burillo, S. 2005, ApJ, 620, 210
Meier, D. S., & Turner, J. L. 2012, ApJ, 755, 104
Meier, D. S., Walter, F., Bolatto, A. D., et al. 2015, ApJ, 801, 63
Ott, J., Weiss, A., Henkel, C., & Walter, F. 2005, ApJ, 629, 767
Palmer, P., Zuckerman, B., Buhl, D., & Snyder, L. E. 1969, ApJ, 156, L147
Rathborne, J. M., Lada, C. J., Muench, A. A., Alves, J. F., & Lombardi, M. 2008, ApJS, 174, 396
Sabatini, G., Giannetti, A., Bovino, S., et al. 2019, MNRAS,
Schilke, P., Benford, D. J., Hunter, T. R., Lis, D. C., & Phillips, T. G. 2001, ApJS, 132, 281
Takano, S., Hofner, P., Winnewisser, G., Nakai, N., & Kawaguchi, K. 2005, PASJ, 57, 549
Tang, X. D., Henkel, C., Menten, K. M., et al. 2018, A&A, 609, A16
Tenenbaum, E. D., Dodd, J. L., Milam, S. N., Woolf, N. J., & Ziurys, L. M. 2010, ApJ, 720, L102
Troscompt, N., Faure, A., Maret, S., et al. 2009, A&A, 506, 1243
Turner, B. E. 1995, ApJ, 455, 556
Urquhart, J. S., König, C., Giannetti, A., et al. 2018, MNRAS, 473, 1059
Urquhart, J. S., Figura, C., Wyrowski, F., et al. 2019, MNRAS, 484, 4444
Wakelam, V., Castets, A., Ceccarelli, C., et al. 2004, A&A, 413, 609
Wang, J., Zhang, Z., & Shi, Y. 2011, MNRAS, 416, L21
Zhang, Z.-Y., Gao, Y., Henkel, C., et al. 2014, ApJ, 784, L31

5.2 Radio Continuum Resolved Studies of Nearby Galaxies with the SKA

A. Alberdi, M.A. Perez-Torres (IAA-CSIC)
R. Beswick, T.W.B.Muxlow (JBO, Univ. Manchester, UK)

5.2.1 Introduction

Star Formation and accretion are two dominant processes that shape galaxies and their evolution. Only in the local Universe, it is possible to resolve and investigate these processes on linear scales matching these physical processes across a representative sample of physical environments and galaxy types (galaxy mass, evolutionary stage, spectral type, black hole mass) (Beswick et al., 2015; Murphy et al., 2018b). The SKA, via high angular resolution observations of large samples of galaxies, and being sensitive to both the compact constituents of the galaxies and the faint diffuse radio emission, will revolutionise our understanding of the interplay between star-formation and accretion, and will provide a local universe benchmark for the evolution of these processes at all redshifts.

5.2.2 Scientific Objectives

The observations of nearby galaxies with SKA1 in bands 1-2 and, especially, at the highest frequencies covered by Band 5/5+ will enable us to resolve individual nearby galaxies in their main constituents: AGN, or a LLAGN, at the heart of the galaxy, depending on the efficiency of the accretion processes; young stellar products (HII regions, stellar clusters, superstellar clusters, stellar jets); end-stellar products (Planetary Nebulae, Radio supernovae, Supernova Remnants); stellar accretion products (microquasars; GRBs; Intermediate mass Black Holes). The identification of the nature of any of the components will be feasible thanks to the morphological and spectral information (see Fig. 30, with a high resolution radio view of the heart of the starburst galaxy M82, with over 100 compact sources). In any case, an angular resolution better than 0.25 arcsec is necessary. Moreover, the high angular resolution radio observations at high frequencies will provide the first extinction-free census of stellar products within nearby galaxies (Murphy et al., 2018).

Continuum observations with SKA1 in the frequency range 13.8–24 GHz, beyond the current band 5b frequency range, would be specially sensitive for this kind of studies. The extension of the frequency range up to 24 GHz and beyond would allow us to probe supernova, microquasar and GRB activity in their early phases, since the synchrotron emission becomes transparent first at these high frequencies. The ability to observe supernovae at a very early stage is particularly relevant for stripped-envelope supernovae, for which the radio emission timescale is very short. This will provide insight into their mass loss history even during the phase immediately preceding their explosion. By combining this information with the later radio emission (at Band 5+ and lower frequencies), detailed light curves of supernovae will be obtained.

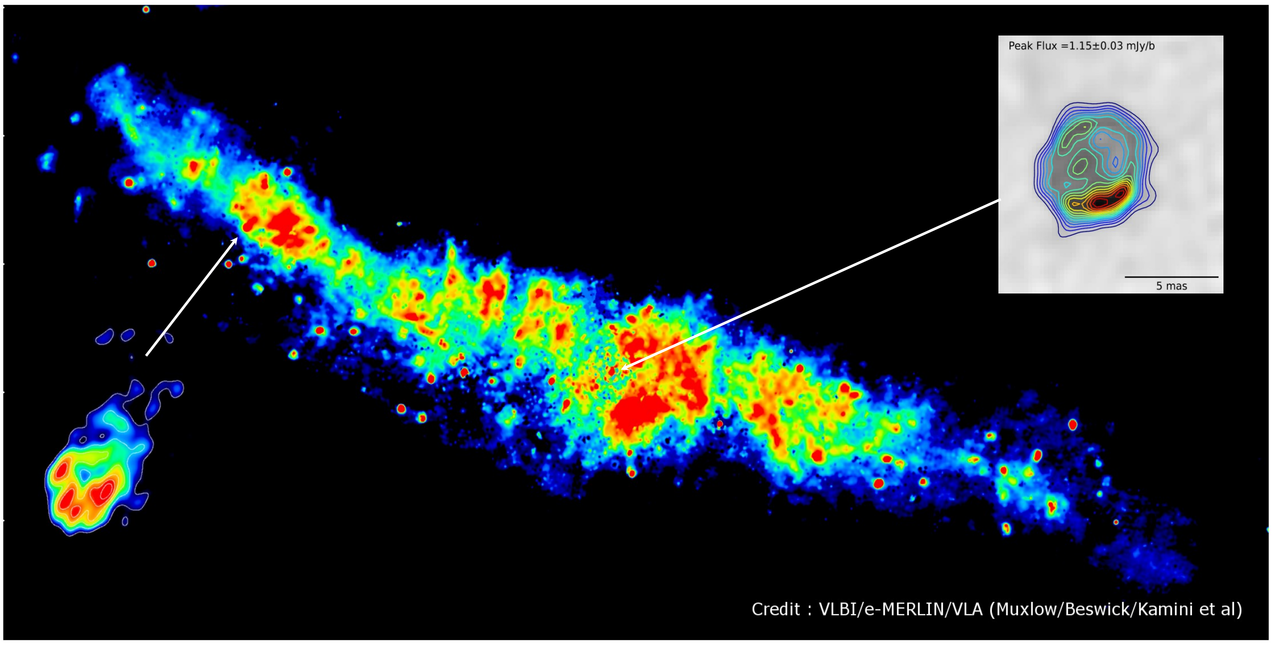

Figure 30: ***A high resolution radio view of the heart of the starburst galaxy M82. By imaging over 100 individual supernovae, supernovae remnants and H*II *regions individually resolved by e-MERLIN, VLBI and the VLA provide new insights into the physics of starformation in local galaxies.***

The extended frequency coverage of Band 5+ would also result in an improved angular resolution of the SKA1-MID array. At 24 GHz, SKA1 will attain an angular resolution better than 200 mas. With Band 5+, this angular resolution will be even better. This will allow us to unambiguously resolve compact sources within galaxies, and disentangle AGN and starburst regions in LIRGs and ULIRGs out to large distances in the universe, a capability currently only afforded by very deep VLBI observations.

At this frequency and resolution, targeted observations of a sample of (U)LIRGs will ensure the detection of the AGN, as well of most supernovae, supernova remnants, and microquasars, permitting an essentially complete census of such sources in the nearby Universe. VLBI observations of Arp299A (Pérez-Torres et al., 2009; Bondi et al., 2012) and of Arp220 (Varenius et al., 2019) have unveiled prolific SN factories in the central 200 pc of their galaxy nuclei. Finally, thanks to the extended spectral coverage of Band 5+, we will be able to obtain useful spectral information for the population of individual star formation products in nearby galaxies.

Moreover, since (U)LIRGs show enhanced star-formation, there should be a large number of massive stars that end their lives as radio supernovae. As a result, the Core-Collapse Supernova Rates should be a couple of orders of magnitude higher that in normal galaxies. Multi-epoch high angular resolution observations will permit to pinpoint the radio Supernovae and measure the core-collapse supernova rate (CCSNR), providing an additional and independent measurement of the Star Formation Rate (SFR). It should be considered that -since the ISM conditions in merger-driven, compact starbursts and in extended, high-luminosity high-z star-forming disks are very different- the IMF could also differ and the relation between the SFR and the CCSNR would need to be carefully calibrated.

Additional scientific results include (Prandoni et al., 2015): i) the characterization of the diffuse versus the compact component emission; ii) the calibration of the radio continuum as a tracer for high-z SFR measurements; iii) the study of the interplay between the accretion and start formation process, in the form of feedback; iv) the understanding of the nature of Radio Quiet AGNs; v) the understanding of the star formation processes at high redshifts. Intermediate redshift ($0.1 < z < 0.3$) and local (U)LIRGs are considered to be nearby versions of high-z star-forming galaxies. Moreover, we already know that at higher redshifts, a significant fraction of the Star Formation in the Universe is happening in LIRGs (z=1) and ULIRGs (z=2). In that sense, ULIRGs can be potentially considered as templates for the understanding of the star-forming galaxies at high redshift. In any case, this should be checked since high-z and low-z star-forming galaxies are different in many respects like the compactness of the star-forming regions or the depletion times.

5.2.3 Prospects for SKA1 beyond band 5

Multi-frequency (Band 1-2 and Band 5/ 5+), sub-arcsecond angular resolution, targeted observations of a well-defined sample of (at least) 100 local galaxies, up to distances of 100 Mpc in order to comply a good linear resolution. The sample will include every galaxy type (dwarfs to more massive), environment (from isolated to merging systems) and evolutionary stage (from early type to late type ones. The sample should be selected favouring the synergies with available and future optical/NIR/mm/radio surveys: GOALS, THINGS (HI, VLA), KINGFISH (FIR, Herschel), LeMMINGs (e-MERLIN/VLA), LIRGI (e-MERLIN/EVN), HERACLES (CO, IRAM PV), SINGS/S4G (Spitzer), MAD/MAGNUM (MUSE, VLT).

The critical observational parameters for our science objectives are the following:

- Observing Frequency: Both SKA Bands 1-2 and 5 are required. The implementation of Band 5+ will permit us to detect the thermal emission and provide the angular resolution (better than 0.25 arcsec) necessary to pinpoint compact radio sources, discriminating between radio core candidates and stellar end-products;

- Angular Resolution: an angular resolution better that 0.25 arcsec is needed to discern AGN from Starburst activity and to decompose the galaxies into their constituents. An angular resolution of 0.5 arcsec corresponds to linear scales of 250 pc at a distance of 100 Mpc;

- Dynamic Range: High dynamic range is required to minimize the effects of the enhanced noise around the brightest sources. Accurate sky models are required.

- Spectral Index Information: the determination of the in-band spectral information at bands 1-2 and 5 (with around 4 sub-bands) will be key to address the nature of the emitting sources.

References

Beswick, R., Brinks, E., Perez-Torres, M., Richards, A. M. S., Aalto, S., Alberdi, A., Argo, M. K., van Bemmel, I., Conway, J. E., Dickinson, C., Fenech, D., Gray, M. D., Kloeckner, H. R., Murphy, E., Muxlow, T. W. B., Peel, M. W., Rushton, A., Schinnerer, E., 2015,Proceedings of Advancing Astrophysics with the Square Kilometre Array (AASKA14)

Bondi, M., Prez-Torres, M. A., Herrero-Illana, R., Alberdi, A., 2012, A&A, 539, 134

Murphy, E. J., Dong, D., Momjian, E., Linden, S., Kennicutt, R. C., Jr., Meier, D. S., Schinnerer, E., Turner, J. L. 2018, ApJS, 234, 24

Murphy, E. J., Condon, J. J., Alberdi, A., Barcos-Muoz, L., Beswick, R. J., Brinks, E., Dong, D., Evans, A. S., Johnson, K. E., Kennicutt, R. C., Jr., Linden, S. T., Muxlow, T. W. B., Prez-Torres, M., Schinnerer, E., Sargent, M. T., Tabatabaei, F. S., Turner, J. L. 2018b, Science with a Next Generation Very Large Array, ASP Conference Series, Vol. 517

Pérez-Torres, M. A., Romero-Cañizales, C., Alberdi, A., et al. 2009, A&A, 507, L17

Prandoni, I. & Seymour, N. 2015,Proceedings of Advancing Astrophysics with the Square Kilometre Array (AASKA14)

Varenius, E., Conway, J. E., Batejat, F., et al. 2019, A&A, 623, A173

5.3 Extra-galactic masers in the nearby Universe

Jacco Th. van Loon (Keele University)
Andrea Tarchi (INAF-Osservatorio Astronomico di Cagliari)
Paola Castangia (INAF-Osservatorio Astronomico di Cagliari)

Masing molecular transitions are powerful probes of physical conditions. Firstly, the line emission is amplified (by stimulated radiative de-excitation of energy levels pumped by photons or collisions) and beamed, and can thus exceed thermal emission (from spontaneous radiative de-excitations) by orders of magnitude. Secondly, maser spectral lines become narrower than the thermal width which allows very detailed kinematic information to be recorded. Thirdly, the masing conditions are very specific, and different masers can be used to probe different regions in the gas and different evolutionary phases of the object under study.

Many molecular transitions can mase, but we here limit ourselves to the more ubiquitous examples that are going to be of primary interest for extra-galactic studies. This Chapter furthermore concerns itself with "stellar" and "interstellar" masers, as opposed to the mega-masers associated with active galactic nuclei that are discussed in another Chapter of this book. There are two main reasons for studying masers in galaxies outside the Milky Way: to obtain galaxy-wide views and to probe environments not found in the Milky Way. For instance, the nearby Large and Small Magellanic Clouds at distances of $d \approx 50$ kpc (LMC) and ≈ 60 kpc (SMC) have interstellar metallicities of ≈ 0.5 and ≈ 0.2 solar.

5.3.1 Setting the stage: masers at < 15 GHz in nearby galaxies

Hydroxyl Hydroxyl (OH) masers are often detected in the outflows from luminous, cool evolved stars: red supergiants or Asymptotic Giant Branch (AGB) stars. These outflows are dusty, making their spectral energy distributions peak at infrared (IR) wavelengths. Hence they are called 'OH/IR stars'. Their mass loss and dust production determine their fate and contribute to the interstellar dust and chemical evolution of galaxies. Unfortunately, both are poorly understood.

The 1612-MHz masers in OH/IR stars form in the outer parts of the outflow, where they are radially beamed and thus measure the wind speed. This is the only available direct test of the radiation driving mechanism, if measured for sources comprising a range in – well known – luminosity and metallicity. Main-line 1665-MHz masers probe deeper layers that have not reached the terminal wind speed, and these masers are much harder to interpret. In the LMC, fourteen OH/IR stars are known (Wood et al., 1992; Goldman et al., 2017, and references therein) including a couple of main-line detections. The main difficulty with detecting these masers is their asymmetry: of the stereotypical double-horned 1612-MHz profile, one peak can be an order of magnitude fainter. Obviously this hampers stellar wind speed measurements. Also, 1612-MHz masers typically vary in brightness by up to a factor two; main-line masers can vary much more dramatically also in the shape and polarisation of the emission profile. Despite deep searches, OH/IR stars have not yet been detected in the SMC (Goldman et al., 2018).

Hydroxyl masers have also been detected in the LMC in star-forming regions (especially the main lines, see Brooks & Whiteoak, 1997, and references therein) and in shocks associated with supernova remnants (at 1720 MHz: Brogan et al., 2004; Roberts & Yusef-Zadeh, 2005), as well as in star-forming regions in M 33, at 0.9 Mpc (Koch et al., 2018). Excited hydroxyl masers have been detected in the LMC at 6 GHz (Caswell, 1995; Green et al., 2008). Further afield, 1667- and 1665-MHz OH masers have also been detected in nearby starburst galaxies with luminosities intermediate between those of the Galactic sources and those (labeled OH mega-masers) found in Ultraluminous InfraRed Galaxies, ULIRGs; for the cases of two prototypical starbursts, M 82 and NGC 253, see, e.g., Argo et al. (2010) and Frayer, Seaquist & Frail (1998).

Methanol Methanol (CH_3OH) is a precursor for the synthesis of complex organic molecules including pre-biotically relevant species. Its masers at 6.7 and 12.2 GHz act as beacons of massive proto-stars, with the 12.2-GHz maser appearing in more advanced stages of development. While not as widespread because of the reduced metallicity, both transitions have been detected in the LMC, including some 6.7 GHz masers peaking at a few Jy (Sinclair et al., 1992; Ellingsen et al., 2010, and references therein). The detection of 6.7-GHz methanol maser emission was reported also in the disc of M 31, at 0.8 Mpc (Sjouwerman et al., 2010). No detection of any of the aforementioned methanol maser transitions has been reported, so far, in galaxies outside the Local Group.

5.3.2 Masers around 22 GHz

Water masers around evolved stars The 22-GHz water (H_2O) masers arising in the outflows from evolved stars probe the wind acceleration zone where they are radially beamed. Comparison to the 1612 MHz hydroxyl profile shows how efficient the acceleration is – the two water masers associated with the most extreme OH/IR stars in the LMC suggest this may be reduced at sub-solar metallicity (van Loon et al., 2001). These water masers often also have a tangentially beamed peak centred at the stellar velocity. This helps interpret the hydroxyl maser profile, especially at low fidelity – a famous example being the most luminous red supergiant in the LMC, WOH G64, where the water detection led to a large upward revision of its wind speed measurement (van Loon et al., 1998; Marshall et al., 2004).

Typically $F_{22} \sim 100(d/50\,\mathrm{kpc})^{-2}$ mJy for the brightest OH/IR stars in a population; three are known in the LMC (van Loon et al., 2001; Imai et al., 2013). The estimated SKA1 line sensitivity at 22 GHz is 1 mJy per 0.1 km s^{-1} channel in 1 hour integration. This should allow to detect not only all known OH/IR stars in the LMC, but also some of the expected new OH discoveries with SKA1. It also should result in the detection of a few OH/IR stars in the SMC, taking into account that the maser photon flux is expected to scale with the IR flux (which scales with metallicity as well as distance). This would add another dimension to testing radiation-driven wind theory, above and beyond that facilitated by OH maser measurements alone.

Water masers in star forming regions Water is the main constituent of ice mantles that grow around grains in molecular clouds; it returns to the gas phase when these mantles evaporate. Water vapour can also form in shocks. Water masers in proto-stellar environments can be two orders of magnitude brighter than those around evolved stars (Whiteoak & Gardner, 1986; Imai et al., 2013, and references therein), simply because there is much more gas available. In the LMC, the brightest water masers are more than an order of magnitude brighter than the brightest water masers associated with OH/IR stars.

Mini-surveys of star-forming regions in the LMC (Lazendić et al., 2002; Oliveira et al., 2006) have identified LHA-120 N113 as the most fertile ground of maser studies – this is also were proto-stellar outflows (Ward et al., 2016) and complex organic molecules (Sewiło et al., 2018) have been found. Water masers around proto-stars are highly variable, which makes them difficult to use as a quantitative measure of anything, but their presence and kinematics are significant. Water masers have also been detected in the SMC (Breen et al., 2013) and in M 33 (Huchtmeier, Eckart & Zensus, 1988; Greenhill et al., 1990).

Indeed, until recently, water masers in Local Group galaxies were found only in M 33 (3 sources), IC 10 (2 sources), the LMC (30 sources) and the SMC (6 sources); see Henkel et al. (2018) and references therein. Among the possible causes for this low detection rate is the difficulty to map the entire body of nearby galaxies (in particular true for the Magellanic Clouds and M 31) as well as the limited sensitivity of the surveys. Only at the end of 2010 were the first detections made of five maser sources in M 31, with the Green Bank Telescope (Darling, 2011). Water maser detections in the Local Group are particularly relevant since subsequent Very Long Baseline Interferometry could be used to derive the proper motions of the host galaxies, and thus the dark matter content of the Local Group and the eventual collision between M 31 and the Milky Way (e.g., Greenhill et al., 1993; Brunthaler et al., 2005, 2007).

In nearby galaxies outside the Local Group, water maser emission associated with star formation activity has been found in starburst galaxies like NGC 253 (Henkel et al., 2004), M 82 (Baudry & Brouillet, 1996) and NGC 3256 (Surcis et al., 2009). The high star-formation rates and physical conditions (high densities, large molecular reservoirs, shocks, et cetera) in these galaxies are conducive to maser action, producing extremely bright maser sources, often labeled “kilo-masers”, with luminosities of up to a few solar luminosities (Tarchi et al., 2011).

Ammonia Ammonia (NH_3) signals early embedded stages of proto-stellar evolution and can be used as a thermometre. Despite the reduced nitrogen content, thermal emission from ammonia at 23.7 GHz was detected in the LMC (Ott et al., 2010). Ammonia masers are found in various transitions in a broad frequency range around 21 GHz (Walsh et al., 2007). The first extra-galactic detection has yet to be made.

Prospects for SKA1 at 22 GHz While blind OH surveys of the entire Magellanic Clouds, for example, are becoming possible with interferometres equipped with focal plane arrays such as the Australian SKA Pathfinder, such surveys are not possible at 22 GHz. Targetted searches are necessarily biased, and inefficient – to detect water masers around evolved stars typically requires at least a full 12-hour track on target.

The field-of-view of an SKA1 operating at 22 GHz would be a few arcminutes, which would speed up surveying star-forming regions but not make much of a difference when observing known OH/IR stars that are few and far between; the sensitivity, on the other hand, would dramatically reduce the amount of time needed for a systematic study. The improvement becomes even more remarkable when targetting star-forming complexes in M 33 or other star-forming galaxies in the Local Group such as the isolated metal-poor dwarves NGC 6822 (0.2 solar, $d = 0.5$ Mpc) or Sextans A (0.1 solar, $d = 1.3$ Mpc). Ammonia should also become more readily available as a probe of proto-stellar physics in the metal-poor LMC and SMC.

Following (Brunthaler et al., 2006) (their Eq. 2), by using the luminosity function of water masers in our Galaxy empirically derived by Greenhill et al. (1990), and accounting for the different star formation rate (SFR) of a target galaxy compared to that of the Milky Way (assumed to be 4 $M_\odot$ yr^{-1}; Diehl et al., 2006), the expected number of masers can be computed for any maser luminosity detection threshold. The latter can be obtained from the 3-σ r.m.s. noise level of the survey, the linewidth and the distance to the target galaxy. Adopting a typical sensitivity for water maser surveys in extended objects of 30 mJy (3-σ r.m.s.) for a 1-km s^{-1} wide channel, the expected number of maser sources in, e.g., NGC 6822 ($d \sim 0.49$ Mpc and SFR ~ 0.06 $M_\odot$ yr^{-1}; Mateo, 1998), M 33 ($d \sim 0.84$ Mpc and SFR ~ 0.33 $M_\odot$ yr^{-1}; Hippelein et al., 2003), and NGC 253 ($d \sim 3.4$ Mpc and SFR ~ 4.9 $M_\odot$ yr^{-1}; Rampadarath et al., 2014) would be $\sim$ 1, 2 and 5, respectively. Typically, the surveys performed so far targetted a number of regions within the galaxy, selected according to criteria aimed at maximising the chances of finding water maser emission in these regions. The total integration time spent in these searches has been of the order of a few tens of hours, yielding average on-source time of 10 minutes per pointing (see, e.g., Brunthaler et al., 2006, for a Very Large Array search in M 33 and NGC 6822).

Taking profit of the predicted enhanced sensitivity of the SKA1-MID array (133 antennæ) for spectral line observations, in 10 minutes a 3-σ r.m.s. noise level of 5 mJy for a 1-km s^{-1} channel can be reached. This would increase the number of detectable masers computed using the relation described above by a factor of five. This increase would be even more remarkable when also considering the reduction in the observing time necessary to perform fully-sampled spectral-line maps covering the full (optical) extension of the galaxies due to the larger SKA1 field-of-view. Recently, Tarchi et al. (2019) reported a search for water maser emission, made with the Sardinia Radio Telescope, covering the whole optical size of three Local Group irregular dwarf galaxies. Aside from a few weak tentative features, it yielded no confident maser detections. Indeed, the authors concluded that significantly deeper maps, made possible by the SKA1, are essential to detect new maser sources in Local Group members, and especially in galaxies with modest star formation rate and/or low metallicity.

Notably, in order to fully exploit the potential of any new maser detection, in terms of proper motion and kinematical studies, follow-up observations at high angular resolution are required. Therefore, the use of the SKA1-MID array in conjuction with existing Very Long Baseline Interferometry networks of antennæ is recommended.

5.3.3 Beyond 25 GHz

Methanol Methanol also has transitions at 36 and 44 GHz. While, as mentioned in Sect. 5.3.1, the search in galaxies beyond the Local Group for 6.7-GHz methanol masers (the so-called Class II masers) much more luminous than those found in the Galaxy has been, so far, unsuccessful, the 36/44-GHz Class I methanol masers turned out to be more promising. Indeed, such luminous methanol masers have been detected in two nearby starburst galaxies, NGC 253 and NGC 4945 (Ellingsen et al., 2017; McCarthy et al., 2017). Recently, bright 36-GHz methanol lines, possibly related to masing gas, have also been observed in other nearby galaxies, such as IC 342 and Maffei 2 (Gorski et al., 2018; Humire et al., 2019).

One advantage of these high-frequency transitions is the increased angular resolution, $< 0\farcs03$ corresponding to $\sim$ 1000 au at the distance of the LMC or $\sim$ 0.1 pc at the distance of M 33. These are typically scales encountered in and around proto-stellar objects.

Silicon monoxide Silicon monoxide (SiO) masers are found both in the dust-free inner zone of the winds from OH/IR stars and around proto-stars. They probe unique regions and conditions in these objects, and their high frequency ($\geq$ 43 GHz) means high angular resolution (but low survey speed).

There has been only one convincing extra-galactic detection, in the LMC from the red supergiant WOH G64 at 86 GHz (van Loon et al., 1996). The 43 GHz transition should be of similar strength. The sensitivity of a high-frequency SKA1 would be expected to be less than twice as poor at 43 GHz compared to 22 GHz. So more known OH/IR stars in the LMC would be expected to be detected, and a mini survey of the Tarantula Nebula or N 113 star-forming regions in the LMC would become interesting.

If we for a moment consider globular clusters also to be extra-galactic systems, silicon monoxide (or water) masers may be detected around their most evolved red giants – for instance in 47 Tucanæ or ω Centauri. CO has been detected in the former (McDonald et al., 2018) but low limits have been set on any hydroxyl emission from globular clusters (van Loon et al., 2006).

References

Argo, M. K., Pedlar, A., Beswick, R. J., Muxlow, T. W. B., & Fenech, D., 2010, MNRAS, 402, 2703
Baudry, A., & Brouillet, N., 1996, A&A, 316, 188
Breen, S. L., Lovell, J. E. J., Ellingsen, S. P., Horiuchi, S., Beasley, A. J., & Marvel, K., 2013, MNRAS, 432, 1382
Brogan, C. L., Goss, W. M., Lazendić, J. S., & Green, A. J., 2004, AJ, 128, 700
Brooks, K. J., & Whiteoak, J. B., 1997, MNRAS, 291, 395
Brunthaler, A., Reid, M. J., Falcke, H., Greenhill, L. J., & Henkel, C., 2005, Science, 307, 1440
Brunthaler, A., et al., 2006, A&A, 457, 109
Brunthaler, A., Reid, M. J., Falcke, H., Henkel, C., & Menten, K. M., 2007, A&A, 462, 101
Caswell, J. L., 1995, MNRAS, 272, L31
Darling, J., 2011, ApJ, 732, L2
Diehl, R., et al., 2006, Nature, 439, 45
Ellingsen, S. P., Breen, S. L., Caswell, J. L., Quinn, L. J., & Fuller, G. A., 2010, MNRAS, 404, 779
Ellingsen, S. P., Chen, X., Breen, S. L., & Qiao, H.-H., 2017, MNRAS, 472, 604
Frayer, D. T., Seaquist, E. R., & Frail, D. A., 1998, AJ, 115, 559
Goldman, S. R., et al. 2017, MNRAS, 465, 403
Goldman, S. R., et al. 2018, MNRAS, 473, 3835
Gorski, M., et al., 2018, ApJ, 856, 134
Green, J. A., et al. 2008, MNRAS, 385, 948
Greenhill, L. J., Moran, J. M., Reid, M. J., Gwinn, C. R., Menten, K. M., Eckart, A., & Hirabayashi, H., 1990, ApJ, 364, 513
Greenhill, L. J., Moran, J. M., Reid, M. J., Menten, K. M., & Hirabayashi, H., 1993, ApJ, 406, 482
Henkel, C., Tarchi, A., Menten, K. M., & Peck, A. B., 2004, A&A, 414, 117
Henkel, C., Greene, J.-E., & Kamali, F., 2018, IAUS, 336, 69
Hippelein, H., et al., 2003, A&A, 407, 137
Huchtmeier, W. K., Eckart, A., & Zensus, A. J., 1988, A&A, 200, 26
Humire, P., et al., 2019, A&A, accepted (arXiv:1911.06776)
Imai, H., Katayama, Y., Ellingsen, S. P., & Hagiwara, Y., 2013, MNRAS, 432, L16
Koch, E., Rosolowsky, E., Johnson, M. C., Kepley, A. A., & Leroy, A., 2018, RNAAS, 2, 24
Lazendić, J. S., Whiteoak, J. B., Klamer, I., Harbison, P. D., & Kuiper, T. B. H., 2002, MNRAS, 331, 969
Mateo, M., 1998, ARA&A, 36, 435
Marshall, J. R., van Loon, J. Th., Matsuura, M., Wood, P. R., Zijlstra, A. A., & Whitelock, P. A., 2004, MNRAS, 355, 1348
McCarthy, T. P., et al., 2017, ApJ, 846, 156
McDonald, I., Boyer, M. L., Groenewegen, M. A. T., Lagadec, E., Richards, A. M. S., Sloan, G. C., & Zijlstra, A. A., 2018, MNRAS, 484, L85
Oliveira, J. M., van Loon, J. Th., Stanimirović, S., & Zijlstra, A. A., 2006, MNRAS, 372, 1509
Ott, J., Henkel, C., Staveley-Smith, L., & Weiß, A., 2010, ApJ, 710, 105
Rampadarath, H., Morgan, J. S., Lenc, E., & Tingay, S. J., 2014, AJ, 147, 5
Roberts, D. A., & Yusef-Zadeh, F., 2005, AJ, 129, 805
Sewiło, M., et al. 2018, ApJ, 853, L19
Sinclair, M. W., Carrad, G. J., Caswell, J. L., Norris, R. P., & Whiteoak, J. B., 1992, MNRAS, 256, P33
Sjouwerman, L. O., Murray, C. E., Pihlström, Y. M., Fish, V. L., & Araya, E. D., 2010, ApJ, 724, L158
Surcis, G., Tarchi, A., Henkel, C., Ott, J., Lovell, J., & Castangia, P., 2009, A&A, 502, 529
Tarchi, A., Henkel, C., Peck, A. B., & Menten, K. M, 2002, A&A, 389, L39
Tarchi, A., Castangia, P., Henkel, C., Surcis, G., & Menten, K. M., 2011, A&A, 525, A91
Tarchi, A., Castangia, P., Surcis, G., et al., 2019, MNRAS, accepted (arXiv:1912.02454)
van Loon, J. Th., Zijlstra, A. A., Bujarrabal, V., & Nyman, L.-Å., 1996, A&A, 306, L29
van Loon, J. Th., te Lintel Hekkert, P., Bujarrabal, V., Zijlstra, A. A., & Nyman, L.-Å., 1998, A&A, 337, 141
van Loon, J. Th., Zijlstra, A. A., Bujarrabal, V., & Nyman, L.-Å., 2001, A&A, 368, 950
van Loon, J. Th., Stanimirović, S., Evans, A., & Muller, E., 2006, MNRAS, 365, 1277
Walsh, A. J., Longmore, S. N., Thorwirth, S., Urquhart, J. S., & Purcell, C. R., 2007, MNRAS, 382, L35
Walterbos, R. A. M. & Braun, R. 1994, ApJ, 431, 156
Ward, J. L., Oliveira, J. M., van Loon, J. Th., & Sewiło, M., 2016, MNRAS, 455, 2345
Whiteoak, J. B., & Gardner, F. F., 1986, MNRAS, 222, 513
Wood, P. R., Whiteoak, J. B., Hughes, S. M. G., Bessell, M. S., Gardner, F. F., & Hyland, A. R., 1992, ApJ, 397, 552

5.4 AGN jets

Kazuhiro Hada (NAOJ), Prashanth Mohan (SHAO), Tao An (SHAO), Takuya Akahori (NAOJ).

Active galactic nuclei (AGN) are powered by accretion onto their compact central supermassive black hole (SMBH). Approximately 10% of known AGN are radio-loud and host powerful relativistic jets. AGN jets are one of the most spectacular phenomena in the Universe and can span observable scales from sub-pc to Mpc (inter-galactic). Studies of their formation, initial collimation and acceleration and physical properties (radiative and kinetic energy densities, magnetic field strength, and composition) are areas of active research in high-energy astrophysics. Moreover, as they can transport a significant fraction of gravitational energy back into their host galaxies and intergalactic space, detailed high resolution studies are essential in the above contexts and in understanding their role in the cosmological evolution of galaxies.

Recently, the Event Horizon Telescope (EHT) operated at 230 GHz has resolved the shadow of SMBH in the nucleus of M87, a nearby radio galaxy with a poweful radio jet (EHT Collaboration et al., 2019). This has opened a new window for high frequency observational studies of AGN. However, the EHT image of M87 does not show any extended jet emission around the photon ring, despite a prominent jet at larger scales. This could be due to the limited imaging sensitivity of the EHT array and/or due to the low-level (∼mJy) jet emission at such high frequencies.

In this context, 15–24 GHz radio observations (including VLBI), are optimal to study sufficiently bright pc-kpc scale jet structures (with typical jet spectra $\propto \nu^{-(0.5-1.0)}$ in the optically-thin regime), aided by the mas/submas VLBI angular resolutions. Indeed, various important jet physics and questions such as the collimation and acceleration are associated with a wide range of distances above subpc/pc scales (roughly corresponding to 100 - $10^4\,R_s$ from the BH), which cannot be probed by mm-wavelength observations. The SKA1-MID and its VLBI capability that achieves unprecedented sensitivity and resolution at 15–24 GHz can uniquely probe a vast range of physical scales associated with the jet, from their formation/propagation region to termination.

The SKA as a distributed observational facility is inherently operational in the VLBI mode, owing to the method of data collection and processing. The wide deep surveys are expected to discover a large number of transients every day, the SKA will thus operate as a VLBI survey type instrument, moving beyond the current observation strategies with distributed VLBI networks which are focused on individual sources.

The theoretical sensitivity $\propto A_{\rm eff}/T_{\rm sys}$ where $A_{\rm eff}$ is the effective aperture area of the observing telescope and $T_{\rm sys}$ is the system temperature which accounts for potential sources of noise, including contributions from the cosmic-microwave background, atmospheric emission, and instrumentation amongst others. With the SKA1-Mid [6], $A_{\rm eff}/T_{\rm sys}$ can reach $\approx 1560\ {\rm m^2K^{-1}}$ (highest at the L-band/1.7 GHz) with a corresponding system equivalent flux density (SEFD) $= 2kT_{\rm sys}/A_{\rm eff} \approx 1.8$ Jy. The signal to noise ratio S/N $\sim \sqrt{\tau \Delta\nu} S_\nu/{\rm SEFD}$ where S_ν is the source flux density (in Jy), τ is the observation integration time and $\Delta\nu$ is the observation bandwidth. With $\tau = 1$ hr and $\Delta\nu = 256$ MHz, and using the calculated SEFD, a 1 mJy (S_ν) source can be detected with an extremely high S/N of ≈ 500. Synergistic observations including SKA-1 Mid and existing VLBI networks can increase the maximum baselines to ≈ 10000 km which offer extremely high sub-mas to mas-scales. The relatively low integration times and high resolutions are ideal for studying AGN jets.

Here we describe some primary science cases on AGN jets that can be best addressed with SKA1-MID and its VLBI capability.

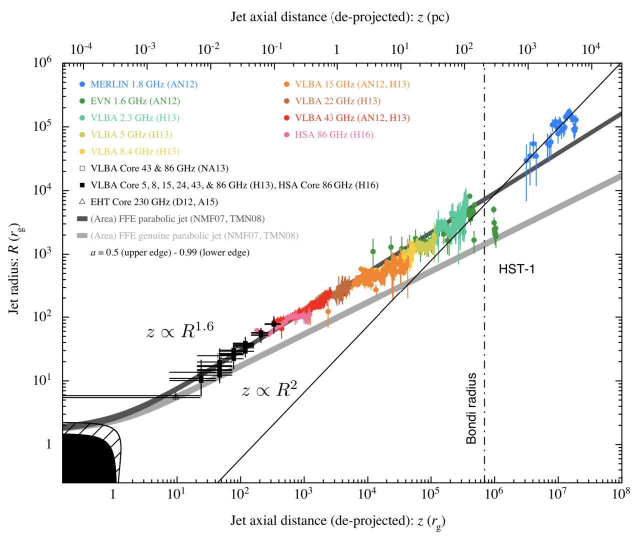

Figure 31: Jet collimation profile of M87 jet (Nakamura et al., 2018)

[6]SKA design documents: *https://www.skatelescope.org/key-documents/*

5.4.1 Acceleration and collimation zone

One of the most remarkable features of AGN jets is that they are extremely collimated (<5 deg) even at large scales. The key question is how and where the flow begins to be collimated after launching. A widely favored scenario of powerful AGN jet formation suggests that a jet is produced by strong magnetic fields amplified by a spinning BH (Blandford & Znajek, 1977) or/and the inner accretion disk (Blandford & Payne, 1982). The flow is initially slow and the subsequent acceleration is realized through gradual conversion of the magnetic energy into kinetic energy, while the ambient pressure from the external medium collimates the flow. As a consequence, the theories suggest that an acceleration and collimation zone (ACZ) is formed over distances $\sim$10–$10^5\,R_{\rm s}$ from the BH (e.g., Komissarov et al., 2009). Recent extensive analyses of the M87 jet based on VLBI and VLA/MERLIN at cm wavelengths have revealed the detailed jet geometry for the corresponding scales (e.g., Nakamura et al., 2018, Fig.1). It was found that the jet shows a parabolic collimation profile over $\sim$100–$10^6\,R_{\rm s}$, which is consistent with the magnetic models. Remarkably, the jet transitions into a conical shape at the Bondi radius, suggesting that the surrounding gases bound by the gravitational potential of SMBH play a key role in confining the jet. However, the number of sources for which the jet collimation profile was determined is still very limited (<10) and mostly biased towards nearby FR-I jets. To test whether such features are common to AGN jets or not, it is important to investigate the jet geometry and structural transitions in a variety of objects (including FR-II objects) by imaging the ACZ of jet flows over a wide range of distances. For FR-II sources (i.e., highly debeamed from us) this would require imaging rms noise levels of $\leq 10\,\mu$Jy even for nearby targets (e.g., 3C452; Giovannini et al., 2001). SKA1-MID-VLBI at 15-24 GHz, along with its submas resolution, will be a unique way to achieve this requirement, while the normal (non-VLBI) SKA1-MID can continuously determine the subsequent jet profile up to kpc-scales.

5.4.2 Magnetic fields in the ACZ: helical scenario and estimation

According to the current leading scenario of AGN jet production, differential rotation in the BH ergosphere or inner accretion disk creates tightly-twisted magnetic fields (e.g., Meier et al., 2001). Helical signatures may be discernible from multi-epoch VLBI images by tracking the jet kinematic evolution (e.g., Li et al., 2018).

If a jet possesses helical magnetic fields, one should see systematic Faraday rotation-measure (RM) gradients across the jet due to the gradual change of the field component along our line-of-sight (Broderick & McKinney, 2010). The first observational hint of such transverse RM gradients was reported in the pc-scale jet of 3C273 (Asada et al., 2002), and to date similar features have been claimed in $\sim$30 pc-scale jets (e.g., Hovatta et al., 2012; Gabuzda et al., 2017), suggesting that the presence of helical fields may be common in AGN jets. However, the previous arguments are mostly based on patchy polarization signals covering only a small fraction of the entire jet area, since the SNR of polarization/RM maps are typically $\sim$10 times lower than those of total intensity images. To definitively test the global field configuration in a jet, we need to obtain polarization/RM maps that cover the whole jet area. A factor of 10 sensitivity improvement by SKA will be able to create jet polarization maps at comparable levels as currently done for total intensity, which may robustly detect RM gradients across the jet in >100 sources. In particular, accurate RM measurements require multiple bands which covers a wide frequency range. Therefore, having SKA1-MID images up to 24 GHz or higher in addition to SKA1-LOW can greatly facilitate this study. Furthermore, the higher angular resolution capability beyond band 5 can better resolve a jet, which is crucial to define transverse RM gradients accurately.

With multi-frequency VLBI observations made at similar epochs, one can estimate the magnetic field strength using the core-shift method (e.g. Mohan et al., 2015; Agarwal et al., 2017). Here, an apparently increasing shift of the VLBI core position with decreasing observational frequency is attributed to optical depth effects mediated by synchrotron self-absorption which enables a transition from optically thin to thick jet emission.

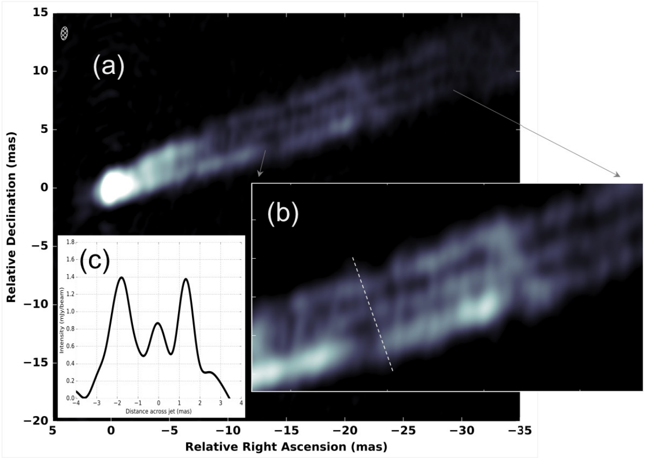

Figure 32: (a) HSA 15 GHz image of the M87 jet. The beam size is 1.14 × 0.55 mas (shown in the upper left corner); (b) Zoom-up view of the parsec-scale region of the jet; (c) Slice of the total intensity at a distance of 15 mas from the core (shown by the dashed line in the panel (b)). The figure is taken from Hada (2017).

5.4.3 High redshift quasars

High frequency, high resolution VLBI observations of quasars at high redshifts ($z > 4$) can potentially unravel the true radio core and the jet base owing to the emission regime being optically thin (e.g. 15/24 GHz corresponds to 75/120 GHz in the source rest frame). For a $z = 4$ source observed at 22 GHz (0.3 mas resolution with a 9000 km baseline), structures probed are at ≈ 2.1 pc corresponding to $\approx 2.2 \times 10^4$ R_S ($R_S = 2GM_\bullet/c^2 = 3 \times 10^{14}$ cm is the Schwarzschild radius for SMBH mass $M_\bullet = 10^9 M_\odot$).

Monitoring observations offer the potential for detection and tracking of core-jet structures, estimation of proper motion and jet geometry, energetics (brightness temperature and radio luminosity) and address long term flux density variations (e.g. Paragi et al., 1999; Zhang et al., 2017). These inputs are crucial for clarifying mechanisms mediating the jet production, collimation and acceleration, and constraining cosmological models (e.g. Gurvits et al., 1999; Kellermann et al., 1999).

Aiding these objectives are polarimetric VLBI observations of AGN which probe polarized regions in the jet, their distribution and evolution (e.g. Li et al., 2018). Magnetic fields along the jet can introduce changes in observed polarized flux densities (Stokes parameters Q, U and I), and enable a Faraday rotation of the electric vector position angle, estimated as the rotation measure (RM). The polarization properties of quasars at high redshifts have not been well studied owing to a relatively smaller sample, detection sensitivity and the detection of only bright and beamed sources (blazars). High sub-mas resolutions, a multi-frequency fast switching capability, and high sensitivity which are characteristics of VLBI arrays including the VLBA and EVN can resolve the Faraday screen and hence probe the zone of transition to thin emission close to the true core.

5.4.4 Spine-sheath jet

A growing number of AGN jets show limb-brightened structures when resolved transversely. Broadband spectral modeling studies on powerful AGN jets suggest that a relativistic jet is not a simple uniform flow but composed of two distinct layers, i.e., a slow outer 'sheath' flow and a fast central 'spine' flow (Ghisellini et al., 2005). Similar arguments are also yielded from GRMHD simulations (e.g., McKinney & Blandford, 2009), suggesting that the central fast spine can be produced by extracting the rotational energy of the spinning BH while the outer sheath may be connected to the innermost part of the accretion disk. Hence, probing the transverse structure of AGN jets is essential to constrain their formation mechanisms. Since jet transverse structures can be typically resolved on mas-submas scales and the central stream is much dimmer than the bright limbs, high-sensitivity radio imaging at 15-24 GHz, thanks to its sub-mas angular resolution with VLBI, would be best suited to address this. Indeed, a recent HSA image of the M87 jet at 15 GHz has begun to discover substructures in the central dim stream of the jet, which could be associated with the interior fast spine component (Hada, 2017, Fig.2). To test how common spine-sheath structures are in AGN jets (particularly in the relatively dimmer FR-II jets as described above), further enhancement of image sensitivity (down to a few μJy levels) at these frequencies is crucial with SKA1-MID-VLBI .

5.4.5 Unresolved Jets

Distant, unresolved AGN systems can be resolved in the frequency domain; synchrotron radio lobes (jets) and AGN core emission are in general predominant at low and high frequencies, respectively. Moreover, short-timescale (say, months to years) variability on the flux and spectrum for unresolved AGN would tell us the dynamics of the AGN system, where the variabilities at low and high frequencies can be ascribed to jets and AGN, respectively. A beyond band 5 observation is complementary with low band observations in the sense that we can obtain a broadband radio spectral-energy distribution (SED) which allows one to quantify the two components separately. We emphasize that the frequencies at Band 5a and 5b (up to 15 GHz) are still in the synchrotron-dominated range based on the observations of nearby Universe. Therefore, extending beyond band 5 particularly above 20 GHz is a unique channel to distinguish unresolved jets from the AGN core.

5.4.6 Outflows and AGN feedback at early stages of jet evolution

The accretion rate can regulate the radio emission in AGN either directly in the form of wide-angle mildly relativistic winds (e.g., Yuan, & Narayan, 2014) or by supplementing the jet synchrotron emission. Statistical studies of AGN indicate an anti-correlation between the accretion rate and the radio loudness (e.g., Greene, Ho & Ulvestad, 2006; Panessa et al., 2007; Sikora, Stawarz & Lasota, 2007). For accretion rates approaching the Eddington limit, AGN tend to be radio quiet (e.g., Greene, Ho & Ulvestad, 2006), and can host powerful outflows, which can quench star-formation activity (e.g., Nardini et al., 2015; Tombesi et al., 2015; Tombesi, 2016) and address the SMBH – host galaxy co-evolution through feedback (e.g., Kormendy & Ho, 2013). Some high-speed ($\sim$0.1 c) outflows may produce strong interactions or shocks and thus may create radio-emitting sources (e.g., Nims, Quataert & Faucher-Giguère, 2015; Zakamska & Greene, 2014). VLBI observations of optically luminous radio-quiet quasars will allow us to search for radio-emitting wide-angle but powerful outflows to provide direct evidence for this mode of AGN feedback (e.g, Giroletti et al., 2017; Wylezalek & Morganti, 2018).

Resolving the spatial size of a radio lobe is essential to precisely evaluate the (monochromatic) luminosity in the radio band. This means that studying small-size jets or younger jets require a higher angular resolution compared to the previous works. In the last decade, late-stage (or evolved) AGN feedback in nearby and giant radio jets has been intensively mapped with 10 km-class baselines. Extending beyond band 5 provides the highest spatial resolution of 20 mas (or $\sim$ 40–120 pc at z= $0.1 - 0.5$) around 25 GHz with the maximum 150 km baseline. This corresponds to $\sim 10^5$ year with the sound velocity of 500 km/s for the intergalactic medium as the expansion velocity of a radio lobe. Therefore, extending beyond band 5 allows us to pioneer an early stage of AGN feedback with the age of 10^5 year from the emergence of the shock wave. The investigation of earlier-stage AGN feedback can thus produce potentially novel information about how the jet pushes out the inflow of the dense intergalactic medium in cool-core clusters.

References

Agarwal, A., Mohan, P., Gupta, A. C., et al. 2017, MNRAS, 469, 813
Asada, K., Inoue, M., Uchida, Y., & Kameno, S., 2002, PASJ, 54, L39
Blandford, R. D., & Znajek, R. L., 1977, MNRAS, 179, 433
Blandford, R. D., & Payne, D. G., 1982, MNRAS, 199, 883
Broderick, A. E., & McKinney, J. C.,, 2010, ApJ, 725, 750
EHT Collaboration, et al., 2019, ApJL, 875, L1
Gabuzda, D. C, et al., 2017, MNRAS, 472, 1792
Ghisellini, G., Tavecchio, F., & Chiaverge, M., 2005, A&A, 432, 401
Giovannini, G., Cotton, W. D., Feretti, L., Lara, L., & Venturi, T., 2001, ApJ, 552, 508
Giroletti M., Panessa F., Longinotti A. L., Krongold Y., Guainazzi M., Costantini E., Santos-Lleo M., 2017, A&A, 600, A87
Greene J. E., Ho L. C., Ulvestad J. S., 2006, ApJ, 636, 56
Gurvits, L. I., Kellermann, K. I., & Frey, S. 1999, A&A, 342, 378
Hada, K., 2017, Galaxies, 5, 2
Hovatta, T., et al., 2012, AJ, 144, 105
Kellermann, K. I., Vermeulen, R. C., Zensus, J. A., et al. 1999, New Astronomy Reviews, 43, 757
Komissarov, S. S., Barkov, M. V., Vlahakis, N., & Konigl, A., 2009, MNRAS, 394, 1182
Kormendy J., Ho L. C., 2013, ARA&A, 51, 511
Li, X., Mohan, P., An, T., et al. 2018, ApJ, 854, 17
McKinney, J. C., & Blandford, R. D., 2009, MNRAS, 394, L126
Meier, D. L., Koide, S., Uchida, Y., 2001, Sciene, 291, 84
Mohan, P., Agarwal, A., Mangalam, A., et al. 2015, MNRAS, 452, 2004
Nakamura, M., et al., 2018, ApJ, 868, 146
Nardini E., et al., 2015, Science, 347, 860
Nims J., Quataert E., Faucher-Giguère C.-A., 2015, MNRAS, 447, 3612
Panessa F., Barcons X., Bassani L., Cappi M., Carrera F. J., Ho L. C., Pellegrini S., 2007, A&A, 467, 519
Paragi, Z., Frey, S., Gurvits, L. I., et al. 1999, A&A, 344, 51
Sikora M., Stawarz L., Lasota J.-P., 2007, ApJ, 658, 815
Tombesi F., Meléndez M., Veilleux S., Reeves J. N., González-Alfonso E., Reynolds C. S., 2015, Nature, 519, 436
Tombesi F., 2016, Astron. Nachr., 337, 410
Wylezalek D., Morganti R., 2018, Nature Astronomy, 2, 181
Yuan, F., & Narayan, R. 2014, ARA&A, 52, 529
Zakamska N. L., Greene J. E., 2014, MNRAS, 442, 784
Zhang, Y., An, T., Frey, S., et al. 2017, MNRAS, 468, 69

6 Cosmology and the History of the Universe

6.1 Mapping star-formation and AGN activity at high spatial resolution out to high redshift with Band 6

Mark T. Sargent (U. of Sussex), Isabella Prandoni (INAF-IRA, Bologna), Eric Murphy (NRAO Charlottesville)

Measuring the cosmic star-formation history (CSFH) is one of the key scientific objectives of radio continuum surveys with the SKA. A major advantage of CSFH studies in the radio regime is that radio photons do not suffer extinction from intervening dust; the radio brightness therefore traces star-formation rate (SFR) regardless of whether it occurs in regions that are transparent or obscured by dust. Interferometric radio observations also provide high-angular resolution imaging which, in the high-frequency domain at $\sim$20 GHz, will resolve the emission from galaxies at cosmic noon ($z \sim 2$) down to the 150 pc scale. Band 6 is unique in that it can probe – either on its own or, depending on the redshift range of interest, in conjunction with lower-frequency SKA bands or ALMA – star-formation activity and cold gas content, thereby constraining both galaxy growth rates and the underlying fuel reservoir.

However, radio-based measurements of the CSFH also come with significant challenges, such as our partial understanding of the astrophysical mechanisms producing radio emission (e.g. the relation between SFR and synchrotron continuum luminosity at GHz frequencies), and difficulties in distinguishing between emission from star-formation and active galactic nuclei (AGN). By covering a key part of the radio spectrum, and by virtue of their high angular resolution, Band 6 observations will make an essential contribution to overcoming both of these issues.

6.1.1 Deciphering the cosmic star-formation history and its drivers in Band 6

Helping SKA realize its full potential as a SFR measurement machine: spectral decomposition and SFR calibration via free-free emission The workhorse band for CSFH studies with SKA1-MID will be band 2 (0.95–1.76 GHz), tracing predominantly non-thermal emission processes (synchrotron radiation) in galaxies. This reliance on low-frequency coverage is driven by field-of-view and sensitivity considerations (the latter reflecting the canonical power-law spectrum of star-forming galaxies, $S_\nu \propto \nu^{-0.7}$), and the desire to simultaneously characterize radio morphologies at sub-arcsec resolution. Measuring star formation activity with data from low-frequency surveys, however, requires an indirect conversion of the radio synchrotron luminosity to a star formation rate. In practice, radio-based SFRs often make use of the empirical far-infrared/radio correlation (Helou et al., 1985; Yun et al., 2001), the redshift evolution of which is controversial (examples of recent studies are: Ivison et al., 2010; Sargent et al., 2010a,b; Mao et al., 2011; Magnelli et al., 2015; Pannella et al., 2015; Calistro Rivera et al., 2017; Delhaize et al., 2017; Molnár et al., 2018) and the physics of which not fully understood.

While multi-tiered band 2 surveys will detect large numbers of sources (Prandoni & Seymour, 2015) and provide the statistical power to study the cosmic evolution of star-formation across all environments and galaxy types, high-frequency observations will be key to maximising the accuracy of empirical star-formation rate calibrations. Band 6 covers a critical frequency range for properly decomposing the rest-frame radio/sub-mm spectrum into its component parts: non-thermal (synchrotron), free-free (Bremsstrahlung), and thermal dust continuum emission all contribute at roughly comparable levels to the emission in this frequency range[7]. Although multi-band frequency coverage from the (sub-)GHz regime all the way into Band 6 will not be available for the majority of the star-forming galaxies detected in multi-tiered SKA surveys, robust spectral decompositions carried out on representative galaxy samples will characterize the diversity in the shapes/curvature and composition of radio spectral energy distributions (SEDs; see, e.g., Marvil et al., 2015; Calistro Rivera et al., 2017; Tisanić et al., 2019, for recent work on radio SED diversity and their redshift evolution). This information can then be synthesized in the form of 'template' radio SEDs which will provide much improved K-correction prescriptions and error budgets for SFR estimates derived from single-band, low-frequency surveys.

Band 6 continuum flux densities can also be used as an independent, 'clean' star formation rate diagnostic as soon as they probe rest-frame frequencies above ~30 GHz where thermal free-free emission is expected to become the dominant emission process (e.g. Condon, 1992; Murphy et al., 2012). In local galaxies the strongest contribution to the 15–25 GHz emission in general stems from synchrotron emission, but for galaxies at higher redshifts Bremsstrahlung will provide an increasingly dominant contribution. Radio free-free emission can be directly related to the ionizing (Lyman continuum) photon rate of newly formed, massive stars, as evidenced by detailed studies of star-forming regions in the Galaxy (e.g., Mezger & Henderson, 1967), nearby dwarf irregulars (e.g., Klein & Graeve, 1986), the nuclei of normal galaxies (e.g., Turner & Ho, 1983, 1994) and starbursts (e.g., Klein et al., 1988; Turner & Ho, 1985), Wolf-Rayet galaxies (e.g., Beck et al., 2000), as well as by high resolution investigations of super star clusters within nearby blue compact dwarfs (e.g., Turner et al., 1998; Kobulnicky & Johnson, 1999; Johnson et al., 2009). Encouraging evidence that the free-free radio continuum still reliably traces star formation at intermediate and high redshift comes from select studies of selected sources in the recent literature, for which free-free SFRs were found to agree well with other SFR estimates (e.g., Galvin et al., 2016; Huynh et al., 2017, H. Algera et al., in prep.).

By directly measuring the ionizing photon rate from massive stars without being affected by dust obscuration, the free-free continuum provides an unbiased estimate of the rate of formation of massive stars. Thanks to the sensitivity and survey speed improvements (approx. 3– and 5–fold, resp.) of SKA1 high-frequency observations over, e.g., VLA Ku- and K-band follow-up, MID bands 5 and 6 will guarantee the first statistically significant measurement of the CSFH via thermal radio emission (see Murphy et al., 2015, for a review of proposed Band 5 observations with SKA1-MID for tracing the CSFH through thermal processes). This is an important milestone in its own right, but – importantly – the deployment of Band 6 on SKA1-MID will also enable calibration of radio synchrotron SFR esti-

[7]Another feature in the radio/sub-mm spectrum is the so-called anomalous microwave emission – see Fig. 33a and Sect. 4.1 in this White Book.

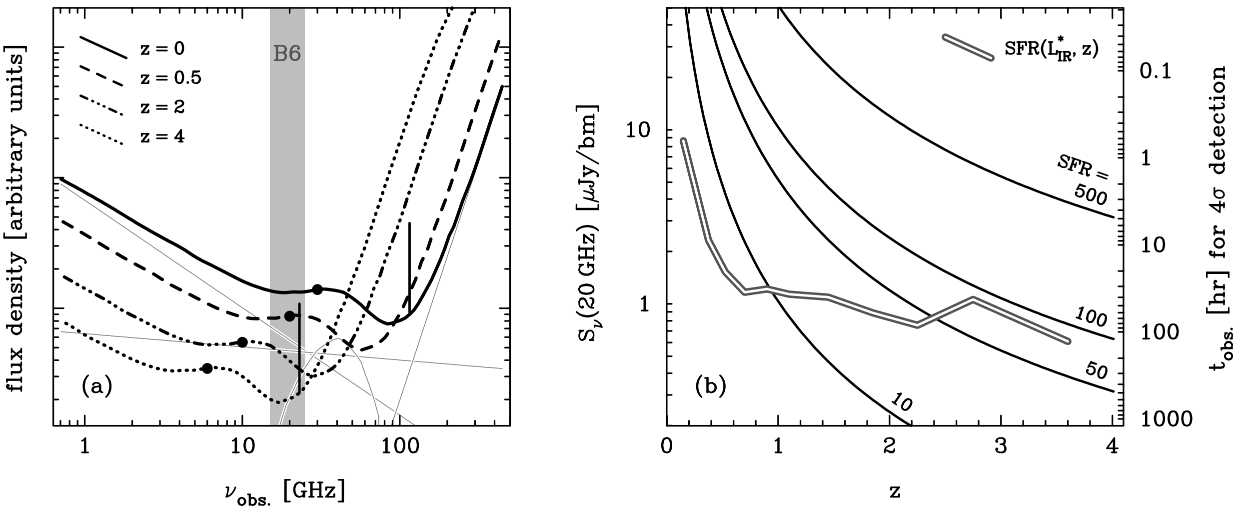

Figure 33: (a) Typical radio-to-submm SED of a star-forming galaxy and its sampling by Band 6 over the redshift range $z \leq 4$ (see legend; the change in normalization is an arbitrary offset for visualization purposes and does not reflect cosmological dimming). Four SED components are shown for the $z = 0$ spectrum: non-thermal synchrotron, thermal free-free, anomalous microwave emission and dust continuum (counterclockwise, starting half-way up the left-hand y-axis). Superimposed on the $z = 0$ and 4 SEDs it the CO(1→0) transition which enters Band 6 at $z \sim 4$. The solid dots on the SEDs highlight $\nu_{\rm rest} = 30$ GHz, where the ratio between thermal and non-thermal flux is assumed to be unity.
(b) Expected 20 GHz flux density of galaxies with SFR = 10, 50, 100 & 500 $M_\odot$/yr, as a function of redshift. The right-hand y-axis gives the integration time required for a S/N = 4 detection in continuum mode with instantaneous bandwidth 5 GHz, assuming tapering to approx. 1 arcsec such that galaxies are unresolved. The line running across the constant SFR curves traces the flux vs. redshift relation for $L^*_{\rm IR}$ galaxies at the knee of the IR luminosity function (Gruppioni et al., 2013); the L^* population remains detectable within 100 hr of observing time at all $z \leq 4$.

mates with measurements based on the free-free process already for galaxies at $z \gtrsim 0.5$ (see Fig. 33a). This represents a very significant extension compared to data from band 5 surveys at 10 GHz, which can provide such a calibration only from $z \sim 2$ onward. In Fig. 33b we show the fluxes and associated observing times required to detect star-forming galaxies (SFGs) in the LIRG and ULIRG category (SFR $\geq 10\,M_\odot$/yr) out to $z \sim 4$. Given the anticipated Band 6 continuum sensitivity[8] of 1.7 μJy at 20 GHz (for $t_{\rm obs.} = 1$ hr), Fig. 33b highlights that it will be possible to detect the L^* population with a 100 hr observation over this entire redshift range. Based on the number densities of galaxies brighter than the knee of the infrared (IR) luminosity function in Gruppioni et al. (2013), we statistically expect a single 20 GHz pointing with area 8.4 arcmin^2 to reveal ∼24, 6 and 2.5 galaxies brighter than L^* within a redshift interval $\Delta z = 0.5$ centred at $z \sim 1$, 2 and 3, respectively. These numbers highlight the promise Band 6 holds both for (a) constraining the CSFH at cosmic noon via thermal emission from those galaxies contributing most to the cosmic SFR density, and (b) assembling sizeable samples of galaxies with free-free SFRs that can serve as calibrators for the relation between SFR and radio synchrotron continuum luminosity.

Toward a 150 pc-scale characterization of star-formation activity and efficiency within galaxies at cosmic noon By virtue of the high angular resolution achieved and by probing dust-unbiased free-free emission, Band 6 will become an excellent tool for studying the growth of structures

[8]With the baseline distribution of the 133 SKA1-MID dishes, the reference rms noise value quoted will be reached over a large range of angular scales (cf. Fig. 12 in Braun et al. 2017 (SKA-TEL-SKO-0000818), *"Anticipated SKA1 Science Performance"*, or Fig. 10 in *arXiv:1912.12699*). Following standard practice, and in keeping with the technical summary in Section 1, we take this reference rms noise value to correspond to twice the natural array sensitivity.

within galaxies and the sites within galaxies that contribute to the rise in the cosmic star-formation rate density back to its peak at $z \sim 2$. SFGs at cosmic noon are different in many ways from their low-redshift counterparts. Significant star-formation activity takes place in giant clumps within turbulent, gas-rich disks (e.g., Elmegreen et al., 2007; Bournaud et al., 2008; Förster Schreiber et al., 2009; Ceverino et al., 2010; Bournaud et al., 2014), which are rapidly replenished by accretion flows leading to a diverse ISM chemistry where low-metallicity gas mixes with or exists alongside in-situ gas that has already been enriched by multiple generations of stars. All the while, bulges begin to form in many of these galaxies, often during heavily obscured central starbursts, heralding the emergence of increasing numbers of quenched and early-type galaxies over the next 10 Gyrs (e.g., Brammer et al., 2011; Ilbert et al., 2013; Davidzon et al., 2017). Understanding how these transformations occur and what quenching mechanisms are at play will be strongly aided by the availability of high-resolution SFR maps, as well as the ability to recognize AGN-related feedback processes (see next section).
In view of the conditions in $z \sim 2$ galaxies, the accuracy of many standard star formation rate diagnostics may not be a given. Rest-frame far-ultraviolet (UV) observations provide a direct measure of emission from the photospheres of young, massive stars, but they are often hampered by extinction effects that vary spatially within, and among, galaxies. Furthermore, changes in metallicity, gas-to-dust ratios and stellar population ages as a function of position within galaxies complicate the combined interpretation of UV and IR emission via hybrid SFR estimators (e.g., Boquien et al., 2016). The ability to utilize free-free SFRs, with their straightforward link to the production rate of ionizing photons, therefore becomes increasingly important at high redshifts. By redshift $z \sim 2$, where the star formation rate density of the Universe is dominated by ultra-luminous, highly dust-obscured galaxies that are essentially opaque at UV/optical wavelengths, Band 6 samples rest frame 60–70 GHz emission, which is completely dominated by the free-free process. With max. baseline lengths of 150 km, an observation at the upper edge of Band 6 at 25 GHz will achieve an angular resolution of $\sim 0.02''$, probing 150–200 pc scales at $z \gtrsim 1$. This is essential for studying star formation in giant clumps, many of which are revealed by lensing magnification (e.g. Cava et al., 2018) to have significantly smaller sizes than has been assumed until recently based on Hubble Space Telescope (HST) imaging surveys (e.g. Guo et al., 2012; Elmegreen et al., 2013). Probing such fine physical scales requires bright sources (see, e.g, Fig. 33 and Fig. 3 in Murphy et al., 2015), but SKA1 should still have the sensitivity to resolve L^* galaxies at high redshift. Deep, detailed SFR maps in Band 6 would be ideal complements to ALMA or – at $z \gtrsim 3.5$ (see Fig. 33a) – simultaneous SKA Band 6 observations with a separate sub-band targeting CO or dense gas tracers like HCN (see Sect. 6.2 in this White Book) that can resolve the molecular gas distribution at similar scales. This will enable us to study spatial variations of star-formation efficiency (via the resolved Kennicutt-Schmidt relation) inside galaxies at the peak epoch of star-formation. Doing so holds the prospect of being able to pinpoint both the regions within galaxies that are responsible for the gradual increase of star-formation efficiency toward high redshift (e.g. Schinnerer et al., 2016; Tacconi et al., 2018), as well as shedding light on the link between galaxy quenching and gas consumption.

6.1.2 The interplay between star formation and nuclear activity

Deep radio fields reveal a significant fraction of sources showing signatures of AGN activity at non-radio wavelengths (e.g. Seyfert galaxies or QSOs). These AGNs are often referred to in the literature as radio-quiet (RQ) AGNs (see, e.g., Padovani et al., 2011; Bonzini et al., 2013), because the vast majority of them do not display large-scale jets or lobes[9]. These radio-quiet (RQ) AGN are not radio-silent: many show radio emission on galactic or sub-galactic scales. The origin of this radio emission is controversial. RQ AGNs have been found to share properties with SFGs. They have similar radio spectra and luminosities (Bonzini et al., 2013, 2015); their radio luminosity functions show similar evolutionary trends (Padovani et al., 2011); their host galaxies have similar colours, optical morphologies, and stellar masses (Bonzini et al., 2013). For all these reasons, it was concluded that the radio

[9] We caution that a classification based on radio loudness (RL) is not fully appropriate for faint radio AGNs. A detailed discussion of AGN classification in view of the latest results from deep radio surveys, is presented in (Padovani, 2017), who proposes to update the terms RL/RQ AGNs into jetted/non-jetted AGNs, based on the presence/lack of strong relativistic jets.

emission in RQ AGNs is triggered by star formation (Padovani et al., 2011; Bonzini et al., 2013, 2015; Ocran et al., 2017). On the other hand, high-resolution radio follow ups of RQ AGN samples with Very Long Baseline Interferometry arrays have shown that a significant fraction of RQ AGNs (20–40%, depending on the sample) contain AGN cores that contribute significantly (50% or more) to the total radio emission (Maini et al., 2016; Herrera Ruiz et al., 2016, 2017). Following a different approach, Delvecchio et al. (2017) concluded that $\sim$30 per cent of the JVLA-COSMOS sources associated with Seyfert galaxies and QSOs display a significant (>3 sigma) excess in radio emission compared to expectations based on their inferred SFRs (derived from SED fitting). The emerging scenario is that RQ AGN are composite systems where star formation and AGN-triggered radio emission can coexist, over a wide range of relative contributions.

This scenario is supported by the modeling work of Mancuso et al. (2017), who showed that the observed radio counts and luminosity functions can be reproduced very well by a three-component population (SFGs, RL and RQ AGNs), where RQ AGNs are the sum of two sub-components: one dominated by star formation (and designated 'radio-silent'), and the other by AGN-triggered radio emission. This simple but physically motivated model implements star formation rate functions (Mancuso et al., 2016), AGN duty cycles, and the conditional probability of an SFG to host an AGN with given bolometric luminosity in the context of in situ co-evolution scenarios. Coupling these ingredients with the radio emission properties associated with star formation and nuclear activity, it provides an estimate of the relative contribution of SFGs and AGNs in different radio luminosity, radio flux, and redshift ranges and shows that radio-emitting SFGs and AGNs are expected to host supermassive black holes accreting with different Eddington ratio distributions and to occupy different loci in the galaxy main-sequence diagrams. These specific predictions are consistent with current data sets (Mancuso et al., 2017; Prandoni et al., 2018; Prandoni, 2018) but need to be tested with larger statistics from deep radio surveys covering wide areas with dense multi-band coverage. Even more interestingly, there is emerging evidence that jet- and radiative-mode feedback may frequently coexist at galaxy scale in RQ AGNs. Indeed, a strong correlation between 1.4 GHz radio luminosity and AGN-driven outflows was found in SDSS-selected AGNs by Mullaney et al. (2013). In addition, a very recent sub-arcsec resolution (eMERLIN+JVLA) radio follow-up study of a local ($z < 0.2$) sample of ten SDSS Type-2 QSOs with ionized outflows has revealed a high incidence (80%) of small-scale (1–25 kpc) radio jets (Jarvis et al., 2019), showing clear signs of interaction with the outflowing gas. This supports a scenario where compact radio jets, with modest radio luminosities, are a crucial feedback mechanism for massive galaxies during a quasar phase. Such a scenario needs to be confirmed on larger statistical basis and on samples probing the peak epoch of the star formation/AGN co-evolution ($z \sim 1-3$).

Thanks to its combination of sensitivity and survey speed, the SKA will allow us to extend the investigation of the interplay between star formation and nuclear activity to a much broader range of redshifts. High resolution (possibly multi-frequency) radio observations offer the most direct and clean way to separate nuclear radio emission from star-formation activity through spectro-morphological classification and represent a very powerful means of providing an unbiased census of both star formation and AGN activity as a function of redshift. This however requires the exquisite *uv* coverage of the SKA, and the spatial resolution offered by Band 6. As discussed in the previous section, Band 6 will be able to resolve high-redshift star forming galaxies at 100–200 pc scales; high fidelity imaging at these spatial scales is crucial to reveal the presence of compact radio cores, and to reliably distinguish (sub-)kpc radio jets from nuclear starbursts or clumpy star formation.

References

Beck, S. C., Turner, J. L., & Kovo, O. 2000, AJ, 120, 244
Bonzini, M., Padovani, P., Mainieri, V., et al. 2013, MNRAS, 436, 3759
Bonzini, M., Mainieri, V., Padovani, P., et al. 2015, MNRAS, 453, 1079
Boquien, M., Kennicutt, R., Calzetti, D., et al. 2016, A&A, 591, A6
Bournaud, F., Daddi, E., Elmegreen, B. G., et al. 2008, A&A, 486, 741
Bournaud, F., Perret, V., Renaud, F., et al. 2014, ApJ, 780, 57
Brammer, G. B., Whitaker, K. E., van Dokkum, P. G., et al. 2011, ApJ, 739, 24
Calistro Rivera, G., Williams, W. L., Hardcastle, M. J., et al. 2017, MNRAS, 469, 3468
Cava, A., Schaerer, D., Richard, J., et al. 2018, Nature Astronomy, 2, 76
Ceverino, D., Dekel, A., & Bournaud, F. 2010, MNRAS, 404, 2151

Condon, J. J. 1992, ARA&A, 30, 575
Davidzon, I., Ilbert, O., Laigle, C., et al. 2017, A&A, 605, A70
Delhaize, J., Smolčić, V., Delvecchio, I., et al. 2017, A&A, 602, A4
Delvecchio, I., Smolčić, V., Zamorani, G., et al. 2017, A&A, 602, A3
Elmegreen, D. M., Elmegreen, B. G., Ravindranath, S., & Coe, D. A. 2007, ApJ, 658, 763
Elmegreen, B. G., Elmegreen, D. M., Sánchez Almeida, J., et al. 2013, ApJ, 774, 86
Förster Schreiber, N. M., Genzel, R., Bouché, N., et al. 2009, ApJ, 706, 1364
Galvin, T. J., Seymour, N., Filipović, M. D., et al. 2016, MNRAS, 461, 825
Gruppioni, C., Pozzi, F., Rodighiero, G., et al. 2013, MNRAS, 432, 23
Guo, Y., Giavalisco, M., Ferguson, H. C., Cassata, P., & Koekemoer, A. M. 2012, ApJ, 757, 120
Helou, G., Soifer, B. T., & Rowan-Robinson, M. 1985, ApJ, 298, L7
Herrera Ruiz, N., Middelberg, E., Norris, R. P., et al. 2016, A&A, 589, L2
Herrera Ruiz, N., Middelberg, E., Deller, A., et al. 2017, A&A, 607, A132
Huynh, M. T., Emonts, B. H. C., Kimball, A. E., et al. 2017, MNRAS, 467, 1222
Ilbert, O., McCracken, H. J., Le Fèvre, O., et al. 2013, A&A, 556, A55
Ivison, R. J., Magnelli, B., Ibar, E., et al. 2010, A&A, 518, L31
Jarvis, M. E., Harrison, C. M., Thomson, A. P., et al. 2019, MNRAS, 485, 2710
Johnson, K. E., Hunt, L. K., & Reines, A. E. 2009, AJ, 137, 3788
Klein, U., & Graeve, R. 1986, A&A, 161, 155
Klein, U., Wielebinski, R., & Morsi, H. W. 1988, A&A, 190, 41
Kobulnicky, H. A., & Johnson, K. E. 1999, ApJ, 527, 154
Magnelli, B., Ivison, R. J., Lutz, D., et al. 2015, A&A, 573, A45
Maini, A., Prandoni, I., Norris, R. P., et al. 2016, A&A, 589, L3
Mancuso, C., Lapi, A., Shi, J., et al. 2016, ApJ, 833, 152
Mancuso, C., Lapi, A., Prandoni, I., et al. 2017, ApJ, 842, 95
Marvil, J., Owen, F., & Eilek, J. 2015, AJ, 149, 32
Mao, M. Y., Huynh, M. T., Norris, R. P., et al. 2011, ApJ, 731, 79
Mezger, P. G., & Henderson, A. P. 1967, ApJ, 147, 471
Molnár, D. C., Sargent, M. T., Delhaize, J., et al. 2018, MNRAS, 475, 827
Murphy, E. J., Bremseth, J., Mason, B. S., et al. 2012, ApJ, 761, 97
Murphy, E., Sargent, M., Beswick, R., et al. 2015, Advancing Astrophysics with the Square Kilometre Array (AASKA14), 85
Mullaney, J. R., Alexander, D. M., Fine, S., et al. 2013, MNRAS, 433, 622
Ocran, E. F., Taylor, A. R., Vaccari, M., et al. 2017, MNRAS, 468, 1156
Padovani, P., Miller, N., Kellermann, K. I., et al. 2011, ApJ, 740, 20
Padovani, P. 2017, Nature Astronomy, 1, 0194
Pannella, M., Elbaz, D., Daddi, E., et al. 2015, ApJ, 807, 141
Prandoni, I., & Seymour, N. 2015, Advancing Astrophysics with the Square Kilometre Array (AASKA14), 67
Prandoni, I. Guglielmino, G., Morganti, R., et al. 2018, MNRAS, 481, 4548
Prandoni, I. 2018, IAUS, 333, 175
Sargent, M. T., Schinnerer, E., Murphy, E., et al. 2010a, ApJS, 186, 341
Sargent, M. T., Schinnerer, E., Murphy, E., et al. 2010b, ApJ, 714, L190
Schinnerer, E., Groves, B., Sargent, M. T., et al. 2016, ApJ, 833, 112
Tacconi, L. J., Genzel, R., Saintonge, A., et al. 2018, ApJ, 853, 179
Tisanić, K., Smolčić, V., Delhaize, J., et al. 2019, A&A, 621, A139
Turner, J. L., & Ho, P. T. P. 1983, ApJ, 268, L79
Turner, J. L., & Ho, P. T. P. 1985, ApJ, 299, L77
Turner, J. L., & Ho, P. T. P. 1994, ApJ, 421, 122
Turner, J. L., Ho, P. T. P., & Beck, S. C. 1998, AJ, 116, 1212
Yun, M. S., Reddy, N. A., & Condon, J. J. 2001, ApJ, 554, 803

6.2 CO at high redshift, and complex molecules

Francoise Combes (Obs. de Paris), Matthieu Béthermin (LAM), Umberto Maio (INAF), Fatemeh Tabatabaei (IAC), Nicole Nesvadba (Observatoire de la Côte d'Azur)

6.2.1 The need to extend the band from 14 to 24 GHz, and even beyond

The extension from Band 5 to Band 5+ for SKA, i.e. the frequency range between 14 GHz and 24 GHz, is very important for high-redshift CO(1-0) line detection, between z=3.8 to 7.2. Several observational campaigns have already detected molecular gas in galaxies in this redshift range, but with higher-J CO line (e.g. the review paper Combes, 2018). However this does not give the total molecular gas content without ambiguity, since the excitation of the gas is variable. Starburst galaxies are frequently revealing highly excited gas, warm and dense, and there is a bias that millimeter surveys only detect active starbursts, and not the more quiescent galaxies. In addition, galaxies have been shown to possess mainly two components, a nuclear region with dense and excited molecular gas, and a more extended disk, with diffuse and sub-thermally excited gas, but representing most of the molecular reservoir. Only a few extremely massive galaxies, or with high gravitational amplification, have been detected in CO(1-0) in the considered redshift range with the VLA, and to better uncover this window, an instrument with a much larger sensitivity and thus surface area is needed. The CO(1-0) is the best line where the CO-to-H_2 conversion ratio can be calibrated, without large errors, and all estimated molecular masses up to now assume some high-J to J=1 flux ratio, to convert to a more secure mass. This is fundamental to understand the star formation efficiency across the Hubble time. The state of the art at present reveal that both the gas fraction and the star formation efficiency are increasing in main sequence galaxies, from z=0 to z=2 (e.g. the PHIBSS survey, Tacconi et al 2013, 2018). We do not know the evolution of these quantities between z=3 and 7, although this is essential to understand the star formation history of the universe.

Because of the short lifetimes of massive stars (<30 million years), early episodes of star formation are likely to quickly pollute the ambient medium with substantial amounts of C, O and alpha elements, inducing the formation of a vast number of molecules, like CO.

CO energy levels are separated by regular gaps of about 115 GHz, with higher-J rotational transitions ranging, in the rest frame, between ∼230-800 GHz. As a consequence, extending SKA1 to the 25-50 GHz band would allow us to trace the very first episodes of cosmic star formation at redshifts well above 10, that are supposedly little contaminated by dust. For example, the CO(3-2) line around 346 GHz would probe star formation at z∼6-13 when detected between 25 and 50 GHz. Harder CO transitions (likely in strongly starburst environments as the ones expected during these epochs), with frequencies up to around 800 GHz, would virtually probe even earlier episodes, as is the case for the CO(7-6) transition at 807 GHz (z=15 for a frequency of 50 GHz). These high-J transitions are interesting, also because data for IRAS, sub-mm galaxies, radio galaxies and QSOs seem to suggest a correlation between higher-J levels and increasing luminosities produced during star formation (Righi et al., 2008). Investigations of such extreme regimes would strengthen our understanding of primordial star formation and metal enrichment as well as the validity in early metal-poor environments of empirical approaches based on CO-to-H_2 conversion factors to infer H_2 abundances.

As far as sensitivity is concerned, and according to the Anticipated SKA1 Science Performance (SKA document2 SKA-TEL-SKO-0000818), the line noise level for SKA1-Mid arrays at 25, 35 and 45 GHz are respectively 0.06, 0.07 and 0.1 mJy for 1h integration time, in channels 100km/s wide. The expected peak flux for typical galaxies in the CO(1-0) line at redshift 3 and higher, are in the range 0.1 to 10mJy, according to their gas content, and excitation (main sequence, quenched galaxies or starburst), with line widths of 200-400km/s. The more massive and gaseous galaxies will be detected in very short telescope integration times, while the weaker and less gaseous ones will require a few hours.

6.2.2 CO and other molecules in absorption

Molecular absorption lines from the cold medium in intervening galaxies is a powerful tool to study high-redshift galaxies with high resolution and high sensitivity, since the optical depth rises up to 1 or saturation, and only the pencil beam of the strong background radio source core is involved. The detection power is then only due to the continuum strength, and only small masses of molecular medium are necessary (Wiklind & Combes, 1996, Combes & Wiklind 1997). Six absorbing systems have been detected with mm-wavelength telescopes, and three of them correspond to lensed quasars, where the absorption comes from the lensing galaxy. In PKS1830-21, a line survey of molecules was possible with ALMA (Muller et al 2011). Since several lines of sight cross the galaxy, its dynamics can be probed. The absorption lines from the cold medium are so narrow, that a high precision on their frequency/velocity is obtained, and these systems are ideal targets to constrain the variation of fundamental constants, by comparing various elements (HI, CI, HCN, CS, CH3OH, etc..; Murphy et al. 2003). With SKA1, many more absorbing systems are expected to be detected, since the strength of continuum sources increases at low frequency (synchrotron emission). These detections will be a side product of large redshifted HI surveys. Once HI and OH are detected, it is possible to search for a large number of lines (CO, CN, etc, e.g. Combes et al 2019).

6.2.3 A large range of various molecules, and diverse tracers

Molecular lines are excellent tracers of star formation and, as of today, hundreds of molecules have been identified in space, the brightest one being carbon monoxide, CO. UV/ optical detections have led to the discovery of simple molecules (CO, CH, CN, CH+, H2, N2), while IR data have been used to study non-polar molecules and ices (H2, H2O, OH, OI, C3, C5, CH3, CH4, C2H2, C6H6, CO2, H2CO, HF, SO2, H2S, HCN, CH3OH). Gas-phase molecules have emissions that are typical of sub-mm regimes (below 1000 GHz), although unambiguous detections of complex species are safely done in the radio band (NH3, H2O, H2CO, HCO+, C6H-, etc.).

Given their fundamental role in cooling the gas in molecular clouds, molecules are expected to be a crucial tool to study early star formation in primordial galaxies, as well as the rise and decline of cosmic star formation from the first galaxies until today (e.g., Madau & Dickinson, 2014). Currently observed primordial star forming galaxies are detected up to $z{\sim}11$, with 19 candidates over the CANDELS+ERS field in the redshift range $9<z<11$ (Bouwens et al., 2019).

Although earlier epochs are still a terra incognita, they present a number of advantages, since they host structures that are still in their infancy, perturbations have not evolved significantly, yet, and large-scale non-linear effects are much more modest than at low z. Therefore, this seems to be a perfect window to isolate the physical processes ruling gas collapse and star formation.

Primordial star formation processes determine the production of photons in different energy bands, marking the end of the dark ages ($z>30$), the start of the cosmic dawn ($15<z<30$) and the onset of the following epoch of reionization ($6<z<15$) (Koopmans et al., 2015). The first star formation events inject large amounts of heavy elements and produce powerful stellar feedback (e.g., Maio et al., 2010). This latter heats the gas and through excitation forms chemical species with higher energy levels.

Besides CO, organic species are commonly observed in star forming regions, typically at mm wavelengths, and may be traced back to carbon-rich fragments originally formed in circumstellar shells (e.g., Ziurys et al 2006).

For example, carbon sulfide, CS, is the sulfur analogue of CO and is a polar molecule like CO. In space, it is commonly found in gaseous form, both in molecular clouds and in planet atmospheres. Because of the various isotopic isomers arising from different C and S isotopes (12C33S, 12C34S, 12C36S, 13C32S, 13C33S, 13C34S), it features a rich spectral pattern of hundreds of rotational and vibrational transitions between 49 GHz and 1075 GHz. Among all these lines, a typically bright one in the interstellar medium is the CS(5-4) at 245 GHz which, if detected between 14 and 24 GHz, would probe star formation activity and metal enrichment at redshifts of $z{\sim}\,9-16$.

Cyanides are additional molecules abundantly found in cosmic environments. Hydrogen cyanide, HCN, is a very common molecule in the dense molecular gas of the interstellar medium and a tracer of high-mass star forming regions. It is often detected together with HCO+ and HNC. These molecules have a plethora of (ro)vibrational transitions at several hundreds of GHz, such as (Imanishi et al., 2017): HCN(1-0) at 89 GHz, HCN(4-3) lines at 355, 363 and 365 GHz, HCN(8-7) lines at 709 and 712 GHz; HCO+(1-0) at 89 GHz, HCO+(3-2) lines at 268 and 269 GHz, HCO+(4-3) lines at 357 and 358 GHz, HCO+(6-5) line at 535 GHz, HCO+(8-7) lines at 713 and 716 GHz; HNC(1-0) at 91 GHz, HNC(8-7) lines at 725 and 730 GHz. Additional transitions in similar frequency ranges are obtained by considering the corresponding molecules formed by different isotopes: H13CN at 259 GHz, H13CO+ at 260 GHz, HN13C(3-2) at 261 GHz, HC15N(3-2) at 258 GHz, etc. These lines are supposed to be optically thin and can be used to estimate flux attenuation by line opacity for the corresponding HCN, HCO+ and HNC lines. Given their spectral frequencies, line emissions by cyanides are optimal to explore high-redshift star formation with SKA1 extensions above 14 GHz.

As an example, there are roughly 30 known molecular lines around 345 GHz - within 268-372 GHz (also available on the APEX online catalogue: http://www.apex-telescope.org/heterodyne/shfi/het345/lines/, or the splatalogue https://www.cv.nrao.edu/php/splat/), which, by adopting the suggested SKA-1 extension, would probe approximately redshifts $10<z<26$.

Further molecular emission can come from particular situations in space, where level populations are inverted, as is the case for radiation-excited species with multiple energy levels having very different decay times. This generates maser emission (microwave amplification by stimulated emission of radiation) from the slower transitions. Such transitions are sensitive to environmental conditions and are often easy to observe even in external galaxies (e.g. NH3). Among the many cases in nature, H, OH, H2O, NH3, SiO, CH2O, CH3OH, HCN masers are detectable in radio, mm and sub-mm bands, from roughly ∼1 GHz up to almost 900 GHz (such as: H recombination masers at 354 and 662 GHz; OH masers between 1.6 and 13 GHz; H2O masers at 22, 321 and 325 GHz; NH3 maser at 24 GHz; SiO masers at 43, 86, 129, 172, 2015 GHz; CH2O maser at 4.8 GHz; CH3OH masers at 217 and 230 GHz; HCN masers at 804 and 891 GHz; etc.; Pardo et al., 1998; Schilke & Menten, 2003). Hence, while masers below ∼100 GHz are interesting for star formation and AGNs at low or intermediate redshift, high-frequency masers above a few 100s of GHz have the potential to be exploited at z>6 to study star formation in the whole epoch of reionization.

All these regimes are optimal to study the development of complex molecules in the early Universe and to set the epoch when first and second-generation stars are actually born. Given the tight dependence of their abundances on the amounts of heavy elements spread by stars during the final phases of their life, these molecules carry out the imprints of the parent stellar population that enriched the Universe in primordial times and probe the reservoir of different heavy elements at different epochs.

Molecular line transitions as the ones mentioned above have been detected by ALMA in ultra-luminous IR galaxies in the nearby Universe, but high-redshift studies are still awaiting. Furthermore, since molecular emission is an excellent tracer of structure formation, the abundance of detected gas clumps at high redshift may help constraining underlying effects due to a variety of processes (e.g. non-Gaussianities, turbulence, dark-matter nature) that could determine variations in the expected mass distribution at early times.

Synergies with other instruments designed to explore the first Gyr, such as Euclid, JWST, WFIRST and ELT, will also allow us to derive optical/near-IR counterparts of early star forming galaxies featuring emission by molecular lines (Zackrisson et al., 2019).

Future extensions even beyond 24 GHz and up to 100 GHz will be further needed to study early atomic gas. Indeed, luminous fine-structure transitions from heavy elements (C, O, Si, Fe, etc.) have line frequencies of the order of thousands GHz (such as CII[158] at 1897 GHz or OI[145] at 2060 GHz) and could reveal primordial metal spreading at redshifts as high as z 20 if observed at 90-100 GHz. In the same epochs (around z 20), very early bursts of star formation in pristine environments could possibly be traced by H2 and HD line emissions (e.g., Kamaya and Silk, 2003), but these would require large collecting areas for frequencies reaching 533 GHz and exploiting future synergies with available mm and sub-mm telescopes, such as ALMA.

6.2.4 Dense molecular gas during the rise and fall of cosmic star formation

The reasons for the rise and decline of cosmic star formation activity from the first galaxies until today are not yet well understood, but it seems very likely that the conditions within the molecular gas from which such stars formed will be of prime importance to understand the underlying physics. The bright 12CO lines, while being our chief probe of molecular gas in high-redshift galaxies, are typically optically thick, and therefore do not probe the gas deep within the densest regions of molecular clouds in these galaxies, where stars form. Fainter lines of, e.g., HCN, HNC, or HCO+ arise from environments with $n{\sim}10^{6-7}$ cm^{-3}, typical of cloud cores, and opaque to even the most highly excited mid-J CO lines. They hold a great potential to probe the dense gas phase, its mass fraction and relation to the on-going star formation (e.g., Garcia-Burillo et al. 2012).

At low-z, the star-formation rates (SFR) of galaxies are tightly correlated with their total dense gas content traced by HCN, with a power law index of 1.0, suggesting that the star formation rate of these galaxies is driven by their dense gas fraction, with roughly constant star formation rate (Gao et al. 2004). At high redshift, however, star formation may intrinsically be more efficient, which should lead to different relationships between star formation rates and dense gas fraction than at low redshift. The most vigorous starbursts are only found at high redshift, which makes this an important measurement also for our understanding of the fundamental processes governing star formation in galaxies. Probing low-J transitions of HCN and CO is essential for such estimates, because higher-J transitions are likely to be dominated by gas excitation effects, which moreover depend on the local radiation field experienced by each molecule, and can therefore not be expected to be the same in both tracers.

While a comprehensive analysis of these tracers will require measuring the spectral line energy distribution in each tracer over ranges in excitation energy, only SKA will be able to probe the critical low-excitation lines in these species, which are too low frequency for ALMA at redshifts $z \gtrsim 1$. Covering the entire redshift range relevant to probe the cosmic rise and fall in cosmic star formation activity ($z \sim 1$-5) in either the 1-0 or 2-1 line of HCN requires a spectral coverage of Band 5 and 6 up to 50 GHz. A frequency cutoff at 25 GHz would produce a gap between z=5 and 6, and make the entire redshift range $z \approx 1 - 2.5$ inaccessible, i.e., the entire decline of cosmic star formation rate density.

Spectrally very close to HCN, and of roughly the same intensities, are the lines of HNC and HCO+, which can be used for a number of diagnostic purposes, together with other tracers of the physical and chemical conditions in dense gas like CS or SiO. For example, enhanced line fluxes can indicate non-thermal excitation processes like X-ray heating (in particular in the presence of AGN, Meijerink et al. 2007), IR pumping (Krips et al. 2008), or mechanical heating from gas outflows or supernova explosions (e.g., Loenen et al. 2008), which may change the gas energetics and contribute to regulating star formation in the dense cloud cores. Taken together with HCN and CO, these lines will allow us not only to measure the dense gas fractions within galaxies at cosmological distances, but also to study the physical processes which contribute to regulating this gas fraction, and its role in forming the stars in the massive galaxies we see today. HCN and other dense gas tracers are typically factors 10-20 fainter than CO. Using typical CO line fluxes already known for gas-rich galaxies at $z \sim 2$-3, with, for example, LFIR = 1×10^{12} $L_\odot$ in far-infrared luminosity, and a fiducial line width FWHM=500 km s^{-1} would suggest that SKA can reach SNR 5 for galaxy-integrated measurements in about 1 hr of observing time with 133 $SKA1-MID$ antennae at 20-30 GHz, and accordingly more for fainter galaxies or spatially resolved studies. This would be sufficient to probe the dense gas content in significant samples of galaxies in this redshift range, enough to enable systematic studies of the local star-formation conditions during the rise and fall of cosmic star formation activity.

6.2.5 [CI] as a probe of the molecular gas in galaxies during the Epoch of Reionization

Although CO(1-0) is an excellent tracer of the overall molecular gas in galaxies, it should become harder to observe with increasing redshift, as cosmic ray heating becomes more important (e.g., Combes et al 1999, Da Cunha et al. 2013). Moreover, shielding becomes less efficient because less evolved galaxies will have lower metallicities, lower gas-mass surface densities, and higher UV radiation fields. In such environments, much of the CO is likely to dissociate even where H_2 can survive (e.g., Bolatto et al. 2013), which would make such gas CO-faint. An interesting tracer of molecular gas in such environments (although not a molecule itself) is [CI]1-0. With an ionization potential of only 11.3 eV, it is generally associated with neutral (molecular and atomic) gas. It is an excellent probe of molecular gas mass in distant galaxies (e.g., Papadopoulos et al. 2004, Alaghband-Zadeh et al. 2013, Nesvadba et al. 2019), including of diffuse gas not even seen in [CII] emission (e.g., Gerin et al. 2015). It is relatively bright, $L_{[CI]1-0}/L_{CO43} \sim 0.1-1$), optically thin, and not strongly affected by changes in UV flux or gas excitation. [CI]1-0, at a rest-frame frequency of 492.16 GHz, is redshifted to frequencies 50 GHz for z=8.8. In galaxies at redshifts z9-10, [CI]1-0 would thus be an excellent probe of the total gas mass in galaxies, and highly complementary to a tracer of UV photon budget or star formation rate like [CII]. Bright [CII] emitting galaxies at the highest redshifts where such lines are currently known, $z \sim 7$, can reach line luminosities of up to log $L_{[CII]} \sim 10^{8.5}$ $L_\odot$ (Smit et al. 2018). Adopting similar line fluxes for galaxies at $z \sim 10$-12, and a ratio of $L_{[CII]}/L_{[CI]}$ of 10-100 (Kaufman et al. 1999), with 133 SKA1-MID antennae, [CI]1-0 from such galaxies could be detected in a few hrs with SNR$\geq$5.

References

Alaghband-Zadeh, S., Chapman, S. C., Swinbank, A. M., et al. 2013, MNRAS, 435, 1493
Bolatto, A. D., Wolfire, M., & Leroy, A. K. 2013, ARA&A, 51, 207
Bouwens, R. J., Stefanon, M., Oesch, P. A., et al. 2019, ApJ, 880, 25
Combes, F., & Wiklind, T. 1997, ApJ, 486, L79
Combes, F., Maoli, R., & Omont, A. 1999, A&A, 345, 369
Combes, F. 2018, A&A Rev., 26, 5
Combes, F., Gupta, N., Jozsa, G. I. G., & Momjian, E. 2019, A&A, 623, A133
da Cunha, E., Groves, B., Walter, F., et al. 2013, ApJ, 766, 13
Gao, Y., & Solomon, P. M. 2004, ApJ, 606, 271
García-Burillo, S., Usero, A., Alonso-Herrero, A., et al. 2012, A&A, 539, A8
Gerin, M., Ruaud, M., Goicoechea, J. R., et al. 2015, A&A, 573, A30
Imanishi, M., Nakanishi, K., & Izumi, T. 2017, ApJ, 849, 29
Kamaya, H., & Silk, J. 2003, MNRAS, 339, 1256
Kaufman, M. J., Wolfire, M. G., Hollenbach, D. J., & Luhman, M. L. 1999, ApJ, 527, 795
Koopmans, L., Pritchard, J., Mellema, G., et al. 2015, Advancing Astrophysics with the Square Kilometre Array (AASKA14), 1
Krips, M., Neri, R., García-Burillo, S., et al. 2008, ApJ, 677, 262
Loenen, A. F., Spaans, M., Baan, W. A., & Meijerink, R. 2008, A&A, 488, L5
Madau, P., & Dickinson, M. 2014, ARA&A, 52, 415
Maio, U., Ciardi, B., Dolag, K., Tornatore, L., & Khochfar, S. 2010, MNRAS, 407, 1003
Meijerink, R., Spaans, M., & Israel, F. P. 2007, A&A, 461, 793
Muller, S., Beelen, A., Guélin, M., et al. 2011, A&A, 535, A103
Murphy, M. T., Webb, J. K., & Flambaum, V. V. 2003, MNRAS, 345, 609
Nesvadba, N. P. H., Cañameras, R., Kneissl, R., et al. 2019, A&A, 624, A23
Papadopoulos, P. P., Thi, W.-F., & Viti, S. 2004, MNRAS, 351, 147
Pardo, J. R., Cernicharo, J., Goicoechea, J. R., & Phillips, T. G. 2004, ApJ, 615, 495
Righi, M., Hernández-Monteagudo, C., & Sunyaev, R. A. 2008, A&A, 489, 489
Schilke, P., & Menten, K. M. 2003, ApJ, 583, 446
Smit, R., Bouwens, R. J., Carniani, S., et al. 2018, Nature, 553, 178
Tacconi, L. J., Neri, R., Genzel, R., et al. 2013, ApJ, 768, 74
Tacconi, L. J., Genzel, R., Saintonge, A., et al. 2018, ApJ, 853, 179
Wiklind, T., & Combes, F. 1996, Nature, 379, 139
Zackrisson, E., Majumdar, S., Mondal, R., et al. 2019, arXiv:1905.00437
Ziurys, L. M. 2006, Proceedings of the National Academy of Science, 103, 12274

6.3 Water masers in distant galaxies

Andrea Tarchi (INAF-Osservatorio Astronomico di Cagliari)
Paola Castangia (INAF-Osservatorio Astronomico di Cagliari)

The study of the physical properties, the structure, and the kinematics of the gas surrounding supermassive black holes (SMBHs) is fundamental to answering some of the open-ended questions regarding active galactic nuclei (AGN), e.g. whether the torus is geometrically thick, if the polar outflow is always present, and whether the broad line region (BLR) and the torus are produced by accretion disk winds (for a recent review see Ramos Almeida et al. 2017).

The radio emission from luminous H_2O masers, the so-called "megamasers"[10], constitutes the only way to directly map the molecular gas at sub-parsec distance from SMBHs. Very Long baseline Interferometry (VLBI) and single-dish monitoring studies can be used to determine the geometry of accretion disks and to estimate the enclosed dynamical masses (Miyoshi et al. 1995; Kuo et al. 2011; Gao et al. 2017). H_2O masers currently provide the most precise method to determine black hole masses in external galaxies, especially in the case of type 2 AGN, where other methods, such as those based on optical broad lines emission, cannot be used. Measuring black hole masses in AGN, allows one to estimate Eddington luminosities and accretion efficiencies. In addition, this studies are extremely relevant to probe the low mass end of the $M_{BH} - \sigma^*$ relation, so far, almost uniquely derived for elliptical galaxies with larger BH masses (e.g., Greene et al. 2010).

Water maser emission can also be associated with ejection mechanisms such as radio jets or wide-angle nuclear outflows (winds). Detailed studies of jet-masers allow us to pinpoint regions of strong interaction of the jets with the interstellar medium of the host galaxy (e.g., Castangia et al. 2019) and

[10] When studied in detail, water megamaser sources have always been found associated with AGN activity. Indeed, in this chapter, we will discuss AGN-related maser sources. A description of the potential of the SKA-1 MID array for studies of stellar and interstellar masers in nearby galaxies is addressed in another chapter of this book.

to derive relevant physical quantities of the jet material, like its velocity and density (e.g., Peck et al. 2003). Water maser observations in Circinus (Greenhill et al. 2003) and NGC 3079 (Kondratko et al. 2005), instead, seem to have resolved outflowing clouds at <1 pc from the SMBH. VLBI maps of the water emission from Circinus have shown the potential of this kind of sources to trace wide-angle nuclear winds up to few parsecs from the central engine.

Each megamaser source is, therefore, a goldmine of information on the (sub)-parsec-scale environment around AGN, making the discovery of new sources and their interferometric follow-ups crucial for their study. However, despite the great number (thousands) of galaxies surveyed in search for 22 GHz water masers, only 178 have been detected (Braatz et al. 2018), the majority being radio-quiet AGN in the local Universe (z < 0.05). The NRAO Key Science Megamaser Cosmology Project (MCP; Braatz et al. 2009), for example, observed about 2800 obscured AGN (Seyfert 2), mainly selected from large optical surveys, such as SDSS, 6dF and 2MRS, detecting water maser emission in only 3% of the targets (Braatz et al. 2018). Higher detection rates have been obtained selecting galaxies on the basis of their IR and X-ray properties. In particular, a sample of galaxies with IRAS point source flux density >50 Jy, yielded a maser detection rate of 23% (Henkel et al. 2005; Surcis et al. 2009). Recently, Panessa et al. (2018) obtained a detection rate of ∼20% in a complete sample of AGN selected in the 20–40 keV energy range. Through a combination of mid-IR (*IRAS*) and X-ray (*XMM-Newton*) data, instead, Severgnini et al. (2012) selected a well defined sample of 36 heavily absorbed AGN ($N_{\rm H} \geq 10^{23}$ cm^{-2}) that have been searched for 22 GHz water maser emission. The maser detection rate of this sample is a remarkable 50%, one of the highest ever obtained in extragalactic maser searches (Castangia et al. 2019).

6.3.1 The role of SKA-1 MID

As mentioned before, the detection rates of water maser surveys have been, so far, disappointingly low, when not associated with particularly well-designed samples. In particular, no water maser source, with the exception of two cases, J0804+3607 (at z=0.66; Barvainis & Antonucci 2005) and J0414+0534 (at z=2.64, Impellizzeri et al. 2008) has been, so far, reported at redshifts larger than 0.1. Indeed, the combination of the high sensitivity required in surveys and the large number of objects to be searched for maser emission has played a role against a more cospicuous number of detections.

With the advent of the SKA project, the possibility will become real to perform either blind surveys of large areas in the sky and/or deep targeted surveys of large samples of selected galaxies up to cosmological redshifts. While systematic searches for unmagnified water masers at cosmological distances ($z > 1$) would require the extraordinary sensitivity of SKA Phase 2 (McKean et al 2011), a significant improvement in the number of detections and follow-up of H_2O masers at intermediate ($0.05 < z < 0.5$) and low ($z < 0.05$) redshifts will be possible already with SKA1-MID, if the frequency coverage will be extended up to 25 GHz. Indeed, the chance to take profit of the performances planned for SKA1 also at frequencies of interest for searches of water maser sources in nearby (around 22 GHz) and distant (therefore, proportionally redshifted) galaxies will allow us to significantly increase the number of maser sources and, in particular, to study these objects in radio loud galaxies (typically located at relatively larger distances from us), and to test the possible evolution of the maser luminosity function (LF) with redshift. A number of studies have indicated galaxy evolution scenarios, mostly related to a strong increase in the galaxy merging rate with redshift, that support an evolution of the maser LF with $(1+z)^m$ with m=4 or m=8 (Darling & Giovanelli 2002, McKean et al. 2011, and references therein).

Targeted searches: In this framework, the SKA1-MID will already be able to deliver relevant results by performing targeted searches of extremely large samples of galaxies. The same spectral-line sensitivity of a 100-m class single-dish (i.e., the antennas that are typically involved in water maser searches) will be reached by SKA1 in a factor 10 less time, thus allowing to search (with comparable sensitivity) much larger samples. This will yield the detection of many more objects locally and, also when considering that the water maser LF is a relatively steep power-law (see Henkel et al. 2005), of a still significant number of maser sources also at larger distances (up to $z \sim 0.5$). These latter sources will likely be detected among the brighter members of the megamaser class. Nevertheless, any such detection will yield the potential to detect and explore the maser phenomenon, and the AGN activity at which it is associated, in classes of galaxies where, so far, no maser have been found.

Blind searches: as shown by (McKean et al., 2011), when approaching cosmological distances $z \geq 1$, blind surveys of water maser sources with SKA-2 will become extremely valuable, particularly if, as expected, an evolution of the water maser LF is present. Under this latter assumption, as shown in Fig. 1[11], also blind searches with the SKA1 array would already yield, at $z \geq 1$, a significant number of expected masers, when areas of the order of a square degree (about 65 pointings, considering the field of view of the SKA1 array at 10 GHz) are searched for, and a sensitivity of $\sim$ 0.15 mJy for a 10-km/s channel (reachable in about 15 hours on-source per pointing, and hence, a total of $\sim$ 1000 hours for each 2.5 GHz band) is attained. This is surely feasible thanks to the enhanced sensitivity and the large field of view of the SKA1 array, and together with the large instantaneous bandwiths ($\sim$ 2.5 GHz) available, that allow one to cover all at once relevant redshift ranges. For smaller redshifts, instead, blind surveys turn out to be less effective than targeted ones, becoming, however, more relevant if and when a large fraction of sky is covered, with high-enough sensitivity, by the surveys. Since this may imply investing a considerable amount of observing time, a good degree of commensality and complementarity with other projects would be ideal. In Fig. 2, we show a plot with the number of masers as a function of redshift ($z \leq 0.7$) for a quarter sky search, with a total integration time of $\sim$3000 hours for each 2.5-GHz band (with integration time and sensitivity, per pointing, of 5 sec and 15 mJy/chan, respectively). Assuming an evolution of the LF with redshift (see above), in the aforementioned survey, at redshift between 0.1 and 0.5, we would expect to detect up to 50 new maser sources, depending on the LF evolution exponents.

Independent of which survey strategy (targeted or blind) will be adopted, it has to be pointed out that the inclusion of the SKA1-MID array in the search for extragalactic water masers will, by definition, be a game-changer since it will permit the detection of many more sources in a part of the sky (the Southern one) so far, largely unexplored or observed with shallow sensitivity. Indeed, the radio astronomical facilities that have access to the sky with declination below –40 degrees are presently not sensitive enough at frequencies higher than 15 GHz. The limited antenna efficiency of the 64-m Parkes telescope at frequencies around 22 GHz and collecting area of the Australian Telescope Compact Array (6 antennas of 22 meters) do not allow to perform searches for water masers, as the one described above, in a reasonable amount of time. In addition, the 70-m Tidbinbilla NASA antenna, that has shown good capabilities for extragalactic spectral-line surveys at K-band (e.g., Surcis et al. 2009), can only be used for a very limited amount of time for astronomical projects.

At last, one further remark also has to be made regarding the relevance of the high angular resolution. Indeed, a large fraction of the studies for which water masers are fundamental require follow-ups at resolution reachable only with Very Long Baseline Interferometry networks. A synergy between the SKA1 (and successors) and the Global VLBI framework is then more than desirable.

Acknowledgements

We would like to thank Gabriele Surcis and Matteo Murgia for valuable and constructive suggestions during the development of this study.

[11]The plot was produced by adapting the computational steps reported by Darling & Giovanelli (2002) for OH megamasers (their Eq. 18) for the water maser case.

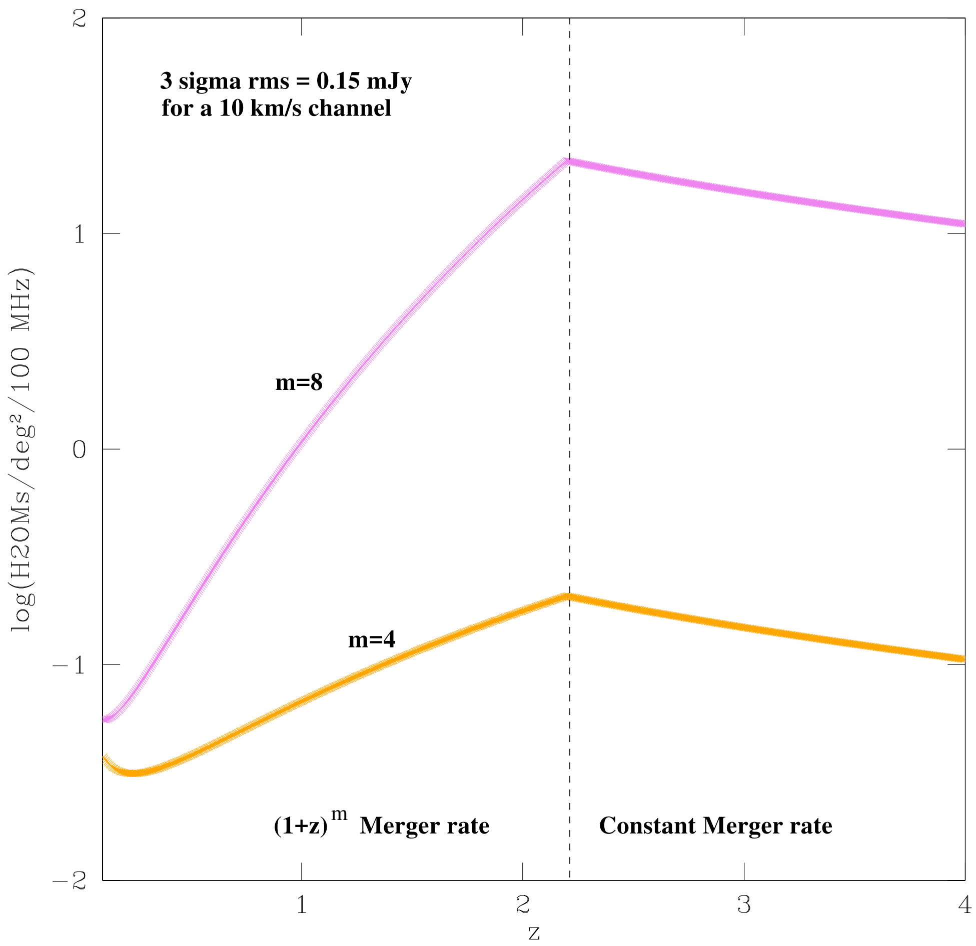

Figure 34: Density of detectable water masers as a function of redshift ($0.1 \leq z \leq 4$), assuming a LF evolution, increasing with redshift by $(1+z)^m$, with m equal to 4 or 8 up to z =2.2, and then becoming constant (see text). The values are computed considering a survey covering an area of a square degree (about 65 pointings, considering the field of view of the SKA-1 array at 10 GHz) and an integration time of 15 hours per pointing, yielding a sensitivity of $\sim$ 0.15 mJy for a 10-km/s channel. As cosmological parameters, we used H_o=70 km/(s Mpc), Ω_M=0.3, and Ω_{Lambda}=0.7.

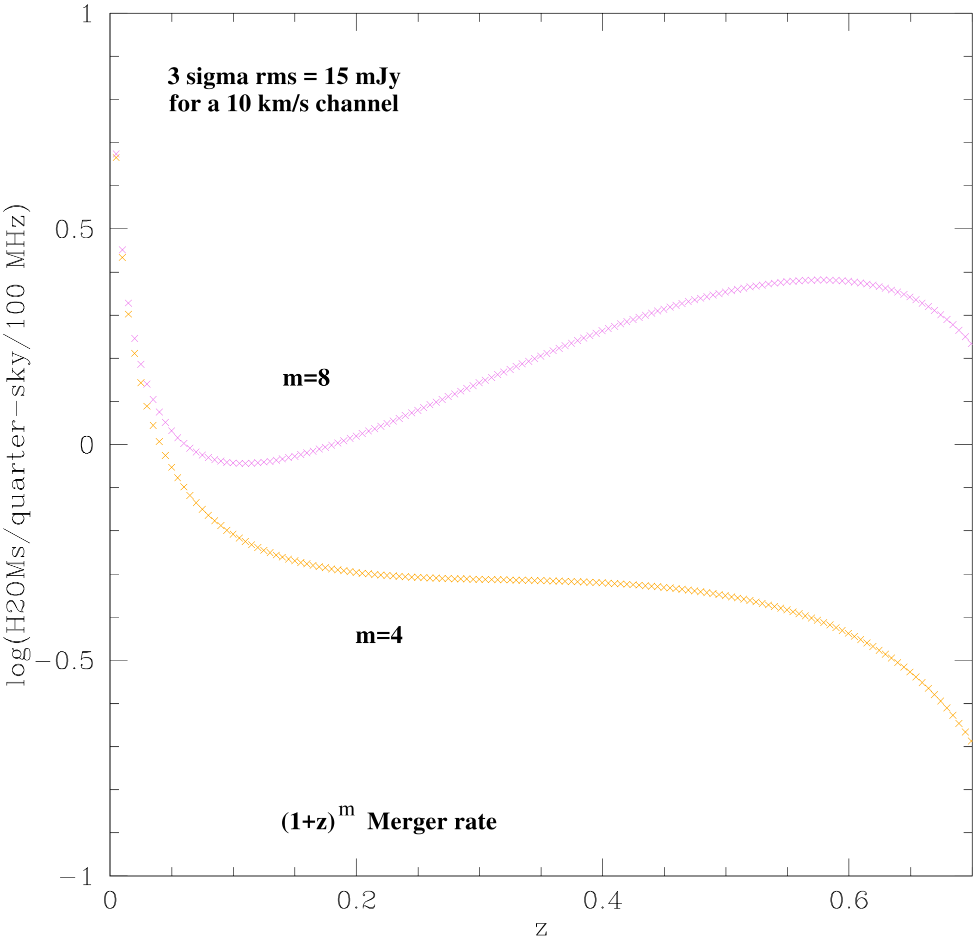

Figure 35: Density of detectable water masers as a function of redshift ($z \leq 0.7$), assuming a LF evolution, increasing with redshift by $(1+z)^m$, with m equal to 4 or 8 (see text). The values are computed considering a quarter sky survey (about 2×10^6 pointings, considering the field of view of the SKA-1 array at 18 GHz), and an integration time of 5 seconds per pointing, yielding a sensitivity of $\sim$ 15 mJy for a 10-km/s channel. As cosmological parameters, we used H_o=70 km/(s Mpc), Ω_M=0.3, and Ω_{Lambda}=0.7.

References

Barvainis R. & Antonucci R., 2005, ApJ, 628, L89
Braatz, J., Condon, J., Henkel, C., et al. 2018, in Astrophysical Masers: Unlocking the Mysteries of the Universe, eds. A. Tarchi, M. J. Reid, P. Castangia, IAU Symp., 336, 86
Braatz, J., Reid, M., Humphreys, E. et al., BAAS, 41, 718
Castangia, P., Surcis, G., Tarchi, A., et al., 2019, A&A, 629A, 25C
Darling J. & Giovanelli R, 2002, ApJ, 572, 810
Gao, F., Braatz, J. A., Reid, M. J., et al. 2017, ApJ, 834, 52
Greene, Jenny E., Peng, C. Y., Kim, M., et al, 2010, ApJ, 721, 26G
Greenhill, L. J., Booth, R. S., Ellingsen, S. P., et al. 2003, ApJ, 590, 162
Henkel, C., Peck, A. B., Tarchi, A., et al. 2005, A&A, 436, 75
Impellizzeri, C. M. V., McKean, J. P., Castangia, P., et al., 2008, Nature, 456, 927
Kondratko, P. T., Greenhill, L. J., & Moran, J. M. 2005, ApJ, 618, 618
Kuo, C. Y., Braatz, J. A., Condon, J. J., et al. 2011, ApJ, 727, 20
McKean, J. P., Impellizzeri, C. M. V., Roy, A. L., Castangia, et al., 2011, MNRAS, 410, 2506
Miyoshi, M., Moran, J., Herrnstein, J., et al. 1995, Nature, 373, 127
Panessa, F., Castangia, P., Tarchi, A., et al., 2018, in Astrophysical Masers: Unlocking the Mysteries of the Universe, eds. A. Tarchi, M. J. Reid, P. Castangia, IAU Symp., 336, 96
Peck, A. B., Henkel, C., Ulvestad, J. S., et al. 2003, ApJ, 590, 149
Ramos Almeida, C., & Ricci, C. 2017, Nat. Astron., 1, 679
Surcis, G., Tarchi, A., Henkel, C., et al. 2009, A&A, 502, 529
Severgnini, P., Caccianiga, A., & Della Ceca, R. 2012, A&A, 542, A46

6.4 Extended emission from radio-loud active galaxies with SKA1-MID Band 6

Dharam V. Lal (National Centre for Radio Astrophysics NCRA-TIFR, Post Box 3, Ganeshkhind PO, Pune 411007, India), Martin J. Hardcastle (School of Physics, Astronomy and Mathematics, University of Hertfordshire, College Lane, Hatfield, Hertfordshire AL10 9AB, UK), Judith H. Croston (School of Physical Sciences, The Open University, Walton Hall, Milton Keynes, MK7 6AA, UK), Tiziana Venturi (Istituto di Radioastronomia, INAF, Via Gobetti 101, 40129 Bologna, Italy)

Band 6 capabilities with SKA1–MID offer two key advantages to continuum radio-loud active galactic nuclei (RLAGN) studies — a greatly extended frequency range and significantly increased resolution. Both are important for constraining the energetic impact of RLAGN on the universe over cosmic time.

6.4.1 Resolution

Historically much work has focused on powerful classical RLAGN, and these objects are often physically large, extending to scales of hundreds of kilo-parsec (kpc) to Mega-parsec (Mpc) (Laing, Riley & Longair, 1983; Bridle & Perley, 1984). To image their extended structure and measure physical size and other parameters of their lobes, such as their Fanaroff-Riley classification (Fanaroff & Riley, 1974) arcsec-scale resolution is often sufficient. The imaging of these largest-scale structures in Band 6 will be limited by the telescope primary beam (~ 1.5 arcmin at the highest frequencies).

However, it is very important to understand the statistics and evolution of the physically small, sub-kpc luminous population, some, but not all, of which are expected to evolve into hundred-kpc scale objects (Figure 36 and An & Baan 2012). It is also increasingly clear that at the much lower sensitivity limits of surveys with the SKA precursors there exists a large population of low-luminosity, physically small AGN, requiring different models to explain the distribution of source properties (e.g. Sadler et al., 2014; Baldi, Capetti & Giovannini, 2015; Whittam et al., 2017; Hardcastle et al., 2019). These objects must be resolved at some scale — indeed comparison of VLA and VLBI-scale data shows that they do have extended emission on the kpc to sub-kpc scale (Baldi et al. in prep.). Resolution is also key on these scales to separate potentially resolved radio emission from emission due to star formation.

Relative to Band 5, Band 6 provides a factor 3 higher resolution, up to 20 milli-arcsec (mas), and relative to existing and planned VLBI arrays it provides good short-baseline coverage which means that extended structures, if present, will not be resolved out. The maximum 20 mas resolution implies the ability to study sub-kpc structures out to all possible redshifts. The sensitivity of SKA1, even at the top of band 6, is such that compact sources with luminosities around 10^{24} W Hz^{-1} at 150 MHz, as seen routinely with LOFAR, can be detected and imaged in short continuum observations out to $z \sim 0.5$. This means that with targeted observations based on a Band 1 or SKA precursor survey, and band 5 and 6 followup, it would be possible to get a complete, unbiased view of the distribution of radio AGN physical sizes and luminosities over cosmic time, an essential input into models of RLAGN energetic impact on their environment since physical size can be used, given a dynamical model, as a proxy of source age in unbiased samples (Hardcastle, 2018; Hardcastle et al., 2019).

In addition, the impact of high-resolution, high-frequency imaging with good short-baseline coverage on our understanding of large, luminous sources should not be ignored. There is increasing evidence that even on hundred-kpc scales compact, pc-scale substructures in jets and hotspots can have an important role in particle acceleration (e.g. Hardcastle et al., 2016). These structures can only be properly understood with an instrument that offers very high resolution and sensitivity together with the short-baseline capability to properly image the surrounding imaging structure. Our understanding of particle acceleration sites such as the jets and hotspots of nearby powerful sources is likely to be revolutionised by the capabilities offered by Band 6.

6.4.2 Spectral studies

Although extragalactic radio sources are the dominant radio source population in the sky at low radio frequencies, they have been relatively poorly studied at mm wavelengths. Where information on radio

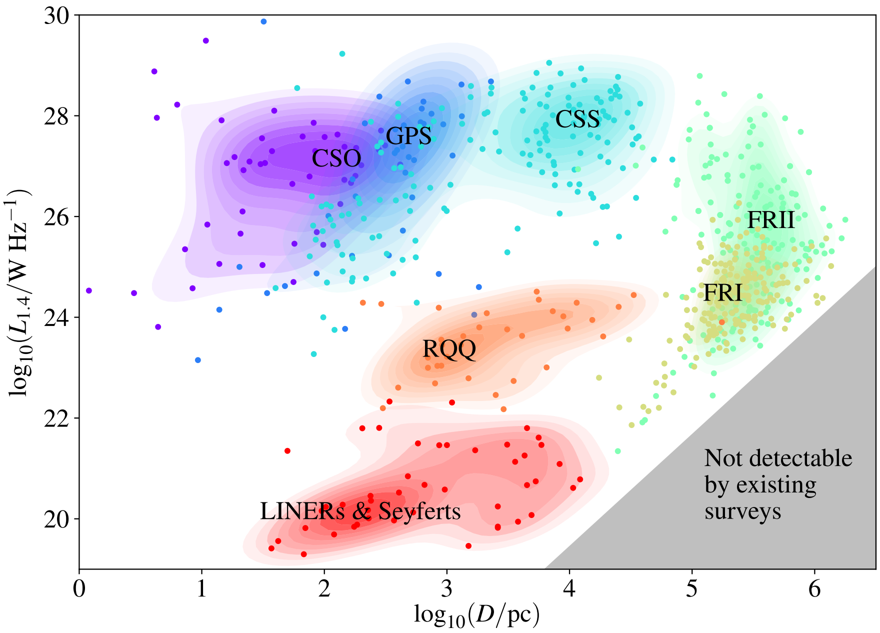

Figure 36: Power/linear-size plot (Baldwin, 1982) for different types of radio-loud and radio-quiet AGN, adapted from plots presented by An & Baan (2012) and Jarvis et al. (2019). Points show individual objects and coloured contours represent a smoothed estimator of source density. The different categories of source shown are: compact symmetric objects (CSO), Giga-Hertz peak spectrum (GPS), compact steep-spectrum (CSS) objects, all objects so classed by An & Baan (2012); FR I, FR II, all objects so classed by either An & Baan (2012) or Mingo et al. (2019) (points are representative); radio quiet quasar (RQQ), objects from Jarvis et al. (2019) and Kukula et al. (1998); Seyfert galaxies and low-ionisation nuclear emission-line region (LINER) sources, objects from Gallimore et al. (2006); and Baldi, Capetti & Massaro (2018). The shaded bottom-right corner shows the effect of surface-brightness limitations. Schematic taken from Hardcastle & Croston (in preparation).

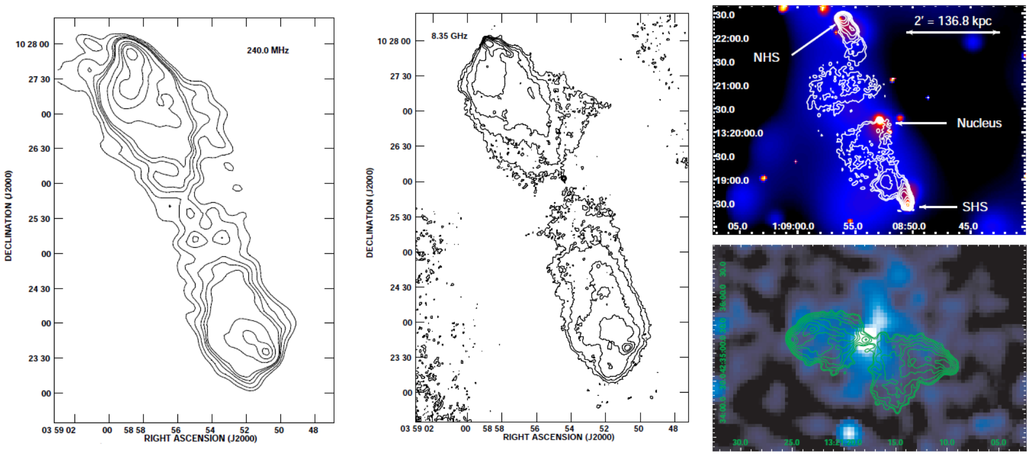

Figure 37: GMRT 240 MHz (left panel) and the VLA 8.4 GHz (middle panel) images of 3C 98 showing (nearly) identical radio morphologies and sizes over a factor of >50 in frequency or a factor of ∼30 in electron energies. Hardcastle & Looney et al. (2001) using observations of a handful of radio galaxies at 90 GHz with limited sensitivity note that by the time we get to 100 GHz there might be obvious morphological differences in lobes. The right panel shows *Chandra image of 3C 33 (upper panel) and 3C 285 (lower panel) in the 0.5–2.0 keV band with 1.5 GHz radio contours overlaid.*

sources at mm wavelengths is available in the literature (Steppe et al., 1995) it tends to be restricted to tables of integrated flux densities. This is presumably due to the intrinsic difficulty of mm-wave observations compared to those at 1–10 GHz; radio galaxies have steep integrated spectra.

However, high-frequency imaging observations of radio galaxies has significant astrophysical importance. It has long been known that the synchrotron spectra of FR II radio galaxies systematically steepen with distance from the hot spots (Alexander & Leahy, 1987), while FR I radio galaxies show spectra that steepen with distance along the jets (Burch, 1977). The steepening is interpreted as evidence for 'synchrotron ageing', whereby the synchrotron energy loss process depletes high-energy electrons in the source as they move away from the acceleration site (Pacholczyk, 1970; Jaffe & Perola, 1973; Leahy, 1991). If we are really observing the effects of synchrotron ageing, then in principle resolved images of the radio spectra allow us to measure plasma age as a function of position in the source, which allows the determination of quantities like total source age and expansion speed, and hence feeds directly into estimates of jet power and environmental impact.

While broad-band radio observations have established the reality of spectral ageing at low frequencies (Lal & Rao, 2004, 2007; Sakelliou & Hardcastle, 2008; Harwood et al., 2013), high-frequency observations are important in this context because the spectral age probed by a frequency ν goes as $\nu^{-1/2}$. Thus, in principle, observations at the top of Band 6 probe electrons an order of magnitude younger than those seen in Band 1. Relative to existing studies with the VLA, GMRT or LOFAR, SKA spectral studies will be able to produce well-sampled, matched-resolution images across two decades in frequency for appropriately sized sources thanks to SKA's unrivalled (u, v) coverage. Note the added value of bridging the gap in frequency between the current plans for SKA1-MID and ALMA, basically allowing a seamless frequency coverage from about 0.4 GHz to hundreds of GHz. For compact, young sources, spectral ageing studies are likely *only* to be possible with the frequencies made available by Band 6 (e.g. Heesen et al., 2014).

Broad-band spectral studies have the capability to answer three key questions:

1. What are the spectra of aged regions? Are they consistent across a broad spectral range with theoretical models?

2. Are the spectral ages derived from detailed imaging consistent with dynamical ages?

3. Determine if the particles responsible for the low-frequency emission are entirely co-spatial with

those responsible for the high-frequency emission as seen in FR II radio galaxies (see also Figure 37).

The first of these questions is important because it gives insight into the micro-physics of the radio structures — in spite of many studies GHz-frequency work does not provide a definitive answer to the question of whether pitch-angle scattering is effective during loss as expected in the models of Jaffe & Perola (1973), for example (e.g. Harwood et al., 2013). High-resolution, high-fidelity, truly broadband images should answer this by unambiguously locating the exponential cutoff in the synchrotron spectrum at high energies if it exists, and maybe allow us to probe inhomogeneities in the magnetic field strengths as well (Tribble, 1993; Hardcastle, 2013).

Both, the second and third questions are fundamental to the interpretation of spectral age measurements. The so-called 'spectral age problem' (Eilek, 1996) is the fact that spectral ages seem to be significantly younger than the expected dynamical ages where these can be modelled. Although the details of this discrepancy depend on factors like the unknown lobe magnetic field strength (and its history), the problem persists even when the best possible field strengths are used (Harwood et al., 2013). Possible solutions include mixing of plasma of different ages in the lobes (Rogers, Shabala & Krause, 2018), and/or *in situ* particle acceleration in the lobe, which should be identifiable as a spectral *flattening* in certain parts of the lobes at high frequency (Lal & Rao, 2007). Existing low-resolution, low-sensitivity studies of small samples of lobes at high radio frequencies cannot test this model (Hardcastle & Looney et al., 2001) but SKA broad-band observations including band 6 will enable us to establish the spectral properties of morphologically defined subsamples of RLAGN on a *statistical* rather than an individual basis. In addition to solving the spectral age problem and helping us to calibrate observed spectral ages as a constraint on radio source models, direct evidence for *in situ* leptonic particle acceleration in the lobes would give a previously unavailable insight into lobe micro-physics and might connect to models of the ultra-high-energy cosmic ray population (Hardcastle, 2010; Matthews et al., 2019).

References

Alexander P., Leahy J. P., 1987, MNRAS, 224, 1
An T., Baan W. A., 2012, ApJ, 760, 77
Baldi R. D., Capetti A., Giovannini G., 2015, A&A, 576, A38
Baldi R. D., Capetti A., Massaro F., 2018, Astronomy and Astrophysics, 609, A1
Baldwin J. E., 1982, in IAU Symposium, Vol. 97, Extragalactic Radio Sources, Heeschen D. S., Wade C. M., eds., pp. 2124
Bridle A. H., Perley R. A., 1984, ARA&A, 22, 319
Burch S. F., 1977, MNRAS, 180, 623
Eilek J. A., 1996, in Energy Transport in Radio Galaxies and Quasars, Hardee P.E., Bridle A.H., Zensus J.A., ed., ASP Conference Series vol. 100, San Francisco, p. 281
Fanaroff B. L., Riley J. M., 1974, MNRAS, 167, 31P
Gallimore J. F., Axon D. J., ODea C. P., Baum S. A., Pedlar A., 2006, AJ, 132, 546
Hardcastle M. J., Looney L. W., 2001, MNRAS, 320, 355
Hardcastle M. J., 2010, MNRAS, 405, 2810
Hardcastle M. J., 2013, MNRAS, 433, 3364
Hardcastle M. J., 2018, MNRAS, 475, 2768
Hardcastle M. J. et al., 2016, MNRAS, 462, 1910
Hardcastle M. J. et al., 2019, A&A, 622, A12
Harwood J. J., Hardcastle M. J., Croston J. H., Goodger J. L., 2013, MNRAS, 435, 3353
Heesen V., Croston J. H., Harwood J. J., Hardcastle M. J., Hota A., 2014, MNRAS, 439, 1364
Jaffe W. J., Perola G. C., 1973, A&A, 26, 423
Jarvis M. E. et al., 2019, MNRAS, 485, 2710
Kukula M. J., Dunlop J. S., Hughes D. H., Rawlings S., 1998, Monthly Notices of the Royal Astronomical Society, 297, 366
Laing R. A., Riley J. M., Longair M. S., 1983, MNRAS, 204, 151
Lal D. V., Rao A. P., 2004, A&A, 420, 491
Lal D. V., Rao A. P., 2007, MNRAS, 374, 1085
Leahy J. P., 1991, in Beams and Jets in Astrophysics, Hughes P.A., ed., Cambridge University Press, Cambridge, p. 100
Matthews J. H., Bell A. R., Blundell K. M., Araudo A. T., 2019, MNRAS, 482, 4303
Mingo B. et al., 2019, MNRAS, 488, 2701
Pacholczyk A. G., 1970, Radio Astrophysics. Freeman, San Francisco
Sadler E. M., Ekers R. D., Mahony E. K., Mauch T., Murphy T., 2014, MNRAS, 438, 796
Sakelliou I., Hardcastle M. J., Jetha N. N., 2008, MNRAS, 384, 87
Steppe H., Jeyakumar S., Saikia D. J., Salter C. J., 1995, A&AS, 113, 409
Tribble P. C., 1993, MNRAS, 261, 57
Turner R. J., Rogers J. G., Shabala S. S., Krause M. G. H., 2018, MNRAS, 473, 4179
Whittam I. H., Jarvis M. J., Green D. A., Heywood I., Riley J. M., 2017, MNRAS, 471, 908

6.5 Observations of the Sunyaev Zel'dovich effect using Band 5+

Yvette Perrott (Victoria University Wellington, New Zealand), Keith Grainge (University of Manchester, UK)

In the Rayleigh-Jeans regime the Sunyaev–Zel'dovich (SZ) spectrum has a ν^2 dependence, meaning that observing at higher frequencies compared to the current Band 5 maximum increases the strength of the signal dramatically. This must be balanced against (i) the decreasing antenna sensitivity and (ii) the lengthening baselines (measured in λ) as the frequency increases, when observing an extended low-surface-brightness source. To address (i), we calculate the overall signal-to-noise ratio (SNR) for an unresolved SZ signal as a function of frequency, and show this in Fig. 38 normalized by the value at the central frequency of the upper half of Band 5 (14.11 GHz). The SNR increases by a factor of ≈ 1.5 by 25 GHz, and reaches a broad maximum of ≈ 2.5 at 37.5 GHz. We will consider simulations at central frequencies of 23.75 GHz and 37.5 GHz (Band 6) with a bandwidth of 2.5 GHz, to compare with simulations at the current highest frequency band centred at 14.11 GHz with 2.5 GHz bandwidth. Since observing time $t \propto (\text{sensitivity/signal})^2$, these SNR improvements result in reductions in observing time by factors of ≈ 2.3 and 6.1 respectively.

To address (ii), the angular scale and structure must be considered using realistic cluster models. In Grainge et al. 2015 (arXiv:1412.5868) we conducted two classes of simulations to investigate the SKA's capabilities as an SZ instrument and we revisit these to examine the effect of shifting the band centre to higher frequency. In Fig. 39 we show the predicted (noise-less) signal in uv-space as sampled by the SKA1-MID antenna configuration at our three reference central frequencies for a $z = 2.0$, $M_{200} = 3 \times 10^{14} M_{\odot}$ cluster. Due to its high redshift and low mass this cluster has a relatively small

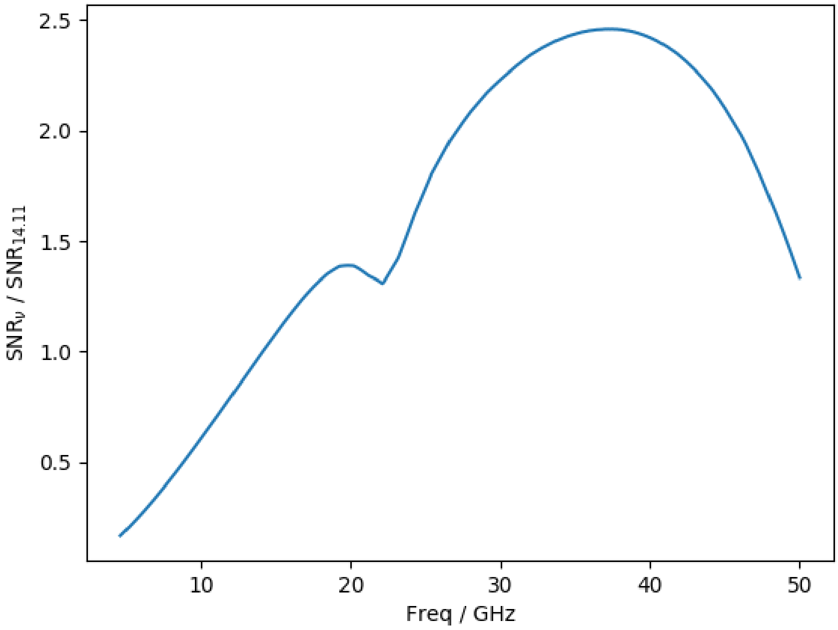

Figure 38: Signal-to-noise ratio as a function of frequency for an unresolved SZ source, normalized by the value at 14.11 GHz.

angular extent. The Figure shows all of the visibilities sampled in a one-hour observation (small points), and bins in uv-space where the signal would be detected at $> 3\sigma$ (large points). It can be seen that even though the signal increases at higher frequency, the combination of higher noise and longer baselines means that the bulk cluster signal detection is less significant.

The increased SNR of the higher-frequency bands are therefore most useful to map small-scale cluster features at high angular resolution. For example, recent observations (Abdulla et al. 2019, 2019ApJ...871..195A) have shown that the suppression of SZ signal in X-ray cavities of clusters is detectable and can be used to put constraints on the composition and energetics of the cavities. We investigated the detectability of cavity signals with radii ranging from 30 kpc (the smallest cavities observed in X-ray; Hlavacek-Larrondo et al 2015, 2015ApJ...805...35H) to 90 kpc (similar to the largest cavities observed in MS 0735.6+7421, e.g. 2019ApJ...871..195A) in a cluster with $M_{200} = 5 \times 10^{14} M_\odot$ at $z = 1.5$. Fig. 40 shows the number of 8-hour observations required to detect these cavities at 5σ in each band; for the smaller cavities the detection at 5σ rapidly becomes too expensive while the higher frequencies remain viable. In Fig. 41 we show a simulated 3-day (with 8 hours per day, i.e. 24 hours total) observation of 40 kpc radii bubbles, with the bulk cluster signal subtracted. The detection clearly improves at higher frequency.

6.5.1 Foregrounds

It should also be noted that the confusing foregrounds are typically synchrotron sources that have a falling $\approx \nu^{-0.7}$ spectrum. Therefore spectral discrimination of the SZ from point source contaminants becomes ≈ 4 and 14 times easier at 23.75 and 37.5 GHz respectively. For clusters with strong halo or relic sources, the effect is even stronger because of the typically much steeper $\approx \nu^{-1.4}$ spectrum. The additional power for spectral discrimation this offers is particularly important since halos and relics are significantly extended and so spatial discrimination will be challenging.

6.5.2 Comparison with ALMA

As noted in Section 6 of Grainge et al. 2015, a future upgrade to ALMA to include a Band 1 receiver would make it a very powereful SZ instrument. It and SKA with Band5+ receivers would be

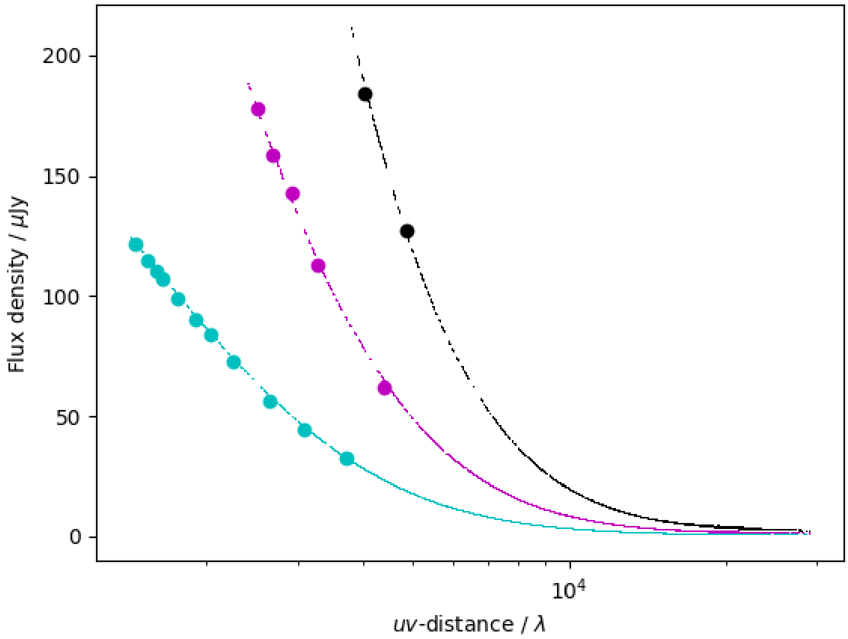

Figure 39: Predicted visibilities for a cluster at $z = 2$, with $M_{200} = 3 \times 10^{14} M_{\odot}$, sampled over a one-hour observation with the SKA1-MID antenna configuration (small points) at 14.11 GHz (cyan), 23.75 GHz (magenta) and 37.5 GHz (black). Large points show bins in uv-space where the predicted SNR is $> 3\sigma$.

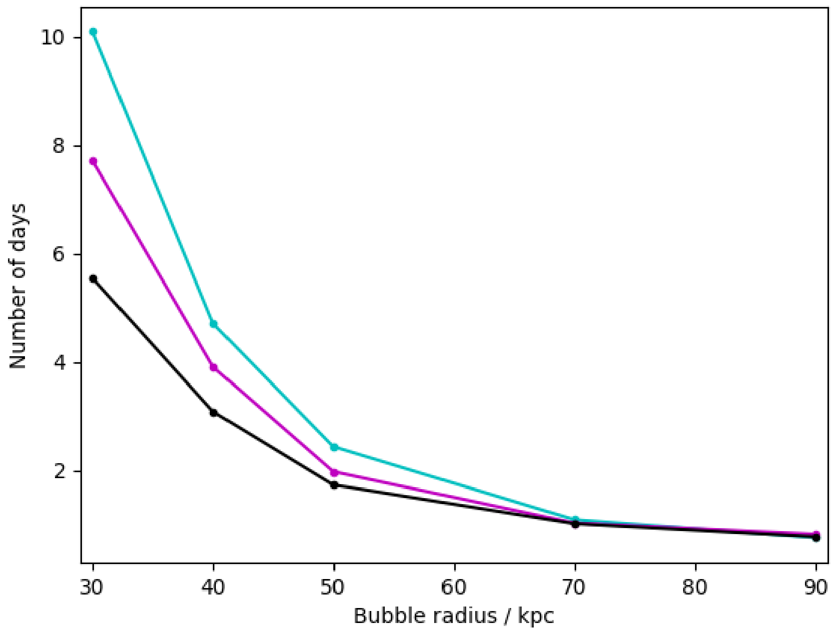

Figure 40: Number of 8-hour observing days required to detect AGN cavities at 5σ in a $M_{200} = 5 \times 10^{14} M_{\odot}$ cluster at $z = 1.5$ with SKA1-MID at 14.11 GHz (cyan), 23.75 GHz (magenta) and 37.5 GHz (black), on a map made with a uv-taper matched to the angular scale of the bubbles.

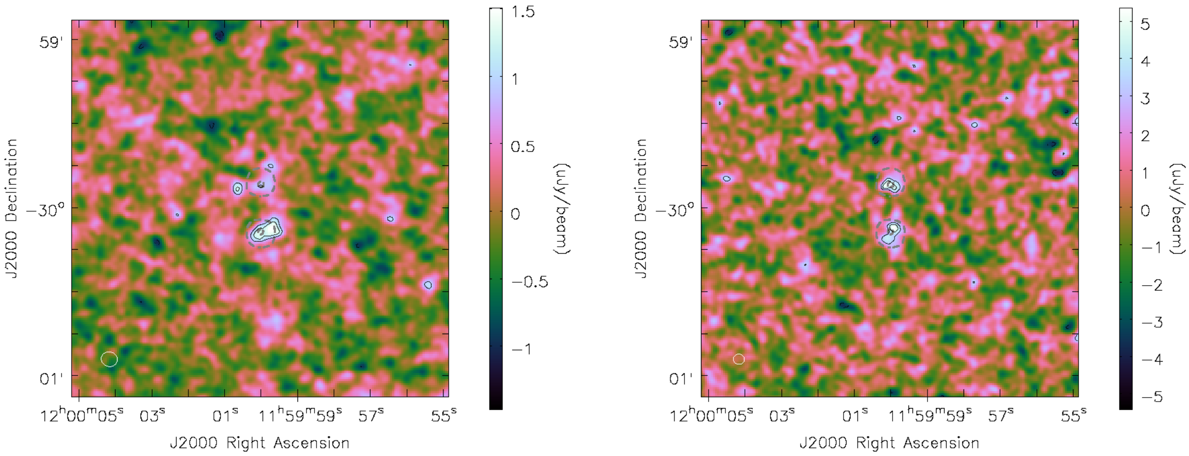

Figure 41: Simulated 3-day, (8 hours per day) observations of 40 kpc radius cavities in a $M_{200} = 5 \times 10^{14} M_\odot$ cluster at $z = 1.5$ with SKA1-MID at 14.11 GHz (left) and 37.5 GHz (right). The maps are made with a 40 kλ uv-taper to match the scale of the bubbles and the bulk cluster emission has been subtracted. Thin black contours show 3, 4, 5σ significance levels; thick, grey, dashed contours show the true bubble outline; and the synthesised beams are shown in white on the bottom left-hand corner of each plot.

very complementary to each other and have very comparable performance. SKA's four times larger number of antennas give it a superior flux density sensitivity and better sensitivity to small scale SZ substructure, but ALMA's access to a very compact configuration gives it superior filling factor and so better sensitivity to the large scale intracluster gas.

6.6 Detection of the Warm-Hot Intergalactic the Nitrogen Hyperfine Structure Line

Kohji Yoshikawa (Center for Computational Sciences, University of Tsukuba)

6.6.1 Science Justification

It has been long since it is first pointed out that most of the cosmological baryons evades the direct detection in the current universe as the "missing baryons" by Fukugita et al. (1998) and Fukugita & Peebles (2004). Numbers of numerical studies (e.g. Cen & Ostriker, 1999; Davé et al., 2001) suggest that diffuse ionized gas with temperature between $\simeq 10^5 - 10^7$ K, which is called "Warm-Hot Intergalactic Medium" (WHIM), in the filamentary structure and the outskirts of galaxy clusters are responsible for major part of the missing baryons.

Observationally, "warm" portions of the WHIM with temperatures of 10^5–10^6 K has been detected through the absorption lines of O VI and C V in FUV and soft X-ray wave bands, respectively, along lines-of-sight towards bright astronomical beacons such as QSOs and blazers in a cosmological distance (e.g. Shull et al., 2012; Nicastro et al., 2017, for a review). It is very recent that relatively "hot" component of WHIM in a temperature range of 10^6–10^7 K is detected through the O VII absorption line (Nicastro et al., 2018). Instead of detecting through absorption lines, direct detection of "hot" WHIM through its emission lines of O VII and O VIII lines with high energy resolution spectroscopy in soft X-ray band are proprosed by Yoshikawa et al. (2003, 2004).

Here, we introduce an alternative method to detect the WHIM using the high-frequency coverage of SKA1-MID, in which hydrogen-like Nitrogen ^{14}N VII and lithium-like ^{14}N V ions are observed through their absorption feature by the hyperfine structure transitions at frequencies of 53 GHz and 4.2 GHz in the rest frame, respectively, along lines-of-sight toward bright radio sources. This method is originally considered by Sunyaev & Docenko (2007) and we revisit this in a more quantitative manner. Actually ^{14}N is the only major isotope which has a non-zero nuclear spin among major heavy elements in the IGM, and ^{14}NV and ^{14}NVII have a hyperfine structure transition and also are the most abundant ions of ^{14}N in a temperature range typical to WHIM as can be seen in Figure 42. Since the abundance of ^{14}NVII ions in the WHIM is dominant in a temperature range of $2\times10^5 \lesssim T \lesssim 3\times10^6$ K under the typical intensity of the UV/X-ray background radiation in the local universe (Haardt & Madau, 2012) (see Figure 42 for details), this method has the capability to detect both the "warm" and "hot" phases of WHIM, while ^{14}NV ions only trace the "warm" component of WHIM. Level population for the hyperfine structure transition is also an important ingredient in estimating the detectability of the absorption features. The critical density $n_{\rm cr}$ of the ^{14}NVII hyperfine structure transition is estimated to be $n_{\rm cr} = 0.5\,{\rm cm}^{-3}$ and $8.5\,{\rm cm}^{-3}$ for a gas temperature $T = 10^5$ K and $T = 10^7$ K, respectively, and they are sufficiently higher than a gas density typical to the WHIM, which means that a optical depth for ^{14}NVII hyperfine structure transition along the line-of-sight getting through WHIM is proportional to gas density as well as path legth. On the other hand, the critical density of ^{14}NV ions is much lower than that of ^{14}NVII ions, and is estimated to be $2.7\times10^{-5}\,{\rm cm}^{-3}$ and $2.7\times10^{-4}\,{\rm cm}^{-3}$ for temperatures $T = 10^5$ K and 10^7 K, respectively, and quite close to typical temperature of WHIM. This means that the detection of the ^{14}NV ions is relatively difficult compared with ^{14}NVII ions because the optical depth of its hyperfine structure transition has relatively weak dependence on gas density in the case of super-critical condition $n \gtrsim n_{\rm cr}$.

Detection of the WHIM via heavy elements other than oxygen, which is already detected in UV and soft X-ray wave bands, is quite important because it provides us with oppotunities to investigate several important physical properties of the WHIM such as temperature, metallicity, and metal abundance pattern, and hence an insight to mechanisms responsible for metal enrichment of WHIM as well as more reliable evidence of WHIM by a combination with observations in UV and soft X-ray wave bands.

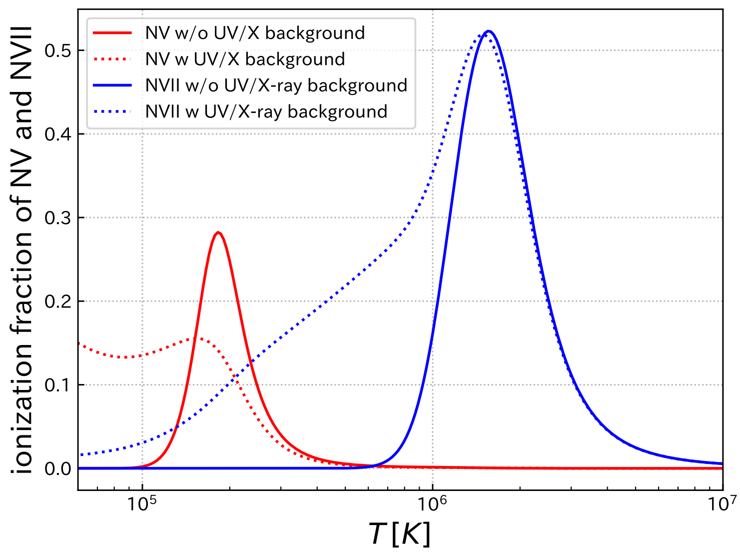

Figure 42: Ionization fraction of ^{14}NVII ion in the ionization equilibrium with and without the typical intensity of UV/X-ray background radiation. We assume the hydrogen number density is $n_{\rm H} = 10^{-4}\,[{\rm cm}^{-3}]$.

6.6.2 Technical Justification

Here, we estimate the observational feasibility to detect the absorption feature with the SKA1-MID over the frequency range of $20\,{\rm GHz} \le \nu \le 50\,{\rm GHz}$. The flux density of the 1-σ noise is estimated to

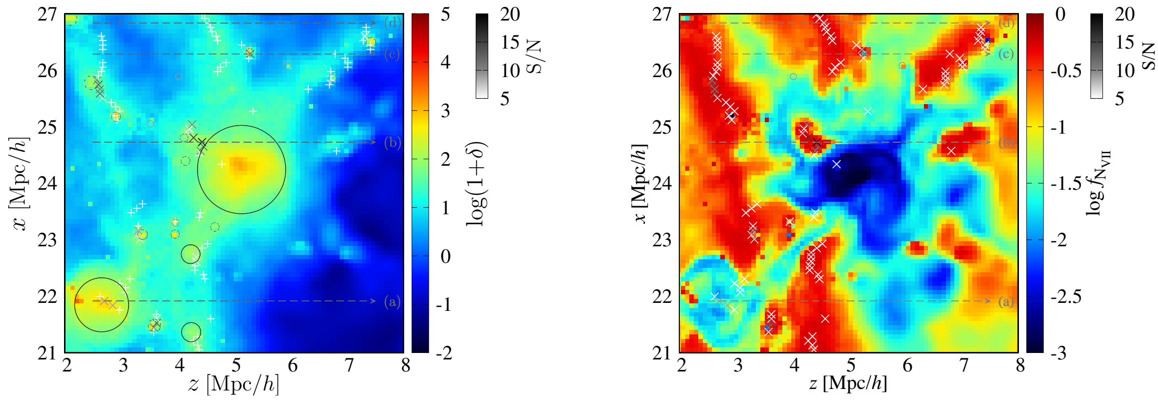

Figure 43: Maps of overdensity (left panel) and ionization fraction of ^{14}N VII ions (right panel) in a slice of the numerical simulation. Horizontal dashed lines are the line-of-sights, along which mock observations are performed. Crosses in each panel indicates the positions of absorbers which can be detected under a ceartain observational condition given below, where gray scale colors of crosses depicts the significance of absorption features as shown in the color bars. Circles shows the locations and virial radii of dark matter halos identified in the numerical result.

be

$$S_{1\text{œ}} = \frac{2k_{\rm B}T_{\rm sys}}{A_{\rm eff}\sqrt{2\Delta\nu\Delta t}} \tag{2}$$

$$= 3\times 10^{-3}\,{\rm mJy}\left(\frac{2\times 10^4\,{\rm m}^2}{A_{\rm eff}}\right)\left(\frac{T_{\rm sys}}{50\,{\rm K}}\right)\left(\frac{\Delta\nu\Delta t}{10\,{\rm MHz}\cdot 6.25\,{\rm h}}\right)^{-1/2}, \tag{3}$$

where $A_{\rm eff}$ is the effective collecting area of the SKA1-MID, $T_{\rm sys}$ is the system temperature, $\Delta\nu$ is the frequency bandwidth, and Δt the observational time. With this 1-σ noise flux density, the detection limit of the optical depth, $\tau_{\rm lim}$, required to achieve 5-σ signal-to-noise ratio is given by

$$\tau_{\rm lim} \simeq \frac{5S_{1\sigma}}{S_{\rm s}} = 1.5\times 10^{-6}\left(\frac{S_{1\sigma}}{3\times 10^{-3}\,{\rm mJy}}\right)\left(\frac{S_{\rm s}}{10\,{\rm Jy}}\right)^{-1}, \tag{4}$$

where $S_{\rm s}$ is the flux density of background radio sources. Actually the optical depth of the WHIM for the hyperfine structure transition of ^{14}N VII ions is typically $\tau_\nu \simeq 10^{-6} - 10^{-5}$ as shown below. Therefore, in observing bright radio sources such as 3C279 which has a flux density of 10 Jy at a frequency of 40 GHz, we can detect WHIM absorbers with an optical depth of 10^{-6} with a meaningful significance.

We present the mock observations to detect ^{14}N VII ions in WHIM using cosmological hydrodynamic simulations (Okamoto et al., 2014) which incorporates phenomenological treatment of star formation, energy feedback by supernovae and AGNs, and metal enrichment. Figure 43 shows maps of gas overdensity and ionization fraction of ^{14}N VII in a slice at redshift $z = 0$ of the numerical simulation where the most massive dark matter halo with a mass of $10^{13}M_\odot$ is centered. We perform a mock observation of absorption by the WHIM along the line-of-sight designated by (b) in Figure 43. Observational absorption features of ^{14}N VII ions in the WHIM is computed by solving cosmological radiation transfer

$$\left(\frac{1}{c}\frac{\partial}{\partial t} + \frac{\partial}{\partial s} - \nu\frac{H}{c}\frac{\partial}{\partial\nu}\right)I_\nu(s,t) = -\chi_\nu I_\nu + 3\frac{H}{c}I_\nu, \tag{5}$$

where s denotes a position along a line of sight towards a bright source, H is the Hubble parameter, and χ_ν the absorption coefficient of the hyperfine strucure transition of ^{14}N VII.

Figure 44 shows an absorption spectrum and profiles of physical quantities along the line-of-sight (b) in Figure 43, which get through a dark matter halo. One can see a relatively strong absorption feature at $\nu - \nu_0 = -55$ MHz with $\exp(-\tau_\nu) - 1 \simeq -\tau_\nu \simeq -10^{-5}$, which is formed by a clump of WHIM at $(x,z) = (4\,h^{-1}\,{\rm Mpc}, 25h^{-1}\,{\rm Mpc})$ near the most massive dark matter halo in Figure 43. Crosses in

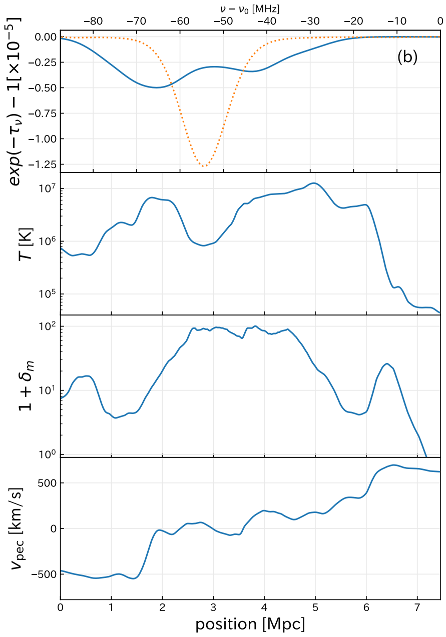

Figure 44: Profiles of the peculiar velocity field parallel to a line-of-sight, gas overdensity relative to the cosmic mean, gas temperature, and relative absorption by the hyperfine structure transition of ^{14}N VII ions along the line-of-sight (b) in Figure 43 from bottom to top. The absorption profile is plotted also as a function of frequency relative to the rest frame frequency of the hyperfine structure transition $\nu_0 = 53.04$ GHz (see the upper horizontal axis). A dotted line in the top panel shows absorption spectrum computed without taking the peculiar velocity field into account in which the position of the absorption feature coincides with that of physical quantities responsible for that absorption feature in the lower panels, while a solid line shows the spectrum in which the pecular velocity of gas is taken into account.

Figure 43 indicate the locations of WHIM which can be detected with the detection limit (signal-to-noise ratio greater than five) mentioned above if line-of-sights toward bright radio sources get through them. It can be seen that WHIM in the filamentary structures connecting to dark matter halos as well as that in the outskirts of dark matter halos.

References

Cen, R., & Ostriker, J. P. 1999, ApJ, 514, 1
Davé, R., Cen, R., Ostriker, J. P., et al. 2001, ApJ, 552, 473
Fukugita, M., Hogan, C. J., & Peebles, P. J. E. 1998, ApJ, 503, 518
Fukugita, M., & Peebles, P. J. E. 2004, ApJ, 616, 643
Haardt, F., & Madau, P. 2012, ApJ, 746, 125
Nicastro, F., Kaastra, J., Krongold, Y., et al. 2018, Nature, 558, 406
Nicastro, F., Krongold, Y., Mathur, S., et al. 2017, Astronomische Nachrichten, 338, 281
Okamoto, T., Shimizu, I., & Yoshida, N. 2014, PASJ, 66, 70
Shull, J. M., Smith, B. D., & Danforth, C. W. 2012, ApJ, 759, 23
Sunyaev, R. A., & Docenko, D. O. 2007, Astronomy Letters, 33, 67
Yoshikawa, K., Yamasaki, N. Y., Suto, Y., et al. 2003, PASJ, 55, 879
Yoshikawa, K., Dolag, K., Suto, Y., et al. 2004, PASJ, 56, 939

6.7 CO Intensity Mapping in the post-EoR

José Fonseca (Università degli Studi di Padova) & Laura Wolz (University of Manchester)

Carbon monoxide (CO) rotational transitions are a probe of the molecular gas in galaxies and of the astrophysical conditions in this interstellar medium. They also trace star-forming galaxies as they are a cooling mechanism of HII clouds. As we can see on the left panel of Fig. 45, the post-EoR emission from the two lowest CO rotation lines is redshifted to the frequency range targeted by band 6. Hence they can be used to study individual galaxies with enough angular resolution. Alternatively one can use the spatial fluctuations of the CO line emission to survey the large scale structure analogous to HI intensity mapping (IM) in band 1 and band 2 Santos et al. (2015). This has also been suggested for the EoR Chang et al. (2015). The first CO rotation line, CO(1-0), with a rest emission frequency of 115.3 GHz can map the universe down to $z \simeq 1.3$, while CO(2-1) traces down to $z \simeq 3.6$. Using the 133 dishes with band 6 one can perform an intensity mapping survey of CO(1-0) and do a cosmological study at higher redshift complementary to current galaxy surveys. Currently the only tentative detection of the CO power spectrum was done by the CO Power Spectrum Survey (COPSS) Keating et al. (2016) using the Sunyaev-Zel'dovich Array over 0.7deg^2 and 3000 hours in the redshift range $z \in [2.3, 3.3]$.

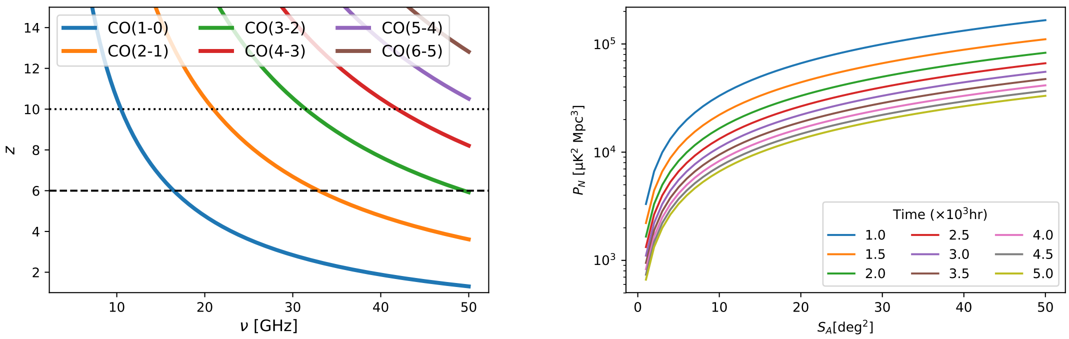

Figure 45: *Left*: The emitting redshift as function of the observed frequency for several CO rotation lines. *Right*: Noise power spectrum of a CO(1-0) intensity mapping survey for different integration times as a function of the survey area.

6.7.1 Survey Design

On the right panel of figure 45 we show the noise power spectrum for different total integration times as a function of the total survey area, assuming an IM survey in single dish mode. It is given by

$$P_{\rm N} = \left(\frac{T_{\rm sys}}{A_e}\right)^2 \frac{S_A}{2N_D t_{\rm tot}} \frac{c(1+z)^2 D^4 \chi^2(z)}{2.22 H(z) \nu_{\rm line}}, \tag{6}$$

where $T_{\rm sys}$ is the system temperature, A_e, the effective area, S_A the survey area, N_D the number of dishes, $t_{\rm tot}$ the integration time, D the dish size and $\nu_{\rm line}$ the line in consideration. Hence for a chosen line one can optimise the covered sky area and the total integration time. As one of our scientific goals is to probe cosmology via distance measures, one requires a survey of at least $\sim 10\,{\rm deg}^2$ to be able to see the Baryon Acoustic Oscillation (BAO) wiggles at $z \sim 3$ (as one can see on the right panel of figure 46). As an example, COMAP (Li et al. (2016)) plans a $10\,{\rm deg}^2$ survey (currently the pathfinder is collecting data). Notwithstanding a larger area permits many more modes to be seen balancing the increase of the noise power spectrum. Using the models of Fonseca et al. (2017) for the CO(1-0) signal, we plot in Figure 46 the expected CO power spectrum at $z = 3$ (with survey depth $\Delta z = 0.4$). The shaded areas correspond to the uncertainties in measuring the power spectrum for different survey designs. One can see from the left panel that although increasing the observation time decreases the noise, the gain is less prominent as cosmic variance starts dominating the uncertainty budget. On the right panel of figure 46 one can see that although increasing the survey area increases the noise power spectrum, this is balanced out by the modes added into the sample, especially on the BAO scales.

Based on this, we propose a 50deg^2 survey over 3000 hours of integration. This seems a good compromise between integration time and survey area. The area is bigger than current and planned CO intensity mapping experiments, while the integration time is of the same order as previously done.

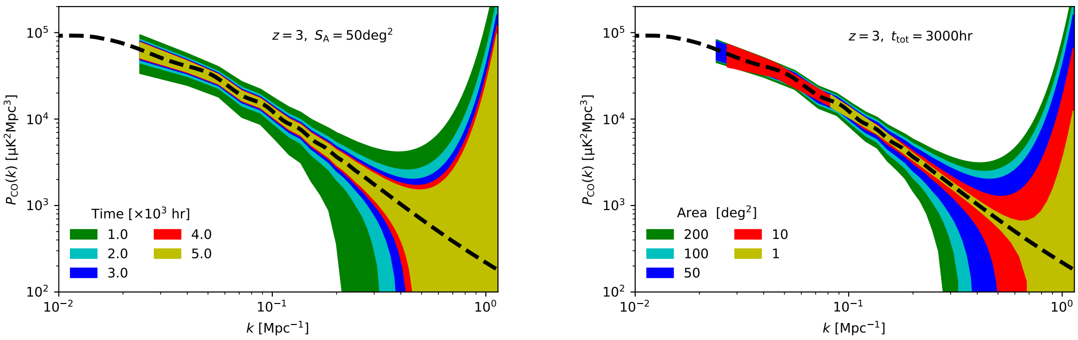

Figure 46: CO power spectrum at $z = 3$ with uncertainties in shaded areas. *Left*: Varying integration times for a fixed $50\,\mathrm{deg}^2$ survey. *Left*: Noise power spectrum of a CO(1-0) intensity mapping survey for different integration times as a function of the survey area.

6.7.2 Forecasted constraints

For the proposed survey we forecast a signal-to-noise ratio in measuring the amplitude of the power spectrum of ~ 3–17 depending on the target redshift. Not only can one perform cosmological studies at higher redshifts than with traditional galaxy surveys, but also one can tightly constrain the evolution of CO gastrophysics up to a 3% conditional error (see figure 47). In addition one can add tomographic information about the BAO, $H(z)$, $D_A(z)$, σ_8 and growth of structure at different redshifts. The CO IM survey can also be cross-correlated with the other spectral line IM surveys such as the proposed HI IM observations with SKA1-LOW.

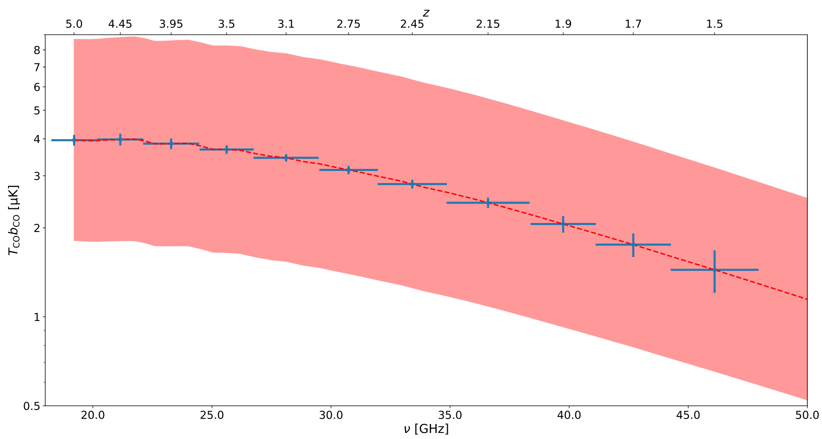

Figure 47: CO temperature times bias. Fiducial model in dashed red, uncertainties in shaded red and forecasted conditional constraints in blue.

6.7.3 Systematics, Contaminants and Others

CO IM will have he same contaminants as the ones observed in HI IM. In addition to synchrotron emission, galactic and extra-galactic free-free emission, and point sources we should also include the contribution of thermal dust which at the considered frequencies become more important than the synchrotron. These continuum galactic and extra-galactic foregrounds can be dealt in the same way as for HI IM Wolz et al. (2015). At higher frequencies the CO(2-1) will be a an interloper line contaminating the low redshift CO(1-0) signal. Despite the fact that line confusion breaks the one-to-one relationship between frequency and redshift one can use the anisotropic power spectrum method to disentangle the two contributions Cheng et al. (2016), and jointly determine gas and cosmological properties (although requiring a more elaborate forward modelling).

References

Santos, M., Bull, P., Alonso, D., et al. 2015, Advancing Astrophysics with the Square Kilometre Array (AASKA14), 19

Chang, T.-C., Gong, Y., Santos, M., et al. 2015, Advancing Astrophysics with the Square Kilometre Array (AASKA14), 4

Keating, G. K., Marrone, D. P., Bower, G. C., et al. 2016, ApJ, 830, 34

Li, T. Y., Wechsler, R. H., Devaraj, K., et al. 2016, ApJ, 817, 169

Fonseca, J., Silva, M. B., Santos, M. G., Cooray, A., 2017, *MNRAS*, 464, 1948

Wolz L., Abdalla, F.B., Alonso, D., et al. 2015, Advancing Astrophysics with the Square Kilometre Array (AASKA14), 35

Cheng, Y.-T., Chang, T.-C., Bock, J., et al. 2016, ApJ, 832, 165

7 Transient Phenomena

7.1 FRB microwave observation

Yueguang He, Siming Liu (Purple Mountain Observatory)

Although nearly one hundred fast radio burst (FRB) events have been detected by radio telescopes, such as GBT, Parkes, Arecibo, UTMOST, ASKAP, CHIME/FRB, DSA-10, in different frequency bands ranging from 400 MHz to 8 GHz since they were first identified in 2001, their origin and related emission mechanisms are still being debated. The extremely high brightness temperature (10^{39}K) implies coherent emission mechanisms (Yang et al., 2018).

Figure 48 shows a burst of the repeating FRB121102 in a star-forming region of an extra-galactic dwarf galaxy with z = 0.193 observed by the 110-meter GBT radio telescope at 4-8 GHz on August 26, 2017. The burst lasted for about a millisecond and had a sub-burst structure that drifts from high to low frequencies, which may be caused by the plasma lensing effect or intrinsic to the radiative processes. The observations of the GBT, in combination with observations of the 305-meter Arecibo radio telescope at 4.1-4.9 GHz, revealed a rotation measurement of $\sim 10^5$rad/m^2 and $\sim 100\%$ linearly polarized emission (Michilli et al., 2018). Such a large rotation measurement and high polarization fraction suggest that bursts from FRB121102 are produced in a strongly magnetized environment. At low frequencies, 8 repeating FRBs have been discovered recently by the CHIME collaboration (2019) in the 400-800 MHz range.

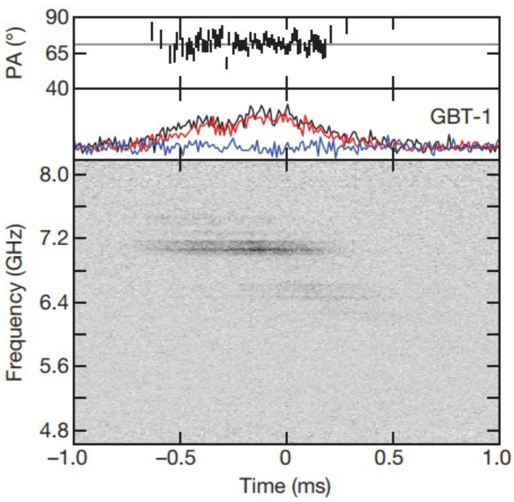

Figure 48: An FRB event observed by the GBT with time and frequency resolutions of 10.24μs and 5.86 MHz, respectively (Michilli et al., 2018).

Properties of detected bursts. Uncertainties are the 68% confidence interval (Michilli et al., 2018).

No.	Barycentric Peak Time (MJD)[a]	Peak Flux Density (Jy)[b]	Fluence (Jy ms)[b]	Gaussian Width[c] (ms)	Spectral Index[d]	DM (pc cm^{-3})[e]
1	56233.282837008	0.04	0.1	3.3±0.3	8.8±1.9	553±5±2
2	57159.737600835	0.03	0.1	3.8±0.4	2.5±1.7	560±2±2
3	57159.744223619	0.03	0.1	3.3±0.4	0.9±2.0	566±5±2
4	57175.693143232	0.04	0.2	4.6±0.3	5.8±1.4	555±1±2
5	57175.699727826	0.02	0.09	8.7±1.5	1.6±2.5	558±6±4
6	57175.742576706	0.02	0.06	2.8±0.4		559±9±1
7	57175.742839344	0.02	0.06	6.1±1.4	-3.7±1.8	
8	57175.743510388	0.14	0.9	6.6±0.1		556.5±0.7±3
9	57175.745665832	0.05	0.3	6.0±0.3	-10.4±1.1	557.4±0.7±3
10	57175.747624851	0.05	0.2	8.0±0.5		558.7±0.9±4
11	57175.748287265	0.31	1.0	3.06±0.04	13.6±0.4	556.5±0.1±1

7.1.1 Spectrum

The above table gives the spectral index of different bursts of FRB121102 observed by the Arecibo (Spitler et al., 2016). The spectral index varies widely from - 10 to + 10. No bursts have been detected beyond 8 GHz. Broad band observations are essential to reveal the nature of the emission mechanism.

7.1.2 Polarization

Summary of the polarization properties of an FRB sample (Caleb et al., 2018)

FRB Name	L(%)	V(%)	Total RM (rad m^{-2})	Galactic RM (rad m^{-2})
110523	44 ± 3	23 ± 30	-186.1 ± 1.4	18 ± 13
121102	100	–	$+1.026 \pm 0.001 \times 10^5$	-25 ± 80
140514	<10	21 ± 7	–	–
150215	43 ± 5	3 ± 1	$-9 < \mathrm{RM} < 12$	–
150418	8.5 ± 1.5	–	36 ± 52	–
150807	80 ± 1	–	12.0 ± 7	13.3
151230	35 ± 13	6 ± 11	–	–
160102	84 ± 15	30 ±11	-220.6 ± 6.4	24.6

Both linearly and circularly polarized emission has been detected from FRBs. The above table summarizes the polarization properties of several FRBs (Caleb et al., 2019). The origin of these polarization properties is another topic of exploration.

7.1.3 Burst rate

Under the assumption of an isotropic distribution of non-repeating FRBs (Fig. 49), a study of the 28 events observed by the Parkes radio telescope found that the evolution of the burst rate with redshift is consistent with the star formation rate at $z < 1.7$, and the model independent local burst rate is $(3.2 \pm 0.3) \times 10^4 \mathrm{Gpc}^{-3}\ \mathrm{yr}^{-1}$. The CHIME telescope has a large field of view, thousands of FRBs can be detected every year. More accurate determination of the burst rate is expected with an increase of the number of detected FRB events.

7.1.4 Technical Justification

With the short duration of FRB pulses and complex sub-pulse structure, it is essential to have high temporal and spectral resolution and high sensitivity observations. Previous observations show that a time resolution better than 10.24 μs and a frequency resolution of 1.56 MHz are needed for observations

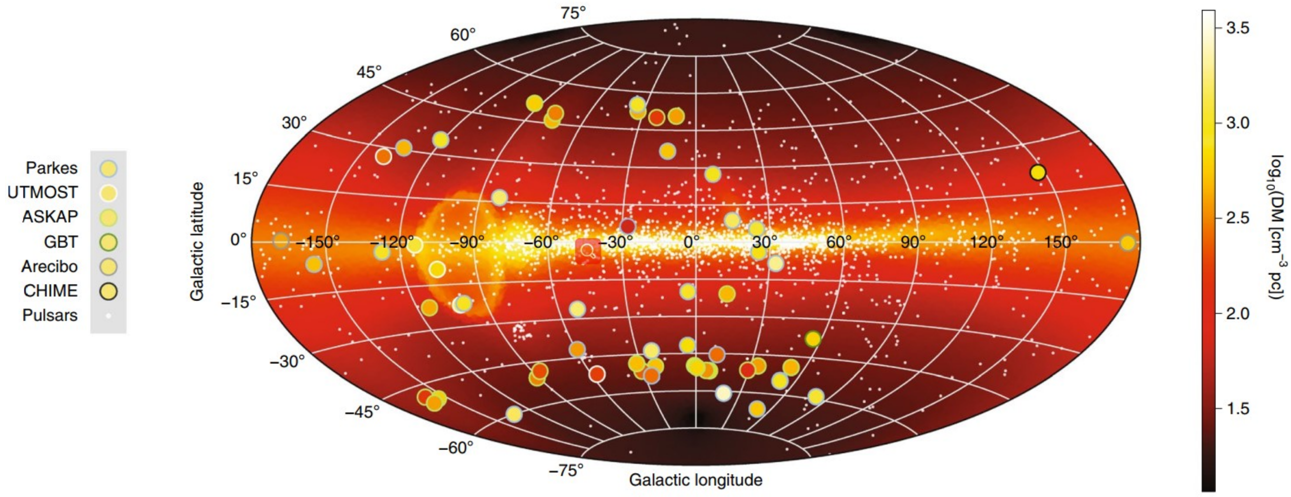

Figure 49: The spatial distribution of published FRBs, in the Galactic coordinates (Credit: Laura Driessen, The Jodrell Bank Centre for Astrophysics, University of Manchester).

above 15 GHz by the SKA. Polarization measurements are also needed. Good spatial resolution will be helpful to identify the host galaxies of FRBs.

References

Yang, Yuan-Pei, Zhang, Bing, 2018, Apj, 868, 31
D. Michilli, j. W. T. Hessels, & C. G. Bassa, 2018, Nature, 553, 182185
L. G. Spitler, P. Lazarus,& W. W. Zhu , 2016, Nature, 531, 7593, 202-205
The CHIME/FRB collaboration, 2019, arXiv:1908.03507
M. Caleb,E. Petroff,B. W. Stappers, 2019, MNRAS, 487, 11911199
M. Caleb,M. Kramer,& F. Jankowski, 2018, MNRAS, 000, 000
M. Caleb,B. W. Stappers,& K. Rajwade, 2019a, MNRAS, 484, 55005508

7.2 Core-collapse Supernovae

Miguel Pérez-Torres (IAA, Granada, Spain), Peter Lundqvist (Stockholm University, Sweden), Antxon Alberdi (IAA, Granada, Spain), Rob Beswick (University of Manchester, UK), Filomena Bufano (INAF, Catania, Italy)

The radio emission from core-collapse supernovae (CCSNe) is essentially non-thermal synchrotron emission from relativistic electrons, and is due to circumstellar interaction (e.g., Chevalier, 1982). In the framework of the SN-circumstellar interaction scenario, the optically thin radio emission from CCSNe scales with the mass-loss wind parameter, $\mathcal{M} = \dot{M}/v_w$, where $\dot{M}$ and v_w are the pre-supernova mass-loss rate and wind speed, respectively. Thus, for the radio emission to be appreciable, the progenitor star must have lost a significant amount of mass via a stellar wind and/or stripping due to a close companion. The presupernova stellar wind speed plays an equally important role: the smaller the wind speed, the more mass is retained in the vicinities of the SN progenitor, and the stronger the circumstellar interaction will be.

This pre-supernova wind, made of thermal electrons, has a power-law density profile, which for a steady, spherically symmetric wind has the following form: $\rho_{\rm CSM} \propto r^{-2}$. This circumstellar wind is the main component responsible for the partial suppression of synchrotron radio emission from supernovae, $S_\nu(t) \propto e^{-\tau_\nu}$, where the optical depth, $\tau_\nu \propto \nu^{-2.1}$.

Therefore, radio observations of CCSNe are a very useful tool for probing the SN-CSM interaction of all CCSN types, from the relatively faint Type IIP to the extremely radio bright Type IIn SNe. In turn, probing the SN-CSM interaction for all CCSN types will allow us to obtain basic, crucial information to characterize their progenitors, including mass-loss rates and, for synchrotron-self-absorbed SNe, the shock radius and the magnetic field–directly from the light curves (see, e.g., Chevalier 1998).

However, the limited sensitivity of pre-eMERLIN/JVLA interferometric arrays has biased past radio observations of CCSNe towards the brightest events, preventing any systematic radio follow-up of CCSNe of all types. All this makes the currently existing radio observations of CCSNe of rather limited use.

7.2.1 Prospects for SKA-1 beyond band 5

The capability of SKA1-MID to observe at frequencies higher than 15 GHz will allow for the possibility of tracing in detail the earliest phases of mass-loss rate in CCSNe, as well as in long GRBs (linked to Type Ib/c SNe), since those supernovae will experience a fast (within days, about a few weeks at most) transition from their optically thick to their optically thin phase, allowing us to understand in detail how the circumstellar interaction proceeds. To this end, the availability of a continuum frequency coverage from around 0.7 GHz up to 50 GHz will be of immense benefit, as quasi-simultaneous multi-frequency coverage of CCSNe will permit study in detail their evolution. Since SNe are optically thick at low frequencies in its early phases, band 5b and band 6 will permit to trace the very early radio light curve, while band 5 and band 2 will be very useful for tracing the late time radio evolution. SKA1 would thus become a "super-VLA" for SN studies, as the sensitivity of the SKA1 will be almost a factor three better than the VLA from 1.4 up to 50 GHz.

Furthermore, the combined use of SKA1 with the EVN and/or other VLBI arrays, e.g., the AVN, will facilitate resolved observations with unprecedented sensitivity, allowing to increase the existing (very small) sample of imaged SNe with VLBI at mas angular resolutions, or even at sub-mas resolution (if observations be done up to $\sim$40 GHz. This high-frequency VLBI-SKA capability will be uniquely powerful allowing spatially resolved observations to trace the time evolution of large samples CCSNe in unprecedented detail.

References

Chevalier, R. A. 1982, ApJ, 259, 302
Chevalier, R. A. 1998, ApJ, 499, 810

7.3 Magnetar Radio Outbursts

Takuya Akahori (NAOJ), Sujin Eie (U. Tokyo/NAOJ), Tomoya Hirota (NAOJ), Takeru Enoto (U. Kyoto), Takahiro Aoki (Yamaguchi U.) and Tomoaki Oyama (NAOJ)

7.3.1 Science Justification

A magnetar hypothesis (Duncan & Thompson, 1992) is that there is an extremely-magnetized neutron star (NS) whose field strength is beyond the quantum critical field of 4.4×10^{13} Gauss (Harding & Lai 2006). The hypothesis can explain slow-rotating but fast spin-down natures of Soft Gamma-ray Repeaters (SGRs) and Anomalous X-ray Pulsars (AXPs), which exhibit sudden enhancement of X-ray and gamma-ray fluxes ("outburst") during a timescale of months (see Woods & Thompson 2006; Kaspi 2007; Mereghetti 2008; Enoto et al. 2017 for reviews). However, the magnetar hypothesis itself does not explain why such a strong magnetic field exists and why only a fraction of NSs can be magnetars. One of the possible origins of strong magnetic field is the standing accretion shock instability (SASI) in the progenitor star. The SASI can drive turbulent dynamo in proto-NS and can amplify its magnetic field significantly (e.g., Endeve et al. 2012). Recently, some slow-fading super-luminous supernovae highlighted magnetar-powered models (Nicholl et al. 2013). Therefore, studying magnetars is also significant for the supernova explosion itself.

We suspect that a violent SASI forms a stronger magnetic field and it kicks the NS significantly. As a result, we expect that magnetars have peculiarly-high velocities. Unfortunately, we do not have enough samples of magnetars and can not examine the difference between proper motions of pulsars and magnetars. Therefore, velocity measurements of magnetars is a straightforward way to examine this hypothesis. Note that pulsars have 200 km/s on average and $\pm$50 km/s in deviation (see e.g., Fig 29 of Enoto et al. 2019).

The velocity measurement is also crucial for studying supernova remnant (SNR) association of a NS, where there are many isolated NSs whose progenitor SNRs are unknown. For the case of pulsars, there are many systems for which the pulsar is inside the SNR on the plane of the sky. The ages of such pulsars and candidate SNR are relatively young, say 1,000 years like the Crab nebula and the Crab pulsar, and hence cross-identification is simple and reliable. Moreover, because pulsars are persistent radio sources, parallax measurement by VLBI allows to derive an accurate distance estimate to the pulsar. Comparison between distances of the pulsar and the SNR also supports the identification, where the distance to the SNR can be given by some techniques including absorption of HI (i.e. neutral hydrogen column density) and absorption of soft X-ray (i.e. free electron column density).

Meanwhile, a firm cross-identification between a magnetar and a SNR is not achieved yet. The key problem is a lack of astrometry; the accurate position and velocity of magnetar, which is necessary to identify its host SNR, is not clear. It has been recognized that magnetars are radio-quiet objects. However, in the last decade, four of several tens of known magnetars exhibited radio emission (radio outburst) and the number of radio-loud magnetars is increasing. Table 1 summarizes the four known radio-loud magnetars and their candidate SNRs. Even when radio outbursts take place, their duty period of several months is challenging for achieving parallax measurement. But within several months, the proper motion can be estimated by determining the absolute position of the magnetar. We consider this possibility with the Beyond Band 5 of SKA.

We also suspect that the SASI forms a peculiar structure of the progenitor's SNR. Therefore, morphological comparison between SNRs of normal pulsars and magnetars could be a clue as to whether the origin of strong magnetic field links its supernova or not. Previous work did not find evidence for higher explosion energies of magnetar-related SNR compared to ordinary SNR (Vink & Kuiper 2006), but the number of samples was very limited. We can check the morphology and velocity differences with future large samples of pulsars and magnetars with the SKA.

Once we obtain the pulse profile of a magnetar at Beyond Band 5 frequencies, we can study its emission mechanism. Particularly, it is useful to refer to pulse properties of normal pulsars. For instance, a pulse profile provides a hint of the location of radiation region. Narrow two-peaks are interpreted as a donuts beam and it points to us twice per single rotation. Excluded the interstellar scintillation, the pulse width is in general narrower at higher frequencies. It is interpreted that higher energy cosmic-rays are accelerated at stronger and more collimated magnetic field nearer to the NS surface.

The above geometrical discussion would elucidate whether radio emission mechanisms of pulsars and magnetars are identical or not, and would highlight physics of the NS core, crust, and magnetosphere. One clear difference between pulsars and magnetars is that the spectral index of magnetar radio outbursts looks to be flat ($\alpha \sim -0.5$, $S \propto \nu^{\alpha}$) while pulsars have steeper spectra ($\alpha \sim -1.8$). Strong radio pulses and flat spectra seen in radio outbursts tell an analogy to the Crab giant radio pulses (GRPs) and repeating fast radio bursts (FRBs). Finally, this use case can be extended to the so-called high-B pulsars, if they exhibit radio emission with a flat spectrum.

7.3.2 Technical Justification

The most important array specification for this science case is the positional accuracy or the angular resolution so as to judge the movement of the magnetar in the plane of the sky. The typical proper motion of 200 km/s for NSs corresponds to $\sim$ 1.7 mas per month if the distance from the Earth is 2 kpc. The requirement is that we detect this motion within a few months during radio outburst. We

Table 7: Summary of radio-loud magnetars.

Name	Period (Sec)	Distance (kpc)	Tranverse Velocity (km/s)	SNR candidate
SGR 0501+452	5.76	1–5?	???	HB9?
4U 0142+61	8.69	3.6?	102 ± 26	???
1E 2259+586	6.98	3.2?	157 ± 17	CTB109?
XTE J1810-197	5.54	3–5?	212 ± 35	G11.2-0.3?

assume the statistical positional uncertainty of the synthesized beam depends on the signal-to-noise ratio (S/N) as $1/\sqrt{S/N}$. Therefore, the sensitivity as well as the array baseline and the observing frequency are key parameters.

Because there are only four samples of magnetar radio outbursts, it is difficult to define their typical flux density. Hence, we simply adopt the latest magnetar radio outburst XTE J1810-197 as a reference for our technical justification. In our December observation (Eie et al., 2019), its time-averaged brightness was estimated to be roughly 14 mJy, 10 mJy, and 8 mJy at 2, 8, and 22 GHz, respectively. The resultant power law fit gives roughly $I = 15.8$ mJy $(\nu/GHz)^{-0.22}$, so that the expected brightness at 43 GHz is 6.9 mJy. Suppose that the Band 5+ sensitivity is 4.68 μJy at 22 GHz and 9.69 μJy at 43 GHz each with a 1 GHz bandwidth and 1 hour exposure for 133 SKA1-MID dishes, the reference source can be detected with $S/N = 1709$ ($\sqrt{1709} = 41.34$) at 22 GHz and 712 ($\sqrt{712} = 26.68$) at 43 GHz. Then, based on the SKA1 Science requirement, the angular resolution is expected to be 18 mas at 22 GHz and 9.3 mas at 43 GHz with the longest, 150 km baseline. The positional accuracy will reach $18/41.34 = 0.43$ mas and $9.3/26.68 = 0.35$ mas at 22 GHz and 43 GHz, respectively. Therefore, the proper motion should exceed 4σ level within one month. Even more, if we can achieve SKA1-VLBI at 22 GHz and 43 GHz, it will give an excellent measurement of astrometry.

We have considered the time-averaged flux in the above justification, although it is known that radio outbursts exhibit pulsation due likely to the rotation of NS. Therefore, if we achieve the pulsar gating, we could obtain a better S/N value.

In summary, the Beyond Band 5 frequency range opens a new science case of magnetar astrometry, which allows us to access a new parameter space of magnetars and to connect the missing link between magnetars and progenitor SNRs.

References

Duncan, R. C., & Thompson, C. 1992, ApJ, 392, L9
Eie, S., Terasawa, T., et al., in preparation.
Endeve, E., Cardall, C. Y., Budiardja, R. D., et al. 2012, ApJ, 751, 26
Enoto, T., Shibata, S., Kitaguchi, T., et al., 2017, ApJS, 231, 8
Enoto, T., Kisaka, S., & Shibata, S. 2019, in press.
Harding, A. K., & Lai, D. 2006, RPPh, 69, 2631
Kaspi, V. M. 2007, Ap&SS, 308, 1
Mereghetti, S. 2008, A&ARv, 15, 225
Nicholl, M., Smartt, S. J., Jerkstrand, A., et al. 2013, Nature, 502, 346
Vink, J. & Kuiper, L. 2006, MNRAS, 370, L14
Woods, P. M., & Thompson, C. 2006, in Compact Stellar X-Ray Sources, ed. W. Lewin & M. van der Klis (Cambridge: Cambridge Univ. Press), 547

7.4 Radio Variability of Active Galactic Nuclei

Jun Yi Koay (ASIAA), Hayley Bignall (CSIRO), Steve Croft (UC Berkeley), Talvikki Hovatta (FINCA, Aalto University)

The intrinsic radio variability of Active Galactic Nuclei (AGNs) on timescales of days, months and years, provides a unique probe of the extreme physics in the vicinity of the central supermassive black holes (see Bignall et al., 2015, and references therein). Such variability can arise from changing accretion rates (e.g., Lin & Shields, 1986), jet precession (e.g., Kudryavtseva et al., 2011), as well as flares, shocks and variable Doppler boosting in the jet (Hughes et al., 1985; Hovatta et al., 2008). Studying AGN variability over a range of radio frequencies, and correlating the variability with that observed across the entire electromagnetic spectrum, can provide a powerful probe of the connection between jets and accretion disks, turbulence and shocks, as well as activity and quiescence in AGNs. Monitoring the radio variability of AGNs can also uncover jetted tidal disruption events (Donnarumma et al., 2015), arising from the tearing apart of stars by tidal forces induced by the gravity of the black hole. These time domain studies of AGNs will address some unresolved questions on the physics of black hole accretion and feedback: How are relativistic jets launched? How do jets evolve following a sudden increase in the black hole accretion rate? How are the jets energetically coupled to, and how do they physically interact, with the other components of an AGN emitting at other wavelengths, such as the accretion disk, the dusty torus, the broad-line emitting region and the surrounding interstellar medium?

7.4.1 Monitoring AGN Variability with SKA1-MID

AGN variability studies are at present limited to small numbers of sources with well sampled flux measurements, or large numbers of sources with poor time sampling. The significant increase in survey speed engendered by the SKA will enable synoptic monitoring studies of hundreds of thousands of sources with a cadence of days or less, thereby increasing the chances of detecting rare events and improving our understanding of AGN variability statistics with respect to other AGN properties (e.g., luminosity, Eddington ratio, and black hole mass).

Current AGN monitoring programs are focused on high flux density sources such as blazars and very nearby Seyfert galaxies. The increased sensitivity of the SKA will enable variability studies of more radio-faint AGN populations. These include the increasing number of 'changing-look' AGNs (e.g., LaMassa et al., 2015; Koay et al., 2016) being discovered; these objects exhibit dramatic, order of magnitude changes in their mass accretion rates on timescales of a few years, thereby challenging our understanding of supermassive black hole accretion. Even in Phase 1, the improved sensitivity of SKA1-MID over existing telescopes is already significant. SKA1-MID will thus provide precision flux measurements as a function of time in much weaker, 1 mJy level sources, potentially measuring ~ 30 μJy level flux variations in these AGNs at a 5σ level with just 5 minutes of integration time per measurement, assuming a 5 GHz continuum bandwidth.

7.4.2 Rising Above Interstellar Scintillation and Opacity Effects with Band 6

However, cm-wavelength AGN variability on timescales of hours, days and even weeks can be dominated by interstellar scintillation (ISS), the twinkling of compact radio sources due to scattering in the ionized and turbulent interstellar medium of our Galaxy (e.g., Rickett, 1990; Lovell et al., 2008). While ISS amplitudes are expected to be strongest at ~ 5 to 8 GHz at mid-Galactic latitudes (Walker, 1998), AGN ISS has been observed at frequencies as high as 15 GHz (Savolainen & Kovalev, 2008; Kara et al., 2012). In fact, a study of the 15 GHz interday variability of 1158 AGNs monitored by the Owens Valley Radio Observatory (OVRO) 40-m telescope over a span of more than 10 years reveals significant levels of ISS in the AGN lightcurves (Koay et al., 2019). This is demonstrated by the Galactic dependence of the source variability amplitudes. The most variable sources in the sample are observed through highly turbulent regions of the ISM, such as the Orion-Eridanus superbubble in the Northern sky (Figure 50). The short term radio variability of AGNs, particularly those observed through such highly-scattered regions of the ISM, need to be interpreted carefully. The blazar TXS 0506+056, the candidate source of high-energy neutrinos detected by IceCube (IceCube Collaboration et al., 2018a,b), is one such source, since it is also observed through the Orion-Eridanus superbubble.

It is therefore crucial that the monitoring of AGN variability be carried out with the SKA1 at frequencies above 15 GHz. This provides an excellent mitigation of the effects of ISS, enabling the study of intrinsic AGN variability with significantly less biases. Concurrent monitoring of the flux variability at multiple frequencies, (e.g., at ≥ 20 GHz and at 5 GHz), will also enable intrinsic variability correlated over both frequency bands to be distinguished from ISS, in turn facilitating studies of ISS and the turbulent properties of the interstellar medium at lower frequencies (Bignall et al., 2015). Additionally, observing at higher frequencies reduces optical depth effects arising from e.g., synchrotron self-absorption, that can lead to variability that is smeared out and less pronounced at lower frequencies. Band 6 receivers on SKA1-MID will thus be key in studying physical phenomena occuring in the inner regions (light-days to light-years in diameter) of AGNs through the monitoring of intrinsic AGN variability, contributing to the Key Science Project: "Strong Field Tests of Gravity Using Pulsars and Black Holes".

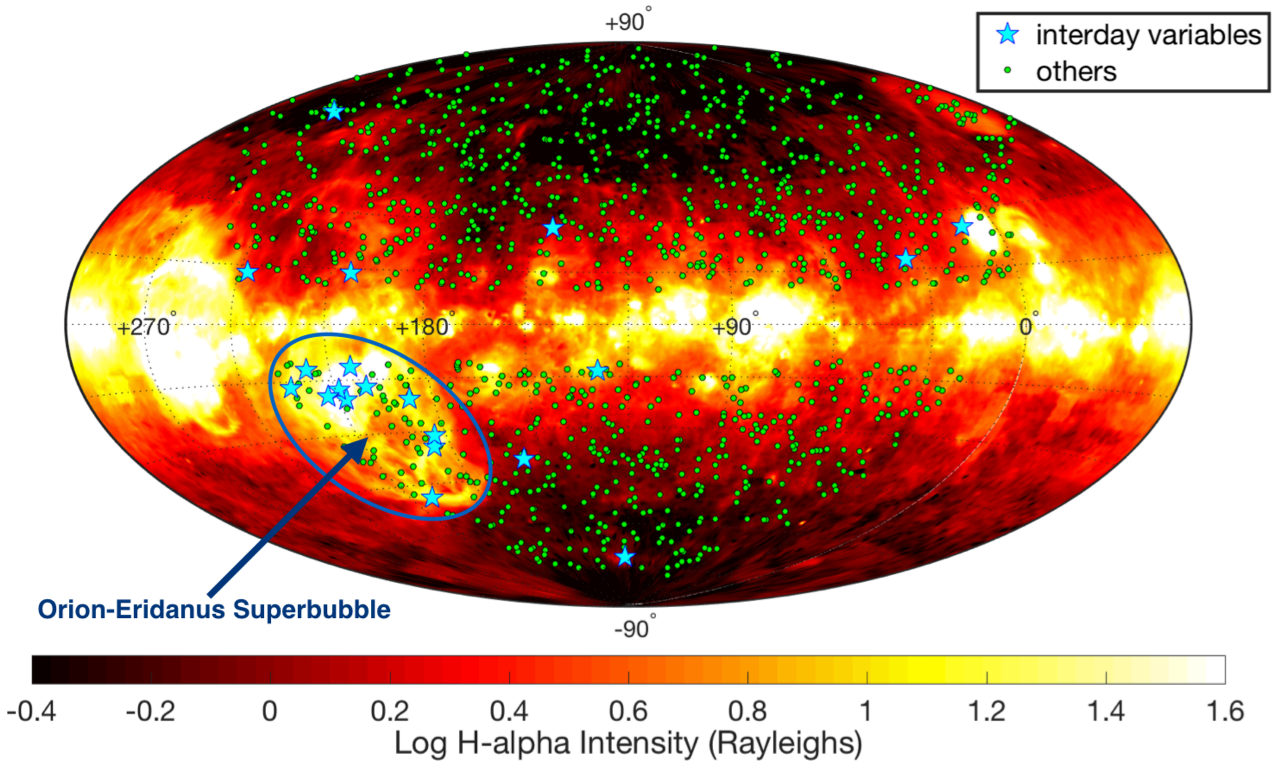

Figure 50: The 1158 AGNs monitored at 15 GHz by the OVRO 40-m telescope, shown here in Galactic coordinates overlayed on an all-sky Hα intensity map from the Wisconsin H-Alpha Mapper (WHAM) Survey (Haffner et al., 2003, 2010). The Hα intensities trace the ionized gas in the ISM, and are thus a proxy for the line-of-sight scattering strength. 20 AGNs that exhibit the most significant interday variability are shown as blue stars, with more than half of them observed through the Orion-Eridanus superbubble. This demonstrates the ISS origins of the interday flux variations, which is significant even at 15 GHz. This figure is taken from the paper by Koay et al. (2019).

References

Bignall H. E., Croft S., Hovatta T., Koay J. Y., Lazio J., Macquart J.-P., Reynolds C., 2015, Advancing Astrophysics with the Square Kilometre Array (AASKA14), 58

Donnarumma I., Rossi E. M., Fender R., Komossa S., Paragi Z., Van Velzen S., Prandoni I., 2015, Advancing Astrophysics with the Square Kilometre Array (AASKA14), 54

Haffner L. M., Reynolds R. J., Tufte S. L., Madsen G. J., Jaehnig K. P., Percival J. W., 2003, ApJS, 149, 405

Haffner L. M. et al., 2010, ASP Conf. Ser., 438, 388

Hovatta T., Nieppola E., Tornikoski M., Valtaoja E., Aller M. F., Aller H. D., 2008, A&A, 485, 51

Hughes P. A., Aller H. D., Aller M. F., 1985, ApJ, 298, 301

IceCube Collaboration, et al., 2018, Science, 361, eaat1378

IceCube Collaboration, et al., 2018, Science, 361, 147

Kara E., Errando M., Max-Moerbeck W., et al., 2012, ApJ, 746, 159

Koay J. Y., Vestergaard M., Bignall H. E., Reynolds C., Peterson B. M., 2019, MNRAS, 460, 304

Koay J. Y., et al., 2019, MNRAS, 489, 5365

Kudryavtseva N. A. et al., 2011, A&A, 526, A51

LaMassa S. M. et al., 2015, ApJ, 800, 144

Lin D. N. C., Shields G. A., 1986, ApJ, 305, 28

Lovell J. E. J. et al., 2008, ApJ, 689, 108-126

Rickett B. J., 1990, ARA&A, 28, 561

Walker M. A., 1998, MNRAS, 294, 307

Savolainen T., Kovalev Y. Y., 2008, A&A, 489, L33

7.5 Broad-Band Radio Light Curves of Relativistic Jets in X-ray Binaries

Haruka Sakemi, Mami Machida (Kyushu University)

7.5.1 Science Justification

From the first detection, astrophysical jets have been well studied both observationally and theoretically. Some important mechanisms are still under discussion, such as driving and acceleration. Since these phenomena happen in an early stage of a jet ejection, it is desirable to reveal the physics of the jet-ejected region. In this region, a jet shows time variation. Recently, type 1.5 AGNs have been detected which are in the middle of the state transition (Noda & Done, 2018). Unfortunatelly, since the typical time scale of variation of an active galactic nucleus (AGN) jet is from 10^6 to 10^7 years, it is impossible to observe the jet variation directly in our lifetime. On the other hand, galactic jets change their state no longer than 100 days, and adequate for studying the evolution of jets.

Galactic jets are classified as X-ray binary (XRB) jets or microquasars. The primary difference between them is energy excess estimated by radio emission. However, the cause of the difference is still unidentified, and it has not been clarified what kind of observation enables us to investigate the cause. Now, we focus on spectral energy distributions (SEDs) and magnetic field structures. SEDs have essential information about the radiation mechanism. Also, magnetic fields play an important role in driving of jets. Then, XRB jets and microquasars should have different features of their SED and magnetic field at the jet-ejected regions.

The intensities of galactic jets are usually from a few mJy beam^{-1} to several tens of mJy beam^{-1} except for some extreme cases such as the SS433 jet (Bell, Roberts, & Wardle, 2011). It means that the observation of galactic jets requires high sensitivity. High spatial resolution and wide frequency coverage are also essential to reveal the SEDs. Also, observation at a few tens of GHz are desirable for polarization analysis because the influence of depolarization is small at these frequencies (Arshakian & Beck, 2011). However, the observation satisfying these requirements has been difficult due to instrumental limitations. First, the current instruments do not fulfill either high spatial resolution or wide frequency coverage. Although the Very Large Array (VLA) and the Australia Telescope Compact Array (ATCA) can observe at wide frequency bands including a few tens of GHz, these cannot resolve the jet-ejected regions at a few tens of AU scale. In the case of VLBI, the spatial resolution reaches to a few AU scales. However, the sensitivity limit of the VLBI often makes it challenging to detect the radio emission from the galactic jets. Therefore, the number of galactic jets is still small whose ejected regions have been studied well.

Extending SKA1 beyond Band 5 (BB5) can approach the spatial resolution of VLBI. Also, 133 antennas realize high sensitivity and many kinds of baseline pairs. It means that BB5 is adequate for the observation of small and diffuse emission regions of galactic jets.

We review the BB5 observation of Circinus X-1 (Cir X-1) and Cygnus X-1 (Cyg X-1). Cir X-1 is the microquasar whose central engine is a neutron star (Linares et al., 2010). It is located in the southern sky, and so the SKA is a powerful tool to study this source. A large-scale radio nebula is surrounding Cir X-1 (Heinz et al., 2013). In addition, it has been pointed out that the jets have possibly helical structure (Coriat et al., 2019). Cir X-1 therefore has similar features to the microquasar SS433. However, the intensity is about one-hundredth of SS433, and high sensitivity observations are required. Recently, the jet lobes of Cir X-1 were observed with the ATCA at 2.1, 5.5, 9.0, 33, and 35 GHz (Coriat et al., 2019). The lobes were resolved at the near size of the each-frequency resolution. Then, the detailed structures have not been revealed, such as the SED. BB5 enables an enormous increase in resolution compared to the ATCA and can clarify the detailed SED. The magnetic field structures have not been revealed, and BB5 is expected to detect polarized emission with a high signal to noise (SN) ratio.

Cyg X-1 is a high mass X-ray binary (Gies & Bolton, 1986). The linear jet was observed with the VLBA at 8.4 and 15.4 GHz (Stirling et al., 2001). The bow shock was also detected at about five pc away from the binary system (Gallo et al., 2005). However, since the jet and the bow shock are far apart, the relation between them is not obvious. The field of view and the sensitivity of BB5 may reveal the relation between them. The polarization analysis of Cyg X-1 has not been reported. Since the spectral index is -0.06 when the accretion disk is the hard state and the flux of the unresolved core is 10.5 mJy at 15 GHz, BB5 should be able to observe polarized emission (Fender et al., 2000).

7.5.2 Technical Justification

In order to reveal the SEDs and to analyze polarization, the frequency coverage is desired to be as wide as possible. Although the frequency resolution influences the bandwidth depolarization, the 1 GHz bandwidth is sufficient. Even though we assume the extreme rotation measure (RM) value $\sim$1000 rad m^{-2} such as AGN, the difference of polarization angle between 15 and 16 GHz is only about two degrees. In order to study the features of jet-ejected regions, the AU-scale resolution is required.

The sensitivity of BB5 is about twice that of the VLA and The European VLBI Network (EVN)-Full, and it enables us to reach enough SN with short observation time. For example, only two minutes of observation is required to detect the unresolved core of Cir X-1 with signal-to-noise of 100 at 15 GHz (Coriat et al., 2019). Also, the bright core of Cyg X-1 can be observed with SN=100 in a few seconds (Fender et al., 2000).

References

Arshakian, T. G., & Beck, R., 2011, MNRAS, 418, 4, 2336
Bell, M. R., Roberts, D. H., & Wardle, J. F. C., 2011, ApJ, 736, 2, 118
Coriat, M., Fender R. P., Tasse, C., et al. 2019, MNRAS, 484, 2, 1672
Fender, R. P., Pooley, G. G., Durouchoux, P., et al. 2000, MNRAS, 312, 4 853
Gallo, E., Fender, R., Kaiser, C., et al. 2005, Nature, 436, 7052, 819
Gies, D. R., & Bolton, C. T., 1986, ApJ, 304, 371
Heinz S., Sell, P., Fender, R. P., et al. 2013, ApJ, 779, 2, 171, 8
Linares, M., Watts, A., Altamirano, D., et al. 2010, ApJL, 719, 1, 84
Noda, H., & Done, C., 2018, MNRAS, 480, 3, 3898
Stirling, A. M., Spencer, R. E., de la Force, C. J., et al. 2001, MNRAS, 327, 4, 1273

7.6 Transient afterglows

Prashanth Mohan (Shanghai Astronomical Observatory, China), Tao An (Shanghai Astronomical Observatory, China) & Jun Yang (Onsala Space Observatory, Sweden)

Afterglows are indicative of high velocity ejecta and shocks from often cataclysmic events (GRB, TDE) interacting with the surrounding gaseous medium. An expanding ejecta and a possible accompanying jet undergo a slowing down and an associated transition in synchrotron emission signatures depending on their dynamical evolutionary stage. An understanding of the physics of shock formation and propagation, and relevant timescales at each stage can be cast into physical models governing the evolution of the composite synchrotron spectrum (multiple contributing components, see e.g. Gao et al., 2013). Multi-epoch, multi-frequency radio observations of these sources at staggered epochs help reveal physical properties in the vicinity of the source of the transient signal. These can include the medium density and distribution, level of equipartition between the magnetic field and particle energy density of the synchrotron emitting particles, and energetics of the explosion. These in turn can help address the nature of the explosion progenitor, including the possibility of an active central engine (compact object system: actively accreting neutron star/magnetar, black hole) which could additionally cause modifications in the afterglow morphology and proper motion. Some prominent sources of radio afterglows ideal for VLBI imaging observations include the TDEs and GRBs whose relevant observational signatures are discussed below.

7.6.1 TDE

The disruption of a star within the tidal radius of a dormant central supermassive black hole (SMBH of $10^6 - 10^8$ $M_\odot$) causes the fall-back accretion of stellar debris (Rees, 1988). This powers a thermal optical/ultra-violet/X-ray flare (comparable in luminosity to bright Supernovae at $\approx 10^{43} - 10^{44}$ erg s^{-1}) which through a dependence on the accretion rate decays as a power law with index 5/3 over months to years (e.g. Evans, & Kochanek, 1989; Strubbe, & Quataert, 2009). The activated central engine can power a transient relativistic jet which upon interaction with the surrounding circum-nuclear medium produces non-thermal afterglow radio emission; the jet launching and duration could depend on two distinct scenarios involving differences in accretion rate and mechanism (Giannios, & Metzger, 2011). In the first, during the early super-Eddington accretion phase (rate > Eddington rate), orbiting stellar debris can shock loosely bound accreted material and launch an outflow $\approx$ 30 - 100 days from the thermal flare (based on a SMBH disrupting a solar mass star with a pericenter distance < tidal radius Strubbe, & Quataert, 2009). In the second, when the accretion rate falls below $\approx$ 0.1 times the Eddington rate (over yr. timescales), the accretion disk can transition to radiatively inefficient and geometrically thick (e.g. Yuan, & Narayan, 2014) which is then highly susceptible to the production of jetted outflows (e.g. Narayan, & Yi, 1995).

7.6.2 GRB

Gamma-ray bursts (GRBs) are highly energetic (γ-ray and X-rays) transient flashes. The event involves prompt emission lasting from ≤ 2 s (short GRB) to > 2 seconds (long GRB) (e.g. Kouveliotou et al., 1993); and, afterglow emission which can last from a few hours to a few months and can be monitored using multi-wavelength (e.g. X-ray, optical/UV, radio) follow up observations (e.g. Nappo et al., 2017). The merger of compact objects (e.g. neutron stars) is expected to produce short GRBs while the collapse of a massive, rapidly rotating star to a compact object is expected to produce long GRBs (e.g. Kumar & Zhang, 2015), both being cataclysmic events. In long GRBs, the prompt emission is likely from shocked regions created during the break-out of the ejected highly relativistic jet from the stellar envelope while afterglow emission is from the interaction of this jet with the interstellar medium (ISM) in its vicinity (e.g. MacFadyen et al., 2001; Kumar & Zhang, 2015). VLBI radio observations are expected to play a key role during both prompt and afterglow phases, tracking the initial fading of the burst emission and studying the re-brightening during jet-ISM interaction, the emission possibly peaking at flux densities of $\sim$ 100 mJy (Paczynski & Rhoads, 1993). Imaging of the afterglow emission region can be used to infer angular size and possibly the shape, expansion rate (kinematics), emission mechanism and constraints on the ISM properties in the vicinity of the GRB including density and distribution.

Objectives from high frequency (15-24 GHz) VLBI imaging thus include i. Detection and characterizing their compact structure defined by the propagating forward-reverse shocks at an early phase (few - tens of days) and by an adiabatic expansion at a later phase ($\approx$ few months), ii. Constraints on proper motion, an indicator of a relativistic jet, iii. Distinguishing between the jet scenarios and helping understand the accretion process, iv. Constraints on detection rate of jetted transients, v. Evolution of the transient energetics and properties of the surrounding medium encountered between the early and late phases.

References

Evans, C. R., & Kochanek, C. S. 1989, ApJ, 346, L13
Gao, H., Lei, W.-H., Zou, Y.-C., et al. 2013, New Astronomy Reviews, 57, 141
Giannios, D., & Metzger, B. D. 2011, MNRAS, 416, 2102
Kouveliotou, C., Meegan, C. A., Fishman, G. J., et al. 1993, ApJ Letters, 413, L101
Kumar, P., & Zhang, B. 2015, Phys. Rep., 561, 1
MacFadyen, A. I., Woosley, S. E., & Heger, A. 2001, ApJ, 550, 410
Nappo, F., Pescalli, A., Oganesyan, G., et al. 2017, A&A, 598, A23
Narayan, R., & Yi, I. 1995, ApJ, 444, 231
Paczynski, B., & Rhoads, J. E. 1993, ApJ Letters, 418, L5
Rees, M. J. 1988, Nature, 333, 523
Strubbe, L. E., & Quataert, E. 2009, MNRAS, 400, 2070
Yuan, F., & Narayan, R. 2014, ARA&A, 52, 529

7.7 Extragalactic Nuclear Transients

Miguel Pérez-Torres (IAA-CSIC), Seppo Mattila (Turku Univ.), Antxon Alberdi (IAA-CSIC), Rob Beswick (JBCA)

Unbiased all-sky surveys over the last decade have revolutionised our view of the transient sky. However, while thousands of core-collapse supernovae (CCSNe) are being discovered each year, transients within the nuclei of galaxies have been largely overlooked until recently, mainly because of limitations in spatially-resolved imaging in the optical/near-IR and imaging algorithms and techniques to recover those transients. Improvements in the latter are now starting to enable the efficient detection of transients at the centres of galaxies in ground-based, seeing-limited searches. The ESA-Gaia ongoing all-sky survey for transients is now also fully operational, and Adaptive Optics (AO) assisted near-IR searches have turned out to be powerful in the detection and localization of transients within galaxy nuclei.

The central few hundred pc of most galaxies are vibrant with transient activity. While unveiling the true nature of these transients is challenging, recent availability of detailed multi-wavelength monitoring starts to show very encouraging results in making accessible the study of extragalactic nuclear transients, which seem to be made up of several populations:

7.7.1 Tidal disruption events

For several decades, astronomers have speculated that a hapless star could wander too close to a nuclear supermassive black hole (SMBH) and be torn apart by tidal forces (Rees, 1988). Despite their importance, many aspects of tidal disruption events (TDEs) are poorly understood. The observed rate and energy of TDEs is significantly lower than expected (e.g., Stone, & Metzger 2016). Optically selected TDEs appear to prefer post-merger and post-starburst host galaxies, which could be related to high stellar densities or perhaps to the presence of a binary SMBH at parsec separations. Radio observations of TDEs can probe also the existence, and pinpoint the exact location, of a hidden AGN (e.g., Mattila et al. 2018).

7.7.2 Nuclear supernovae

The properties and rates of core-collapse supernovae (CCSNe) within the nuclear regions of galaxies have remained largely unexplored due to the surveys almost exclusively being ground-based, seeing-limited, and working at optical wavelengths. The characterisation of this population of SNe is important for both their relative and absolute rates and how these change as a function of the environment, and to better constrain the fraction of SNe missed by surveys as a function of redshift (Mattila et al., 2012) to allow detailed comparisons with the cosmic star formation history (Strolger et al., 2015).

VLBI observations of Arp299A (Pérez-Torres et al., 2009) and of Arp220 (Varenius et al., 2019) have unveiled prolific SN factories in the central 200 pc of their galaxy nuclei. Furthermore, a fraction of the nuclear events can be unusually energetic as a result of an efficient conversion of the SN kinetic energy into radiation by the dense ambient medium. In the dense environments, runaway collisions could form more massive stars (Portegies-Zwart & van den Heuvel 2007), potentially leading to unusually high energetic and radiatively efficient SNe. If injections of $\gtrsim 10^{52}$ erg/SN are common in the innermost nuclear regions, and efficiently coupled to the surrounding gas, SNe may play a more important role in driving outflows and regulating star formation than previously assumed.

7.7.3 Extremely energetic nuclear transients

A subset of extremely energetic nuclear transients has been recently identified. These events (e.g., PS1-10adi,Kankare et al. 2017) are characterised by relatively narrow emission lines, indicating the presence of a dense circumstellar medium, along with radiated energies above 10^{52} erg. There are a number of explanations that have been suggested for their origin: (1) an extremely energetic SN with efficient conversion of kinetic energy into radiation by interaction between a fast expanding ejecta and a dense ambient medium (Kankare et al., 2017); (2) a TDE where the stellar debris interacts with a pre-existing accretion disk; (3) interaction between accretion-disk winds and clouds in the surrounding broad-line region. Finally, our near-IR searches have recently identified a completely new class of extremely energetic ($\sim 10^{52}$ erg) heavily dust obscured nuclear transients in Luminous Infrared Galaxies (LIRGs), e.g. Arp299B-AT1 (Mattila & Pérez-Torres 2018), which we have identified to arise from a hidden TDE population. EVN observations of Arp299B-AT1 proved to be crucial in unveiling the nature of this transient, by tracing the evolution of both its radio light curve and morphology, which unequivocally indicates a jet-like structure (Fig. 51).

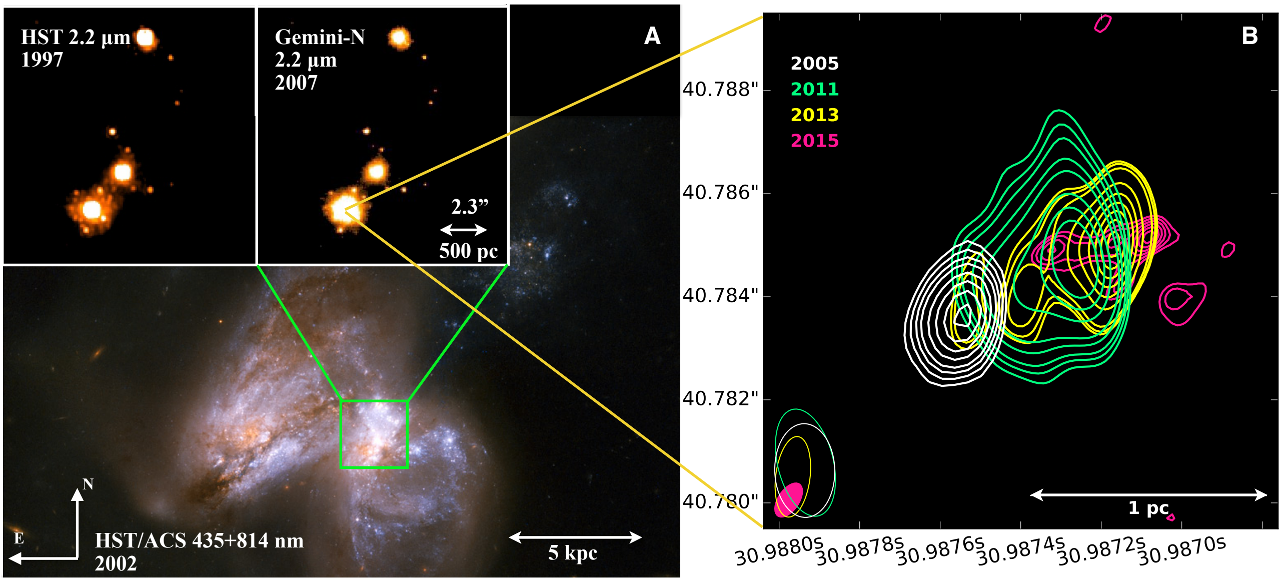

Figure 51: ***The transient Arp 299-B AT1 and its host galaxy Arp 299.*** ***(A)*** *A color-composite optical image from the HST, with high-resolution, 12.5 by 13 arcsec size near-IR 2.2-mm images [insets* ***(B)*** *and* ***(C)****] showing the brightening of the B1 nucleus (7).* ***(D)*** *The evolution of the radio morphology as imaged with VLBI at 8.4 GHz [7 × 7 milli-arcsec (mas) region with the 8.4-GHz peak position in 2005, right ascension (RA) = 11h28m30.9875529s, declination (Dec) = 58°33'40".783601 (J2000.0)]. The VLBI images are aligned with an astrometric precision better than 50 mas. The initially unresolved radio source develops into a resolved jet structure a few years after the explosion, with the center of the radio emission moving westward with time. The radio beam size for each epoch is indicated in the lower-right corner. (From Mattila et al. 2018.)*

7.7.4 Prospects for SKA-1 beyond band 5

Extragalactic nuclear transients are known to emit copious amount of synchrotron radio emission, which is partially suppressed mainly by surrounding thermal electrons, via the well-known free-free absorption mechanism with its characteristic absorption dependence with frequency, $\tau_\nu \propto \nu^{-2.1}$. This means that the early phases (first hours to days to months) of TDEs, nuclear SNe and other energetic extragalactic nuclear transients are likely to be hidden from our view at low-frequencies. If SKA-1 will go beyond band 5, this would allow for the possibility of tracing in detail the early evolutionary phases of these phenomena. Even more important is the combined use of SKA with the EVN and/or other arrays, which will allow to carry out VLBI observations with unprecedented angular resolution and sensitivity, allowing for the possibility of discerning apart the nuclear transient event from any putative underlying AGN, thanks to the sub-pc resolution (e.g., at 23 GHz, and assuming maximum baselines of $\sim$8000 km) and sensitivity (here assumed to be of $\sim 6\mu$Jy/beam after 1-hr on-source with SKA1, at band 6), up to luminosity distances of about 300 Mpc. The volume that could be sampled with better sensitivity that is currently possible would thus increase by at least an order of magnitude, which would allow to carry out studies on a meaningful statistical sample.

References

Kankare, E., Kotak, R., Mattila, S., et al. 2017, Nature Astronomy, 1, 865
Mattila, S., Dahlen, T., Efstathiou, A., et al. 2012, ApJ, 756, 111
Mattila, S., Pérez-Torres, M., Efstathiou, A., et al. 2018, Science, 361, 482
Pérez-Torres, M. A., Romero-Cañizales, C., Alberdi, A., et al. 2009, A&A, 507, L17
Portegies Zwart, S. F., & van den Heuvel, E. P. J. 2007, Nature, 450, 388
Rees, M. J. 1988, Nature, 333, 523
Stone, N. C., & Metzger, B. D. 2016, MNRAS, 455, 859
Strolger, L.-G., Dahlen, T., Rodney, S. A., et al. 2015, ApJ, 813, 93
Varenius, E., Conway, J. E., Batejat, F., et al. 2019, A&A, 623, A173